

Michael Mains · J.R. Blough *Editors*

# Topics in Modal Analysis & Testing, Volume 10

Proceedings of the 35th IMAC, A Conference and Exposition  
on Structural Dynamics 2017



# Conference Proceedings of the Society for Experimental Mechanics Series

## *Series Editor*

Kristin B. Zimmerman, Ph.D.  
Society for Experimental Mechanics, Inc.,  
Bethel, CT, USA

More information about this series at <http://www.springer.com/series/8922>

Michael Mains • J.R. Blough  
Editors

# Topics in Modal Analysis & Testing, Volume 10

Proceedings of the 35th IMAC, A Conference and Exposition  
on Structural Dynamics 2017

*Editors*

Michael Mains  
Application Solutions - Structural Analysis  
Brüel & Kjær  
Cincinnati, OH, USA

J.R. Blough  
Michigan Technological University  
Houghton, MI, USA

ISSN 2191-5644                      ISSN 2191-5652 (electronic)  
Conference Proceedings of the Society for Experimental Mechanics Series  
ISBN 978-3-319-54809-8              ISBN 978-3-319-54810-4 (eBook)  
DOI 10.1007/978-3-319-54810-4

Library of Congress Control Number: 2017935404

© The Society for Experimental Mechanics, Inc. 2017

This work is subject to copyright. All rights are reserved by the Publisher, whether the whole or part of the material is concerned, specifically the rights of translation, reprinting, reuse of illustrations, recitation, broadcasting, reproduction on microfilms or in any other physical way, and transmission or information storage and retrieval, electronic adaptation, computer software, or by similar or dissimilar methodology now known or hereafter developed.

The use of general descriptive names, registered names, trademarks, service marks, etc. in this publication does not imply, even in the absence of a specific statement, that such names are exempt from the relevant protective laws and regulations and therefore free for general use.

The publisher, the authors and the editors are safe to assume that the advice and information in this book are believed to be true and accurate at the date of publication. Neither the publisher nor the authors or the editors give a warranty, express or implied, with respect to the material contained herein or for any errors or omissions that may have been made. The publisher remains neutral with regard to jurisdictional claims in published maps and institutional affiliations.

Printed on acid-free paper

This Springer imprint is published by Springer Nature  
The registered company is Springer International Publishing AG  
The registered company address is: Gewerbestrasse 11, 6330 Cham, Switzerland



# Preface

*Topics in Modal Analysis & Testing* represents one of ten volumes of technical papers presented at the 35<sup>th</sup> IMAC, A Conference and Exposition on Structural Dynamics, organized by the Society for Experimental Mechanics, and held in Garden Grove, California, January 30–February 2, 2017. The full proceedings also include volumes on *Nonlinear Dynamics*; *Dynamics of Civil Structures*; *Model Validation and Uncertainty Quantification*; *Dynamics of Coupled Structures*; *Sensors and Instrumentation*; *Special Topics in Structural Dynamics*; *Structural Health Monitoring & Damage Detection*; *Rotating Machinery*, *Hybrid Test Methods*, *Vibro-Acoustics and Laser Vibrometry*; and *Shock & Vibration, Aircraft/Aerospace and Energy Harvesting*.

Each collection presents early findings from experimental and computational investigations on an important area within Structural Dynamics. *Topics in Modal Analysis & Testing* represents papers on enabling technologies for Modal Analysis measurements and applications of Modal Analysis in specific application areas.

The organizers would like to thank the authors, presenters, session organizers, and session chairs for their participation in this track.

Cincinnati, OH, USA  
Houghton, MI, USA

M. Mains  
J.R. Blough

# Contents

<b>1</b>	<b>Fluid-Structure Interaction in a Labyrinth Gas Seal Coupled to a Flexible Stator</b> .....	<b>1</b>
	A. Dairien, F. Thouverez, L. Blanc, P. Héliès, and J. Dehouve	
<b>2</b>	<b>Modal Analysis of Tower Crane with Cracks by the Dynamic Stiffness Method</b> .....	<b>11</b>
	Dang Xuan Trong and Nguyen Tien Khiem	
<b>3</b>	<b>High-Noise High-Speed Footage Data in Experimental Modal Analysis</b> .....	<b>23</b>
	Jaka Javh, Janko Slavič, and Miha Boltežar	
<b>4</b>	<b>Morlet-Wave Damping Identification: Application to High-Speed Video</b> .....	<b>27</b>
	Janko Slavič, Marko Mihalec, Jaka Javh, and Miha Boltežar	
<b>5</b>	<b>Fluid-Coupled Vibration Control Inspired by Dragonfly Wings</b> .....	<b>31</b>
	Yunjie Wang, Yajun Yin, and Gangtie Zheng	
<b>6</b>	<b>Improving Modal Parameter Estimation by Complementary Output–Output Relations</b> .....	<b>37</b>
	Oscar Olarte and Patrick Guillaume	
<b>7</b>	<b>Operational Modal Analysis in Frequency Domain Using Gaussian Mixture Models</b> .....	<b>47</b>
	Ankit Chiplunkar and Joseph Morlier	
<b>8</b>	<b>Understanding Modal Vectors</b> .....	<b>55</b>
	George Fox Lang	
<b>9</b>	<b>Best Practices for Using Order-Based Modal Analysis for Industrial Applications</b> .....	<b>69</b>
	Emilio Di Lorenzo, Simone Manzato, Bart Peeters, Francesco Marulo, and Wim Desmet	
<b>10</b>	<b>Could the Veering Phenomenon be a Mechanical Design Instrument?</b> .....	<b>85</b>
	Carlo Rosso, Elvio Bonisoli, and Fabio Bruzzone	
<b>11</b>	<b>Impulse Excitation of Piezoelectric Patch Actuators for Modal Analysis</b> .....	<b>97</b>
	V. Ruffini, T. Nauman, and C.W. Schwingshackl	
<b>12</b>	<b>Modal Parameter Estimation in Multi-Patch Operational Modal Analysis: Perspectives and Approaches</b> ..	<b>107</b>
	D. Mironovs and S. Chauhan	
<b>13</b>	<b>Modeling and Nonlinear Parameter Identification of an Electric-Power Steering System</b> .....	<b>127</b>
	Cassio T. Faria, Giorgio Pulvirenti, and Theo Geluk	
<b>14</b>	<b>A Framework for Additive Manufacturing Process Monitoring &amp; Control</b> .....	<b>137</b>
	Ian T. Cummings, Megan E. Bax, Ivan J. Fuller, Adam J. Wachtor, and John D. Bernardin	
<b>15</b>	<b>Reliability of Using Stereo Photogrammetry to Estimate Modal Parameters</b> .....	<b>147</b>
	Danilo Damasceno Sabino, Peyman Poozesh, Joao Antonio Pereira, and Christopher Niezrecki	
<b>16</b>	<b>Constant Mass Metastructure with Vibration Absorbers of Linearly Varying Natural Frequencies</b> .....	<b>153</b>
	Katherine K. Reichl and Daniel J. Inman	

<b>17</b>	<b>Study on Random Decrement Signature Under Different Triggering Level and Length of Time History</b> ....	159
	Jinzhi Wu, Xiujuan Zheng, Jie Hu, Yigang Zhang, and Fuh-Gwo Yuan	
<b>18</b>	<b>Experimental Study on the Rotor Dynamics Influence Upon the Modal Characteristics of an Induction Machine</b> .....	167
	F. Chauvicourt, M. Ballweg, W. Desmet, H. Van der Auweraer, and C.T. Faria	
<b>19</b>	<b>Optimal Modal Parameter Estimation for Highly Challenging Industrial Cases</b> .....	173
	Mahmoud El-Kafafy, Bart Peeters, and Patrick Guillaume	

# Chapter 1

## Fluid-Structure Interaction in a Labyrinth Gas Seal Coupled to a Flexible Stator

A. Dairien, F. Thouverez, L. Blanc, P. Héliès, and J. Dehouve

**Abstract** This paper deals with the prediction of aeroelastic instabilities occurring in labyrinth gas seal of turbomachinery components. The purpose of this work is to carry out a numerical investigation on an advanced labyrinth gas seal model comprising a non-deformable rotor, and a flexible stator. The flexibility of the static part induces pressure and velocity fluctuations within the leakage flow. The model retains several cavities formed by the teeth located on the shaft and a strong coupling between the fluid and the structure is assumed.

A qualitative analysis is performed to identify the various causes of aeroelastic instability occurrence. Then, a comparison with the literature is carried out in order to propose a better approach to predict such instabilities.

**Keywords** Fluid-structure coupling • Labyrinth gas seal • Turbomachinery • Aeroelastic instability • Nonlinearity

### Nomenclature

$t$	Time variable
$n$	Number of harmonics of the Fourier series
$i$	Cavity number
$\epsilon$	Order parameter
$\theta$	Angular position
$R_s$	Shaft radius
$R_c$	Stator radius
$y_i$	Linear function
$y_{1i}$	Periodic function
$x_{n,i}^c$	Time coefficient associated to cosine function
$x_{n,i}^s$	Time coefficient associated to sine function
$\mathbb{M}$	Mass matrix of the linear system
$\mathbb{C}$	Viscous damping matrix of linear system
$\mathbb{K}$	Linear stiffness matrix of the linear system
$\ddot{\mathbf{X}}$	Coefficients vector differentiated twice with respect to time

---

A. Dairien (✉)

École Centrale de Lyon, Laboratoire de Tribologie et Dynamique des Systèmes, UMR-CNRS 5513, 36 avenue Guy de Collongue, 69134 Écully Cedex, France

Airbus Safran Launchers, Forêt de Vernon, BP802, 27208 Vernon Cedex, France  
e-mail: [alexa.dairien@doctorant.ec-lyon.fr](mailto:alexa.dairien@doctorant.ec-lyon.fr)

F. Thouverez • L. Blanc

École Centrale de Lyon, Laboratoire de Tribologie et Dynamique des Systèmes, UMR-CNRS 5513, 36 avenue Guy de Collongue, 69134 Écully Cedex, France

P. Héliès

Airbus Safran Launchers, Forêt de Vernon, BP802, 27208 Vernon Cedex, France

J. Dehouve

Centre National d'Études Spatiales, Direction des Lanceurs, 52, rue Jacques Hillairet, 75612 Paris Cedex, France

$\dot{X}$	Coefficients vector differentiated once with respect to time
$X$	Coefficients vector in the time domain
$f_{ac}$	Acoustic frequency
$c$	Sound velocity

## 1.1 Introduction

Aerospace turbopumps usually use labyrinth gas seals to prevent the gas driving the turbine to leak in the gap between the rotor and the stator parts. Current trends in turbopumps design focus on the minimization of the clearances, so as to optimise the efficiency, and on the reduction of the stator weight. However, these trends may lead to aeroelastic instability issues which can damage the structures surrounding the labyrinth gas seal, mainly static parts according to post-mortem observations.

Since the 1960s, studies have been carried out to better understand and prevent such instabilities. Alford [2] was the first to show that the side support location of the seal has an importance in preventing self-excited vibrations. Alford discloses also a stability criterion which correlates pressure drop in the seal to natural frequency, weight, and length. A second criterion is later suggested by Abbot [1], involving the location of side support. His work reveals that if the support is located on the high pressure side, the seal is stable as long as the mechanical frequency is lower than the acoustic one. The phenomenon is reversed when support is located on the low pressure side.

To tackle these new challenges, more predictive models must be developed in order to take the stator flexibility and the leakages reduction issues into account. The purpose of this work is to carry out a numerical investigation on an advanced labyrinth gas seal model involving a non-deformable rotor, and a flexible stator. The flexibility of the static part induces pressure and velocity fluctuations within the leakage flow. The model retains several cavities defined by the teeth located on the shaft and a strong coupling between the fluid and the structure is assumed.

## 1.2 Strong Fluid-Structure Coupling

The model governing the behaviour of the flow within a cavity is inspired by Childs analytical model and Navier-Stokes equations [3]. The model describing the flow is then coupled to a mechanical system corresponding to a flexible stator (cf. Fig. 1.1b). A cylinder model, which takes into account the diameter modes in the plane orthogonal to the flow and a normalized longitudinal displacement following the first bending mode, is used (cf. Fig. 1.1c). The normalized longitudinal displacement is assumed to be proportional to the square of the distance from the bearing location. Assuming a strong coupling implies that the action of the fluid to the structure is taken into account and conversely. It is especially interesting to work with a strong coupling for a such confined environment.

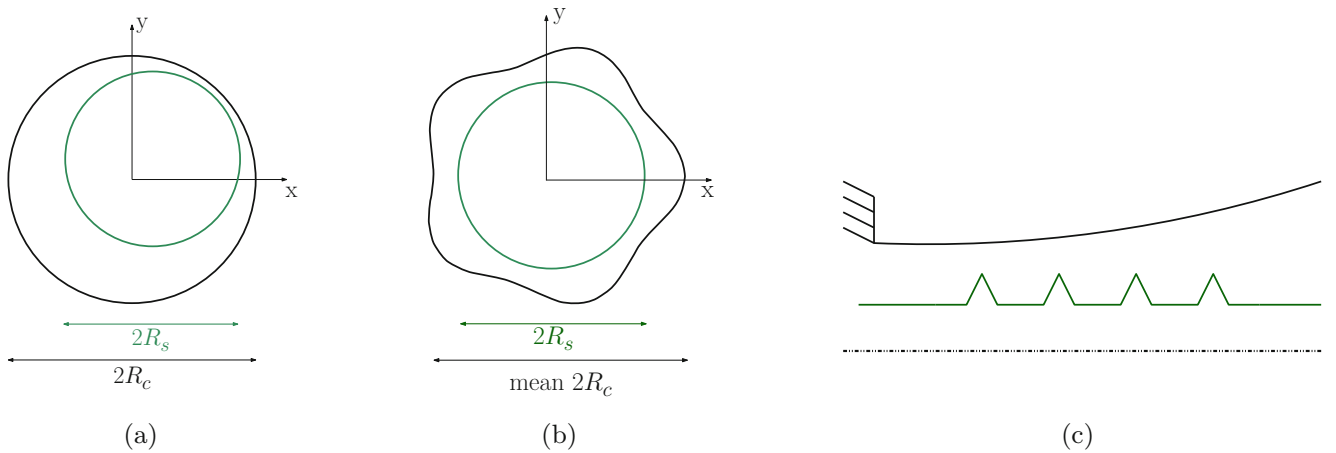


**Fig. 1.1** (a) Childs's model : elliptic movement of the rotor, non-deformable rotor, non-deformable stator. (b) Flexible cylinder model: fixed and non-deformable rotor, fixed and flexible stator. (c) Flexible cylinder model : visualisation of normalized longitudinal displacement following the first bending mode

The structure can be supported on the low pressure side as well as on the high pressure side. Taking into account these boundary conditions allows a comparison with the results given by Abbott [1].

The coupled system obtained is made of nonlinear differential equations. To overcome these nonlinearities, a perturbation method is used. It consist in determining approximate solutions of the nonlinear equations by a power series of a scale factor parameter ( $\epsilon$ ) associated to the nonlinear terms and truncated at the first order. This method allows to turn a nonlinear system into a set of linear problems. The solution can be written as follow:

$$y_i(N, t, \theta) = y_{0i} + \epsilon y_{1i}(N, t, \theta) \quad (1.1)$$

where the periodic function  $y_{1i}$  is sought in the form :

$$y_{1i}(N, t, \theta) = \sum_{n=1}^N (x_{n,i}^c(t) \cos(n\theta) + x_{n,i}^s(t) \sin(n\theta)) \quad (1.2)$$

with  $n$ , corresponding to the number of harmonics of the Fourier series,  $i$  the cavity number,  $\theta$  the angular position. At zeroth order ( $\epsilon = 0$ ), the nonlinear differential equations become state equations describing the mean leakage flow, pressure and circumferential velocity within the seal (without any stator displacement). The flow becomes sonic just after going through the last tooth. Then, at first order, the system is solved by replacing the variable  $y_{1i}$  by its expression (1.2), and searching for the values  $\{x_{n,i}^c, x_{n,i}^s\}$ . These coefficients are related to three variables : radial displacement, circumferential velocities, and pressures within cavities.

To solve this two-dimensional problem, a Galerkin approach with a Fourier transform with respect to the space variables, is used. The system can be described by the second order homogeneous differential equation:

$$\mathbb{M}\ddot{X} + \mathbb{C}\dot{X} + \mathbb{K}X = 0 \quad (1.3)$$

where  $X$  is the coefficients vector  $\{x_{n,i}^c, x_{n,i}^s\}$  with  $n = 1, \dots, N$  corresponding to the trigonometric functions in Eq. (1.2).

The model comprises a pre-rotating flow which can be combined with the axial leakage flow, in addition to the shaft rotation. Because of the circumferential velocity within each seal cavity, shear stress in circumferential direction are acting on both stator and rotor walls. In this work, the model is extended to several cavities. The upstream and downstream cavities modal participations are considered within the  $n$ th cavity equations

### 1.3 Validation of the Zeroth Order

The table below (cf. Table 1.1) gives an axial mass flow rate comparison between current work and calculations found in the literature for validation purposes (Fig. 1.2).

**Table 1.1** Comparative axial mass flow rate and pressures distributions within the labyrinth seal

	Current work	Dursen [4]	Rosen [6]	Experimental [4]
Mass flow rate ( $\text{kg s}^{-1}$ )	0.02036	0.02072	0.02117	0.02
Pressure within cavity (kPa)	225.447	224.592	222.781	222.5

Seal operating conditions		Seal geometry	
Inlet pressure	241.3 kPa	No. of teeth	2
Outlet pressure	206.8 kPa	Shaft radius	101.60 mm
Inlet temperature	298.2 K	Clearance	0.16 mm
Inlet swirl velocity	16.8 m/s	Tooth pitch	12.91 mm
Shaft rotational speed	1800 rpm	Tooth height	5.03 mm
		Tooth tip width	0.20 mm

**Fig. 1.2** Seal geometry and study conditions [4]

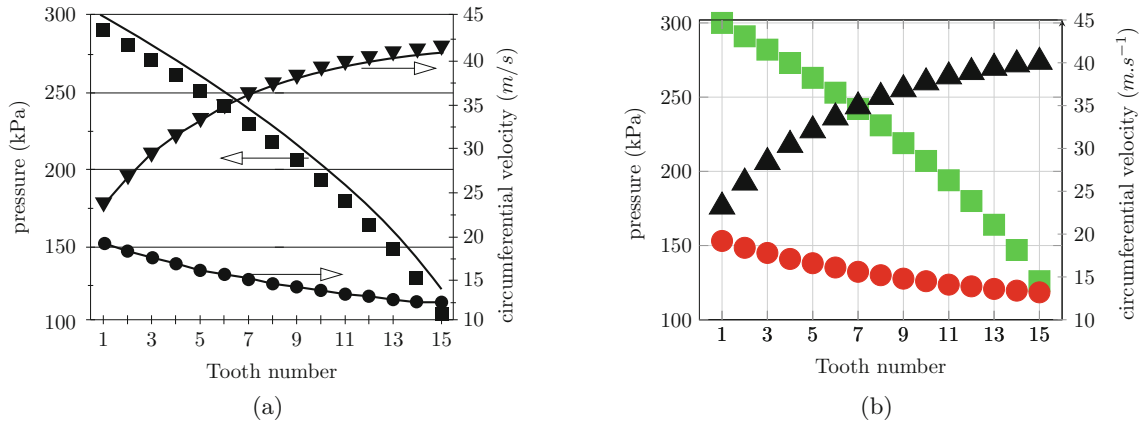


**Fig. 1.3** Pressures distributions and circumferential velocity within the labyrinth gas seal. (a) Pressures distributions and circumferential velocity within the labyrinth gas seal (Dursen [4] and Rosen [6]). (b) Pressures distributions and circumferential velocity within the labyrinth gas seal of current works

Mass flow rate and pressure calculations correlate rather well with the literature results. Dursen's works [4] also present pressures distributions and circumferential velocities obtained by Rosen and himself on Fig. 1.3 ( $\blacktriangledown$  circumferential velocity with 16,000 rpm shaft rotation,  $\bullet$  circumferential velocity with no shaft rotation,  $\blacksquare$  pressures distributions).

The seal geometry comprises 16 teeth, the shaft radius is 77 mm and the radial clearance is 0.3 mm. The inlet pressure is taken equal to 308 kPa and the outlet pressure is 101 kPa. The temperature of the seal is 300 K and the preswirl is equal to  $20 \text{ m s}^{-1}$ .

These graphs allow a direct comparison of pressures distributions and circumferential velocity obtained for a stationary seal. Our results are quite similar to those found in the literature. The model at Zeroth order is verified and validated.

## 1.4 Stability Analysis

Some modal analysis results of different configurations are presented in this section. All parameters values are given below Figs. 1.4, 1.5, 1.9 and 1.10. On the left-hand-side of the page (cf. Figs. 1.7a, 1.6a, 1.12a, 1.11a) are gathered the evolution of acoustic and structural frequencies according to the inlet circumferential velocity. On the right-hand-side (cf. Figs. 1.7b, 1.6b, 1.12b, 1.11b) are plotted the corresponding evolution of the reduced damping ratio. Acoustic modes are obtained from the linearization of Navier-Stokes equations [cf. Eq. (1.2)]. The seal becomes unstable when one of the reduced damping ratio curves becomes positive. The two nodal diameter mode is studied in this section.

### 1.4.1 Sensitivity to the Radial Clearance and Swirl Velocity

A sensitivity study to the radial clearance is proposed in this section. Only the preswirl is taken into account (no shaft rotation). The model is shown on Figs. 1.4 and 1.5 for two different values of radial clearance. On both cases, uncoupled modes are plotted with dashed lines. When there is neither coupling nor preswirl, the natural frequency of the flexible cylinder is lower than the acoustic one. The theoretical acoustic frequency for a 2 nodal diameter mode is given by the formula :

$$f_{ac} = \frac{n_d c}{2\pi R} = 1363 \text{ Hz} \quad (1.4)$$

where  $n_d$  is the nodal diameter mode,  $c$  the sound velocity and  $R$  the shaft radius. The actual acoustic frequency is lower than the theoretical one because of fluid damping coefficients related to pressure terms in Navier-Stokes linearized equations.

The model is solved in the fixed frame of reference. The flow vibration which evolves in the rotating frame of reference is split into two acoustic waves : forward and backward, respectively (cf. Figs. 1.6a, 1.7a). An analogy with a Campbell diagram can be made except that we are looking at the evolution of acoustic and structural frequencies according to the inlet circumferential velocity instead of the shaft velocity. There is a crossing point between the backward acoustic wave and the

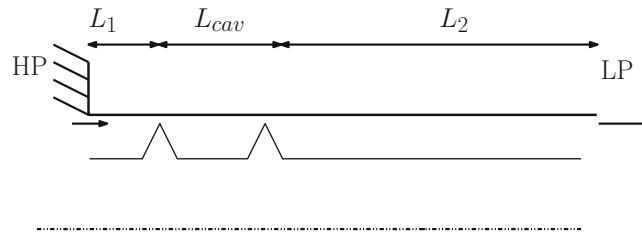


**Fig. 1.4** Configuration HP-1: 50  $\mu\text{m}$  radial clearance,  $L_1 = 5$  mm, one cavity,  $L_{cav} = 50$  mm,  $L_2 = 100$  mm, thickness: 4.5 mm, inlet pressure: 8 bars, outlet pressure: 1 bar, nodal diameter :  $n_d = 2$ , material : aluminium, no shaft rotation

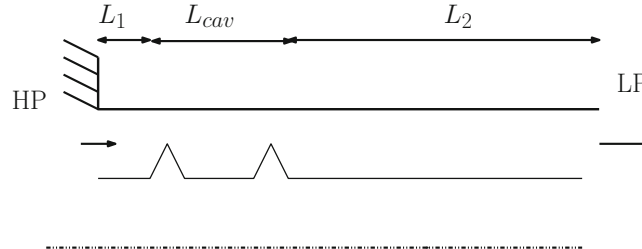


**Fig. 1.5** Configuration HP-2: 150  $\mu\text{m}$  radial clearance,  $L_1 = 5$  mm, one cavity,  $L_{cav} = 50$  mm,  $L_2 = 100$  mm, thickness: 4.5 mm, inlet pressure: 8 bars, outlet pressure: 1 bar, nodal diameter :  $n_d = 2$ , material : aluminium, no shaft rotation

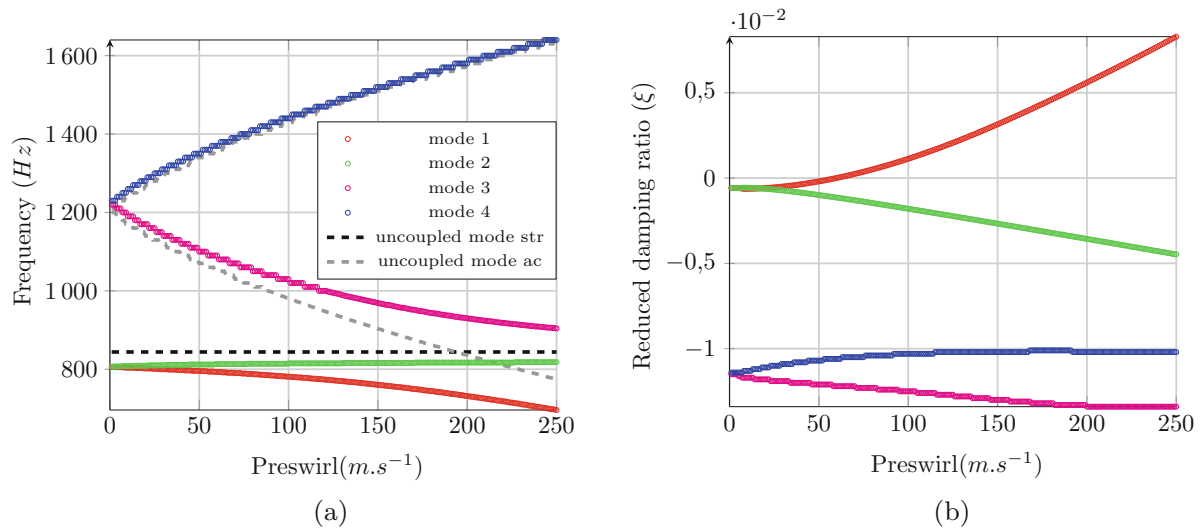


**Fig. 1.6** Configuration HP-1 (cf. Fig. 1.4). (a) Frequency. (b) Reduced damping ratio

structural wave. At that point the frequency resonance of the structure is the same than for the acoustic wave. A frequency coincidence between an acoustic and a structural mode is associated to a state change (cf. [1]).

If all attention is paid to the coupled system, it can be noticed that acoustic mode frequencies are higher than the uncoupled ones (cf. Figs. 1.6a, 1.7a). Also, structural frequencies are lower when only structure is considered. A coupling operates instantaneously between the structure and the circumferential flow within the cavity.

The structural mode is also split into two modes because of the coupling (cf. Figs. 1.6a, 1.7a). A slow veering is observable between the backward acoustic and backward structural modes. An exchange of mode shapes between the flow and the structure arises. A crossing point is no longer observed because of the strong interaction between the circumferential flow within the cavity and the stator.

On Fig. 1.6b, the reduced damping ratio associated to the backward structural mode becomes unstable at a certain preswirl velocity value. Contrary to the uncoupled system which tells us that critical velocity is around  $200 \text{ m s}^{-1}$ , the coupled one becomes unstable at a lower preswirl velocity. The point where the system get unstable mainly depends on the radial clearance. Indeed, when the radial clearance is increased (cf. Fig. 1.7a), the instability disappears. Moreover, it has been



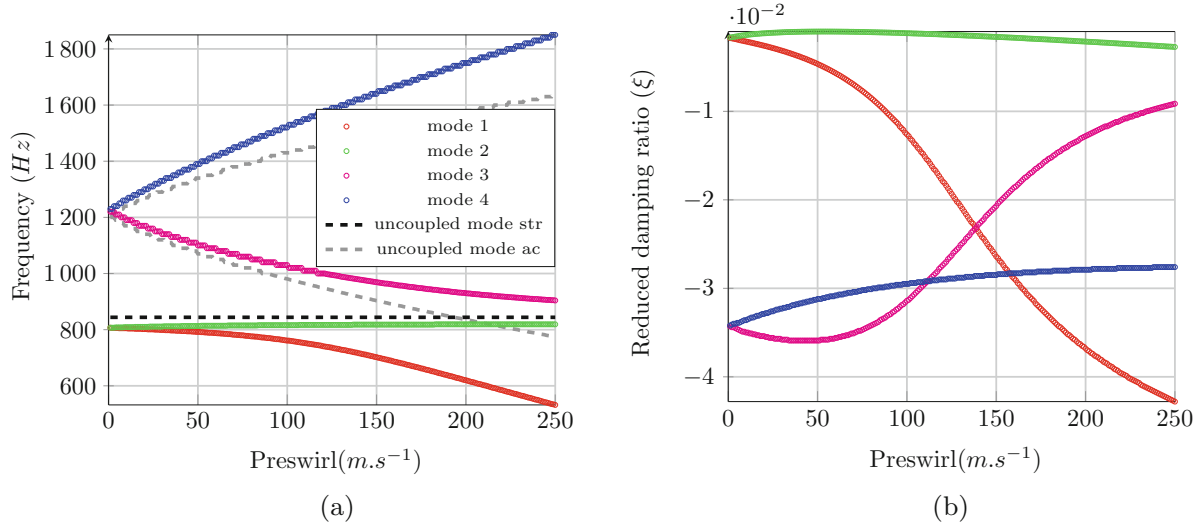


**Fig. 1.7** Configuration HP-2 (cf. Fig. 1.5). (a) Frequency. (b) Reduced damping ratio

observed that for an intermediary radial leakage clearance, the instability arises at the same circumferential velocity than the uncoupled frequency coincidence point. Minimizing radial clearance drives ultimately to higher swirl velocities and thus to aeroelastic stability issues.

#### 1.4.2 Three-Cavities Labyrinth Gas Seal and Sensitivity to the Teeth Position

This section focuses on a labyrinth gas seal comprising three cavities. The results obtained on the uncoupled model are plotted on Fig. 1.8. Then, two configurations are investigated to compare the sensitivity to the teeth position: the first one has teeth near the fixed support (cf. Fig. 1.9) and the second one has teeth far from it (cf. Fig. 1.10).

The plot on Fig. 1.8 shows that there are three pairs of acoustic modes due to the three cavities. Three intersections with the structural mode can be observed. All acoustic frequencies are quite similar at  $0 m.s^{-1}$ , but a closer look reveals some small differences. This can be explained by the fact that mean pressures are different within each cavity and also, the modal participation of the upstream and downstream cavities are taken into account within the  $n$ th cavity equations.

When teeth are located near the high pressure side support, a well-defined veering is visible (cf. Fig. 1.11a). In that configuration, an exchange of mode shapes between the fluid and the structure around  $100 m.s^{-1}$  occurs. The swap is also visible on the reduced damping ratio. The curves on Fig. 1.11b still remain on the negative plane of the plot. The system remains stable at any value of inlet swirl velocity. On the other hand, an aeroelastic instability appears when teeth are located far from the high pressure side support (cf. Fig. 1.12b). The teeth position has thus an impact on the stability of the system. Alford's experimental results allow us to know the critical value of the amplitude of deflection where stability issues occur [2]. The analytical cylinder model is able to give a relative amplitude of the radial displacement which allows us to agree with Alford's work.

At zero preswirl velocity, one of the three cavity modes moves to a higher frequency (cf. Fig. 1.12a). A stronger coupling than the previous case occur between flows within cavities in addition to the coupling between structure and the gas flow. It has been observed on further results that the highest acoustic frequencies are related to the modal participation corresponding to the first and second cavities, respectively, where means pressures are the highest.

Tangential velocities in real aerodynamics and thermodynamics conditions are much higher than  $250 m.s^{-1}$ . Parameters values are chosen in order to be compared to upcoming experimental investigations. Also, Malvano [5] shows that if there is a sonic section, it can only be at the outlet section of the seal itself. The current model verifies the sonic condition before solving the perturbation equations.

First results presented here are only focused on the high pressure side support and allow us to start a comparison with Abbott's findings [1]. The mechanical frequency vibration is taken to be lower than the acoustic one for a two nodal diameter.

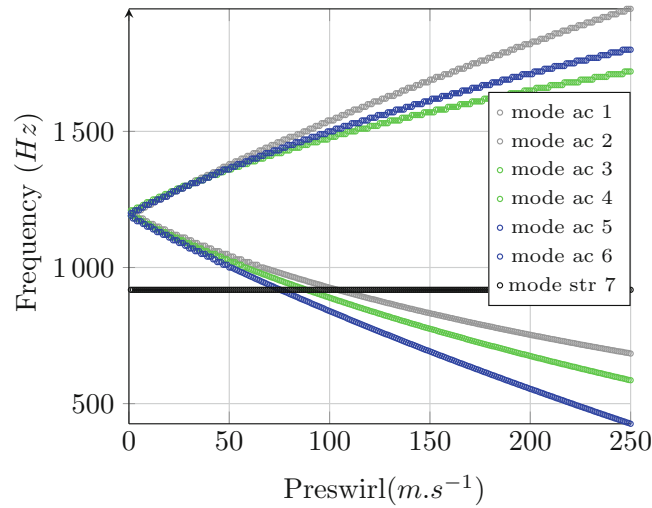


**Fig. 1.8** Structural and acoustic natural frequencies of the uncoupled system

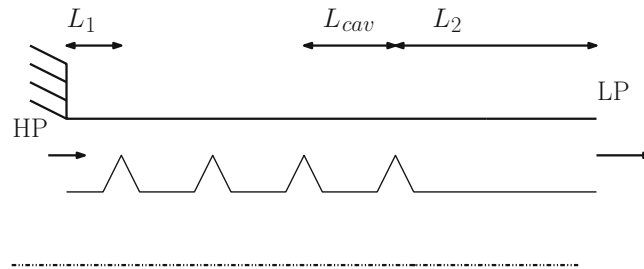


**Fig. 1.9** Configuration HP-3  $L_1 = 5$  mm,  $L_{cav} = 25/3$  mm,  $L_2 = 100$  mm, thickness: 4.5 mm, clearance:  $100 \mu\text{m}$ , inlet pressure: 16 bars, outlet pressure: 1 bar, nodal diameter :  $n_d = 2$ , material : aluminium, no shaft rotation

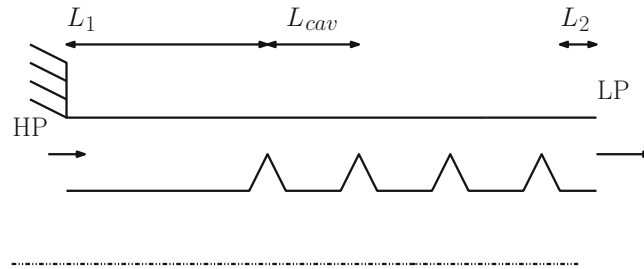


**Fig. 1.10** Configuration HP-4  $L_1 = 100$  mm,  $L_{cav} = 25/3$  mm,  $L_2 = 5$  mm, thickness: 4.5 mm, clearance:  $100 \mu\text{m}$ , inlet pressure: 16 bars, outlet pressure: 1 bar, nodal diameter :  $n_d = 2$ , material : aluminium, no shaft rotation

In this conditions, the reduced damping ratio, related to the mechanical frequency, is stable for a particular range of circumferential velocity values : the seal supported on the high pressure side is stable as long as the inlet circumferential velocity is below a critical value.

Contrary to Abbott’s findings, current work uses the inlet circumferential velocity as a variable input parameter which highly influences the aeroelastic seal stability. Further results have been conducted on low pressure side support and reveal that the aeroelastic instability occurs from a lower inlet swirl velocity than a high pressure side support. Thus, there is a range of preswirl velocities where the low pressure side support is unstable whereas the high pressure one is not. This observation is in agreement with Abbott’s work.

Actually, a comparison with Abbott’s results is a complex process for several reasons. First, his model assumes a mechanical vibration of a given amplitude, number of nodal diameters and frequency, which are used as input in the flow calculations. The coupling is not as strong as within the present work. In addition to that, the paper does not provide geometric and flow key informations.

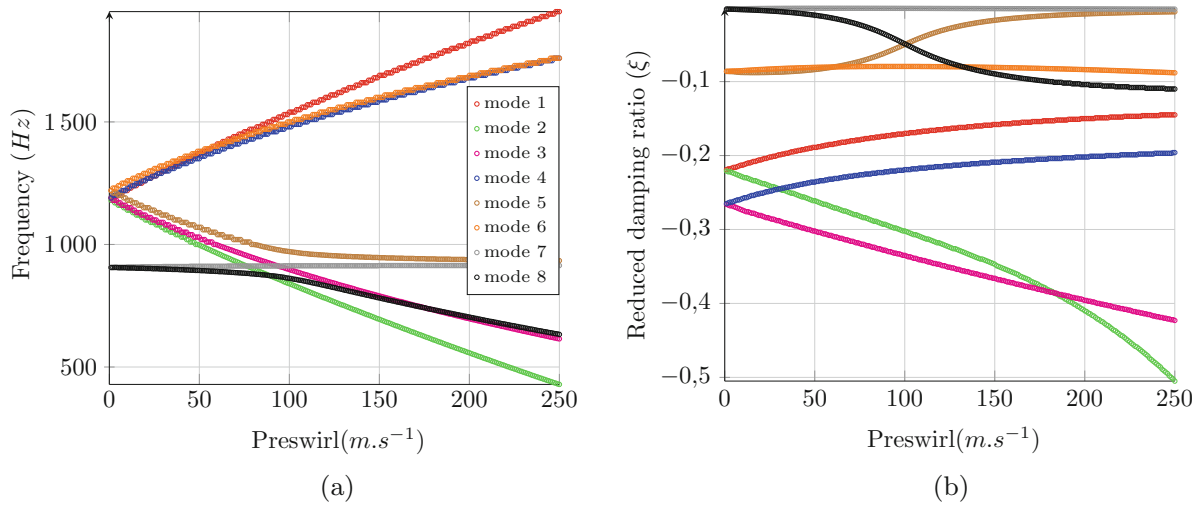


**Fig. 1.11** HP-3 configuration. (a) Frequency. (b) Reduced damping ratio

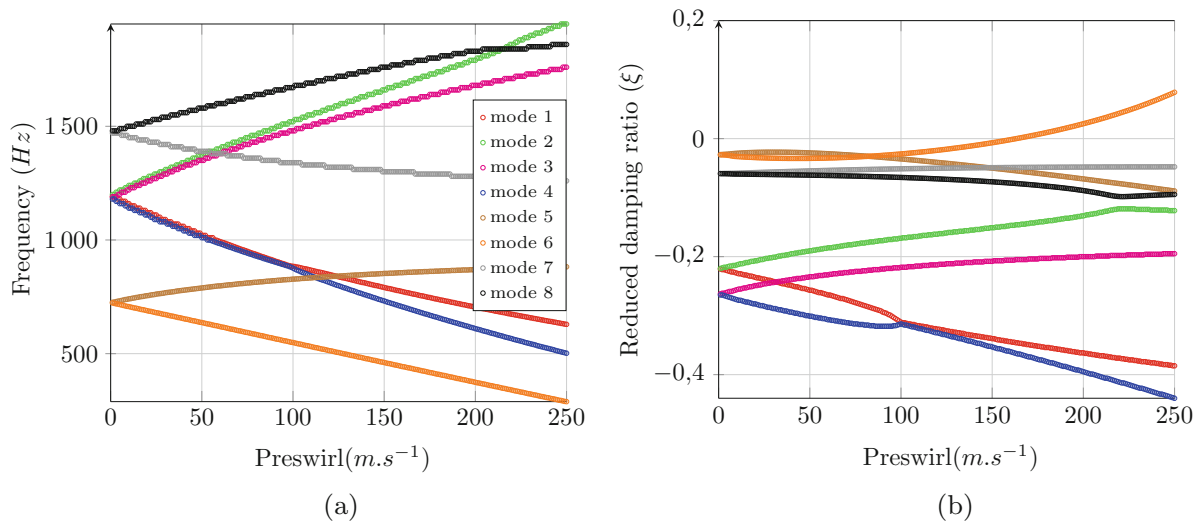


**Fig. 1.12** HP-4 configuration. (a) Frequency. (b) Reduced damping ratio

To conclude, in both cases (high and low side support locations), the instability indeed occurs, and on a particular range of preswirl, the present is in agreement with the left-hand-side of Abbott's graphs ( $f_m < f_{ac}$ ).

## 1.5 Conclusion

This investigation takes into account a strong coupling between the dynamics of the stator, including diameter modes, and the behavior of the labyrinth seal. The model is able to take into account flow interactions between seal cavities, shaft rotation, inlet swirl velocity and the high or low pressure side support.

The stability phenomenon is very sensitive to the radial clearance and to the inlet circumferential velocity. The wear of the teeth or of the abradable in operation should reduce the risk for an instability to occur but it is still important to counteract instability occurrence mainly because it can promptly lead to high cycle fatigue failures. The model used in this paper partially agrees with literature.

Concerning the side support position, teeth location within the seal may have an impact on seal stability at a specific preswirl value. The model is in agreement with Alford's conclusions.

It has been noticed that there is a range of preswirl velocities where the low pressure side support is unstable whereas the high pressure one is not. This observation is in agreement with a part of Abbott's work and go further by considering the inlet swirl velocity as a variable.

Conducting a modal analysis on a rotordynamic model strongly coupled to the gas flow is a novel and interesting approach to investigate the coupling between the fluid and the stator. Here, it is highlighted that inlet swirl velocity is responsible for instability to occur. This study provides better predictions capabilities x—since more interactions are taken into account—along with new interesting insights on the dynamics of such systems, especially in terms of aeroelastic stability.

**Acknowledgements** The authors are grateful to Airbus Safran Launchers and the Centre National d'études Spatiales for providing the financial support for this project, and for giving permission to publish this work.

## References

1. Abbott, D.R.: Advances in labyrinth seal aeroelastic instability prediction and prevention. *J. Eng. Power* **103**(2), 308–312 (1981)
2. Alford, J.S.: Protection of labyrinth seals from flexural vibration. *J. Eng. Power* **86**(2), 141 (1964)
3. Childs, D.: An Iwatsubo-based solution for labyrinth seals: comparison to experimental results. *J. Eng. Gas Turbines Power* **108**(2), 325–331 (1986)
4. Dursun, E., Kasakia Jacob, Y.: Air flow in cavities of labyrinth seals. *Int. J. Eng. Sci.* **33**(15), 2309–2326 (1995)
5. Malvano, R., Vatta, F., Vigliani, A.: Rotordynamic coefficients for labyrinth gas seals: single control volume model. *Meccanica* **36**(6), 731–744 (2001)
6. Rosen, M.C.: Report uva/643092/mae86/346. Univ. of Virginia (1986)

## Chapter 2

# Modal Analysis of Tower Crane with Cracks by the Dynamic Stiffness Method

Dang Xuan Trong and Nguyen Tien Khiem

**Abstract** The dynamic stiffness method is a powerful approach that enables to obtain more exact solution in dynamic analysis of structures, especially, when high frequency vibrations need to be investigated. On the other hand, the dynamic characteristics of high frequency modes of a structure are more sensitive to local damage such as crack. Therefore, the dynamic stiffness method gets to be a most efficient approach to analysis and identification of engineering structures. This report is devoted to modal analysis of tower crane with cracks by using the dynamic stiffness method. First, dynamic stiffness model of tower crane is conducted on the base of cracked beam element where crack is treated by an equivalent spring. Then, the established model is used for modal analysis of a typical tower crane.

**Keywords** Tower crane • Cracked structure • Modal analysis • Dynamic stiffness method

## 2.1 Introduction

Cranes are frequently employed in the practice of construction and transportation. Since they are getting larger and higher the structural health monitoring needs to undertake regularly. One of the task in the structural health monitoring is to check for integrity of cranes that implies detecting possible damages in the structure before they could lead to an accident. Both theoretical investigation and practical application show that the vibration-based technique is the most efficient up-to-day in damage detection problem of structures. Fundamental of the vibration-based technique is to use dynamical characteristics as indicators for damage identification. Therefore, dynamic analysis is an important subject in the structural health monitoring of cranes.

A comprehensive review on dynamics and control of cranes was given by Abdel-Rohman et al. [1] where the simplest models of cranes were discussed. The finite element method was employed by Ju and Choo [2–4], Yu and Han [5] and Nasser [6] for dynamic analysis of tower cranes in various formulation of the problem. Dynamics of overhead and mobile cranes has been studied also in [7–9] respectively. It has to note herein that the study accomplished by Wang et al. [10] is the first effort to apply the dynamic analysis of cranes for their damage identification based on the finite element model.

This study is devoted to develop the dynamic stiffness method for modeling dynamics of cracked tower crane. Herein, crack is treated as local damage that makes structural stiffness reduced at a member position. So the crack can be modeled by an equivalent spring, stiffness of which is calculated from severity of the damage (crack depth). Numerical analysis of natural frequencies in dependence on the crack position and depth is carried out to illustrate the developed theory.

---

D.X. Trong  
Occupational Safety and Health Inspection and Training Joint Stock Company, 733 Xo Viet Nghe Tinh, Ward 26,  
Binh Thanh District, Ho Chi Minh City, Vietnam  
e-mail: [dotrongatldtp@yahoo.com](mailto:dotrongatldtp@yahoo.com)

N.T. Khiem (✉)  
Institute of Mechanics, VAST, 264, Doi Can, Ba Dinh, Hanoi, Vietnam  
e-mail: [khiemvch@gmail.com](mailto:khiemvch@gmail.com); [ntkhiem@imech.vast.vn](mailto:ntkhiem@imech.vast.vn)

## 2.2 Dynamic Stiffness Modeling of Cracked Beam Element

### 2.2.1 Dynamic Stiffness Method Formulation

Let's consider a structure element, motion of which is described by the equation

$$\mathbf{L}\{u(x, y, z, t)\} + \mathbf{M}\ddot{u}(x, y, z, t) = q(x, y, z, t), \quad (2.1)$$

where  $u(x, y, z, t)$ ,  $q(x, y, z, t)$  stand for distributed displacement and load fields,  $L$  is a linear differential operator,  $M$  represents the inertia operator. Using the Fourier transform the Eq. (2.1) becomes

$$\mathbf{L}\{U(x, y, z, \omega)\} - \omega^2 \mathbf{M}\{U(x, y, z, \omega)\} = Q(x, y, z, \omega), \quad (2.2)$$

where  $U(x, y, z, \omega)$ ,  $Q(x, y, z, \omega)$  are complex amplitudes of the displacement and load fields. Suppose that a nodal displacement  $\{U_e(\omega)\}$  and nodal force  $\{N_e(\omega)\}$  amplitudes in the local coordinates are defined as

$$\{U_e(\omega)\} = \mathbf{d}\{U(\bar{x}, \bar{y}, \bar{z}, \omega)\}; \{N_e(\omega)\} = \mathbf{N}\{U(\bar{x}, \bar{y}, \bar{z}, \omega)\}, \quad (2.3a,b)$$

$\mathbf{d}$ ,  $\mathbf{N}$  are differential operators and  $(\bar{x}, \bar{y}, \bar{z})$  - coordinates of the element nodes. It was proved that general solution of the differential equation (2.2) can be represented in the form

$$\{U(x, y, z, \omega)\} = [\mathbf{H}(x, y, z, \omega)]\{C\} + \{U_q(x, y, z, \omega)\} \quad (2.4)$$

where  $C$  is a constant vector;  $H$  is a matrix-function composed of independent solution of homogeneous equation

$$\mathbf{L}\{U(x, y, z, \omega)\} - \omega^2 \mathbf{M}\{U(x, y, z, \omega)\} = 0, \quad (2.5)$$

and  $U_q(x, y, z, \omega)$  is a particular solution of Eq. (2.2). Putting (2.4) into (2.3a) yields

$$\{U_e(\omega)\} = \mathbf{d}\{U(\bar{x}, \bar{y}, \bar{z}, \omega)\} = [\mathbf{B}_e(\omega)]\{C\} + \{\bar{U}_q(\omega)\}, \quad (2.6)$$

where

$$[\mathbf{B}_e(\omega)] = \mathbf{d}[\mathbf{H}(\bar{x}, \bar{y}, \bar{z}, \omega)]; \{\bar{U}_q(\omega)\} = \mathbf{d}\{U_q(\bar{x}, \bar{y}, \bar{z}, \omega)\}. \quad (2.7)$$

Therefore,  $\{C\} = [\mathbf{B}_e(\omega)]^{-1}\{U_e(\omega) - \bar{U}_q(\omega)\}$  and

$$\{U(x, y, z, \omega)\} = [\mathbf{H}(x, y, z, \omega)] \cdot [\mathbf{B}_e(\omega)]^{-1}\{U_e(\omega) - \bar{U}_q(\omega)\} + \{U_q(x, y, z, \omega)\}. \quad (2.8)$$

Using (2.8) the nodal force (2.3b) is calculated as

$$\{N_e(\omega)\} = [\mathbf{D}_e(\omega)]\{U_e(\omega)\} - \{P_e(\omega)\} \quad (2.9)$$

with

$$[\mathbf{D}_e(\omega)] = \mathbf{N}[\mathbf{H}(x, y, z, \omega)] \cdot [\mathbf{B}_e(\omega)]^{-1}; \{P_e(\omega)\} = \mathbf{N}\{\tilde{U}_q(x, y, z, \omega - U_q(x, y, z, \omega))\};$$

$$\{\tilde{U}_q(x, y, z, \omega)\} = [\mathbf{H}(x, y, z, \omega)] \cdot [\mathbf{B}_e(\omega)]^{-1}\{\bar{U}_q(\omega)\}. \quad (2.10)$$

The frequency-dependent matrix  $[\mathbf{D}_e(\omega)]$  and vector  $\{P_e(\omega)\}$  in (2.10) are called respectively dynamic stiffness and nodal load vector of the structure element.

For a structure that consists of  $n$  elements the dynamic stiffness model is conducted as follows. Assuming that  $T_e$  is transfer matrix between local (for an element) and total (for whole structure) coordinates, i.e.

$$U_e = T_e U; N_e = T_e N; P_e = T_e P, \quad (2.11)$$

where  $U; N; P$  are respectively total displacement, internal and external force vectors, Eq. (2.9) can be rewritten as

$$\{N(\omega)\}_e = [T_e^{-1} D_e(\omega) T_e] \{U(\omega)\} - \{P(\omega)\}_e \quad (2.12)$$

Since all internal forces are balanced at every node,  $\sum_e \{N(\omega)\}_e = 0$ , we obtain

$$[D(\omega)] \{U(\omega)\} = \{P(\omega)\}. \quad (2.13)$$

The matrix  $D(\omega)$  defined in (2.13) by

$$[D(\omega)] = \sum_e [T_e^{-1} D_e(\omega) T_e] \quad (2.14)$$

is acknowledged as total dynamic stiffness matrix of the structure.

### 2.2.2 Dynamic Stiffness Model for Cracked Bar and Beam Elements

First, let's consider a bar element of length  $\ell$ , Young modulus  $E$  and material density  $\rho$ . For the element Eq. (2.2) is

$$U''(x, \omega) - \lambda^2 U(x, \omega) = Q_u(x, \omega), \lambda = \omega/c, c = \sqrt{E/\rho}, \quad (2.15)$$

where  $U(x, \omega)$ ,  $Q_u(x, \omega)$  are longitudinal displacement and load; double prime denotes the second derivative with respect to spatial variable  $x$  ( $d^2/dx^2$ ). Suppose that the bar is cracked at positions  $e_1, \dots, e_m$  with depth  $a_1, \dots, a_m$ . If the cracks are modeled by translational springs of stiffness  $T_1, \dots, T_m$ , solution of Eq. (2.15) should satisfy the following conditions at cracks

$$\begin{aligned} U'(e_j + 0) &= U'(e_j - 0) = U'(e_j); U(e_j + 0) = U(e_j - 0) + \gamma_j U'(e_j); \\ \gamma_j &= EA/T_j = f_u(a_j), j = 1, 2, 3, \dots, m. \end{aligned} \quad (2.16)$$

The function  $f_u(a)$  is defined in Appendix 1. Hence, it can be shown that the functions

$$\varphi_1(x) = \cos \lambda x + \sum_{j=1}^m \mu_{1j} K_u(x - e_j), \varphi_2(x) = \sin \lambda x + \sum_{j=1}^m \mu_{2j} K_u(x - e_j); \quad (2.17)$$

$$K_u(x) = \begin{cases} \cos \lambda x & : x > 0 \\ 0 & : x \leq 0 \end{cases}; \begin{cases} \mu_{1j} \\ \mu_{2j} \end{cases} = \lambda \gamma_j \begin{cases} -\sin \lambda e_j - \sum_{i=1}^{j-1} \mu_{1i} \sin \lambda (e_j - e_i) \\ \cos \lambda e_j - \sum_{i=1}^{j-1} \mu_{2i} \sin \lambda (e_j - e_i) \end{cases} \quad (2.18)$$

are independent solutions of homogeneous equation (2.15) satisfying conditions (2.16). Therefore, general solution of Eq. (2.15) can be represented as

$$U(x, \omega) = C_1 \varphi_1(x) + C_2 \varphi_2(x) + U_q(x, \omega); U_q(x, \omega) = (1/\lambda) \int_0^x \sin \lambda (x - \tau) Q_u(\tau, \omega) d\tau. \quad (2.19)$$

So, for nodal displacements and forces introduced by  $U_1(\omega) = U(0, \omega)$ ,  $U_2(\omega) = U(L, \omega)$  and  $N_1(\omega) = -EAU'(0, \omega)$ ,  $N_2(\omega) = EAU'(L, \omega)$  one is able to obtain

$$\begin{Bmatrix} N_1 \\ N_2 \end{Bmatrix} = \frac{EA}{\varphi_2(L)} \begin{bmatrix} D_{11}(\omega) & D_{12}(\omega) \\ D_{21}(\omega) & D_{22}(\omega) \end{bmatrix} \begin{Bmatrix} U_1 \\ U_2 \end{Bmatrix} - \begin{Bmatrix} P_1(\omega) \\ P_2(\omega) \end{Bmatrix}, \quad (2.20)$$

where

$$D_{11} = \varphi_1(L)\varphi_2'(0) - \varphi_2(L)\varphi_1'(0); D_{12} = -\varphi_2'(0); D_{21} = \varphi_2(L)\varphi_1'(L) - \varphi_1(L)\varphi_2'(L); D_{22} = \varphi_2'(L); \quad (2.21)$$

$$P_1 = EA [U_q'(0)\varphi_2(0) - U_q(L)\varphi_2'(L)] / \varphi_2(L); P_2 = EA [U_q(L)\varphi_2'(L) - U_q'(L)\varphi_2(L)] / \varphi_2(L). \quad (2.22)$$

Obviously, the Dynamic Stiffness Matrix (DSM) and external load vector are defined by formulas (2.21–2.22) and shape functions (2.17) that would be calculated for the crack parameters  $\mu_{1j}, \mu_{2j}, j = 1, \dots, m$  determined from (2.18) as solution of the linear algebraic equation

$$[\mathbf{A}] \{\boldsymbol{\mu}\} = \{\mathbf{b}\}; \quad (2.23)$$

$$[\mathbf{A}] = [a_{ij}, i, j = 1, \dots, m], a_{ij} = 1 \text{ for } i = j; 0 \text{ if } i < j \text{ and equals to } \sin \lambda(e_i - e_j) \text{ when } i > j;$$

$$\{\mathbf{b}\} = \{b_j, j = 1, \dots, m\}; b_j = \lambda \gamma_j \begin{cases} -\sin \lambda e_j & \text{for } \boldsymbol{\mu}_1; \\ \cos \lambda e_j & \text{for } \boldsymbol{\mu}_2. \end{cases} \quad (2.24)$$

In the case of undamaged bar,  $\mu_{1j} = \mu_{2j} = 0, j = 1, \dots, m$  the DSM is reduced to

$$\mathbf{D}_0(\omega) = \frac{EA}{L} \begin{bmatrix} \lambda L / \tan \lambda L & -\lambda L / \sin \lambda L \\ -\lambda L / \sin \lambda L & \lambda L / \tan \lambda L \end{bmatrix}. \quad (2.25)$$

Now, consider beam element that is described by equation

$$d^4 W(x, \omega) / dx^4 - \lambda^4 W(x, \omega) = Q_w(x, \omega), \lambda^4 = \rho A \omega^2 / EI. \quad (2.26)$$

Assuming likely to the above that the beam contains  $m$  cracks of depth  $a_1, \dots, a_m$  at positions  $e_1, \dots, e_m$  and adopting rotational spring model for the cracks, one gets the conditions for flexural vibration at crack positions as

$$\begin{aligned} W(e_j - 0) &= W(e_j + 0); W''(e_j - 0) = W''(e_j + 0); W'''(e_j - 0) = W'''(e_j + 0); \\ W'(e_j + 0) &= W'(e_j - 0) + \theta_j W''(e_j - 0); \theta_j = EI / R_j; j = 1, 2, \dots, m, \end{aligned} \quad (2.27)$$

where  $R_j$  is stiffness of the rotational springs and so called crack magnitudes  $\theta_j$  is calculated by  $\theta_j = f_w(a_j)$  (see Appendix). It can be also proved that general solution of Eq. (2.26) can be expressed in the form

$$W(x, \omega) = C_1 \Phi_1(x) + C_2 \Phi_2(x) + C_3 \Phi_3(x) + C_4 \Phi_4(x) + W_q(x, \omega), \quad (2.28)$$

where

$$\begin{aligned} W_q(x, \omega) &= \int_0^x h(x - \tau) Q_w(\tau, \omega) d\tau; h(x) = [\sinh \lambda x - \sin \lambda x] / 2\lambda^2; \Phi_1(x) = \cosh \lambda x + \sum_{j=1}^m \mu_{1j} K_w(x - e_j); \\ \Phi_2(x) &= \sinh \lambda x + \sum_{j=1}^m \mu_{2j} K_w(x - e_j); \Phi_3(x) = \cos \lambda x + \sum_{j=1}^m \mu_{3j} K_w(x - e_j); \Phi_4(x) = \sin \lambda x + \sum_{j=1}^m \mu_{4j} K_w(x - e_j); \end{aligned} \quad (2.29)$$

$$S(x) = (\sinh \lambda x + \sin \lambda x) / 2\lambda; K_w(x) = \begin{cases} 0: & x \leq 0; \\ S(x): & x > 0; \end{cases}$$



where

$$\begin{aligned}\mu_{1j}(x) &= \gamma_j \left[ \lambda^2 \cosh \lambda e_j + \sum_{k=1}^{j-1} \mu_{1k} K_w (e_j - e_k) \right]; \mu_{2j}(x) = \gamma_j \left[ \lambda^2 \sinh \lambda e_j + \sum_{k=1}^{j-1} \mu_{2k} K_w (e_j - e_k) \right]; \\ \mu_{3j}(x) &= \gamma_j \left[ -\lambda^2 \cos \lambda e_j + \sum_{k=1}^{j-1} \mu_{3k} K_w (e_j - e_k) \right]; \mu_{4j}(x) = \gamma_j \left[ -\lambda^2 \sin \lambda e_j + \sum_{k=1}^{j-1} \mu_{4k} K_w (e_j - e_k) \right].\end{aligned}$$

It is easily to verify that four vectors  $\boldsymbol{\mu}_1, \boldsymbol{\mu}_2, \boldsymbol{\mu}_3, \boldsymbol{\mu}_4$  are solutions of the equation

$$\mathbf{A}\boldsymbol{\mu} = \mathbf{b}, \quad (2.30)$$

with common matrix  $\mathbf{A} = [a_{ki} = \delta_{ki} + K_w(e_k - e_i), k, i = 1, \dots, m]$  and right hand side vectors  $\mathbf{b}$  is one of the vectors respectively

$$\begin{aligned}\mathbf{b}_1 &= \lambda^2 \{\gamma_1 \cosh \lambda e_1, \dots, \gamma_m \cosh \lambda e_m\}^T; \quad \mathbf{b}_2 = \lambda^2 \{\gamma_1 \sinh \lambda e_1, \dots, \gamma_m \sinh \lambda e_m\}^T; \\ \mathbf{b}_3 &= -\lambda^2 \{\gamma_1 \cos \lambda e_1, \dots, \gamma_m \cos \lambda e_m\}^T; \quad \mathbf{b}^b = -\lambda^2 \{\gamma_1 \sin \lambda e_1, \dots, \gamma_m \sin \lambda e_m\}^T.\end{aligned} \quad (2.31)$$

Using expression (2.28) the nodal displacements and forces can be expressed as

$$\begin{aligned}\mathbf{V}(\omega) &= \begin{Bmatrix} W_1 \\ \Theta_1 \\ W_2 \\ \Theta_2 \end{Bmatrix} = \begin{Bmatrix} W(0, \omega) \\ W'(0, \omega) \\ W(L, \omega) \\ W'(L, \omega) \end{Bmatrix} = \begin{bmatrix} \Phi_1(0) & \Phi_2(0) & \Phi_3(0) & \Phi_4(0) \\ \Phi_1'(0) & \Phi_2'(0) & \Phi_3'(0) & \Phi_4'(0) \\ \Phi_1(L) & \Phi_2(L) & \Phi_3(L) & \Phi_4(L) \\ \Phi_1'(L) & \Phi_2'(L) & \Phi_3'(L) & \Phi_4'(L) \end{bmatrix} \begin{Bmatrix} C_1 \\ C_2 \\ C_3 \\ C_{14} \end{Bmatrix} + \begin{Bmatrix} 0 \\ 0 \\ W_q(L) \\ W_q'(L) \end{Bmatrix}; \\ \mathbf{F}(\omega) &= \begin{Bmatrix} Q_1 \\ M_1 \\ Q_2 \\ M_2 \end{Bmatrix} = EI \begin{Bmatrix} W'''(0, \omega) \\ W''(0, \omega) \\ W'''(L, \omega) \\ W''(L, \omega) \end{Bmatrix} = EI \begin{bmatrix} \Phi_1'''(0) & \Phi_2'''(0) & \Phi_3'''(0) & \Phi_4'''(0) \\ \Phi_1''(0) & \Phi_2''(0) & \Phi_3''(0) & \Phi_4''(0) \\ \Phi_1'''(L) & \Phi_2'''(L) & \Phi_3'''(L) & \Phi_4'''(L) \\ \Phi_1''(L) & \Phi_2''(L) & \Phi_3''(L) & \Phi_4''(L) \end{bmatrix} \begin{Bmatrix} C_1 \\ C_2 \\ C_3 \\ C_{14} \end{Bmatrix} + EI \begin{Bmatrix} 0 \\ 0 \\ W_q'''(L) \\ W_q''(L) \end{Bmatrix}.\end{aligned}$$

Excluding constants  $C_j, j = 1, 2, 3, 4$  from the latter equations leads to

$$\{\mathbf{F}(\omega)\} = [\mathbf{D}(\omega)] \{\mathbf{V}(\omega)\} + \{\mathbf{P}(\omega)\}, \quad (2.32)$$

where

$$\mathbf{D}(\omega) = EI \begin{bmatrix} S_1'''(0) & S_2'''(0) & S_3'''(0) & S_4'''(0) \\ S_1''(0) & S_2''(0) & S_3''(0) & S_4''(0) \\ S_1'''(L) & S_2'''(L) & S_3'''(L) & S_4'''(L) \\ S_1''(L) & S_2''(L) & S_3''(L) & S_4''(L) \end{bmatrix} \cdot \begin{bmatrix} S_1(0) & S_2(0) & S_3(0) & S_4(0) \\ S_1'(0) & S_2'(0) & S_3'(0) & S_4'(0) \\ S_1(L) & S_2(L) & S_3(L) & S_4(L) \\ S_1'(L) & S_2'(L) & S_3'(L) & S_4'(L) \end{bmatrix}^{-1} \quad (2.33)$$

and

$$\mathbf{P}(\omega) = EI \{0, 0, W_q'''(L), W_q''(L)\}^T - [\mathbf{D}(\omega)] \{0, 0, W_q(L), W_q'(L)\}^T. \quad (2.34)$$

## 2.3 Application of the DSM for Tower Crane

### 2.3.1 Governing Equation

Let's consider free vibration a tower crane shown in Fig. 2.1. Its model consists of four 2D beam elements {E1,E2,E3,E4}; two bar element {E5,E6} and 4 nodes {N1, . . . ,N4} with the nodal displacement vector  $\{V_1, V_2, \dots, V_{12}\} = \{U_1, W_1, \Theta_1, \dots, U_4, W_4, \Theta_4\}$ . The concentrated masses  $m_i$  produce the concentrated forces  $-m_i\omega^2 U$ ,  $-m_i\omega^2 W$  at nodes. Using the theory presented above one is able to construct the equations of motion in the frequency domain for the structure as

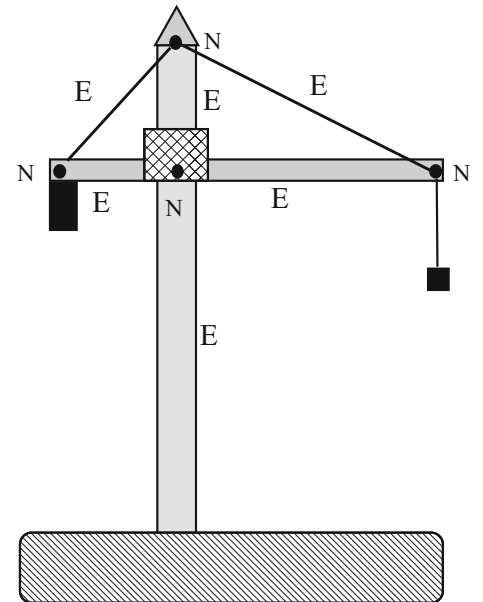
$$[\mathbf{K}(\omega)] \cdot \{\mathbf{V}\} = 0, \quad (2.35)$$

where  $[\mathbf{K}(\omega)]$  is  $12 \times 12$  dimension dynamic stiffness matrix for the structure

$$\mathbf{K}(\omega) = \begin{bmatrix} K_{11} & 0 & K_{13} & K_{14} & 0 & 0 & K_{17} & 0 & K_{19} & K_{1,10} & 0 & 0 \\ 0 & K_{22} & K_{23} & 0 & K_{25} & K_{26} & 0 & 0 & 0 & 0 & K_{2,11} & K_{2,12} \\ K_{31} & K_{32} & K_{33} & 0 & K_{35} & K_{36} & K_{37} & 0 & K_{39} & 0 & K_{3,11} & K_{3,12} \\ K_{41} & 0 & 0 & K_{44} & K_{45} & 0 & K_{47} & K_{48} & 0 & 0 & 0 & 0 \\ 0 & K_{52} & K_{53} & K_{54} & K_{55} & K_{56} & K_{57} & K_{58} & 0 & 0 & 0 & 0 \\ 0 & K_{62} & K_{63} & 0 & K_{65} & K_{66} & 0 & 0 & 0 & 0 & 0 & 0 \\ K_{71} & 0 & K_{73} & K_{74} & K_{75} & 0 & K_{77} & K_{78} & K_{79} & K_{7,10} & K_{7,11} & 0 \\ 0 & K_{82} & 0 & K_{84} & K_{85} & 0 & K_{87} & K_{88} & 0 & K_{8,10} & K_{8,11} & 0 \\ K_{91} & 0 & K_{93} & 0 & 0 & 0 & K_{97} & 0 & K_{99} & 0 & 0 & 0 \\ K_{10,1} & 0 & 0 & 0 & 0 & 0 & K_{10,7} & K_{10,8} & 0 & K_{10,10} & K_{10,11} & 0 \\ 0 & K_{11,2} & K_{11,3} & 0 & 0 & 0 & K_{11,7} & K_{11,8} & 0 & K_{11,10} & K_{11,11} & K_{11,12} \\ 0 & K_{12,2} & K_{12,3} & 0 & 0 & 0 & 0 & 0 & 0 & 0 & K_{12,11} & K_{12,12} \end{bmatrix} \quad (2.36)$$

with the elements

**Fig. 2.1** Node and element model of tower crane



$$\begin{aligned}
K_{11} &= EI_1 H_1''''(\beta_1, \ell_1) - EI_3 H_1''''(\beta_3, 0) + EF_4 h_2'(\alpha_2, \ell_4) - EF_2 h_1'(\alpha_2, 0) - m_1 \omega^2; K_{13} = EI_1 H_2''''(\beta_1, \ell_1) - EI_3 H_2''''(\beta_3, 0); \\
K_{14} &= -EF_2 h_2'(\alpha_2, 0); K_{17} = -EI_3 H_3''''(\beta_3, 0); K_{19} = -EI_3 H_4''''(\beta_3, 0); K_{1,10} = EF_4 h_1'(\alpha_4, \ell_4); K_{26} = EI_2 H_4''''(\beta_2, 0); \\
K_{22} &= EI_2 H_1''''(\beta_2, 0) - EI_4 H_3''''(\beta_4, \ell_4) + EF_1 h_2'(\alpha_1, \ell_1) - EF_3 h_1'(\alpha_3, 0) - m_1 \omega^2; K_{23} = EI_2 H_2''''(\beta_2, 0) - EI_4 H_4''''(\beta_4, \ell_4); \\
K_{25} &= EI_2 H_3''''(\beta_2, 0) - EF_3 h_2'(\alpha_3, 0); K_{31} = EI_1 H_1''(\beta_1, \ell_1) - EI_3 H_1''(\beta_3, 0); K_{32} = EI_2 H_1''(\beta_2, 0) - EI_4 H_3''(\beta_4, \ell_4); \\
K_{2,11} &= -EI_4 H_1''(\beta_4, \ell_4); K_{2,12} = -EI_4 H_2''(\beta_4, \ell_4); K_{33} = EI_1 H_2''(\beta_1, \ell_1) - EI_3 H_2''(\beta_3, 0) + EI_2 H_2''(\beta_2, 0) - EI_4 H_4''(\beta_4, \ell_4); \\
K_{34} &= EI_2 H_3''(\beta_2, 0); K_{35} = f_{26}^0 = EI_2 H_4''(\beta_2, 0); K_{37} = -EI_3 H_3''(\beta_3, 0); K_{39} = -EI_3 H_4''(\beta_3, 0); K_{3,11} = -EI_4 H_1''(\beta_4, \ell_4); \\
K_{3,12} &= -EI_4 H_2''(\beta_4, \ell_4); K_{41} = EF_2 h_1'(\alpha_2, \ell_2); K_{44} = EF_2 h_2'(\alpha_2, \ell_2) + EF_6 [h_2'(\alpha_6, \ell_6) \cos^2 \psi_2]; K_{53} = EI_2 H_2''(\beta_2, \ell_2); \\
K_{45} &= EF_6 [h_2'(\alpha_6, \ell_6) \cos \psi_2 \sin \psi_2]; K_{47} = EF_6 [h_1'(\alpha_6, \ell_6) \cos^2 \psi_2]; K_{48} = EF_6 [h_1'(\alpha_6, \ell_6) \cos \psi_2 \sin \psi_2]; \\
K_{54} &= EF_6 [h_2'(\alpha_6, \ell_6) \cos \psi_2 \sin \psi_2]; K_{55} = EI_2 H_3''''(\beta_2, \ell_2) + EF_6 [h_2'(\alpha_6, \ell_6) \sin^2 \psi_2] + m \omega^2; K_{62} = EI_2 H_1''(\beta_2, \ell_2); \\
K_{58} &= EF_6 [h_1'(\alpha_6, \ell_6) \sin^2 \psi_2]; K_{63} = EI_2 H_2''(\beta_2, \ell_2); K_{65} = EI_2 H_3''(\beta_2, \ell_2); K_{66} = EI_2 H_4''(\beta_2, \ell_2); \\
K_{71} &= EI_3 H_1''''(\beta_3, \ell_3); K_{73} = EI_3 H_2''''(\beta_3, \ell_3); K_{74} = -EF_6 [h_2'(\alpha_6, 0) \cos^2 \psi_2]; K_{56} = EI_2 H_4''''(\beta_2, \ell_2); \\
K_{75} &= -EF_6 [h_2'(\alpha_6, 0) \cos \psi_2 \sin \psi_2]; K_{77} = EI_3 H_3''''(\beta_3, \ell_3) + EF_5 [h_2'(\alpha_5, \ell_5) \cos^2 \psi_4] - EF_6 [h_1'(\alpha_6, 0) \cos^2 \psi_2]; \\
K_{78} &= EF_5 [h_2'(\alpha_5, \ell_5) \cos \psi_4 \sin \psi_4] - EF_6 [h_1'(\alpha_6, 0) \cos \psi_2 \sin \psi_2]; K_{79} = EI_3 H_4''''(\beta_3, \ell_3); K_{12,3} = EI_4 H_4''(\beta_4, 0); \\
K_{57} &= EF_6 [h_1'(\alpha_6, \ell_6) \cos \psi_2 \sin \psi_2]; K_{7,10} = EF_5 [h_1'(\alpha_5, \ell_5) \cos^2 \psi_4]; K_{7,11} = EF_5 [h_1'(\alpha_5, \ell_5) \cos \psi_4 \sin \psi_4]; \\
K_{82} &= EF_3 h_1'(\alpha_3, \ell_3); K_{84} = EF_6 [h_2'(\alpha_6, 0) \cos \psi_2 \sin \psi_2]; K_{85} = EF_3 h_2'(\alpha_3, \ell_3) + EF_6 [h_2'(\alpha_6, 0) \sin^2 \psi_2]; \\
K_{87} &= EF_5 [h_2'(\alpha_5, \ell_5) \cos \psi_4 \sin \psi_4] + EF_6 [h_1'(\alpha_6, 0) \cos \psi_2 \sin \psi_2]; K_{12,11} = EI_4 H_1''(\beta_4, 0); K_{12,12} = EI_4 H_2''(\beta_4, 0) \\
K_{88} &= EF_5 [h_2'(\alpha_5, \ell_5) \sin^2 \psi_4] + EF_6 [h_1'(\alpha_6, 0) \sin^2 \psi_2]; K_{8,10} = EF_5 [h_1'(\alpha_5, \ell_5) \cos \psi_4 \sin \psi_4]; K_{12,2} = EI_4 H_3''(\beta_4, 0); \\
K_{8,11} &= EF_5 [h_1'(\alpha_5, \ell_5) \sin^2 \psi_4]; K_{91} = EI_3 H_1''(\beta_3, \ell_3); K_{93} = EI_3 H_2''(\beta_3, \ell_3); K_{97} = EI_3 H_3''(\beta_3, \ell_3); \\
K_{99} &= EI_3 H_4''(\beta_3, \ell_3); K_{10,1} = EF_4 h_1'(\alpha_4, 0); K_{10,7} = EF_5 [h_2'(\alpha_5, 0) \cos^2 \psi_4]; K_{10,8} = EF_5 [h_2'(\alpha_5, 0) \cos \psi_4 \sin \psi_4]; \\
K_{10,10} &= EF_5 [h_1'(\alpha_5, 0) \cos^2 \psi_4] + EF_4 h_2'(\alpha_2, 0) + m_2 \omega^2; K_{10,11} = EF_5 [h_1'(\alpha_5, 0) \cos \psi_4 \sin \psi_4]; \\
K_{11,2} &= EI_4 H_3''''(\beta_4, 0); K_{11,3} = EI_4 H_4''''(\beta_4, 0); K_{11,7} = -EF_5 [h_2'(\alpha_5, 0) \cos \psi_4 \sin \psi_4]; K_{11,8} = -EF_5 [h_2'(\alpha_5, 0) \sin^2 \psi_4]; \\
K_{11,10} &= -EF_5 [h_1'(\alpha_5, 0) \cos \psi_4 \sin \psi_4]; K_{11,11} = EI_4 H_1''''(\beta_4, 0) - EF_5 [h_1'(\alpha_5, 0) \sin^2 \psi_4] - m_2 \omega^2; K_{11,12} = EI_4 H_2''''(\beta_4, 0),
\end{aligned} \tag{2.37}$$

calculated from the shape functions (2.17) and (2.29) given in Appendix. Therefore, natural frequencies are roots of the equation

$$\det [\mathbf{K}(\omega)] = 0, \tag{2.38}$$

with respect to  $\omega$ , for instance,  $\omega_1, \omega_2, \omega_3, \dots$ . As the natural frequencies have been found associated mode shapes are determined as follows

For element E1:

$$U_1(x) = h_2(\alpha_1, \ell_1, x) C_2; W_1(\beta_1, x) = H_3(\beta_1, \ell_1, x) C_1 + H_4(\beta_1, \ell_1, x) C_3; \tag{2.39}$$

For element E2:

$$U_2(x) = h_1(\alpha_2, x) C_1 + h_2(\alpha_2, x) C_4; \tag{2.40}$$

$$W_2(\beta_2, \ell_2, x) = H_1(\beta_2, \ell_2, x) C_2 + H_2(\beta_2, \ell_2, x) C_3 + H_3(\beta_2, \ell_2, x) C_5 + H_4(\beta_2, \ell_2, x) C_6;$$

For element E3

$$U_3(x) = h_1 (\alpha_3, \ell_3, x) C_2 + h_2 (\alpha_3, \ell_3, x) C_5; \tag{2.41}$$

$$W_3 (\beta_3, \ell_3, x) = H_1 (\beta_3, \ell_3, x) C_1 + H_2 (\beta_3, \ell_3, x) C_3 + H_3 (\beta_3, \ell_3, x) C_4 + H_4 (\beta_3, \ell_3, x) C_9;$$

For element E4

$$U_4(x) = h_1 (\alpha_4, \ell_4, x) C_1 + h_2 (\alpha_4, \ell_4, x) C_{10}; \tag{2.42}$$

$$W_4 (\beta_4, x) = H_1 (\beta_4, \ell_4, x) C_{11} + H_2 (\beta_4, \ell_4, x) C_{12} + H_3 (\beta_4, \ell_4, x) C_2 + H_4 (\beta_4, \ell_4, x) C_3.$$

The vector  $\mathbf{C} = \{C_1, \dots, C_{12}\}^T$  are normalized solution of Eq. (2.35) for a given natural frequency  $\omega_k$ .

### 2.3.2 Effect of Crack on Natural Frequencies of Crane

For illustration of the presented above theory, a numerical analysis of first three natural frequencies of a crane with the material and geometry parameters given in Table 2.1. First, the case of single crack of various depth appeared at a fixed position on every element is considered and results are tabulated in Table 2.2. Then, the variation of the frequencies caused by single crack with various position along the elements is computed and results are presented in Figs. 2.2, 2.3, 2.4.

The numerical results show that crack at the column (first element) changes significantly only the third frequency while all the frequencies are substantially reduced for crack appeared at the horizontal elements (second and fourth). Damages in the elements 5 and 6 where bending vibration is ignored do not affect on the natural frequencies. In more detail, as shown in Fig. 2.2, first and second frequencies are changed when crack appears at the top of column. The first frequency may increase for crack near the left end (center of crane) of second element what can be seen in Fig. 2.3. For crack appears near the free end of fourth element, i.e. the left horizontal beam, the first frequency is almost unchanged (Fig. 2.4).

**Table 2.1** Material and geometrical parameters of crane

Parameters	Element 1	Element 2	Element 3	Element 4	Element 5	Element 6
E	2.1e11	2.1e11	2.1e11	2.1e11	2.1e11	2.1e11
$\rho(\text{kg/m}^3)$	380	290	380	290	505	505
A (m <sup>2</sup> )	1.56	0.64	0.64	0.64	0.08	0.08
L (m)	44	60	5.6	16	17	60.3
I (m <sup>4</sup> )	0.546	0.034	0.546	0.034	-	-

Concentrated masses (kg):  $m_1 = 80$ ;  $m_2 = 480$ ;  $m_3 = 1800$

**Table 2.2** Effect of crack depth on three lowest natural frequencies (single crack at each element)

No crack	Crack at element 1		Crack at element 2					Crack at element 5	
	5%	10%	5%	10%	15%	20%	30%	5%	10%
2.2723	2.2722	2.2722	0.7117	0.7029	0.7012	0.7006	0.7002	2.2723	2.2723
38.6217	38.6216	38.6216	13.1932	9.4320	7.6070	6.5445	5.1497	38.6217	38.6217
106.4684	85.7995	85.7995	17.0338	17.0376	17.0375	17.0336	17.0371	106.4684	106.4684
No crack	Crack at element 3		Crack at element 4					Crack at element 6	
	5%	10%	5%	15%	20%	20%	30%	5%	10%
2.2723	2.2722	2.2722	2.2723	2.2723	1.8242	1.4583	1.0467	2.2723	2.2722
38.6217	21.8242	21.8242	4.2279	2.4864	2.2722	2.2722	2.2722	38.6216	38.6216
106.4684	38.6298	38.6298	35.2471	37.2833	38.0574	38.3740	38.6190	106.4684	106.4684

n of crack at elements: E1: 20/44; E2: 30/60; E3: 3/5.6; E4: 10/16; E5: 30/50

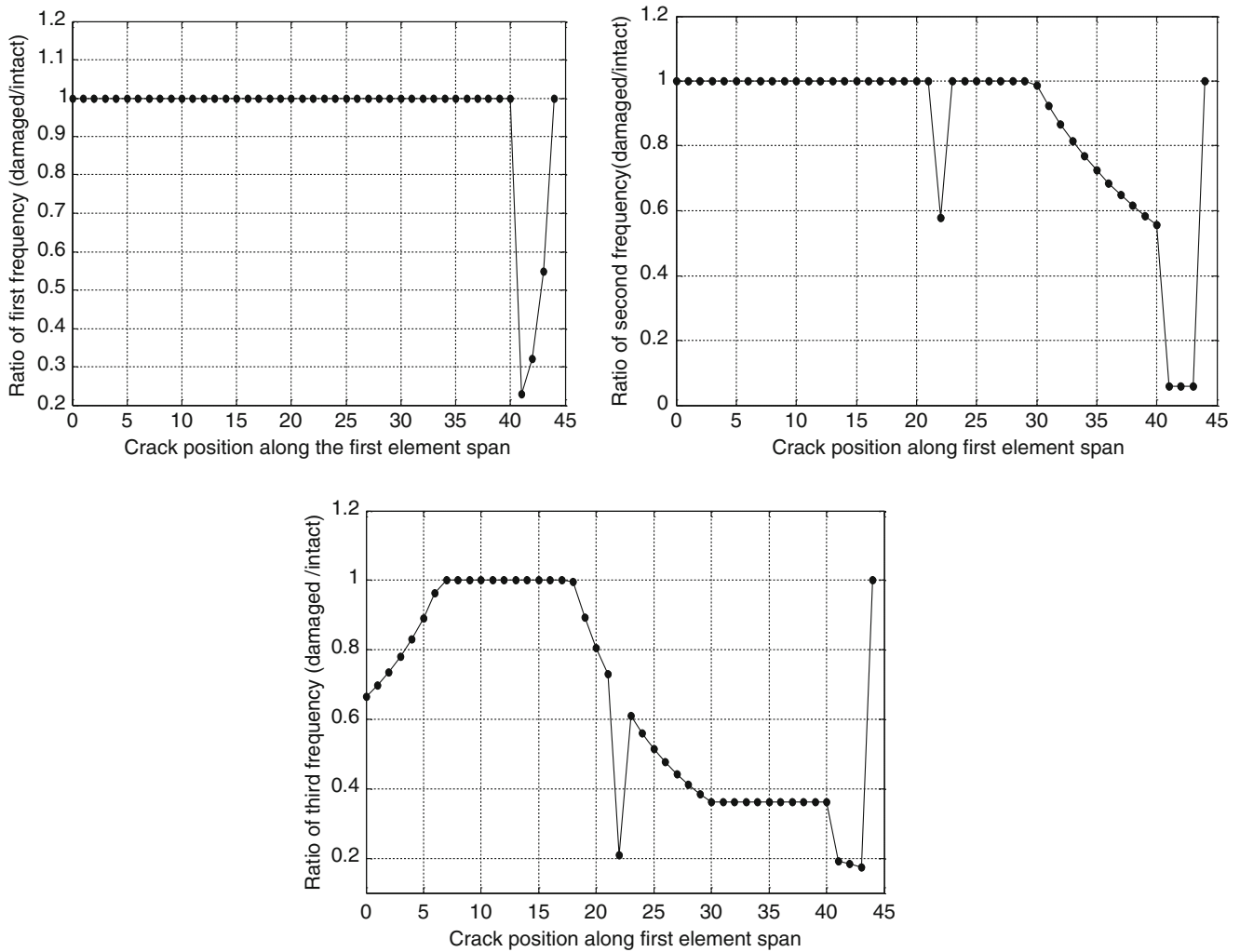
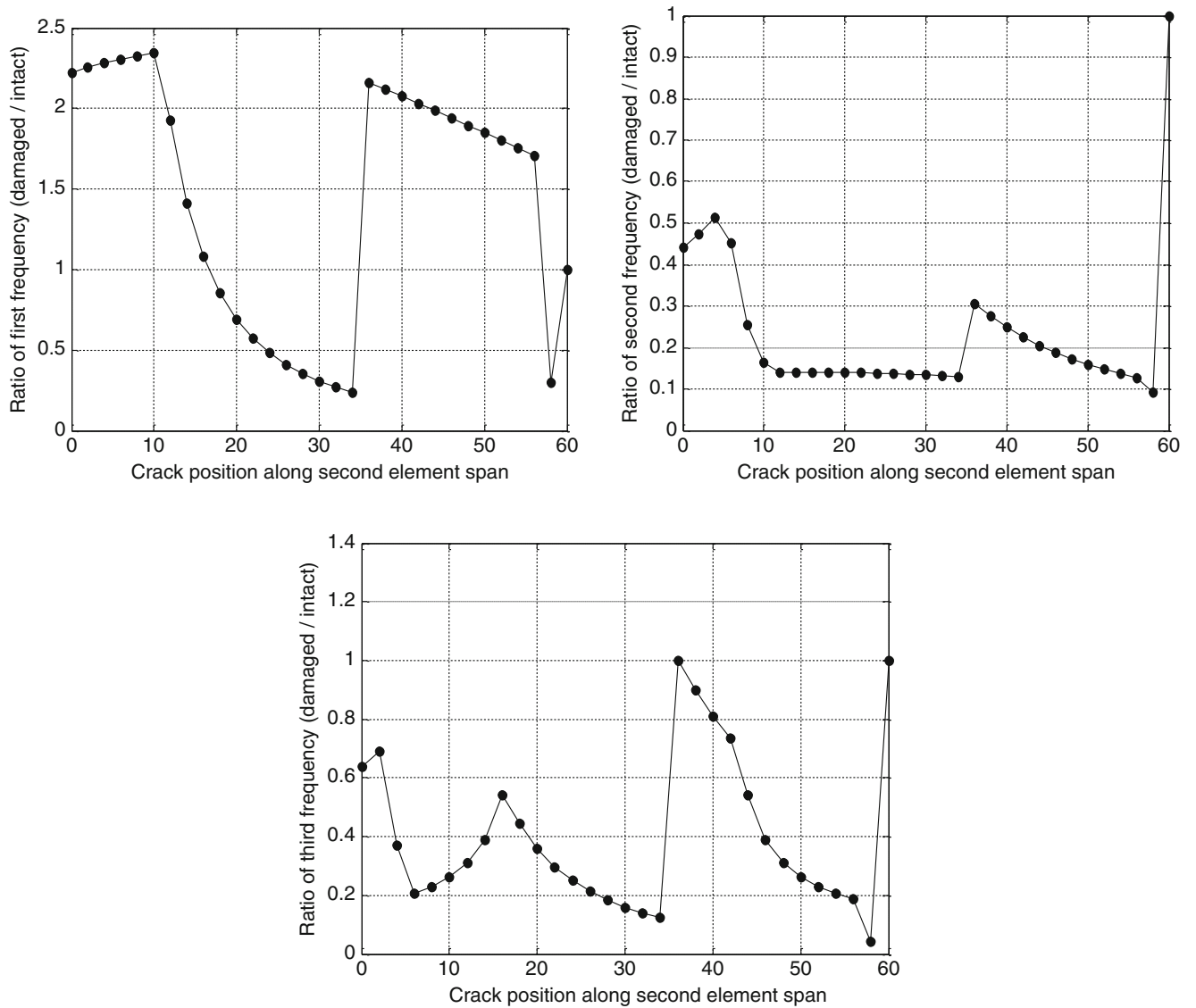


Fig. 2.2 Variation of first three natural frequencies caused by a crack at various position on first element

## 2.4 Conclusion

So, in the present report, the dynamic stiffness matrix for a typical tower crane is obtained in an explicit form. This dynamic stiffness model has been used for numerical analysis of natural frequencies of the crane in dependence on the position and depth of crack appeared at every structural element. The obtained numerical results show that crack in elements of the crane can be surely detected by measurement of natural frequencies.

**Acknowledgement** This work was completed under support from National Foundation for Science and Technology Development of Vietnam.



**Fig. 2.3** Variation of first three natural frequencies caused by a crack at various position on second element

## Appendix 1: Formulas for Calculation of Crack Magnitude from Crack Depth

$$\gamma = E_0 A / T = 2\pi (1 - \nu_0^2) h f_u(z), z = a/h;$$

$$f_u(z) = z^2 \left( 0.6272 - 0.17248z + 5.92134z^2 - 10.7054z^3 + 31.5685z^4 - 67.47z^5 + 139.123z^6 - 146.682z^7 + 92.3552z^8 \right);$$

$$\theta = EI/R = 6\pi (1 - \nu_0^2) h f_w(z);$$

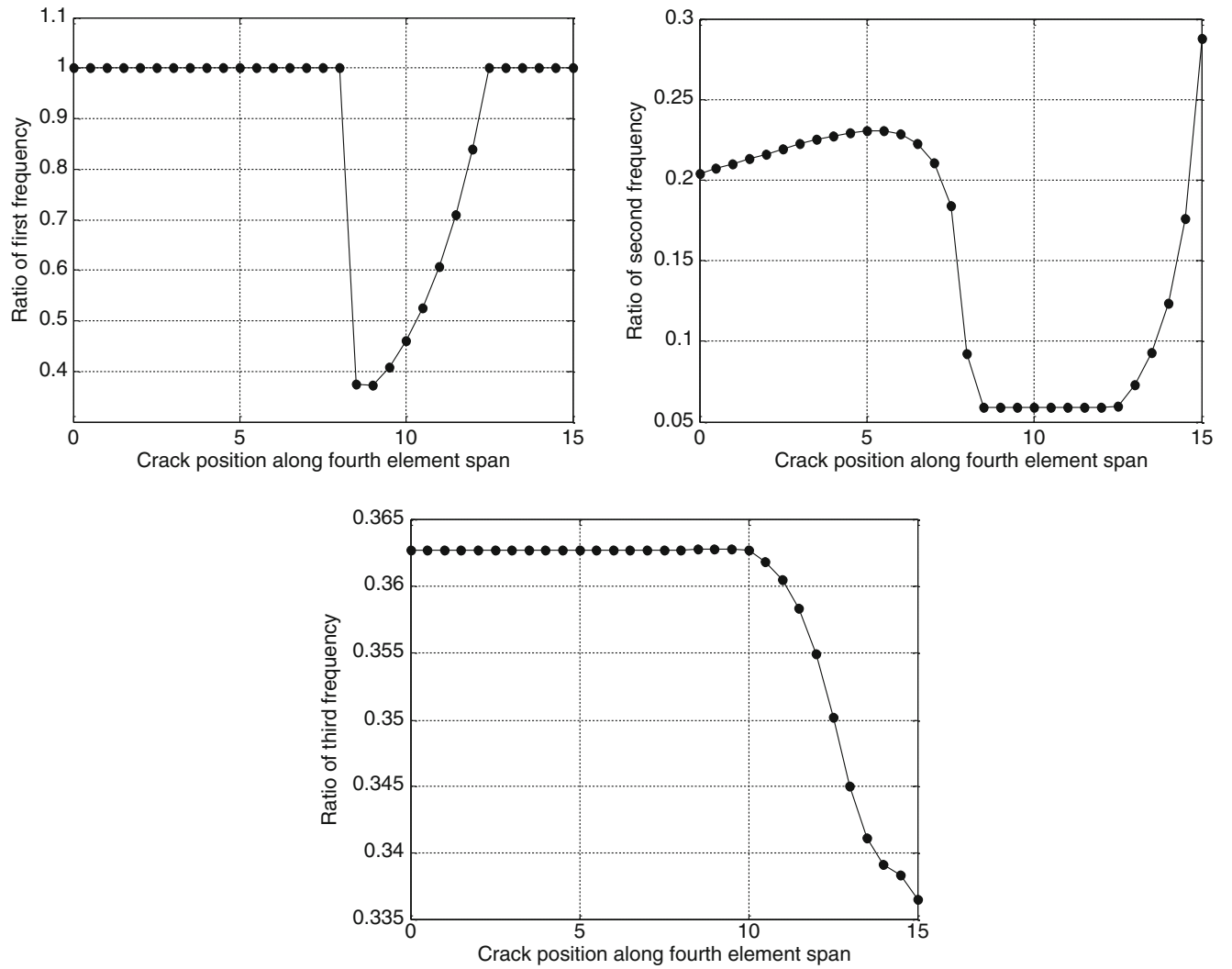


**Fig. 2.4** Variation of first three natural frequencies caused by a crack at various position on fourth element

$$f_w(z) = z^2 \left( 0.6272 - 1.04533z + 4.5948z^2 - 9.9736z^3 + 20.2948z^4 - 33.0351z^5 + 47.1063z^6 - 40.7556z^7 + 19.6z^8 \right).$$

## Appendix 2: Shape Function for Bar and Beam Elements

$$h_1(\alpha, \ell, x) = [\varphi_2(\alpha, \ell) \varphi_1(\alpha, x) - \varphi_1(\alpha, \ell) \varphi_2(\alpha, x)] / d; h_2(\alpha, \ell, x) = [\varphi_1(\alpha, 0) \varphi_2(\alpha, x) - \varphi_2(\alpha, 0) \varphi_1(\alpha, x)] / d;$$

$$d(\alpha, \ell) = \varphi_1(\alpha, 0) \varphi_2(\alpha, \ell) - \varphi_1(\alpha, \ell) \varphi_2(\alpha, 0); H_j(\beta, \ell, x) = (1/\Delta) \sum_{k=1}^4 (-1)^{j+k} \Delta_{jk} \Phi_k(\beta, x), j = 1, 2, 3, 4.$$

$$\begin{aligned} \Delta_{11} &= \det \begin{bmatrix} \Phi'_2(\beta, 0) & \Phi'_3(\beta, 0) & \Phi'_4(\beta, 0) \\ \Phi_2(\beta, \ell) & \Phi_3(\beta, \ell) & \Phi_4(\beta, \ell) \\ \Phi'_2(\beta, \ell) & \Phi'_3(\beta, \ell) & \Phi'_4(\beta, \ell) \end{bmatrix}; \Delta_{12} = \det \begin{bmatrix} \Phi_2(\beta, 0) & \Phi_3(\beta, 0) & \Phi_4(\beta, 0) \\ \Phi_2(\beta, \ell) & \Phi_3(\beta, \ell_2) & \Phi_4(\beta, \ell) \\ \Phi'_2(\beta, \ell) & \Phi'_3(\beta, \ell_2) & \Phi'_4(\beta, \ell) \end{bmatrix}; \Delta_{13} = \det \begin{bmatrix} \Phi'_2(\beta, 0) & \Phi'_3(\beta, 0) & \Phi'_4(\beta, 0) \\ \Phi_2(\beta, 0) & \Phi_3(\beta, 0) & \Phi_4(\beta, 0) \\ \Phi'_2(\beta, \ell) & \Phi'_3(\beta, \ell) & \Phi'_4(\beta, \ell) \end{bmatrix}; \\ \Delta_{14} &= \det \begin{bmatrix} \Phi_2(\beta, 0) & \Phi_3(\beta, 0) & \Phi_4(\beta, 0) \\ \Phi'_2(\beta, 0) & \Phi'_3(\beta, 0) & \Phi'_4(\beta, 0) \\ \Phi_2(\beta, \ell) & \Phi_3(\beta, \ell) & \Phi_4(\beta, \ell) \end{bmatrix}; \Delta_{21} = \det \begin{bmatrix} \Phi'_1(\beta, 0) & \Phi'_3(\beta, 0) & \Phi'_4(\beta, 0) \\ \Phi_1(\beta, \ell) & \Phi_3(\beta, \ell) & \Phi_4(\beta, \ell) \\ \Phi'_1(\beta, \ell) & \Phi'_3(\beta, \ell) & \Phi'_4(\beta, \ell) \end{bmatrix}; \Delta_{22} = \det \begin{bmatrix} \Phi_1(\beta, 0) & \Phi_3(\beta, 0) & \Phi_4(\beta, 0) \\ \Phi_1(\beta, \ell) & \Phi_3(\beta, \ell) & \Phi_4(\beta, \ell) \\ \Phi'_1(\beta, \ell) & \Phi'_3(\beta, \ell) & \Phi'_4(\beta, \ell) \end{bmatrix}; \\ \Delta_{23} &= \det \begin{bmatrix} \Phi'_1(\beta, 0) & \Phi'_3(\beta, 0) & \Phi'_4(\beta, 0) \\ \Phi_1(\beta, 0) & \Phi_3(\beta, 0) & \Phi_4(\beta, 0) \\ \Phi'_1(\beta, \ell) & \Phi'_3(\beta, \ell) & \Phi'_4(\beta, \ell) \end{bmatrix}; \Delta_{24} = \det \begin{bmatrix} \Phi_1(\beta, 0) & \Phi_3(\beta, 0) & \Phi_4(\beta, 0) \\ \Phi'_1(\beta, 0) & \Phi'_3(\beta, 0) & \Phi'_4(\beta, 0) \\ \Phi_1(\beta, \ell) & \Phi_3(\beta, \ell) & \Phi_4(\beta, \ell) \end{bmatrix}; \Delta_{31} = \det \begin{bmatrix} \Phi'_1(\beta, 0) & \Phi'_2(\beta, 0) & \Phi'_4(\beta, 0) \\ \Phi_1(\beta, \ell) & \Phi_2(\beta, \ell) & \Phi_4(\beta, \ell) \\ \Phi'_1(\beta, \ell) & \Phi'_2(\beta, \ell) & \Phi'_4(\beta, \ell) \end{bmatrix}; \\ \Delta_{32} &= \det \begin{bmatrix} \Phi_1(\beta, 0) & \Phi_2(\beta, 0) & \Phi_4(\beta, 0) \\ \Phi_1(\beta, \ell) & \Phi_2(\beta, \ell) & \Phi_4(\beta, \ell) \\ \Phi'_1(\beta, \ell) & \Phi'_2(\beta, \ell) & \Phi'_4(\beta, \ell) \end{bmatrix}; \Delta_{33} = \det \begin{bmatrix} \Phi'_1(\beta, 0) & \Phi'_2(\beta, 0) & \Phi'_4(\beta, 0) \\ \Phi_1(\beta, 0) & \Phi_2(\beta, 0) & \Phi_4(\beta, 0) \\ \Phi'_1(\beta, \ell) & \Phi'_2(\beta, \ell) & \Phi'_4(\beta, \ell) \end{bmatrix}; \Delta_{34} = \det \begin{bmatrix} \Phi_1(\beta, 0) & \Phi_2(\beta, 0) & \Phi_4(\beta, 0) \\ \Phi'_1(\beta, 0) & \Phi'_2(\beta, 0) & \Phi'_4(\beta, 0) \\ \Phi_1(\beta, \ell) & \Phi_2(\beta, \ell) & \Phi_4(\beta, \ell) \end{bmatrix}; \\ \Delta_{41} &= \det \begin{bmatrix} \Phi'_1(\beta, 0) & \Phi'_2(\beta, 0) & \Phi'_3(\beta, 0) \\ \Phi_1(\beta, \ell) & \Phi_2(\beta, \ell) & \Phi_3(\beta, \ell) \\ \Phi'_1(\beta, \ell) & \Phi'_2(\beta, \ell) & \Phi'_3(\beta, \ell) \end{bmatrix}; \Delta_{42} = \det \begin{bmatrix} \Phi_1(\beta, 0) & \Phi_2(\beta, 0) & \Phi_3(\beta, 0) \\ \Phi_1(\beta, \ell) & \Phi_2(\beta, \ell) & \Phi_3(\beta, \ell) \\ \Phi'_1(\beta, \ell) & \Phi'_2(\beta, \ell) & \Phi'_3(\beta, \ell) \end{bmatrix}; \Delta_{43} = \det \begin{bmatrix} \Phi'_1(\beta, 0) & \Phi'_2(\beta, 0) & \Phi'_3(\beta, 0) \\ \Phi_1(\beta, 0) & \Phi_2(\beta, 0) & \Phi_3(\beta, 0) \\ \Phi'_1(\beta, \ell) & \Phi'_2(\beta, \ell) & \Phi'_3(\beta, \ell) \end{bmatrix}; \\ \Delta_{44} &= \det \begin{bmatrix} \Phi_1(\beta, 0) & \Phi_2(\beta, 0) & \Phi_3(\beta, 0) \\ \Phi'_1(\beta, 0) & \Phi'_2(\beta, 0) & \Phi'_3(\beta, 0) \\ \Phi_1(\beta, \ell) & \Phi_2(\beta, \ell) & \Phi_3(\beta, \ell) \end{bmatrix}; \Delta = \det \begin{bmatrix} \Phi_1(\beta, 0) & \Phi_2(\beta, 0) & \Phi_3(\beta, 0) & \Phi_4(\beta, 0) \\ \Phi'_1(\beta, 0) & \Phi'_2(\beta, 0) & \Phi'_3(\beta, 0) & \Phi'_4(\beta, 0) \\ \Phi_1(\beta, \ell) & \Phi_2(\beta, \ell) & \Phi_3(\beta, \ell) & \Phi_4(\beta, \ell) \\ \Phi'_1(\beta, \ell) & \Phi'_2(\beta, \ell) & \Phi'_3(\beta, \ell) & \Phi'_4(\beta, \ell) \end{bmatrix}. \end{aligned}$$

## References

1. Abdel-Rahman, E.M., Nayfeh, A.H., Masoud, Z.N.: Dynamics and control of cranes. A review. *J. Vib. Control.* **9**(7), 863–909 (2003)
2. Ju, F., Choo, Y.S.: Dynamic characteristics of tower cranes. *Proceedings of the 2nd International Conference on Structural Stability and Dynamics*, pp. 260–266, World Scientific, Singapore (2002)
3. Ju, F., Choo, Y.S.: Dynamic analysis of tower cranes. *J. Eng. Mech.* **131**(1), 88–96 (2005)
4. Ju, F., Choo, Y.S., Cui, F.S.: Dynamic response of tower induced by the pendulum motion of the payload. *Int. J. Solids Struct.* **43**(2), 376–389 (2006)
5. Yu, Y., Han, Z.: The modeling analysis for tower crane based on finite element technology. *Dev. Innov. Mach. Electr. Prod.* **20**(3), 93–95 (2007)
6. Nasser, M.A.: Dynamic analysis of cranes. *Proceedings of the IMAC XIX*, paper No. 194301, pp. 1592–1599
7. Oguamanam, D.C.D., Hansen, J.S.: Dynamic response of an overhead crane system. *J. Sound Vib.* **243**(5), 889–906 (1998)
8. Ghigliazza, R.M., Holmes, P.: On the dynamics of cranes or spherical pendula with moving supports. *Int. J. Non linear Mech.* **37**(6), 1211–1221 (2002)
9. Eden, J.F., Homer, P., Butler, A.J.: The dynamic stability of mobile cranes. *Proc. Inst. Mech. Eng., Part D.* **199**(D4), 283–293 (1985)
10. Wang, S., Shen, R., Jin, T., Song, S.: Dynamic behavior analysis and its application in tower crane structure damage identification. *Adv. Mater. Res.* **368-373**, 2478–2482 (2012)



## Chapter 3

# High-Noise High-Speed Footage Data in Experimental Modal Analysis

Jaka Javh, Janko Slavič, and Miha Boltežar

**Abstract** Vibration measurements using optical full-field systems based on high-speed footage are typically heavily burdened by noise, as the displacement amplitudes of the vibrating structures are often very small (ranging in micrometers, depending on the structure) and therefore troublesome to measure as they are close or below the noise level of the measurement system. This paper demonstrates the modal parameter identification on such noisy measurements. It is shown that by using state of the art identification methods (Least Squares Complex Exponential or Least Squares Complex Frequency combined with Least Squares Frequency Domain), identification is still possible. The modal parameter identification improves the quality of the measured modal data and serves as a reduced model of the structures dynamics.

**Keywords** High-speed camera • Modal parameter identification • Noise • Optical flow • LSCE • LSCF

### 3.1 Introduction

Optical measurement techniques using high-speed cameras are increasingly being used in modal analysis to measure full field displacements [1–3]. The most promising techniques for the identification of motion from image sequences are; Digital Image Correlation [4], Gradient-based Optical Flow [5, 6] and Phase-based methods [7].

The dynamic response of a structure can be described with a modal model of the structure. This model comprises of eigenvalues (natural frequencies and damping) and mode shapes (modal constants). Among the large range of modal parameter identification methods, the LSCE (‘Least Squares Complex Exponential’) [8] and the LSCF (‘Least Squares Complex Frequency’) [9] are the most commonly used, because they are fast and robust.

### 3.2 Measurement Set-up

A solid beam with dimensions  $15 \times 30 \times 500$  mm was measured in free-free conditions. The beam was chosen because its response is well known and the results can easily be evaluated. An accelerometer was attached at one side of the beam and a modal hammer was used to excite it. The response was measured with a high-speed camera as well. The camera filmed the thinner side of the beam, thereby measuring the bending of the beam (Fig. 3.1). The camera filmed at 200,000 fps at a resolution of  $1024 \times 64$  pixel and captured 698.984 frames (a sampling period of  $\sim 3.5$  s), producing 64 GB of data. The accelerometer and the modal hammer force sensor were sampled with 50,000 Hz for a matching sampling period as the camera. A hard metal tip was used on the modal hammer and the hit was of a considerable strength ( $\sim 0.2$  Ns) for the higher frequencies to be made visible.

---

J. Javh • J. Slavič (✉) • M. Boltežar

Faculty of Mechanical Engineering, University of Ljubljana, Aškerceva cesta 6, 1000 Ljubljana, Slovenia

e-mail: [Janko.slavic@fs.uni-lj.si](mailto:Janko.slavic@fs.uni-lj.si)

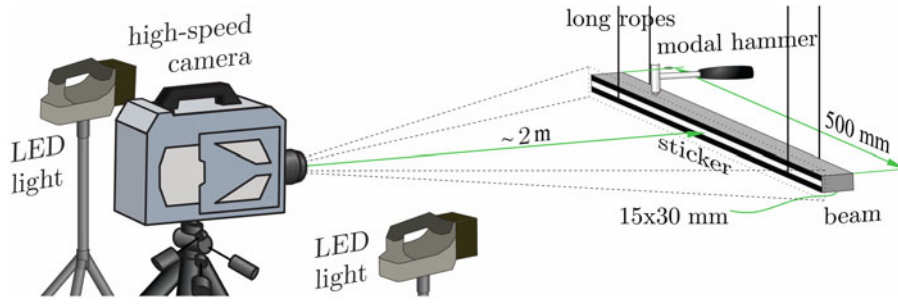


Fig. 3.1 The measurement set-up

### 3.3 Optical Flow

The method used to identify motion from the image sequence was a simplified gradient based optical flow [10]. The method produces the most direct route from the optical information to the displacement, by relating the image intensity values  $I(x, y, t)$ , where  $x$  and  $y$  are the pixel locations and  $t$  is time, to displacements  $\Delta s$  over the intensity gradient  $\nabla I$ :

$$|\nabla I| \Delta s = I(x_j, y_k, t) - I(x_j, y_k, t + \Delta t) \quad (3.1)$$

The displacements are most evident where the gradient is highest. The displacement of a pixel can only be determined in the direction of the image gradient. In our case this is not a problem because only displacement in the  $y$ -direction of the camera's projected plane are of interest. Otherwise, the displacements in 2D can be measured by using a speckle pattern and using a subset of pixels to produce an estimate of motion and 3D measurements can be performed by using a stereoscopic set-up. A sticker with black and white lines was applied to the beam to make the displacements more evident to the camera. The displacement was identified at 7521 points on the beam.

### 3.4 Modal Parameter Identification

LSCE is a time domain method based on the impulse response function. By solving a system of equations overdetermined by multiple response location measurements and additional time points, a polynomial can be constructed and the eigenvalues determined as the roots of this polynomial. The identification is repeated for multiple orders of identification  $M$  and the eigenvalues hand picked from stabilization diagrams. The picked eigenvalues are then used to determine the modal constants  $r_j A_j$  for every response location  $j$  separately, by solving an additional system of equations.

LSCF is a frequency domain variant that benefits from the fact that the system of equations used to determine the eigenvalues is not overdetermined and therefore less computationally demanding, also the stabilization diagrams typically exhibit numerical poles as unstable, making the true poles stand out. After the eigenvalues are determined, determining the modal constants is a matter of solving an overdetermined system of linear equations (the 'Least Squares Frequency Domain' method).

### 3.5 Results

Due to high noise and a large frequency range (0–9500 Hz) a high order of identification ( $M = 500$ ) was used to produce a more apparent stabilization diagram. The spectrum was measured up to 100 kHz but cut to 9500 Hz for the parameter identification, because the first lobe of the hammer impulse force spectrum ranged only up to 10 kHz. The stabilization diagram for the camera measurement using LSCE and LSCF was performed. Only eigenvalues up to the third mode at  $\sim 2730$  Hz are identified, the higher modes seem to be cluttered under the noise level, as indicated in the LSCF stabilization diagram in Fig. 3.2a where the FRF of a point bellow the accelerometer measured by the camera are plotted along with the FRF measured by the accelerometer. The noise level of the displacements measured with the camera is at  $\sim 0.0001$  pixel. This is why the accelerometer data was used to identify the eigenvalues and the camera measurements to identify the modal constants in the following step.

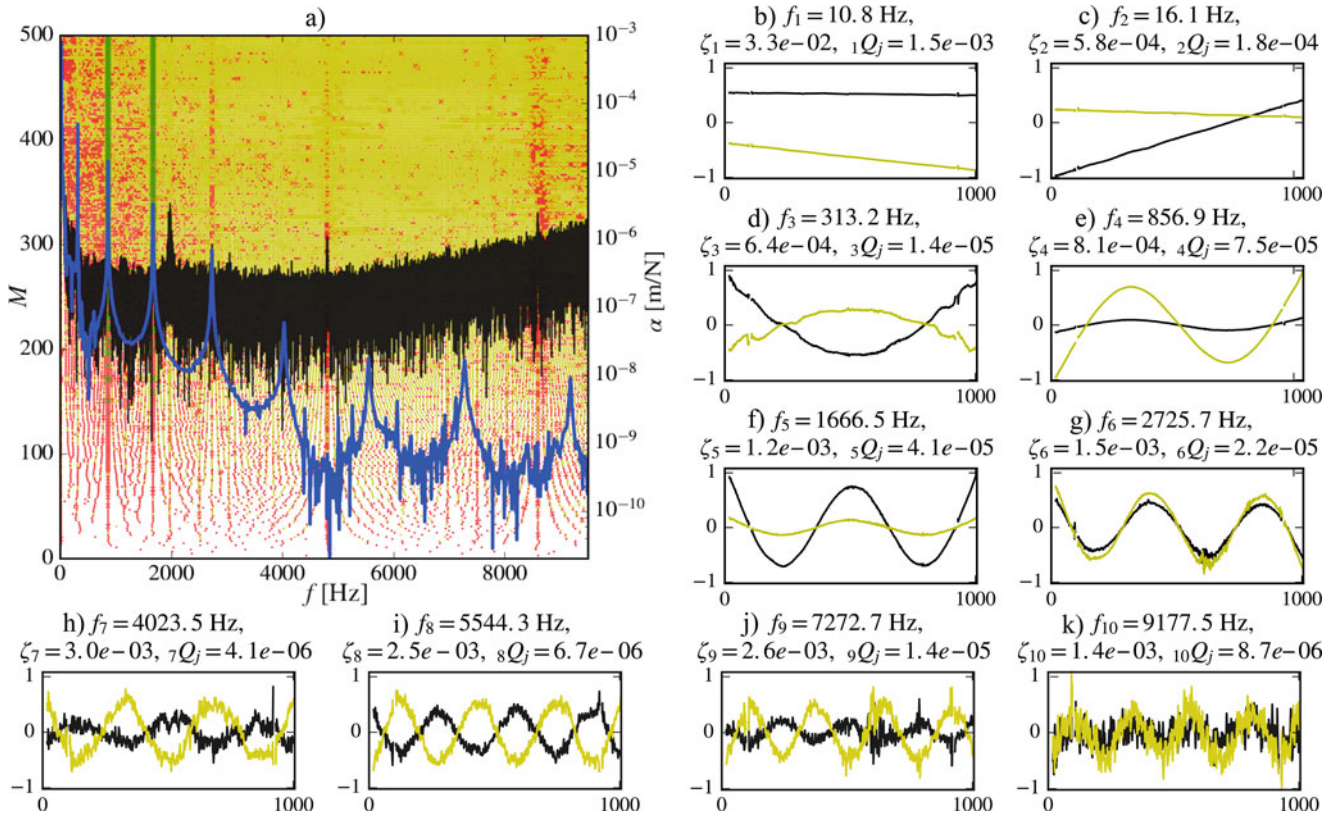


Fig. 3.2 The identified mode shapes

Some points are situated at the same length of the beam and were averaged to produce improved modal constant values with less noise. The modal constants averaged over the beam thickness obtained with LSFD and eigenvalues based on the accelerometer data are plotted in Fig. 3.2b–k. The mode shapes are plotted with respect to the beam length. The shapes are normalized and accompanied with a scaling constant  ${}_rQ_j$ . The yellow lines represent the real values and the black line represent the imaginary values of the identified modal constants. The highest modes were identified despite being at or below the level of noise, proving that the modal information is present and can be extracted from very noisy measurements.

## References

1. Siebert, T., Wood, R., Splithof, K.: High speed image correlation for vibration analysis. *J. Phys.* **181**(1), 1589–1603 (2009)
2. Pan, B., Tian, L., Song, X.: Real-time, non-contact and targetless measurement of vertical deflection of bridges using off-axis digital image correlation. *NDT&E Int.* **76**, 73–80 (2016)
3. Yang, Y., Dorn, C., Mancini, T., Talken, Z., Kenyon, G., Farrar, C., Mascarenas, D.: Blind identification of full-field vibration modes from video measurements with phase-based video motion magnification. *Mech. Syst. Signal Process.* **85**, 567–590 (2017)
4. Peters, W., Ranson, W.: Digital imaging techniques in experimental stress analysis. *Opt. Eng.* **21**(3), 427–432 (1982)
5. Lucas, B., Kanade, T.: An iterative image registration technique with an application to stereo vision. In: *International Joint Conference on Artificial Intelligence*, pp. 674–679 (1981)
6. Horn, B., Schunck, B.: Determining optical flow. In: *Technical Symposium East. International Society for Optics and Photonics*, pp. 319–331 (1981)
7. Fleet, D., Jepson, A.: Computation of component image velocity from local phase information. *Int. J. Comput. Vis.* **5**(1), 77–104 (1990)
8. Brown, D., Allemang, R., Zimmerman, R., Mergeay, M.: Parameter estimation techniques for modal analysis, SAE Technical paper (1979)
9. Guillaume, P., Verboven, P., Vanlanduit, S.: Frequency-domain maximum likelihood identification of modal parameters with confidence intervals. In: *Proceedings of ISMA*, vol. 23, pp. 16–18 (1998)
10. Javh, J., Slavič, J., Boltežar, M.: Determining subpixel full-field displacements from videos by using optical flow. In: *Proceedings of ICoEV 2015 International Conference on Engineering Vibration*, pp. 1589–1603 (2015)

## Chapter 4

# Morlet-Wave Damping Identification: Application to High-Speed Video

Janko Slavič, Marko Mihalec, Jaka Javh, and Miha Boltežar

**Abstract** The optical flow based approach to measure displacements at impact response was recently shown to give very good results where the subpixel resolution is at the level of 1/10000 of a pixel. This study researches the applicability of the optical flow approach to the damping identification with the Morlet Wave methods. The Morlet wave method bases on the continuous wavelet transform but is not impacted by the edge-effect. It was shown that the damping identification is reliable and opens up new questions with regards to the spatial distribution of the identified damping.

**Keywords** Damping identification • Morlet wave • High-speed camera • Optical flow

Damping identification is widely regarded as one of the most challenging aspects of the modal parameter identification. In recent time, continuous wavelet transform (CWT) [1] has been widely implemented and it was shown to be one of the best and most reliable methods for damping identification, especially at noisy data [2–4]. One of the weaknesses of CWT is the high numerical load; the transform has to be calculated for the entire time-scale domain which makes the CWT slow in comparison to other methods [1].

The Morlet–Wave (MW) method was proposed to improve the speed and reduce the edge-effect of the CWT [5]. The MW damping approach bases on:

$$M(n_1, n_2, k, \omega) = \frac{|I(n_1, k, \omega)|}{|I(n_2, k, \omega)|}, \quad (4.1)$$

where:

$$I = \int_0^T f_m(t) \psi_{u,s}^*(t) dt \quad (4.2)$$

is the integral of the signal  $f_m(t)$  multiplied by the Morlet Wavelet  $\psi_{u,s}^*(t)$ . In Eq. (4.1)  $n_1$  and  $n_2$  are parameters defining the Morlet Wavelet,  $k$  is the number of oscillations the damping identification takes into account and  $\omega$  is the analyzed natural frequency. Assuming a damped response with damping ratio  $\delta$ , the fraction  $M$  can also be determined analytically (or numerically) leading to the identification of the unknown damping ratio  $\delta$  (for details please see [5]). Since the MW method calculates the integral at a single time-scale point, the approach is numerically significantly faster compared to CWT. Compared to CWT, the MW approach is similarly resistant to noise, but has no edge-effect and is therefore much more robust for blind application.

Due to technical improvements in high-speed video cameras, full-field optical methods are increasingly being used for modal analysis. Frequently, digital image correlation approach is used for the displacement analysis in image processing [6]; however, this research uses a simplified gradient-based optical flow method to identify the vibration displacements. For details on the optical flow approach, please see [7, 8].

The experiment setup is shown in Fig. 4.1. A monochrome Photron Fastcam SA-Z was used to measure the vibrations of a freely supported steel beam (shape  $500 \times 15 \times 30$  mm). A white sticker was used for high gradient based optical flow displacement identification. At approx. 2 m distance, the beam width was 1000 pixel and for each pixel transverse displacement was measured. The camera frame rate was set at 200,000 fps and 698.984 frames were captured, however a shorter time history was used in the analysis. Figure 4.2 shows the response of five selected pixels in the time domain.

---

J. Slavič (✉) • M. Mihalec • J. Javh • M. Boltežar  
Faculty of Mechanical Engineering, University of Ljubljana, Ljubljana, Slovenia  
e-mail: [janko.slavic@fs.uni-lj.si](mailto:janko.slavic@fs.uni-lj.si)



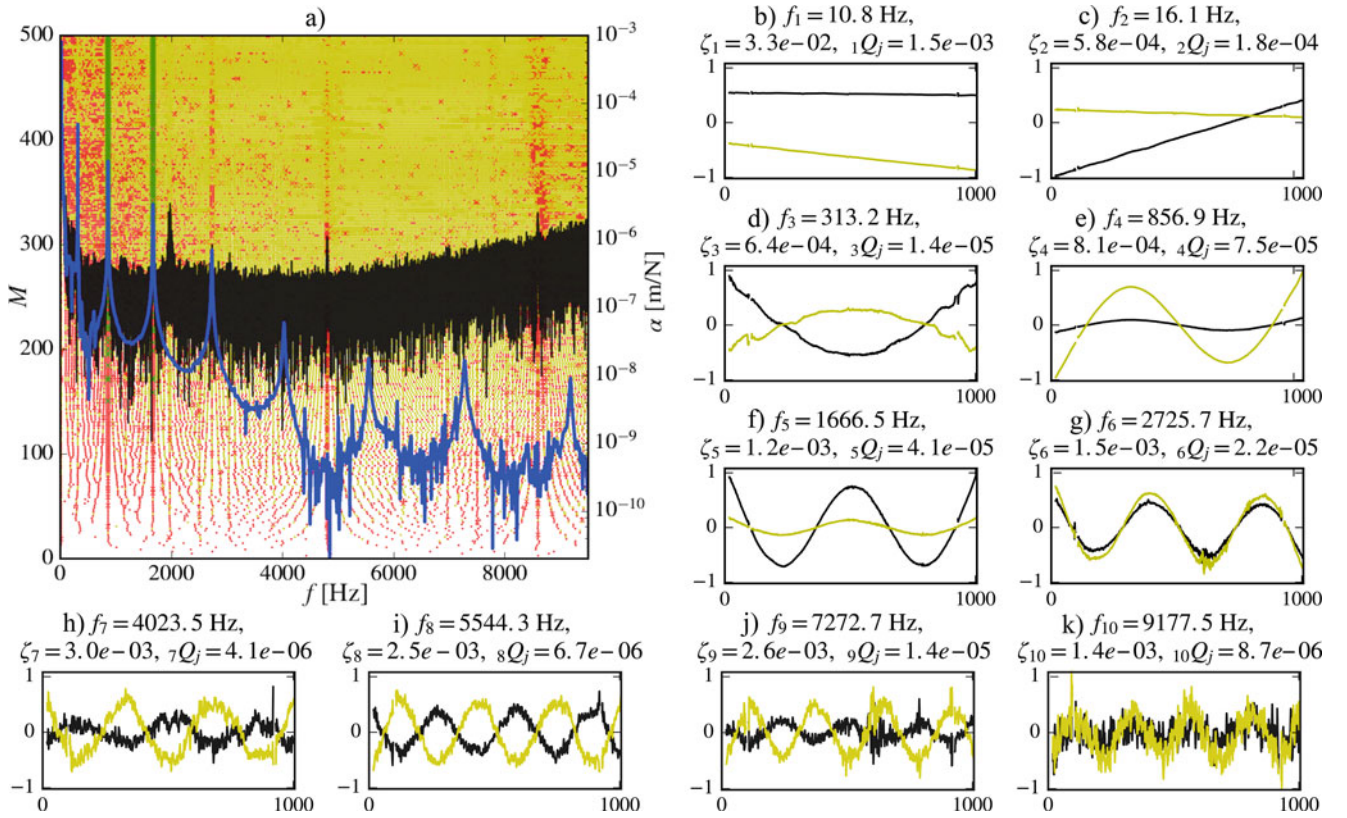


**Fig. 4.1** Experiment setup

Applying the MW damping identification to the time domain response, the damping ratio can be identified at a particular location, see Fig. 4.3. The uncertainty of the integral  $I$  in Eq. (4.2) depends on the mode shape and therefore absolute value  $|I|$  is used to weight the identified damping ratio at different positions along the beam to obtain an averaged damping ratio.

We can conclude that applying the Morlet Wave based damping identification to the optical flow displacement identification showed as very reliable and numerically stable.

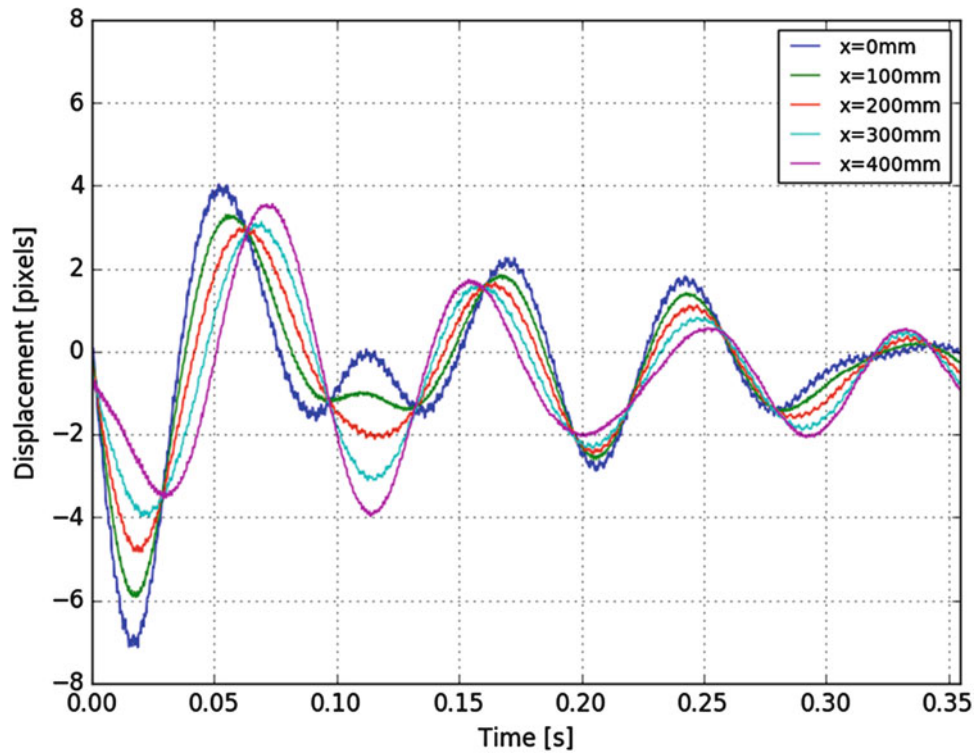


Fig. 4.2 Time domain response at selected positions of the impact excited beam

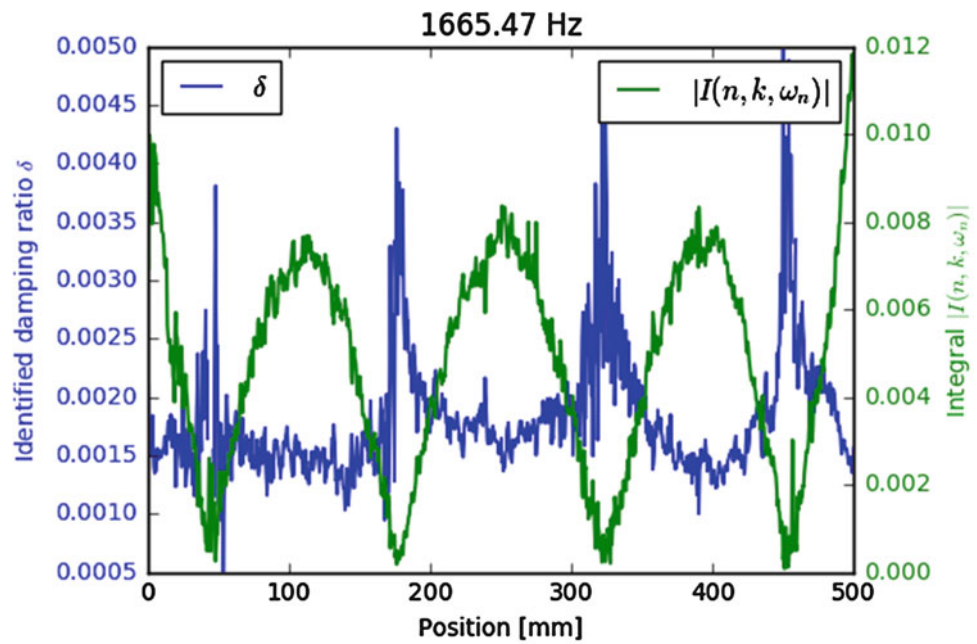


Fig. 4.3 Morlet Wave damping identification at the third natural frequency

## References

1. Mallat, S.: A Wavelet Tour of Signal Processing. A Wavelet Tour Signal Process, pp. 20–41. Elsevier (1999), Academic Press, London
2. Staszewski, W.J.: Identification of damping in M dof systems using time-scale decomposition. *J. Sound Vib.* **203**(2), 283–305 (1997)
3. Slavič, J., Simonovski, I., Boltežar, M.: Damping identification using a continuous wavelet transform: application to real data. *J. Sound Vib.* **262**(2), 291–307 (2003)
4. Yin, H.P., Duhamel, D., Argoul, P.: Natural frequencies and damping estimation using wavelet transform of a frequency response function. *J. Sound Vib.* **271**(3–5), 999–1014 (2004)
5. Slavič, J., Boltežar, M.: Damping identification with the Morlet-wave. *Mech. Syst. Signal Process.* **25**(5), 1632–1645 (2011)
6. Sutton, M.A., Orteu, J.J., Schreier, H.W.: Image Correlation for Shape, Motion and Deformation Measurements. Basic Concepts, Theory and Applications, p. 341. Springer, Verlag (2009)
7. Javh, M., Jaka, S., Janko, B.: Determining subpixel full-field displacements from videos by using optical flow. In: Proceedings of ICoEV 2015, International Conference on Engineering Vibration, pp. 1589–1603 (2015)
8. Javh, M., Jaka, B., Matija, S., Janko, B.: A high-speed camera measurement set-up for deflection shape analysis. In: Proceedings of ISMA2016 International Conference on Noise and Vibration Engineering [and] USD2016 International Conference on Uncertainty in Structural Dynamics, pp. 1115–1122 (2016)

# Chapter 5

## Fluid-Coupled Vibration Control Inspired by Dragonfly Wings

Yunjie Wang, Yajun Yin, and Gangtie Zheng

**Abstract** Dragonfly wings have excellent aerodynamic performance and damping capacity, which is driving people's attention. The existing researches on it are mainly from the vein structure and focusing on the static performance demonstration of dragonfly wings. Flutter analysis is very important during the process of aircraft design. With the inspiration of internal flow of dragonfly wings, the Coriolis force on the pipe wall while vibrating is discussed. By establishing a two-dimensional wing model, using quasi-steady aerodynamic equation, the aerodynamic force and the Coriolis force generated while fluttering were calculated. Theoretical calculation and numerical method are used to find critical velocity with and without internal flow. Coriolis force is proved effective on reducing two-dimensional wing flutter.

**Keywords** Flutter • Dragonfly • Coriolis force • Vibration • Wing

### 5.1 Introduction

Highly evolved in their living environment for millions of years, all living creatures are able to perfectly adapt to their living conditions. By studying their abilities, Bionics provides plenty of results that help us improve our living conditions.

With the most amazing ability among insects, Dragonflies achieve this ability because of their two-paired wings. By these wings, they could performance amazing flying patterns like straight flight, stopping in air, even backwards flight, which other flying creatures cannot. So far, there have been many applications inspired by dragonfly wings, especially in aerospace design. Also there have been many papers about aerodynamic and aero elastic achievements about dragonfly wings [1–3]. Although people have found the blood circulation inside insect wings, which is called Arnold circulation, as early as 1960s [4], not until now do people realize the importance of it [5].

It is known that insect wings are combined by protein and fiber [6, 7], but this combination requires specific temperature and humidity to remain its best property. Old researches referred that blood circulation inside helps the wings to keep wet in order to stop them from failing. But some other opinions are put forward that inner flow helps not only structure property but also dynamic performance while wings are flapping and vibrating inside airflow. Blood circulation helps redistribute the mass of the wing to prevent vibration and meanwhile provide a larger damping ratio, making the vibration decrease faster. All these effects could prevent vibration from happening thus ensuring a higher flying velocity, which becomes much important on today's aircraft design, when we are pursuing higher velocity and lower mass.

Flutter phenomenon happens when elastic structure moves in gas or liquid. Considering aircraft wing, aerodynamic force interacts with the elastic force of the wing, causing wing's violent vibration. There is a flutter critical velocity when vibration of the wing is out of control if aircraft move faster than it. Normally, redesigning the translational stiffness and rotational stiffness of the wing is the most effective way to increase flutter critical velocity [8, 9].

This paper provides a new perspective about how blood circulation changes the dynamic property of insert wings using fluid-structure coupling method. It also proposes an effective structure inspired by dragonfly wings which is easily applicable, uses both experimental and theoretical method to prove the damping effect of this structure and runs a simulation of it.

---

Y. Wang (✉) • Y. Yin • G. Zheng  
School of Aerospace Engineering, Tsinghua University, Beijing, 100084, China  
e-mail: 972559901@qq.com



## 5.2 Mechanism

Coriolis force, or Coriolis acceleration, appears when object moves in non-inertial reference frame. It follows the following equation.

$$\vec{a}_c = 2\vec{\omega} \times \vec{v} \quad (5.1)$$

Considering a bottom-fixed beam with inner flow, shown in Fig. 5.1.

As the beam vibrating, it generates angular velocity vertical to the showing plane. Along with the liquid flowing velocity, Coriolis force takes place the same direction with the beam's vibration direction, which affects the beam's vibration. And the direction of the flow is a very important factor about whether the Coriolis force will reduce the vibration or not.

Analysis aerodynamic forces by considering a two-dimensional wing with outside stiffness, as shown in Fig. 5.2. This two-dimensional wing has a chord length of  $2b$ ; its movements contains a vertical movement  $h$  (downward as positive); and rotation movement  $\alpha$  rotating  $E$ , the center of rigidity (clockwise as positive); The distance between center of rigidity and the middle point of the chord is  $ab$ , with  $a$  being a zero-dimension coefficient,  $a$  is positive when center of rigidity is behind the middle point of the chord. Flow speed is  $V$ ; both springs has stiffness of  $K_h$  and  $K_\alpha$ .

Without considering shape change of the wing, the downwash velocity is

$$w(x) = V\alpha + \dot{h} + [x - (1 + a)b]\dot{\alpha} \quad (5.2)$$

According to non-steady aerodynamic theory, the aerodynamic force and moment on the wing per unit length are as follow

$$\begin{aligned} L &= 2\pi\rho V^2 b \left[ \alpha + \frac{\dot{h}}{V} + \left(\frac{1}{2} - a\right) b \frac{\dot{\alpha}}{V} \right] \\ M_L &= \frac{b}{2} L - \frac{1}{2} \pi \rho V b^3 \dot{\alpha} \end{aligned} \quad (5.3)$$

Transfer this moment into the moment by the center of rigidity  $M_E$ .

$$M_E = 4\pi\rho V^2 b^2 \left( \frac{1+a}{2} - \frac{1}{4} \right) \left[ \alpha + \frac{\dot{h}}{V} + \left(\frac{1}{2} - a\right) b \frac{\dot{\alpha}}{V} \right] - \frac{1}{2} \pi \rho V b^3 \dot{\alpha} \quad (5.4)$$

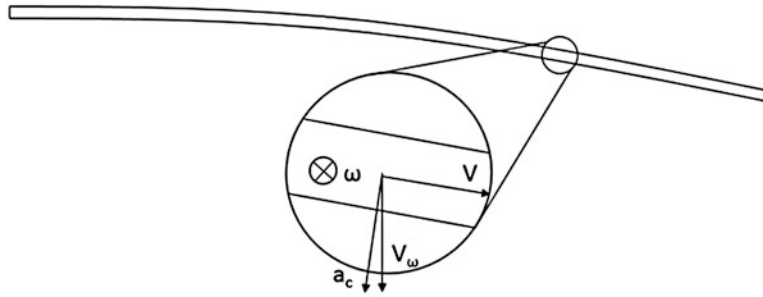


Fig. 5.1 Mechanism of Coriolis force

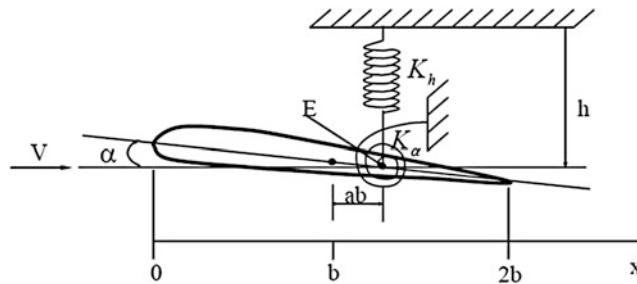


Fig. 5.2 Figure of two-dimension wing

Use the Lagrange equation (5.5) to analysis the wing's movement.

$$\frac{d}{dt} \left( \frac{\partial T}{\partial \dot{q}_i} \right) - \frac{\partial T}{\partial q_i} + \frac{\partial U}{\partial q_i} = Q_i \quad (5.5)$$

The kinetic energy of two-dimension wing is,

$$T = \frac{1}{2} m \dot{h}^2 + S_a \dot{h} \dot{\alpha} + \frac{1}{2} I_a \dot{\alpha}^2 \quad (5.6)$$

In which:

$m$  is the mass per unit length;

$S_a$  is static moment of mass of per unit length to center of stiffness;

$I_a$  is inertia moment of mass of per unit length to center of stiffness.

Whereas the potential energy of the wing is,

$$U = \frac{1}{2} K_h h^2 + \frac{1}{2} K_\alpha \alpha^2 \quad (5.7)$$

Substitute to Lagrange Equation, we have

$$\begin{cases} m \ddot{h} + S_a \ddot{\alpha} + K_h h = Q_h \\ S_a \ddot{h} + I_a \ddot{\alpha} + K_\alpha \alpha = Q_\alpha \end{cases} \quad (5.8)$$

$L$  is aerodynamic force (upward as positive),  $M$  is aerodynamic moment (clockwise as positive). This is the flutter equations. Different aerodynamic force calculating will result a different flutter critical velocity. However, the fact that critical velocity gets larger when two of the fundamental frequencies of the two-dimensional wing get farther from each other remains unchanged.

### 5.3 Two Dimensional Wing Flutter Simulation

Based on the two-dimensional wing vibration equation mentioned before, by numeral simulation, the effect of increasing flutter critical velocity by inner flow can be proved.

Since flutter phenomenon comes from aerodynamics forces and moments interacting with the wing's stiffness, putting fluid circulation far from stiffness center should have the best effects. This kind of arrangement has the largest moment with the same amount of Coriolis forces.

Set liquid circulation inside the wing as shown in Fig. 5.3. Assume inner flow velocity is  $v_l$ , liquid density is  $\rho_l$ , cross section of the tube is  $S$ , and the radius of curvature when vibrating is  $l$ . Assume tube location is at the very edge of the wing, the Coriolis force could be calculated as in Eq. (5.9),  $F_f$  is the Coriolis force on leading edge,  $F_b$  is the Coriolis force on trailing edge.

$$F_f = -2 \frac{[\dot{h} - (1+a)b\dot{\alpha}]}{l} v_l \rho_l S \quad F_b = 2 \frac{[\dot{h} + (1-a)b\dot{\alpha}]}{l} v_l \rho_l S \quad (5.9)$$

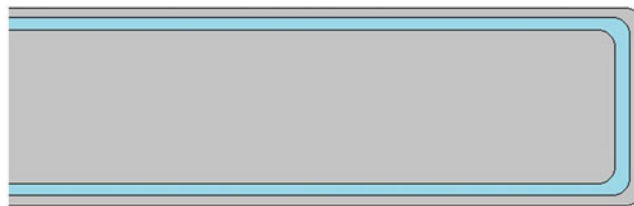


**Fig. 5.3** Liquid circulation arrangement inside the wing

Or,

$$F_f = -2 \frac{[\dot{h} - (1+a)b\dot{\alpha}]}{l} \rho_l Q \quad F_b = 2 \frac{[\dot{h} + (1-a)b\dot{\alpha}]}{l} \rho_l Q \quad (5.10)$$

For this kind of arrangement, substitute aerodynamic forces, aerodynamic moments and Coriolis force into flutter equations.

$$\begin{cases} Q_h = -L + F_f + F_b \\ Q_\alpha = M_E - F_f(1+a)b + F_b(1-a)b \end{cases} \quad (5.11)$$

$$\begin{cases} \ddot{h} = \frac{h_n - 2h_{n-1} + h_{n-2}}{\Delta t^2} \\ \dot{h} = \frac{h_n - h_{n-1}}{\Delta t} \\ \ddot{\alpha} = \frac{\alpha_n - 2\alpha_{n-1} + \alpha_{n-2}}{\Delta t^2} \\ \dot{\alpha} = \frac{\alpha_n - \alpha_{n-1}}{\Delta t} \end{cases} \quad (5.12)$$

Discretize these equations by following methods,

$$\begin{cases} \ddot{h} = \frac{h_n - 2h_{n-1} + h_{n-2}}{\Delta t^2} \\ \dot{h} = \frac{h_n - h_{n-1}}{\Delta t} \\ \ddot{\alpha} = \frac{\alpha_n - 2\alpha_{n-1} + \alpha_{n-2}}{\Delta t^2} \\ \dot{\alpha} = \frac{\alpha_n - \alpha_{n-1}}{\Delta t} \end{cases} \quad (5.13)$$

The following iterative equation is obtained,

$$\begin{cases} a_1 h_n + b_1 \alpha_n + c_1 = 0 \\ a_2 h_n + b_2 \alpha_n + c_2 = 0 \end{cases} \quad (5.14)$$

In which:

$$\begin{cases} a_1 = \frac{m}{\Delta t^2} + K_h + \frac{2\pi\rho Vb}{\Delta t} \\ b_1 = \frac{S_a}{\Delta t^2} + 2\pi\rho Vb + \frac{2\pi\rho Vb^2 \left(\frac{1}{2} - a\right)}{\Delta t} - \frac{4ab\rho_l Q}{l\Delta t} \\ c_1 = \frac{m}{\Delta t^2} (h_{n-2} - 2h_{n-1}) + \frac{S_a}{\Delta t^2} (\alpha_{n-2} - 2\alpha_{n-1}) - \frac{2\pi\rho Vb}{\Delta t} h_{n-1} \\ \quad - \frac{2\pi\rho Vb^2 \left(\frac{1}{2} - a\right)}{\Delta t} \alpha_{n-1} + \frac{4ab\rho_l Q}{l\Delta t} \alpha_{n-1} \\ a_2 = \frac{S_a}{\Delta t^2} - \frac{P}{V\Delta t} + \frac{4b\rho_l Q}{l\Delta t} \\ b_2 = \frac{I_a}{\Delta t^2} + K_\alpha + \frac{8ab^2\rho_l Q}{l\Delta t} - P - \frac{P \left(\frac{1}{2} - a\right) b}{V\Delta t} + \frac{\pi\rho Vb^3}{2\Delta t} \\ c_2 = \frac{S_a}{\Delta t^2} (h_{n-2} - 2h_{n-1}) + \frac{I_a}{\Delta t^2} (\alpha_{n-2} - 2\alpha_{n-1}) - \frac{4b\rho_l Q}{l\Delta t} h_{n-1} \\ \quad - \frac{8ab^2\rho_l Q}{l\Delta t} \alpha_{n-1} + \frac{P}{V\Delta t} h_{n-1} + \frac{P \left(\frac{1}{2} - a\right) b}{V\Delta t} \alpha_{n-1} - \frac{\pi\rho Vb^3}{2\Delta t} \alpha_{n-1} \\ P = 4\pi\rho V^2 b^2 \left(\frac{1+a}{2} - \frac{1}{4}\right) \end{cases} \quad (5.15)$$

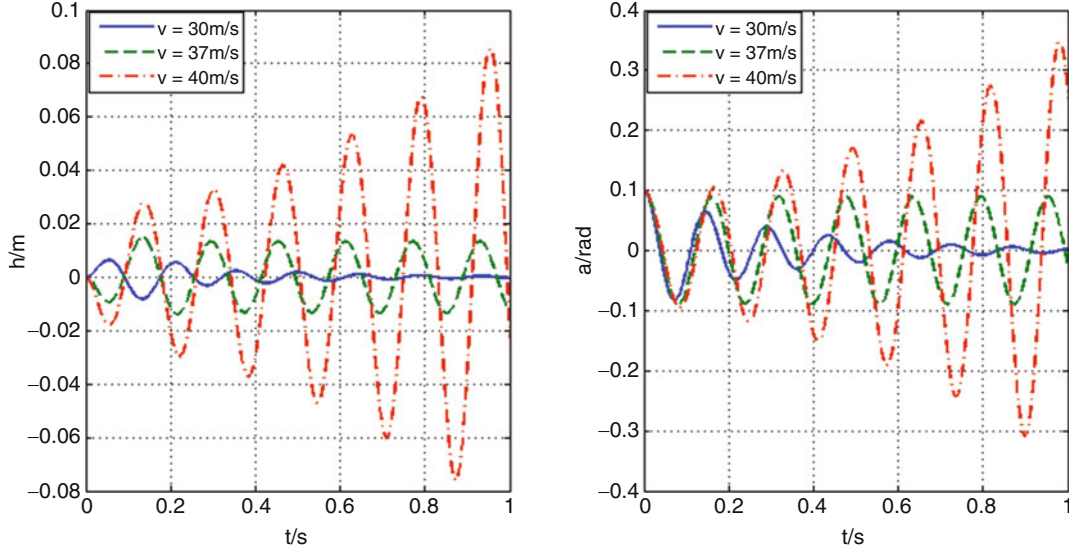


**Fig. 5.4** 2D wing flutter with 0 inner flow velocity under different incoming air velocity (vertical movement on the left; rotation movement on the right)

By solving them, we have  $h_n$  and  $\alpha_n$ , which are vertical movement and rotational movement of step  $n$ , when those of step  $n-1$  and step  $n-2$  are known. This method is very effective on simulating quasi-steady two-dimensional flutter problem.

Using an example to prove the effect of Coriolis force on flutter reduction, in which  $S_a = 0.25\text{mb}$ ,  $I_a = 0.5\text{mb}^2$ ,  $e/b = 0.4$ ,  $\omega_\alpha = 50\text{ rad/s}$ ,  $\omega_h = 25\text{ rad/s}$ ,  $b = 1\text{ m}$ ,  $m = 1\text{ kg}$ , air density  $\rho = 0.0636\text{ kg/m}^3$ . When liquid speed is 0, then all  $Q$  can be neglected. Using simplified quasi-steady aerodynamic equation,

$$L = \frac{1}{2}\rho V^2(2b)\frac{\partial C_L}{\partial \alpha}\left(\alpha + \frac{\dot{h}}{V}\right) \quad M = L \cdot e \quad (5.16)$$

We have following flutter equation

$$\begin{cases} m\ddot{h} + S_a\ddot{\alpha} + K_h h + \frac{1}{2}\rho V^2(2b)\frac{\partial C_L}{\partial \alpha}\left(\alpha + \frac{\dot{h}}{V}\right) = 0 \\ S_a\ddot{h} + I_a\ddot{\alpha} + K_\alpha \alpha - \frac{1}{2}\rho V^2(2b)\frac{\partial C_L}{\partial \alpha}\left(\alpha + \frac{\dot{h}}{V}\right)e = 0 \end{cases} \quad (5.17)$$

Assume two-dimension wing is doing simple harmonic vibration.

$$h = h_0 e^{i\omega t}, \quad \alpha = \alpha_0 e^{i\omega t} \quad (5.18)$$

Combining (5.17) and (5.18), the flutter critical velocity is calculated as 36.08 m/s.

With inner flow existing, the flutter equation is difficult to theoretically solve. Numeral method is applied to find the critical velocity. By adding 0.1 rad deviation on rotation movement, the development of vibration could tell whether the air flow velocity is below or above the critical velocity. Set the cross section of the tube  $0.002\text{ m}^2$ , liquid density  $1000\text{ kg/m}^3$ , liquid velocity  $9\text{ m/s}$ , Fig. 5.4 shows 2D wing flutter with 0 inner flow velocity under different incoming air velocity, Fig. 5.5 shows 2D wing flutter with  $9\text{ m/s}$  inner flow velocity under different incoming air velocity.

It is apparent that critical velocity is  $37\text{ m/s}$  when inner flow is  $0\text{ m/s}$ , and  $45\text{ m/s}$  when inner flow is  $9\text{ m/s}$ . the critical velocity is increased by 21.6%. the critical velocity when inner flow is  $0\text{ m/s}$  is  $37\text{ m/s}$ , which is close to  $36.08\text{ m/s}$ .

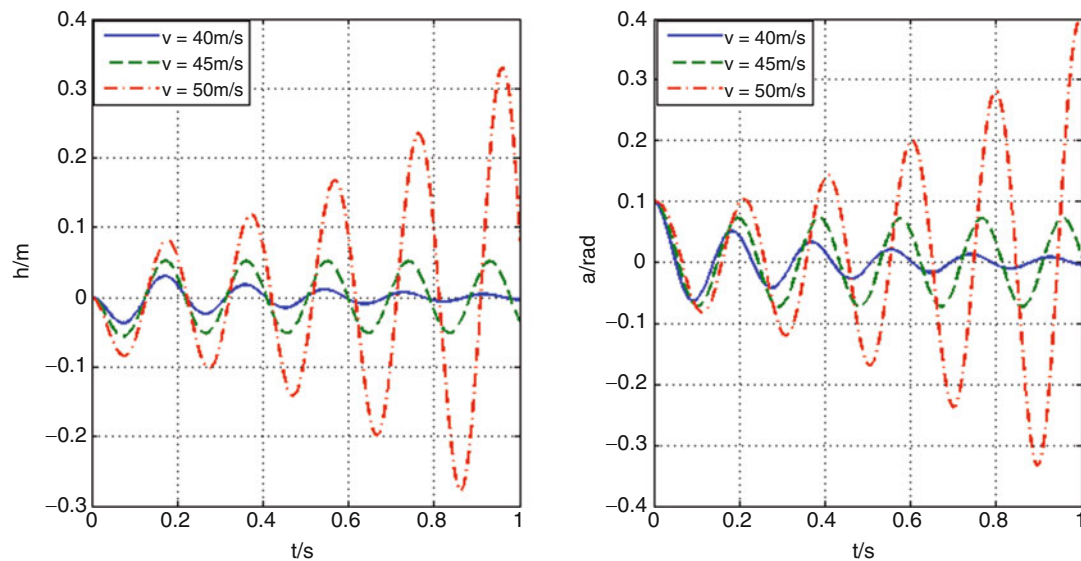


**Fig. 5.5** 2D wing flutter with 9 m/s inner flow velocity under different incoming air velocity (vertical movement on the *left*; rotation movement on the *right*)

## 5.4 Conclusion

Dragonfly has an amazing wing structure. As man-made aircrafts gain their flying velocity, vibration of their wings becomes more destructive. The understanding of the mechanism of dragonfly wings offers not only more opportunity to solve wing flutter problem, but also applications in other damping-demanded situations.

Inspired by dragonfly wing's structure, this article presents a reasonable fluid-structure-coupling model, which is proved to be effective and believable on its damping effect of reducing flutter vibration and increasing critical velocity. However, this result is obtained by simply analysis two-dimensional wing, with only two fundamental frequencies. Three-dimensional wing has multiple frequencies, which makes them easy to interact and trigger flutter act. Using this method for flutter control should be much harder.

Also, this article provides a new aspect of seeing the mechanism of Arnold circulation. This circulation may has damping effect as long as maintaining performance of dragonfly wings.

## References

1. Azuma, A., Azuma, S., Watanabe, I., Furuta, T.: Flight mechanics of a dragonfly. *J. Exp. Biol.* **116**(1), 79–107 (1985)
2. Wakeling, J., Ellington, C.: Dragonfly flight. II. Velocities, accelerations and kinematics of flapping flight. *J. Exp. Biol.* **200**(3), 557–582 (1997)
3. Reavis, M.A., Luttges, M.W.: Aerodynamic forces produced by a dragonfly. *AIAA J.* **88**(0330), 1–13 (1988)
4. Arnold, J.W.: Blood circulation in insect wings. *Mem. Entomol. Soc. Can.* **96**(S38), 5–60 (1964)
5. Zhao, H., Yin, Y., Zhong, Z.: Arnold circulation and multi-optimal dynamic controlling mechanisms in dragonfly wings. *Acta Mech. Solida Sin.* **26**(3), 237–244 (2013)
6. Zhao, H., Yin, Y., Zhong, Z.: Micro and nano structures and morphologies on the wing veins of dragonflies. *Chin. Sci. Bull.* **55**(19), 1993–1995 (2010)
7. Wainwright, S.A.: *Mechanical Design in Organisms*. Princeton University Press, Princeton (1982)
8. Yang, Z., Zhao, L.: *Aircraft Aerodynamic elastics*, [J]. (2004)
9. Hodges, D.H., Pierce, G.A.: *Introduction to Structural Dynamics and Aeroelasticity*[M]. Cambridge University Press (2002)

# Chapter 6

## Improving Modal Parameter Estimation by Complementary Output–Output Relations

Oscar Olarte and Patrick Guillaume

**Abstract** Frequency domain modal parameter estimation from input–output data requires direct measurement or estimation of the input and output signals. In different applications those measurements, especially the excitation signals, are difficult to obtain and/or the assumptions could be poor or inappropriate (high uncertainty or high levels of noise). In this situations, the output–output relations can be used as auxiliary or complementary equations. The current work presents a framework for the identification of modal parameters estimation using maximum likelihood estimation incorporating the output–output relations in addition to the input–output ones. Since the output–output relations are independent of the input signals and its related uncertainty they will improve the system estimation. The ML estimator presents properties of consistency and efficiency and converge to the noiseless solution, but it involve calculating the inverse of the covariance matrix. An extended practice is to consider or assume that the noise of the frequency responses is uncorrelated, in this sense the covariance matrix becomes diagonal and the computational time is reduced. However, the price to pay is that the efficiency of the estimator is altered (the estimator does not reach the Cramer-Rao lower bound). The current work shows that incorporating the output–output relations to the input–output set of equations generates results closer to the ML estimator with a reduced computational load.

**Keywords** Modal parameters estimation • Identification • Maximum likelihood estimator • Output–output relations • Estimator efficiency

### 6.1 Introduction

The goal of system identification is develop mathematical models based on observed data, it is the base of measurement base processes as design, control and monitoring. In general the modeling of a system can be carried out based on principles (physical laws) or data driven. Models based on principles are preferred since are extrapolable, reliable and scalable. However, they require plenty knowledge and detailed expertise in the process domain. In this sense, identification based on data-driven is fundamental when the process is complex that rule out the approach based on principles. Data-driven identification presents facilities like the ability to built models with minimal process knowledge, flexibility in the model structure and convenience to develop or implement the model in code-computer.

Usually an input–output (transfer function relation) frequency domain approach require the direct measurement or estimation of the input–output signals. However, in some applications such measurements, specially the inputs of the system, are difficult to assess and/or the assumptions could be poor or inappropriate (high levels of noise or uncertainty). In this situations the output–output relations can be used as auxiliar or complementary relations. Similar to a traditional input–output transfer functions the output–output functions are defined as the frequency-domain ratio between two outputs, and it describes the relative admittance between the two measurements. In [1] and [2] the output–output relations are interpreted as the response data normalized by a reference response instead of by the input excitation. These functions contain specific (local) information compared to the Transfer functions, because the characteristic polynomial, which contains all the system poles (resonances), will be canceled in the output–output implementation, and only the system zeros (anti-resonances) will remain. Therefore, the features derived from the output–output functions are independent of the system poles but depend solely on the zeros of the system.

---

O. Olarte (✉) • P. Guillaume

Mechanical Engineering Department, Vrije Universiteit Brussel, Acoustics and Vibration Research Group, Pleinlaan 2, 1050 Brussel, Belgium  
e-mail: oolarter@vub.ac.be; Patrick.Guillaume@vub.ac.be

Contrary to the resonances of the system, which are influenced by structural parameters globally, anti-resonances are principally affected by local properties and are sensitive to detailed structural modeling. As a result, transmissibilities (output–output relations) seems to be a useful characteristic in the identification sensible to local structural details and effects [3, 4].

Different applications of identification using transmissibility functions are present in the area of damage detection and structural health monitoring. Using neural networks [5, 6] show that transmissibility allows detection of small stiffness variation allowing identify the appearance and location of the changes in the system parameters. The location of the system parameters has been effective on both discrete [7] and continuous [8] system applications. In [9, 10] and [11] based on measured transmissibilities and novelty detection, the research groups develop the experimental validation of a structural health monitoring methodology from simple laboratory structures to complex and realistic structures such as aircraft wing, and the results from detection and localization are validated. In [7] and [12] diagnostic technology based on transmissibility is used to reduce the dimension of response measurements and demonstrate analytically and experimentally the sensitivity of transmissibility to both linear and nonlinear system changes.

The current work presents the combination of input–output and output–output relations for the identification of multivariable systems. The article starts showing the errors in variables frequency domain framework followed by the description of the mle estimator for input–output relations. Subsequently introduces the approach based on input–output and output–output relations for the parameter estimation. A comparison between the different approaches is presented by mean of a simulation example, showing the convenience of the method here proposed. Finally the conclusions are presented.

## 6.2 Errors in Variables

Consider a linear time-invariant multivariable system with  $N_i$  inputs and  $N_o$  outputs as is represented in Fig. 6.1. The figure shows the schematic of the MIMO system together with the most important sources of errors during a non-parametric identification process. If  $M$  time domain records are observed, we have:

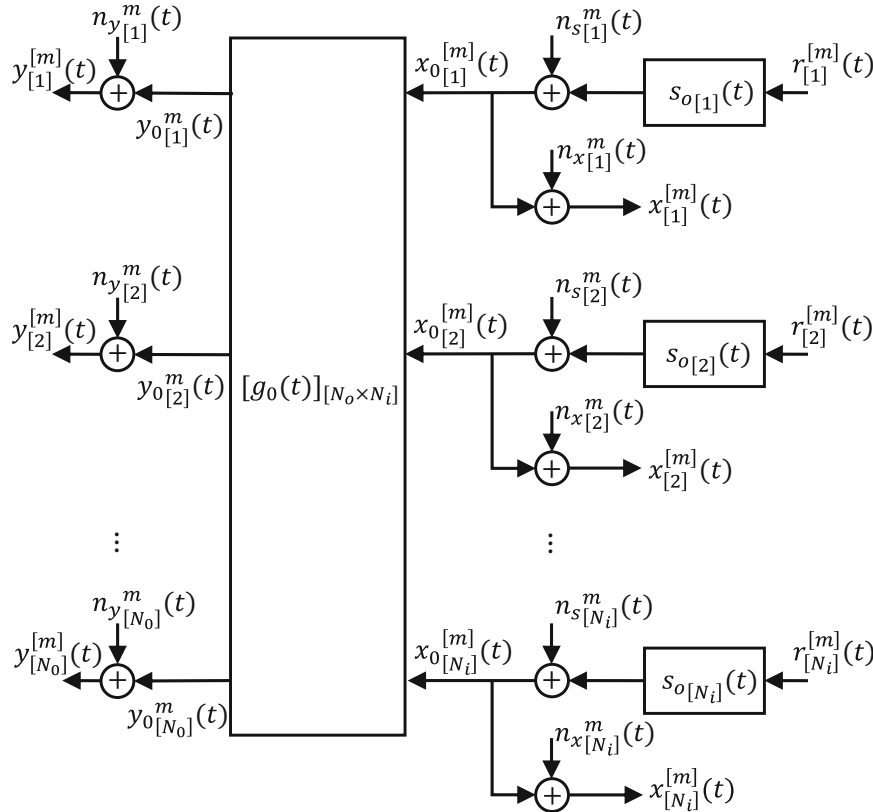


Fig. 6.1 Time domain errors in variables

$$\begin{aligned}x^{[m]}(t_n) &= x_0^{[m]}(t_n) + e_x^{[m]}(t_n) \\y^{[m]}(t_n) &= y_0^{[m]}(t_n) + e_y^{[m]}(t_n)\end{aligned}\quad (6.1)$$

with  $t_n = nT_s$ ,  $n = 0, 1, \dots, N_s$  and  $T_s$  the sampling period. The vectors  $x^{[m]}$  and  $y^{[m]}$  are the measurement input and output of the multivariate system  $h_0(t)$  at time  $t = T_n$  at the  $m$ th measurement record. The  $x_0^{[m]}(t_n)$  and the  $y_0^{[m]}(t_n)$  are the true but unknown input and output respectively. The noise sources  $e_x^{[m]}(t_n)$  and  $e_y^{[m]}(t_n)$  include the noise sources  $n_x^{[m]}(t_n)$ ,  $n_y^{[m]}(t_n)$  and  $n_s^{[m]}(t_n)$ .

In the frequency domain the relation between the noisy input  $X^{[m]}(\omega_f)$  and the noisy output  $Y^{[m]}(\omega_f)$  and the noiseless ones ( $X_0^{[m]}(\omega_f)$  and  $Y_0^{[m]}(\omega_f)$ ) is given by the frequency domain errors-in-variables stochastic model

$$\begin{aligned}X^{[m]}(\omega_f) &= X_0^{[m]}(\omega_f) + E_X^{[m]}(\omega_f) \\Y^{[m]}(\omega_f) &= Y_0^{[m]}(\omega_f) + E_Y^{[m]}(\omega_f)\end{aligned}\quad (6.2)$$

with angular frequency  $\omega_f = 2\pi f/N_s T_s$  and  $f = 0, 1, \dots, N_s/2 - 1$ . The schematic of the frequency domain errors in variables noise model is presented in Fig. 6.2.

The relation between the true input  $X_0^{[m]}(\omega_f)$  and true output  $Y_0^{[m]}(\omega_f)$  is given by

$$Y_0^{[m]}(\omega_f) = G_0(\omega_f) X_0^{[m]}(\omega_f) \quad (6.3)$$

where the matrix  $G_0(\omega_f)$  stands for the frequency response function (FRF) matrix of the system at the expected line  $f$ .

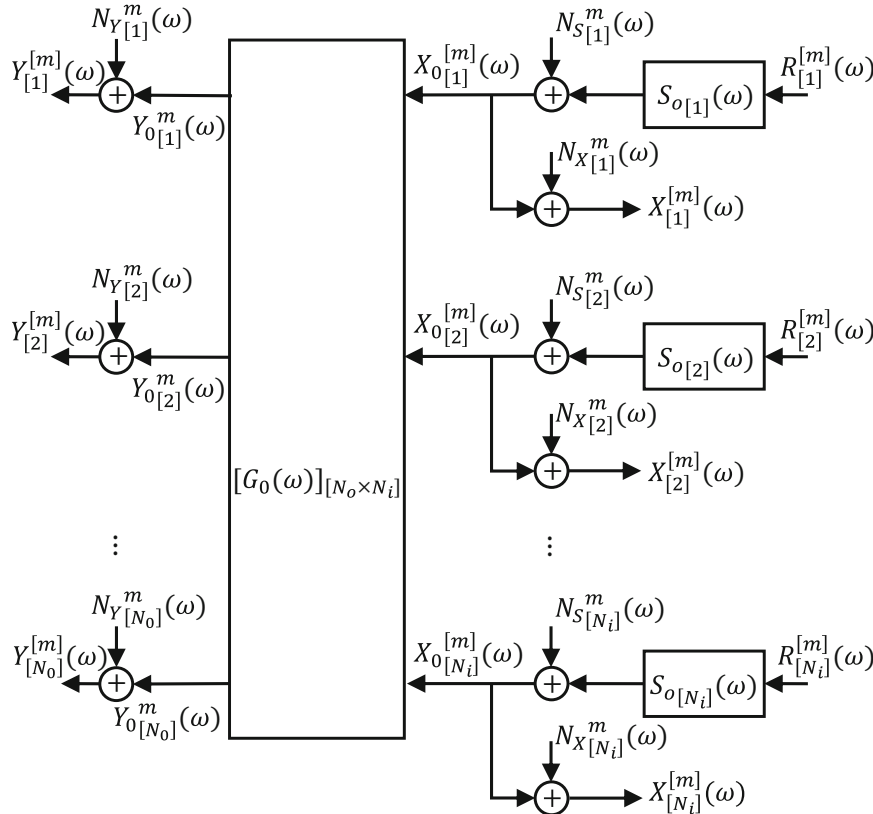


**Fig. 6.2** Frequency domain errors in variables



In Fig. 6.2  $N_X^{[m]}(\omega_f)$  and  $N_Y^{[m]}(\omega_f)$  represent the input and output measurement noise. The effect of the actuators on the reference signals  $R_{[i]}^{[m]}(\omega_f)$  is represented by the transfer functions  $S_{0[i]}(\omega_f)$  and the associated noise is represented by  $N_{s[i]}^{[m]}(\omega_f)$ . Hence the frequency domain errors in variables model can be written as:

$$\begin{aligned} X^{[m]}(\omega_f) &= S_0(\omega_f)R^{[m]}(\omega_f) + E_X^{[m]}(\omega_f) \\ Y^{[m]}(\omega_f) &= G_0(\omega_f)S_0(\omega_f)R^{[m]}(\omega_f) + E_Y^{[m]}(\omega_f) \end{aligned} \quad (6.4)$$

with the error vectors  $E_X^{[m]}(\omega_f)$  and  $E_Y^{[m]}(\omega_f)$  representing all possible disturbing spectral noise sources.

$$\begin{aligned} E_X^{[m]}(\omega_f) &= N_S^{[m]}(\omega_f) + N_X^{[m]}(\omega_f) \\ E_Y^{[m]}(\omega_f) &= G_0(\omega)N_S^{[m]}(\omega_f) + N_Y^{[m]}(\omega) \end{aligned} \quad (6.5)$$

### 6.3 Maximum Likelihood Estimator (*mle*)

The parametric transfer function considered here is scalar matrix description or common denominator transfer function described as

$$G(s) = \frac{N(s)}{d(s)} \quad (6.6)$$

where  $N(s)$  is a q-output x p-input polynomial matrix. The  $n_{ij}(s)$  locations of the  $N(s)$  matrix are given by

$$n_{ij}(s) = a_0^{ij} + a_1^{ij}s + \dots + a_{\alpha_{ij}}^{ij}s^{\alpha_{ij}} \quad (6.7)$$

while the denominator of (6.6) is given by

$$d(s) = b_0 + b_1s + \dots + b_\beta s^\beta \quad (6.8)$$

The index  $\alpha_{ij}$  and  $\beta$  refer the order of the polynomials  $n_{ij}(s)$  and  $d(s)$  respectively.

Assuming that the noise on the real and imaginary part of the spectra of the input and output signals are independent, zero mean, Gaussian random variables, it can be proven [13] that the MLE of the parameters is found by minimizing the cost function

$$v = \frac{1}{2} \sum_{k=1}^F \xi^H(k) C_\xi^{-1}(k) \xi(k) \quad (6.9)$$

with  $H$  the complex conjugate transport operation and

$$\xi(k) = [N(k), -d(k)I] \begin{bmatrix} X(k) \\ Y(k) \end{bmatrix} \quad (6.10)$$

The matrix  $C_\xi^{-1}(k)$  is the inverse of the covariance matrix

$$C_\xi(k) = [N(k), -d(k)I] Cov \left\{ \begin{bmatrix} X(k) \\ Y(k) \end{bmatrix} \right\} [N(k), -d(k)I]^H \quad (6.11)$$

with  $Cov \{ \cdot \}$  the covariance matrices of the perturbation noise of the inputs and outputs at the frequency lines  $k$ . The perturbation noise can be determined from a priori measurements [14, 15].

The cost function (6.9) is a non-linear function of the parameters. A Gauss-Newton method can be useful to determine the minimum of the cost function, while the least squares (LS) solution can be used as starting values. The LS solution is obtained by setting the  $C_{\xi}^{-1}(k)$  equal to the identity matrix in (6.9).

### 6.3.1 *mle Diagonal Implementation*

The mle estimator is optimum since follow the properties of consistency and efficiency and converge to the noiseless solution [16]. However, the procedure requires determine the inverse of the covariance matrix (6.11) which carries a significant computation load.

In order to reduce the computational load it is possible to assume independence between the inputs and outputs and that the contributions from non-diagonal terms are reduced compared with the diagonal terms. In this sense the covariance matrix (6.11) becomes a diagonal matrix and from here a fast and practical implementation is achieved. However, in general this estimation differs from the mle solution. It is consistent (converge to the true parameters asymptotically) but not efficient [17].

## 6.4 Extension of Diagonal-*mle* Using Output–Output Relations

The equation error (6.10) considers the input–output relation and from here its dependency of the input signal and related noise. However, along the output–output relations this dependency is set aside.

Output–output relations are obtained by the ratio of two response spectra. This is, the ratio between the output  $q$  and  $r$  is  $T_{q,r}(\omega) = \frac{Y_q(\omega)}{Y_r(\omega)}$ . Using (6.3) and (6.6) the output–output equations are reduced to:

$$T_{q,r}(\omega) = \frac{Y_q(\omega)}{Y_r(\omega)} = \frac{G_{q,p}(\omega)X_p(\omega)}{G_{r,p}(\omega)X_p(\omega)} = \frac{N_{q,p}(\omega)}{N_{r,p}(\omega)} \quad (6.12)$$

with  $N_{q,p}(\omega)$  and  $N_{r,p}(\omega)$  the numerator polynomials occurring in the transfer function  $G_{q,p} = \frac{N_{q,p}(\omega)}{d(\omega)}$  and  $G_{r,p} = \frac{N_{r,p}(\omega)}{d(\omega)}$ . Observe that the common denominator  $d(\omega)$  and the current excitation signal is eliminated by taking the ratio between the response-output spectra. The fact that the equations become independent of the system poles, input excitation and associated noise allows that the set of equations can be used to improve the identification, specially when the input signal is highly corrupted by noise.

The equation error and associated covariance can be extended to the output–output equations as:

$$\xi(k) = \begin{bmatrix} N(k) & -d(k)I \\ 0 & M(k) \end{bmatrix} \begin{bmatrix} X(k) \\ Y(k) \end{bmatrix} \quad (6.13)$$

and covariance matrix

$$C_{\xi}(k) = \begin{bmatrix} N(k) & -d(k)I \\ 0 & M(k) \end{bmatrix} Cov \left\{ \begin{bmatrix} X(k) \\ Y(k) \end{bmatrix} \right\} \begin{bmatrix} N(k) & -d(k)I \\ 0 & M(k) \end{bmatrix}^H \quad (6.14)$$

with  $M$  the matrix of the numerator relation obtained by (6.12).

The mle solution of (6.9) requires the inverse of (6.14) which is a singular matrix since there exist linear dependency between the rows. However, as in the previous case, it is assumed that covariance matrix is diagonal, or in other words it is assumed that the noise is uncorrelated between the inputs and outputs, and that the contribution of the non-diagonal terms are irrelevant, the covariance matrix (6.14) is a diagonal matrix that include the input–output and output–output relations and allow a fast implementation. This implementation will provide consistent estimators although non efficient. However, the estimation using the output–output relation will provide better results in terms of efficiency than the diagonal-*mle* implementation.

## 6.5 Example Simulation

A simulation example is considered as illustration of the effect of the output–output relations in the mle estimator. The results compares the mle estimator (*mle*), the fast-diagonal-implementation (*Dmle*) and the extended-diagonal-mle (extended to the output–output relations –  $D^+mle$ ) under two scenarios: 1. The noise at the outputs is uncorrelated. This is, the term  $N_Y(\omega_f)$  in equation (6.5) correspond to independent noise realizations and 2. the noise at the outputs is correlated. The term  $N_Y(\omega_f)$  in equation (6.5) is composed by correlated noise ( $N_{Y_{corr}}(\omega)$ ) and uncorrelated noise ( $N_{Y_{uncorr}}(\omega)$ ). Along the simulations the SNR of the inputs and outputs will be variate for different values in order to show the behavior of the estimators and identify the capabilities and advantages of the different methods.

The results between the different estimators will be compared by mean of the generalized variance (GV) of the parameters of the system. The GV of a p-dimensional random vector variable  $X$  is defined as the determinant of its variance-covariance matrix. The general variance can be seen as a scalar measure of overall multidimensional scatter [18]. Lower the GV value is, lower variance in the parameters.

The simulated system used for the exemplification is a 2x2 MIMO system with common denominator. The numerator matrix  $N(s)$  is:

$$N(s) = \begin{bmatrix} s^2 + 2 & s^2 + 25 \\ 3s^2 + 5s + 1 & s^2 + 3s + 7 \end{bmatrix} \quad (6.15)$$

and common denominator is:

$$d = s^6 + 81s^4 + 1104s^2 + 1024 \quad (6.16)$$

### 6.5.1 Uncorrelated Outputs

For the uncorrelated case, it will be variate the SNR in the inputs and outputs of the system. The SNR of the input will variate from 1 to 50 dB while the SNR of the outputs from 1 to 70 dB. Figure 6.3 shows the GV of the parameters of the system.

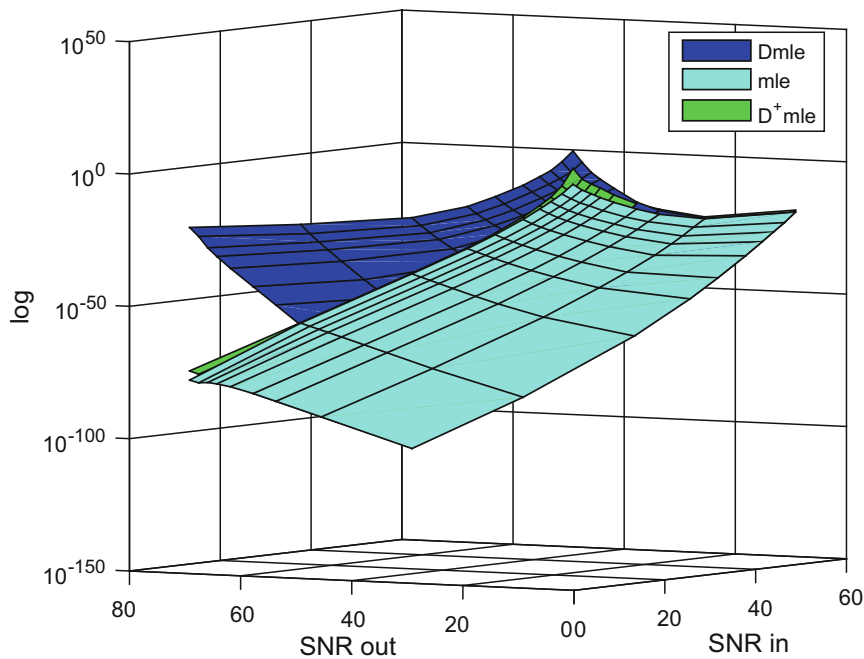


**Fig. 6.3** Generalized variance of the identified parameters of the model for uncorrelated outputs

From this results it is possible to identify, as is expected, that the *mle* estimator generates the lower scatter matrix (lower variance). However, it is important to note that the  $D^+mle$  estimator present similar results, even when in its formulation the non-diagonal terms in the variance-covariance matrix have been removed. On the other hand, the *Dmle* estimator only generates similar values when the SNR at the input is high enough. At low SNR at the inputs, this estimator moves away from the *mle* solution for high SNR at the outputs. In this sense, the output–output relations, used in the definition of the  $D^+mle$  estimator, allows improving the parameters estimation whit results close to the *mle* formulation, avoiding the implementation and calculation of the inverse of the covariance matrix. This result is important since, as has been mentioned in the introduction, there exist a considerable number of cases where the estimation of the input signal is highly contaminated by noise.

### 6.5.2 Correlated Outputs

The previous result has shown that the  $D+mle$  estimator generates close results to the *mle* estimator. However, such result was under the general assumption that the noise at the outputs were uncorrelated. This means that there is not information about the output outside of the principal diagonal of the variance–covariance matrix. In the current scenario such information is present in the variance–covariance matrix and from here that more information is remove once the diagonal implementations are considered (*Dmle* and  $D^+mle$ ).

In the current scenario there are three variables: the level of noise at the inputs (variates from 1 to 30 dB). The independent noise at the outputs (variates from 1 to 50 dB) and the correlated noise at the outputs (variate from 1 to 70 dB). Figure 6.4 shows the GV of the parameters of the model for four different levels of noise at the input (1, 10, 20 and 30 dB). Similar as in the previous case, in general, the  $D^+mle$  presents a closer response to the *mle* than the *Dmle* estimator even when there are outputs correlation. It is clear that the correlation level reduces the similarities *mle*– $D^+mle$  but it happens for high levels of correlated noise, while for low levels the results *mle*– $D^+mle$  are quite equivalent.

## 6.6 Conclusion

The work shows that the inclusion of output–output relation in the diagonal implementation of the *mle* estimator improves the identification reaching close results to the complete or full *mle* implementation. Comparing the diagonal implementations ( $D^+mle$  and *Dmle*) the  $D^+mle$  estimator generates better results under scenarios where the *Dmle* implementation moves considerably away of the *mle* results. This result is originated because the output–output relations included in the  $D^+mle$  implementation are independent of the input signals and related uncertainty and from here that the results from the  $D^+mle$  outpoints the *Dmle* when the input signals present considerable uncertainty. Such differences are more accentuated if also the output signals present low noise levels.

This new result can be used to further improve the frequency-domain maximum likelihood modal parameter estimator [17] without jeopardizing the fast implementation.

**Acknowledgements** This work was partially supported by SRP-OPTIMEch Vrije Universiteit Brussels (VUB).

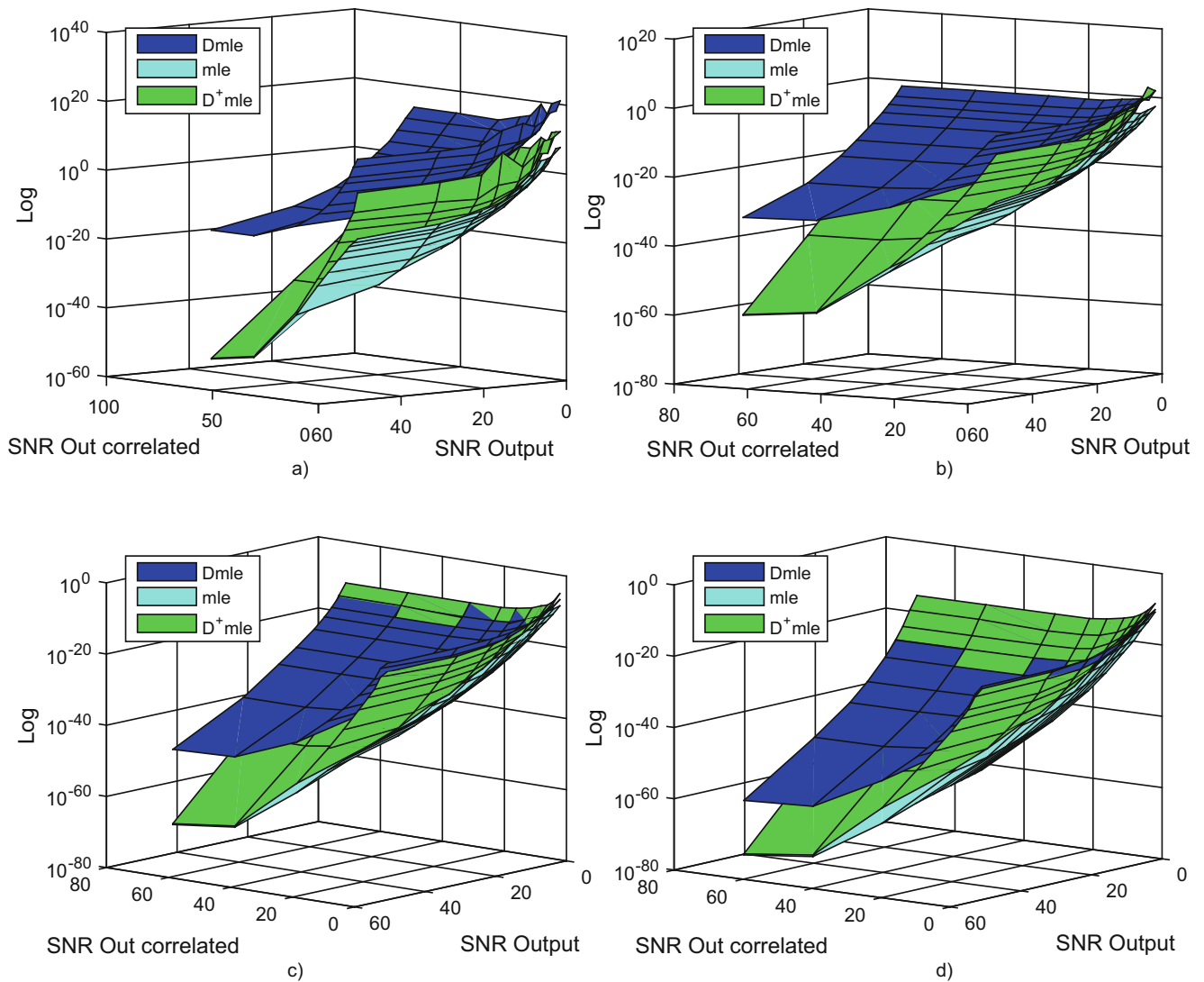


**Fig. 6.4** Generalized variance of the identified parameters of the model in presence of correlated noise at the outputs for four different levels of noise at the input: (a) 1 dB, (b) 10 dB, (c) 20 dB, (d) 30 dB

## References

1. Weijtjens, W., De Sitter, G., Devriendt, C., Guillaume, P.: Operational modal parameter estimation of MIMO systems using transmissibility functions. *Automatica* **50**(2), 559–564 (2014)
2. Devriendt, C., Steenackers, G., Sitter, G.D., Guillaume, P.: From operating deflection shapes towards mode shapes using transmissibility measurements. *Mech. Syst. Signal Process.* **24**(3), 665–677 (2010)
3. Devriendt, C., Guillaume, P.: Identification of modal parameters from transmissibility measurements. *J. Sound Vib.* **314**(1–2), 343–356 (2008)
4. Mao, Z., Todd, M.: A model for quantifying uncertainty in the estimation of noise-contaminated measurements of transmissibility. *Interdiscip. Integr. Aspects Struct. Health Monit. Mech. Syst. Signal Process.* **28**, 470–481 (2012)
5. Worden, K.: Structural fault detection using a novelty measure. *J. Sound Vib.* **201**(1), 85–101 (1997)
6. Worden, K., Manson, G., Fieller, N.: Damage detection using outlier analysis. *J. Sound Vib.* **229**(3), 647–667 (2000)
7. Johnson, T.J., Adams, D.E.: Transmissibility as a differential indicator of structural damage. *J. Vib. Acoust.* **124**(4), 634–641 (2002)
8. Afolabi, D.: An anti-resonance technique for detecting structural damage. In: *Proceedings of Fifth International Model Analysis Conference*, pp. 491–495 (1987)
9. Worden, K., Manson, G., Allman, D.: Experimental validation of a structural health monitoring methodology: part i. novelty detection on a laboratory structure. *J. Sound Vib.* **259**(2), 323–343 (2003)
10. Manson, G., Worden, K., Allman, D.: Experimental validation of a structural health monitoring methodology: part ii. novelty detection on a GNAT aircraft. *J. Sound Vib.* **259**(2), 345–363 (2003)

11. Manson, G., Worden, K., Allman, D., Experimental validation of a structural health monitoring methodology: part III. Damage location on an aircraft wing. *J. Sound Vib.* **259**(2), 365–385 (2003)
12. Johnson, T.: Analysis of dynamic transmissibility as a feature for structural damage detection. Master’s thesis, Purdue University (2001)
13. Guillaume, P., Pintelon, R., Schoukens, J.: Description of a parametric maximum likelihood estimator in the frequency domain for multi-input, multi-output systems and its application to flight flutter analysis. *Mech. Syst. Signal Process.* **4**(5), 405 – 416 (1990)
14. Schoukens, J., Pintelon, R., Renneboog, J.: A maximum likelihood estimator for linear and nonlinear systems—a practical application of estimation techniques in measurement problems. *IEEE Trans. Instrum. Meas.* **37**(1), 10–17 (1988)
15. Schoukens, J., Pintelon, R., van der Ouderaa, E., Renneboog, J.: Survey of excitation signals for FFT based signal analyzers. *IEEE Trans. Instrum. Meas.* **37**(3), 342–352 (1988)
16. Pintelon, R., Schoukens, J.: *System Identification: A Frequency Domain Approach*. Wiley, Hoboken (2012)
17. Guillaume, P., Verboven, P., Vanlanduit, S.: Frequency-domain maximum likelihood identification of modal parameters with confidence intervals. In: ISMA23th (ed.) *Proceedings of the 23rd International Seminar on Modal Analysis*, Leuven, pp. 359–366 (1998)
18. Wilks, S.S.: Multidimensional statistical scatter. In: Anderson, T.W. (ed.) *Collected Papers: Contributions to Mathematical Statistics*, pp. 597–614. Wiley, New York (1967)

## Chapter 7

# Operational Modal Analysis in Frequency Domain Using Gaussian Mixture Models

Ankit Chiplunkar and Joseph Morlier

**Abstract** Operational Modal Analysis is widely gaining popularity as a means to perform system identification of a structure. Instead of using a detailed experimental setup Operational Modal Analysis relies on measurement of ambient displacements to identify the system. Due to the random nature of ambient excitations and their output responses, various statistical methods have been developed throughout the literature both in the time-domain and the frequency-domain. The most popular of these algorithms rely on the assumption that the structure can be modelled as a multi degree of freedom second order differential system. In this paper we drop the second order differential assumption and treat the identification problem as a curve-fitting problem, by fitting a Gaussian Mixture Model in the frequency domain. We further derive equivalent models for the covariance-driven and the data-driven algorithms. Moreover, we introduce a model comparison criterion to automatically choose the optimum number of Gaussian's. Later the algorithm is used to predict modal frequencies on a simulated problem.

**Keywords** Operational modal analysis • Gaussian mixture • Frequency domain

## Nomenclature

$[M]$	Mass matrix
$[C]$	Damping matrix
$[K]$	Stiffness matrix
$\{x(t)\}$	Displacement vector at time $t$
$\{f(t)\}$	Force vector at time $t$
$k(\tau)$	Auto-correlation function at time-lag $\tau$
$S(s)$	Spectral density at $s$
$GP$	Gaussian process
$Q$	Number of Gaussian's
$GMM$	Gaussian mixture model
$OMA$	Operational modal analysis
$BIC$	Bayesian information criterion
$MLE$	Maximum likelihood estimate
$k$	Number of free parameters in an algorithm

## 7.1 Introduction

Modal analysis has been widely used as a means of identifying dynamic properties such as modal frequencies, damping ratios and mode shapes of a structural system. Traditionally, the system is subjected to artificial input excitations and output deformations (displacements, velocities or accelerations) are measured. These later help in identifying the modal parameters of the system, this process is called Experimental Modal Analysis (EMA). In the last few decades several algorithms

---

A. Chiplunkar  
Flight Physics, Airbus Operations S.A.S., 316 route de Bayonne, 31060 Toulouse, France

J. Morlier (✉)  
Université de Toulouse, CNRS, ISAE-SUPAERO, Institut Clément Ader (ICA), 10 avenue Edouard Belin, 31077 Toulouse Cedex 4, France

primarily using the assumption of second order differential, Multi Degree of Freedom (MDOF) system [Eq. (7.1)] have been developed to find modal parameters in EMA [1, 2].

$$[M]\{\ddot{x}(t)\} + [C]\{\dot{x}(t)\} + [K]\{x(t)\} = \{f(t)\} \quad (7.1)$$

Here,  $[M]$ ,  $[C]$  and  $[K]$  denote the mass, damping and stiffness matrices respectively. While,  $\{x(t)\}$  and  $\{f(t)\}$  denote the displacement and force vectors at the time  $t$ .

Since the last decade Operational Modal Analysis (OMA) has gained considerable interest in the community. OMA identifies the modal parameters only from the output measurements while assuming ambient excitations as random noise. OMA is cheaper because it does not require expensive experimental setup and can be used in real time operational use cases such as health monitoring [3–5]. Several algorithms in OMA can be seen as extensions of EMA algorithms based on the similar assumption of second order MDOF system.

In this paper we approach the problem of finding modal parameters as a problem of curve fitting. We drop the assumption of second order differential MDOF system and use a Gaussian Mixture Model (GMM) [6, 7] to fit the spectral density. Moreover we introduce a criteria called Bayesian Information criteria (BIC) which performs a trade-off on the accuracy of the fit and complexity of the model to estimate the modal order [8–10].

The remaining paper proceeds as follows, Sect. 7.2 gives an overview of the traditional operational modal analysis. Section 7.3 details the changes made to current algorithms and introduces the BIC. Section 7.4 demonstrates the capabilities of the algorithm on a simulated dataset and finally Sect. 7.5 concludes the paper with future outlook.

## 7.2 Operational Modal Analysis

As stated earlier the operational modal analysis is an output dependent modal identification technique. The only thing required is the measurement from the accelerometers placed on the structure. Figure 7.1a shows an example of ambient measurements  $x(t)$  on a structure. In almost all OMA algorithms the measurement  $x(t)$  is assumed to be generated from a random force excitation.

The following subsections describe the various time-domain Sect. 7.2.1 and frequency-domain algorithms Sect. 7.2.2 for performing OMA.

### 7.2.1 Time-Domain OMA

In the time-domain a general auto-regression moving average (ARMA) model can be applied to the measurement  $x(t)$  [11]. Here, the modal parameters can be computed from the coefficients of polynomials in ARMA models [12].

If we assume that a second order differential [Eq. (7.1)] completely describes the system dynamics. Then Natural Excitation Technique [13] proves that the auto-correlation function  $k(\tau)$  in Eq. (7.2) can be written as sum of decaying

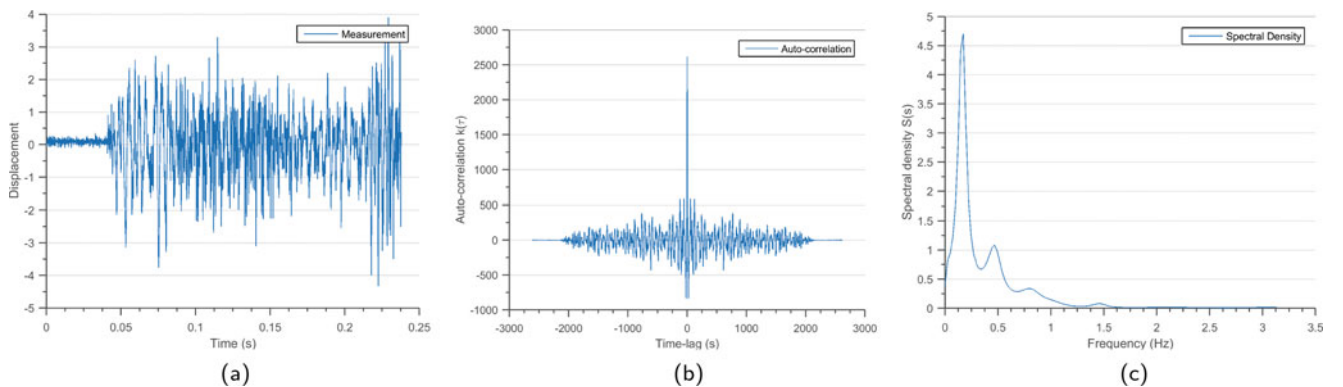


**Fig. 7.1** Different types of measurements for estimation of Modal parameters in OMA. (a) Measured output on accelerometers  $x(t)$ . (b) Auto-correlation  $k(\tau)$  of the measured output (a). (c) Power spectrum density  $S(s)$  of the output (a)



sinusoid's as described by Eq. (7.3). The auto-correlation describes the similarity between measurement as a function of time lag  $\tau$  between them Fig. 7.1b.

$$k(\tau) = \int x(t)x(t - \tau)dt \quad (7.2)$$

Here,  $k(\tau)$  denotes the auto-correlation for random vector  $x(t)$  as a function of time lag  $\tau$ .

$$k(\tau) = \sum A_i \exp(-\lambda_i \tau) \sin(B_i \tau) \quad (7.3)$$

Here,  $\lambda_i$  and  $A_i$  denotes the modal frequency and mode shapes for the  $i^{\text{th}}$  mode. The above coefficients are found by minimizing the least square error between the measured  $k(\tau)$  from Eq. (7.2) and the predicted  $k(\tau)$  from Eq. (7.3). This process is very similar to the Least Square Complex Exponential (LSCE) [1, 14, 15] algorithm developed for time-domain EMA.

### 7.2.2 Frequency-Domain OMA

If we assume the measurement  $x(t)$  to be a stationary random process, then according to Bochner's theorem [16] the spectral density or power spectrum  $S(s)$  can be represented as Eq. (7.4).

$$S(s) = \int k(\tau) \exp(-2\pi i s^T \tau) d\tau \quad (7.4)$$

Here,  $S(s)$  is the power spectrum for the measurement  $x(t)$ , where  $s$  lies in the frequency-damping plane. Figure 7.1c shows the power spectrum calculated for the measurement  $x(t)$  shown in Fig. 7.1a.

Initially the Peak Picking technique (PP) [17] was used in the frequency-domain to identify modal frequencies and shapes. The PP technique is a very easy way to identify modes but becomes inefficient for complex structures [18]. This gave rise to the Frequency Domain Decomposition (FDD) [19] where modal frequency are denoted as the eigenvalues of spectral density matrix Eq. (7.5).

$$S(j\omega) = U \Sigma U^H \quad (7.5)$$

Here, modal frequencies and mode shapes can be derived from  $\Sigma$  and  $U$  respectively using FDD [19] or Enhanced-FDD [20].

Majority of frequency-domain algorithms in EMA fit a Rational Fractional Polynomial (RFP) [2] in the frequency domain for modal identification [21, 22]. The Rational Fractional Polynomial equation (7.6) form can be derived if we assume the system to be second order differential equation (7.1).

$$S(j\omega) = \frac{\sum a_k(j\omega)^k}{\sum b_l(j\omega)^l} \quad (7.6)$$

Here, the poles of the polynomial denote the modal frequencies, while other modal parameters can be derived from the coefficients  $a_k$  and  $b_l$ . The coefficients of the polynomial can be found by minimizing the least squared error. RFP based algorithms face problems since as the number of modes increase the matrix becomes ill-conditioned which gives rise to stability issues in prediction of modal parameters. In the next section we will drop the assumption of second order differential system and treat the modal identification as a purely curve-fitting problem.

## 7.3 Gaussian Mixture Models (GMM)

Two of the above mentioned OMA algorithms "Natural Excitation Technique" in the time domain and "Rational Fractional Polynomial" in the frequency domain, have a core assumption of second order differential system. This assumption fails for non-linear systems and for cases where modal frequencies are very close. In the following section we propose to use Gaussian Mixture Models to fit the power spectrum curve.

Scale location mixtures of Gaussian's can approximate a curve to arbitrary precision with enough components [23]. Due to the above property GMM's are widely used in machine learning tasks such as speech recognition [24], financial modelling [25], handwriting recognition [26] and many more.

Due to the formulation of GMM, the mean, standard deviation and weight information of the gaussian's can be used to derive the modal frequency, damping and mode shape of the system respectively. For a positive half power spectrum the GMM will be equivalent to Eq. (7.7).

$$S(s) = \sum_i^Q w_i \frac{1}{\sqrt{2\pi\sigma_i^2}} \exp\left\{\frac{1}{2\sigma_i^2}(s - \mu_i)^2\right\} \quad (7.7)$$

Here,  $\mu_i$ ,  $\sigma_i$  and  $w_i$  are the mean, standard deviation and weight respectively of the  $i^{\text{th}}$  gaussian. While,  $Q$  denotes the number of gaussians used in the GMM. The mean, standard deviation and weight can be found by minimizing the least square error between measured power spectrum and predicted power spectrum  $S(s)$ . The method to estimate  $Q$  will be explained in more detail in Sect. 7.3.1.

The GMM model in the frequency-domain can be transformed to perform covariance-driven modal identification using Eq. (7.4). If we assume  $x(t)$  to be a stationary random process then using to Eqs. (7.7) and (7.4) we can get Eq. (7.8) in the time domain [27].

$$k(\tau) = \sum_i^Q w_i \cos(2\pi\mu_i\tau) \exp\{-2\pi^2\sigma_i^2\tau^2\} \quad (7.8)$$

Here,  $\mu_i$ ,  $\sigma_i$  and  $w_i$  are the mean, standard deviation and weight respectively of the  $i^{\text{th}}$  gaussian. While,  $Q$  denotes the number of gaussians used in the GMM,  $\tau$  is the time lag between two measurement instances. The parameters can be found by minimizing the least squared error.

Moreover, if we assume that  $x(t)$  is a zero-mean gaussian process, then we can transform GMM in frequency-domain to time-domain. Equations (7.7) and (7.8) are equivalent to fitting a zero-mean gaussian process with a spectral mixture covariance function [28].

$$x(t) = GP(0, cov_{SM}(t, t')) \quad (7.9)$$

Here,  $GP$  denotes a gaussian process [29], while  $cov_{SM}$  represents a spectral mixture covariance function which resembles Eq. (7.8) [28].

We would like to emphasize that keeping the computational complexities aside, fitting a spectral mixture gaussian process in time-domain Eq. (7.7), fitting Eq. (7.8) for covariance-driven modal identification and fitting a GMM Eq. (7.7) in the frequency-domain are equivalent. In fact the initial idea of this paper was to fit a Gaussian Process (GP) in the data domain, but GP's are computationally heavy and we achieved a good accuracy by fitting the GMM in frequency domain. Refer to Table 7.1 for a more comprehensive view at various fitting functions.

### 7.3.1 Bayesian Information Criteria (BIC)

While the modal parameters can be chosen by minimizing the least square error, how to choose the number of modes is a recurring question in several OMA algorithms. This problem is partially resolved by using stabilization diagrams or mode identification functions [21, 30, 31]. But in practical situations engineering judgement is required to estimate the optimal modal order.

Here, we use the Bayesian Information Criteria (BIC) [32] which penalises more complex models to estimate the parameter  $Q$  in Eq. (7.7). It has been shown earlier that the BIC when applied to GMM's does not underestimate the true number of components [33].

$$BIC(Q) = n \ln(MLE) + k \ln(n) \quad (7.10)$$

**Table 7.1** Comparison of fitting functions

Measurement; e.g. Fig. 7.1a	Auto-correlation; e.g. Fig. 7.1b	Power spectrum; e.g. Fig. 7.1c
$x(t)$	$k(\tau) = \int x(t)x(t-\tau)dt$	$S(s) = \int k(\tau)\exp(-2\pi is^T\tau)d\tau$
Assumption: second order differential		
	$k(\tau) = \sum A_i \exp(-\lambda_i \tau) \sin(B_i \tau)$	$S(j\omega) = \frac{\sum a_k(j\omega)^k}{\sum b_l(j\omega)^l}$
Assumption: Gaussian mixture model		
$x(t) = GP(0, cov_{SM})$	$k(\tau) = \sum w_i \cos(2\pi\mu_i\tau) \exp\{-2\pi^2\sigma_i^2\tau^2\}$	$S(s) = \sum w_i \frac{1}{\sqrt{2\pi\sigma_i^2}} \exp\{\frac{1}{2\sigma_i^2}(s - \mu_i)^2\}$

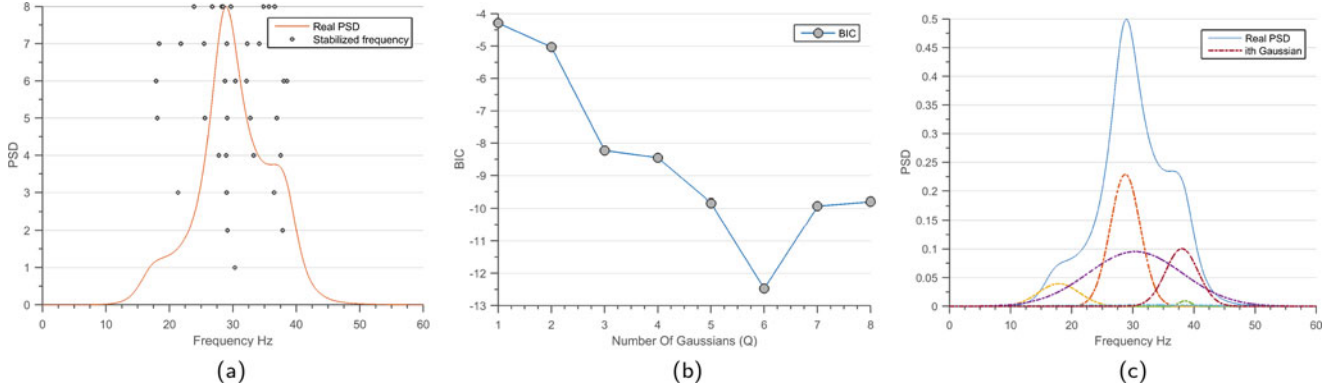


**Fig. 7.2** Results of applying GMM on a spectral density. (a) Stabilization diagram with increasing number of gaussians  $Q$ , the dots denote the stabilized frequencies. We can observe that as the number of  $Q$  increases the algorithm starts finding better and better modes. (b) The BIC criterion with increasing number of gaussian's  $Q$ . We can see that that the BIC is minimum for  $Q = 6$  and hence if we add anymore gaussian's for our dataset we will be performing over-fitting. (c) Distribution of gaussians for  $Q = 6$ . We can see that the three modal frequencies have majority of the participation in representing the spectral density

Here,  $n$  denotes the number of data-points to fit,  $MLE$  denotes the maximum likelihood estimation of the fit and  $k$  denote the number of free parameters to fit. The BIC performs a trade-off between the data-fit term  $n \ln(MLE)$  and the complexity penalty term  $k \ln(n)$ , basically penalizing for over-fitting. Lowest value of BIC is preferred.

## 7.4 Results

In this section we conduct experiments, applying our approach on a simple 3 degree of freedom system with close by modes. As stated earlier in Sect. 7.3 we fit a Gaussian Mixture Model (GMM) on the spectral density. Later we will compare the Bayesian Information Criteria to find the optimal value of number of gaussians for the measurement.

The toolbox used for this paper is Matlab's Curve Fitting Toolbox [34]. All experiments were performed on an Intel quad-core processor with 4Gb RAM. Using the curve fitting toolbox the fitting can be performed by a few lines of code. When compared to other frequency-domain techniques like RFP which suffer from ill-conditioned matrices, the GMM technique is highly stable and finds the coefficient's in seconds.

Figure 7.2a shows the stabilization diagram with increasing number of gaussians  $Q$ . We can observe that as the number of  $Q$  increases the algorithm starts finding better and better modes. We can also observe that there are three modes which start stabilizing from  $Q = 5$ . Figure 7.2b shows the BIC criterion with increasing number of gaussian's  $Q$ . We can see that that the BIC is minimum for  $Q = 6$  and hence if we add anymore gaussian's for our dataset we will be performing over-fitting.

Figure 7.2c shows the six constituent gaussians which represent the  $Q = 6$  case. The three principal peaks represent the modal frequencies of the system, these correspond to the stabilized frequencies from Fig. 7.2a. The remaining three peaks are there to compensate for the spectral density not explained by the three principal peaks.

In the current setting of the GMM model we only propose a quick and easy way to identify the most important frequencies of a structural system. Neither the mode shapes nor the damping ratios are estimated in the current format. As can be observed from Fig. 7.2c the mode shapes are not only dependent on the principal gaussian's but also on the neighbouring gaussian's. Since some part of the spectral density is defined by non-stabilized gaussian's, in future we would like to derive a method to estimate mode-shape and damping ratio such that the contributions of neighbouring gaussian's are also taken into account.

## 7.5 Conclusion

In this paper we have proposed to identify model frequencies of a system by curve-fitting a mixture of gaussians in the frequency domain. While the common assumption that the structure can be modelled as a MDOF second order differential system causes stability issues in presence of non-linear systems. The GMM model is mathematically stable, gives results in seconds and can fit a function upto arbitrary accuracy. Moreover we introduce the BIC to identify the optimum number of gaussians and perform a trade-off between accuracy of fit and over-fitting.

Without doubt this is very nascent stage of application of GMM for system identification and there remains problems such as identification of mode-shape and damping ratio in this algorithm. We wish to tackle these problems in the future. We also wish to apply the algorithm on a real world dataset and compare with respect to other time domain and frequency domain techniques.

**Acknowledgements** The author's are really indebted to the encouragement and support provided by, Jonatan Santiago Tonato, Emmanuel Rachelson, Michele Colombo and Sebastien Blanc.

## References

- Guillaume, P., Verboven, P., Vanlanduit, S., Van Der Auweraer, H., Peeters, B.: A poly-reference implementation of the least-squares complex frequency-domain estimator. *Proc. IMAC* **21**, 183–192 (2003)
- Richardson, M.H., Formenti, D.L.: Parameter estimation from frequency response measurements using rational fraction polynomials. *Proceedings of the 1st International Modal Analysis Conference*, vol. 1, pp. 167–186. Union College, Schenectady, NY (1982)
- Peeters, B., Van der Auweraer, H., Pauwels, S., DeBille, J.: Industrial relevance of Operational Modal Analysis—civil, aerospace and automotive case histories. In: *Proceedings of IOMAC, the 1st International Operational Modal Analysis Conference* (2005)
- Shahdin, A., Morlier, J., Niemann, H., Gourinat, Y.: Correlating low energy impact damage with changes in modal parameters: diagnosis tools and FE validation. *Struct. Health Monit.* **10**(2), 199–217, (2010). <http://journals.sagepub.com/doi/abs/10.1177/1475921710373297>
- Rainieri, C., Fabbrocino, G., Cosenza, E.: Automated Operational Modal Analysis as structural health monitoring tool: theoretical and applicative aspects. *Key Engineering Materials*, vol. 347, pp. 479–484, Trans Tech Publ. (2007)
- Lindsay, B.G., et al.: The geometry of mixture likelihoods: a general theory. *Ann. Stat.* **11**(1), 86–94 (1983)
- McLachlan, G., Peel, D.: *General introduction*. In: *Finite Mixture Models*. Wiley, Hoboken (2000)
- Blumer, A., Ehrenfeucht, A., Haussler, D., Warmuth, M.K.: Occam's razor. In: Shavlik, J.W., Dietterich, T.G. (eds.) *Readings in Machine Learning*, pp. 201–204. Morgan Kaufmann, San Francisco (1990). [doi:10.1002/0471721182.ch1](https://doi.org/10.1002/0471721182.ch1)
- Schwarz, G., et al.: Estimating the dimension of a model. *Ann. Stat.* **6**(2), 461–464 (1978)
- Roeder, K., Wasserman, L.: Practical Bayesian density estimation using mixtures of normals. *J. Am. Stat. Assoc.* **92**(439), 894–902 (1997)
- Ljung, L.: *System identification*. In: *Signal Analysis and Prediction*, pp. 163–173. Springer, Birkhäuser/Boston (1998)
- Andersen, P.: Identification of civil engineering structures using vector ARMA models. Ph.D. thesis, unknown (1997)
- James III, O., Came, T.: The Natural Excitation Technique (NExT) for modal Parameter extraction from operating structures (1995)
- Spitznogle, F.R., Quazi, A.H.: Representation and analysis of time-limited signals using a complex exponential algorithm. *J. Acous. Soc. Am.* **47**(5A), 1150–1155 (1970)
- Ibrahim, S., Mikulcik, E.: A method for the direct identification of vibration parameters from the free response (1977)
- Bochner, S.: *Lectures on Fourier Integrals (AM-42)*, vol. 42. Princeton University Press, Princeton (2016)
- Gade, S., Møller, N., Herlufsen, H., Konstantin-Hansen, H.: Frequency domain techniques for operational modal analysis. In: *1st IOMAC Conference* (2005)
- Zhang, L.: An overview of major developments and issues in modal identification, *Proc. IMAC XXII*, Detroit, pp. 1–8 (2004)
- Brincker, R., Zhang, L., Andersen, P.: Modal identification from ambient responses using frequency domain decomposition. In: *Proceedings of the 18th International Modal Analysis Conference (IMAC)*, San Antonio, TX (2000)
- Brincker, R., Ventura, C., Andersen, P.: Damping estimation by frequency domain decomposition. In: *19th International Modal Analysis Conference*, pp. 698–703 (2001)
- Allemang, R.J., Brown, D.: A unified matrix polynomial approach to modal identification. *J. Sound Vib.* **211**(3), 301–322 (1998)
- Chauhan, S., Martell, R., Allemang, R., Brown, D.: Unified matrix polynomial approach for operational modal analysis. In: *Proceedings of the 25th IMAC*, Orlando, FL (2007)
- Plataniotis, K.N., Hatzinakos, D.: *Advanced Signal Processing Handbook Theory and Implementation for Radar, Sonar, and Medical Imaging Real Time Systems*. CRC, Boca Raton (2000)
- Stuttle, M.N.: A Gaussian mixture model spectral representation for speech recognition. Ph.D. thesis, University of Cambridge (2003)
- Xu, L., Jordan, M.I.: On convergence properties of the EM algorithm for Gaussian mixtures. *Neural Comput.* **8**(1), 129–151 (1996)
- Bishop, C.M.: *Pattern recognition*. Machine Learning, vol. 128. Springer, New York (2006)
- Wilson, A.G., Adams, R.P.: Gaussian process kernels for pattern discovery and extrapolation supplementary material and code (2013). <http://mlg.eng.cam.ac.uk/andrew/smkernelsupp.pdf>
- Wilson, A.G., Adams, R.P.: Gaussian process kernels for pattern discovery and extrapolation. In: *ICML* (3), pp. 1067–1075 (2013)
- Rasmussen, C.E.: *Gaussian Processes in Machine Learning*. Advanced Lectures on Machine Learning, pp. 63–71. Springer, Berlin/Heidelberg (2004)

30. Williams, R., Crowley, J., Vold, H.: The multivariate mode indicator function in modal analysis. In: International Modal Analysis Conference, pp. 66–70 (1985)
31. Shih, C., Tsuei, Y., Allemang, R., Brown, D.: Complex mode indication function and its applications to spatial domain parameter estimation. *Mech. Syst. Signal Process.* **2**(4), 367–377 (1988)
32. Findley, D.F.: Counterexamples to parsimony and BIC. *Ann. Inst. Stat. Math.* **43**(3), 505–514 (1991)
33. Leroux, B.G., et al.: Consistent estimation of a mixing distribution. *Ann. Stat.* **20**(3), 1350–1360 (1992)
34. MathWorks, I.: Curve Fitting Toolbox 1: User’s Guide. MathWorks, Natick (2006)

# Chapter 8

## Understanding Modal Vectors

George Fox Lang

**Abstract** This monograph reviews the properties and characteristics of modal vectors from both an analytic and experimental viewpoint. The commonly understood and well documented normal modes of undamped and proportionally damped models and structures are reviewed in detail. The less well documented and understood complex modes attributed to non-proportional damping are also explored in detail. New information relating to complex mode scaling, modal mass and associated frequency response functions is presented.

**Keywords** Vector scaling • Vector length • Modal mass • Complex modes • Modal A&B

### 8.1 Undamped Systems

Early vibration modeling focused upon “lumped-mass” models, wherein a structure to be analyzed was envisioned as a series of masses attached together and to ground by linear springs. The initial intent was to determine the (undamped) natural or resonance frequencies of vibration and the deformation pattern or normal mode shape associated with each resonance. Later efforts incorporated linear dampers between the mass elements and the resonance solution contained an additional element, the viscous damping factor. As the number of degrees-of-freedom (DOF) or independent mass motions increased, matrix algebraic methods became the analytic norm and mode shapes were represented by modal vectors each containing an ordered list of non-dimensional signed displacements, one for each DOF in the model.

In general, undamped structures may be represented by a mass matrix and a stiffness matrix. The general form of the motional equations is:

$$[M] \{\ddot{x}\} + [K] \{x\} = \{F\} \quad (8.1)$$

... where the vector  $\{F\}$  is an ordered list of the forces applied to the N mass lumps,  $\{x\}$  is the vector of resulting displacements in the same order and  $\{\ddot{x}\}$  is the vector of corresponding accelerations at each DOF. The NxN matrix  $[M]$  contains real-valued elements of mass (force/acceleration) dimension, while  $[K]$  contains real-valued elements of stiffness (force/displacement) dimension. The N diagonal elements of  $[M]$  are the physical masses,  $m_{ij}$  and the off-diagonal elements reflect any dynamic coupling between them. The  $[K]$  matrix contains the stiffness terms reflecting the interconnecting spring constants,  $k_{ij}$  (and their static coupling) between the masses.

### 8.2 Matrix Iteration

There are many ways to solve such a system of N simultaneous equations for its N resonance frequencies,  $f_n$ . One of the oldest (circa 1938) and simplest, *Duncan-Collar Matrix Iteration* [1] also provides some physical insight regarding modal vectors and their interplay with the mass and stiffness matrices. We are seeking the frequencies of free (unforced) sinusoidal vibration and their corresponding mode shapes. Hence we require:

$$\{F\} = \{0\} \quad (8.2)$$

---

G.F. Lang (✉)  
Sound and Vibration Magazine, Bay Village., OH 44140, USA  
e-mail: [gflang@verizon.net](mailto:gflang@verizon.net)

... and

$$\{\ddot{x}\} = -\omega^2 \{x\} \quad (8.3)$$

... where  $\omega = 2\pi f$  is the circular or radian natural frequency of vibration. Substitute (8.2) and (8.3) in (8.1), resulting in:

$$[K] \{x\} = \omega^2 [M] \{x\} \quad (8.4)$$

Finally, multiply (8.4) by the inverse of  $[K]$  and divide it by  $\omega^2$  resulting in:

$$\frac{1}{\omega^2} \{x\} = [K]^{-1} [M] \{x\} \quad (8.5)$$

... which is of the Lambda Matrix form:

$$\lambda \{x\} = [D] \{x\} \quad (8.5a)$$

The left side of Eq. (8.5) multiplies the displacement vector  $\{x\}$  by a scalar ( $\lambda = \frac{1}{\omega^2}$ ), while the right multiplies the same vector by the *dynamic matrix*,  $[D] = [K]^{-1}[M]$ . Multiplying vector  $\{x\}$  by a scalar changes its length, but leaves its direction unchanged. In contrast, multiplying a vector by a matrix changes both its length and direction. Hence we are seeking N unique vectors that are not rotated by  $[D]$  and their corresponding length extension,  $\lambda = \frac{1}{\omega^2}$ .

It's worth interrupting the derivation of the matrix iteration method to point out that experimentalists have long been fond of the  $[K]^{-1}$  matrix. Its displacement/force elements are called *influence coefficients*, and unlike the *stiffness* elements of a  $[K]$  matrix, they are relatively easy to measure in the laboratory. One has only to apply a unit force to one DOF (say  $a$ ) and measure the displacement at all of the desired DOF. This provides the entire  $a$ th row of  $[K]^{-1}$ . This process is repeated N times to fully populate the matrix. If additional DOF are subsequently added to the model, they do not influence the validity of these  $N^2$  measurements. In contrast, trying to apply a unit displacement to one DOF while holding the remaining N-1 at zero (to measure a row of  $[K]$ ) is difficult. Simultaneously measuring the N forces required to do this is really difficult. Adding (or deleting) a degree-of-freedom from the model invalidates all of the prior measurements. Analysts like spring-rates or stiffnesses; experimentalists like influence coefficients. Both appreciate matrix iteration as a breakthrough.

The matrix iteration method is based upon a long-accepted arithmetic technique: guessing followed by validation. Start by guessing the elements of vector  $\{x\}$ . Normalize the "guess vector" by dividing all of its elements by the largest element in the vector. This results in a vector with elements in the range  $\pm 1$ . Multiply this normalized vector by the dynamic matrix  $[D]$  as in (8.5a). The resulting vector is extended and (probably) rotated; normalize it by dividing its elements by its largest element and retain this second normalizing value as a trial *eigenvalue*,  $\lambda_1 = \frac{1}{\omega^2}$ . If the normalized guess and normalized result vectors agree element-for-element (within an acceptable error tolerance) the process can stop. If not, the result vector is used as the next guess vector and the iteration continues. Eventually, this process converges on the lowest frequency mode; that is, the  $\{x\}$  vector with the largest *eigenvalue*  $\lambda_1$ . This vector is retained as the first *eigenvector*  $\{x\}_1$ . The associated undamped natural frequency is retained as  $f_1 = \omega/2\pi = 1/2\pi \sqrt{\lambda_1}$ .

Once the first mode is found, it may be eliminated from further iterative consideration by exploiting its *generalized orthogonality* properties. The details of this elimination will not be discussed here. Suffice to say, the first mode can be swept from Eq. (8.5a) so that the iterative process may progress to identify the remaining N-1 modes in ascending frequency order.

### 8.3 Orthogonality of Normal Modes

To better understand modal vector orthogonality, let's assume all N modes shape have been found. A complete solution to (8.5) consists of N *natural frequencies*,  $f_n$ , each associated with a *mode shape vector*  $\{\phi\}_n$ . If we stack these N solution vectors side-by-side, they form an NxN transformation matrix  $[\phi]$  that may be used to express any motion of the structure as a summation of motions in the N mode shapes. That is:

$$\{x\} = [\{\phi\}_1 \{\phi\}_2 \cdots \{\phi\}_n] \{q\} = [\phi] \{q\} \quad (8.6)$$

... where  $\{q\}$  is a vector of modal participation factors, the amount of each mode to add to the summation.



If we substitute definition (8.6) in the equations of forced motion (8.1) and then pre-multiply the equations by the transpose of the transformation, forming (8.7), something quite miraculous happens—both resulting “generalized” matrices are diagonal; all of their off-diagonal elements are zero. Thus, when applied as a *congruence transformation*, the modal vectors uncouple the equations of motion making each dynamic equation independent of all the others.

$$[\phi]^T [M] [\phi] \{\ddot{q}\} + [\phi]^T [K] [\phi] \{q\} = [\phi]^T \{F\} \quad (8.7)$$

... or ...

$$[M_{gen}] \{\ddot{q}\} + [K_{gen}] \{q\} = [\phi]^T \{F\} = \{F_{gen}\} \quad (8.7a)$$

This wonderful simplification of the equations was forsworn, owing to specific mathematical properties [2] of the [M] and [K] matrices. The *Beltrami-Michell compatibility* equations guarantee that the [M] matrix must be *symmetric*. In like manner, *Maxwell-Betti reciprocity* assures us that the [K] matrix is also symmetric. Further, the modeled structure is statically stable; it won't fall over and it can't fly off into space if impulsed. This means that [K] must be a *positive-definite* matrix. The symmetry of both matrices and the positive-definite nature of the stiffness matrix are necessary and sufficient conditions to assure:

- Equation (8.5) will have N distinct positive eigenvalues,  $\lambda_n$ , leading to N distinct natural frequencies,  $f_n$ .
- Each natural frequency will have a distinct mode shape vector (an eigenvector),  $\{\phi\}_n$ , associated with it.
- The N eigenvectors will demonstrate generalized orthogonality with respect to [M] and [K].

That is:

$$\{\phi\}_k^T [M] \{\phi\}_l = 0 \quad (8.8a)$$

... while

$$\{\phi\}_n^T [M] \{\phi\}_n = M_n > 0 \quad (8.8b)$$

... and

$$\{\phi\}_k^T [K] \{\phi\}_l = 0 \quad (8.8c)$$

... while

$$\{\phi\}_n^T [K] \{\phi\}_n = K_n > 0 \quad (8.8d)$$

## 8.4 Modal Mass and Vector Scaling

Each diagonal element,  $M_n$ , of the generalized mass matrix,  $[M_{gen}]$ , is called a *modal mass*. When the corresponding modal vector,  $\{\phi\}_n$ , is normalized by dividing all of its elements by the largest element, the modal mass,  $M_n$ , will be less than the total mass in the model. If every DOF in  $\{\phi\}_n$  moved equally (as in a rigid body translation) the modal mass would be exactly equal to the total masses in the model. Since our flexible model has a positive-definite [K] matrix, such a rigid body mode shape is highly unlikely. Therefore, the “weight” of each modal mass will generally be less than the “scale weight” of the model or test object. Still, knowing the modal mass associated with a  $\pm 1$  scaled modal vector is bounded by the object's physical mass is useful; it means  $M_n$  indicates *the portion of the structure in motion* in the  $n$ th mode. The corresponding  $K_n$  has no equivalent physical interpretation.

Other modal vector-length scalings are possible. For example, one might choose to set all of the modal vector lengths to unity. To find the square of the length of a vector, you pre-multiply the vector by its transpose. Then dividing every element of the vector by the square-root of this (always positive) number results in a vector of unit length. That is:

$$L_n^2 = \{\phi\}_n^T \{\phi\}_n = \{\phi\}_n^T [I] \{\phi\}_n \quad (8.9)$$



$$\{\phi\}_n^{L=1} = \frac{1}{\sqrt{L_n^2}} \{\phi\}_n \quad (8.9a)$$

Note from Eq. (8.9) that multiplying a vector by its transpose is equivalent to calculating its “generalizing” squared-length with respect to an identity matrix. Normalizing the length of the modal vectors loses the inference of how much of the structure’s mass is in motion in a given mode shape; it provides no corresponding physical understanding. A less obvious, but more useful option is to *orthonormalize* each modal vector. To orthonormalize the mode shapes, we simply divide each modal vector element by the square-root of its resulting modal mass,  $M_n$ . That is, we divide all of the vector elements by a “generalized” vector length, using the symmetric mass matrix as the focus of the generalization. Specifically:

$${}_{gen}L_n^2 = \{\phi\}_n^T [M] \{\phi\}_n = M_n \quad (8.10)$$

$$\{\phi\}_n^{M=1} = \frac{1}{\sqrt{{}_{gen}L_n^2}} \{\phi\}_n = \frac{1}{\sqrt{M_n}} \{\phi\}_n \quad (8.10a)$$

When orthonormalized modal vectors are used to generalize the equations of motion, the result becomes:

$$\begin{bmatrix} 1 & 0 & 0 \\ 0 & \ddots & 0 \\ 0 & 0 & 1 \end{bmatrix} \begin{Bmatrix} \ddot{q}_1 \\ \vdots \\ \ddot{q}_N \end{Bmatrix} + \begin{bmatrix} \omega_1^2 & 0 & 0 \\ 0 & \ddots & 0 \\ 0 & 0 & \omega_N^2 \end{bmatrix} \begin{Bmatrix} q_1 \\ \vdots \\ q_2 \end{Bmatrix} = \begin{bmatrix} \phi_{1,1} & \dots & \phi_{1,N} \\ \vdots & \ddots & \vdots \\ \phi_{N,1} & \dots & \phi_{N,N} \end{bmatrix}^T \begin{Bmatrix} F_1 \\ \vdots \\ F_N \end{Bmatrix} \quad (8.11)$$

... abbreviated as ...

$$[I] \{\ddot{q}\} + [\omega_n^2] \{q\} = \{F_{gen}\} = [\phi]^T \{F\} \quad (8.11a)$$

That is, orthonormalized modal vectors transform the physical mass matrix to an *identity matrix* and the stiffness matrix to a *diagonal matrix with  $\omega_n^2$  elements on the diagonal*. Hence, each modal or generalized mass equals 1 mass unit, while the diagonal elements of the generalized stiffness matrix are the squared circular natural frequencies (radian/second)<sup>2</sup>. At first glance, it would appear that this is less useful than maximum element scaling. Maximum element scaling to  $\pm 1$  seems to provide a good solution (and it is a natural part of matrix iteration). But, like it or not, the experimentalist is actually damned to *measure orthonormalized modes* all of the time! When dealing with experimental measurements made from a real structure, no physical mass or stiffness matrices are known. All we know are the locations and directions of each DOF pair between which acceleration/force Frequency Response Functions (FRF) measurements are made.

## 8.5 Measurable Frequency Response Functions

Let’s derive the analytic expression for an FRF from the orthonormalized equations (8.11a). We will start by applying the Laplace transform to this equation (with all initial conditions assumed to be zero-valued). This results in:

$$[I] s^2 \{q\} + [\omega_n^2] \{q\} = [\phi]^T \{F\} \quad (8.12)$$

... or ...

$$\begin{bmatrix} s^2 + \omega_1^2 & 0 & 0 \\ 0 & \ddots & 0 \\ 0 & 0 & s^2 + \omega_N^2 \end{bmatrix} \begin{Bmatrix} q_1 \\ \vdots \\ q_N \end{Bmatrix} = \begin{bmatrix} \phi_{1,1} & \dots & \phi_{N,1} \\ \vdots & \ddots & \vdots \\ \phi_{1,N} & \dots & \phi_{N,N} \end{bmatrix} \begin{Bmatrix} F_1 \\ \vdots \\ F_N \end{Bmatrix} \quad (8.12a)$$

Since the resulting matrix is diagonal, its inversion is trivial. This allows us to solve (8.12a) for  $\{q\}$  resulting in:

$$\begin{Bmatrix} q_1 \\ \vdots \\ q_N \end{Bmatrix} = \begin{bmatrix} \frac{1}{s^2 + \omega_1^2} & 0 & 0 \\ 0 & \ddots & 0 \\ 0 & 0 & \frac{1}{s^2 + \omega_N^2} \end{bmatrix} \begin{bmatrix} \phi_{1,1} & \dots & \phi_{N,1} \\ \vdots & \ddots & \vdots \\ \phi_{1,N} & \dots & \phi_{N,N} \end{bmatrix} \begin{Bmatrix} F_1 \\ \vdots \\ F_N \end{Bmatrix} \quad (8.13)$$

Assume a single force is applied to the structure at DOF,  $a$ . That is:

$$\begin{Bmatrix} F_1 \\ \vdots \\ F_N \end{Bmatrix} = \begin{Bmatrix} 0 \\ F_a \\ 0 \end{Bmatrix} \quad (8.14)$$

The resulting generalized force is then:

$$[\phi]^T \{F\} = \begin{bmatrix} \phi_{1,1} & \dots & \phi_{N,1} \\ \vdots & \ddots & \vdots \\ \phi_{1,N} & \dots & \phi_{N,N} \end{bmatrix} \begin{Bmatrix} 0 \\ F_a \\ 0 \end{Bmatrix} = \begin{Bmatrix} \phi_{a1} \\ \vdots \\ \phi_{aN} \end{Bmatrix} F_a \quad (8.15)$$

The response displacements (at all DOF) to this single force may be stated:

$$\begin{Bmatrix} x_1 \\ \vdots \\ x_N \end{Bmatrix} = \begin{bmatrix} \phi_{1,1} & \dots & \phi_{1,N} \\ \vdots & \ddots & \vdots \\ \phi_{N,1} & \dots & \phi_{N,N} \end{bmatrix} \begin{Bmatrix} q_1 \\ \vdots \\ q_N \end{Bmatrix} \quad (8.16)$$

... so that the displacement at DOF,  $b$ , is simply:

$$x_b = \{\phi_{b1} \dots \phi_{bN}\} \begin{Bmatrix} q_1 \\ \vdots \\ q_N \end{Bmatrix} = \{\phi_{b1} \dots \phi_{bN}\} \begin{bmatrix} \frac{1}{s^2 + \omega_1^2} & 0 & 0 \\ 0 & \ddots & 0 \\ 0 & 0 & \frac{1}{s + \omega_N^2} \end{bmatrix} \begin{Bmatrix} \phi_{a1} \\ \vdots \\ \phi_{aN} \end{Bmatrix} F_a \quad (8.17)$$

... or ...

$$\frac{x_b}{F_a} = \sum_{n=1}^N \frac{\phi_{an}\phi_{bn}}{s^2 + \omega_n^2} \quad (8.17a)$$

The acceleration at  $b$  due to a force at  $a$  is thus:

$$\frac{\ddot{x}_b}{F_a} = \sum_{n=1}^N \frac{\phi_{an}\phi_{bn}s^2}{s^2 + \omega_n^2} \quad (8.18)$$

Evaluating the transfer function expression of (8.18) for  $s = j\omega$  provides the desired acceleration/force FRF. Specifically:

$$\frac{\ddot{x}_b}{F_a} = \sum_{n=1}^N \phi_{an}\phi_{bn} \frac{\omega^2}{(\omega^2 - \omega_n^2)} = \sum_{n=1}^N A_{abn} \frac{\omega^2}{(\omega^2 - \omega_n^2)} \quad (8.19)$$

Notice that the measurement does not explicitly identify the orthonormalized modal coefficients  $\phi_{an}$  and  $\phi_{bn}$ . Instead, their product is acquired as the single real-valued constant  $A_{abn}$ . Less obvious is the fact that  $A_{abn}$  also carries the acceleration/force (1/mass) dimensional units of the FRF. Had we started the derivation of (8.19) from Eq. (8.7) rather than orthonormalized equation (8.11), it would be obvious that the general statement for  $A_{abn}$  is:

$$A_{abn} = \frac{\phi_{an}\phi_{bn}}{M_n} \quad (8.20)$$

That is, in Eq. (8.19) the  $\phi_{an}\phi_{bn}$  product is actually divided by 1 mass unit (i.e.  $\phi_{an}\phi_{bn}/1.0$ ). For vectors of any scaling the FRF statement may always be written:

$$\frac{\ddot{x}_b}{F_a} = \sum_{n=1}^N \frac{\phi_{an}\phi_{bn}}{M_n} \frac{\omega^2}{(\omega^2 - \omega_n^2)} = \sum_{n=1}^N A_{abn} \frac{\omega^2}{(\omega^2 - \omega_n^2)} \quad (8.21)$$

FRF measurement and subsequent curve-fitting do not separately identify the three frequency-independent terms  $\phi_{an}, \phi_{bn}$  and  $M_n$ . Measurement and fitting merely returns the amplitude constant,  $A_{abn}$ . Given no other available basis for modal vector normalization, all of the  $M_n$  terms are assumed equal to 1 and the  $\phi_{an}\phi_{bn}$  term is assumed to be the product of two orthonormalized modal coefficients. In order to determine the individual modal coefficients from a vector of  $\phi_{an}\phi_{bn}$  products, a *driving point* measurement such as  $\ddot{x}_b/F_b$  must be measured and used as a reference. Taking the square root of its  $A_{bbn}$  value provides orthonormalized  $\phi_{bn}$  which may be subsequently divided into the remaining  $A_{abn}$  to determine the remaining orthonormalized elements of  $\{\phi\}_n$ .

It is the *ratio* of  $\phi_{an}\phi_{bn}$  to  $M_n$  that determines the magnitude of the acceleration/force FRF. If the vectors are rescaled to a longer length, the modal mass must be increased to compensate. If the *units* of measured modal mass are subsequently changed to be compatible with another model, the elements of all the vectors must be changed by a factor equal to the square-root of the mass change. For example, if orthonormalized measurements are made using input units of  $\text{lb}_f$  and  $\text{g}'\text{s}$ , the modal masses will all be one  $\text{lb}_m$ . If the resulting modal vectors are to be used in a model that is scaled to 1 kg, all of the experimental vector elements must be divided by 1.4848 as there are 2.2046  $\text{lb}_m$  per kg.

## 8.6 Proportionally Damped Models

Now let's consider the practical and very important presence of damping. This energy dissipating mechanism is most frequently represented by a resisting force proportional to velocity; so-called *viscous damping*. Viscous damping is modeled by dashpots between mass elements or between a mass element and ground. The matrix equations of damped motion may be stated:

$$[M] \{\ddot{x}\} + [C] \{\dot{x}\} + [K] \{x\} = \{F\} \quad (8.22)$$

... where the real elements of the symmetric  $[C]$  matrix are called damping coefficients and have the units of force/velocity.

Unfortunately, linear algebra for this three-matrix problem is nowhere near as advanced as that for the two-matrix model previously discussed. However, for a narrow range of damped structures, the undamped solution will solve the damped three-matrix problem. This narrow range is termed *proportionally damped*. A system is proportionally damped if the damping matrix can be expressed as a linear combination of the mass and stiffness matrices. That is if:

$$[C] = \alpha [M] + \beta [K] \quad (8.23)$$

... where  $\alpha$  and  $\beta$  are real constants.

When the damping matrix is subjected to congruence transformation using the matrix of modal vectors,  $[\phi]$ , the result is the diagonal generalized damping matrix,  $[C_{gen}]$ . That is:

$$[\phi]^T [C] [\phi] = [\phi]^T [\alpha [M] + \beta [K]] [\phi] = \alpha [\phi]^T [M] [\phi] + \beta [\phi]^T [K] [\phi] = \alpha [M_{gen}] + \beta [K_{gen}] = [C_{gen}] \quad (8.24)$$

Hence the real modal vectors of the undamped solution also uncouple the equations of motion for the proportionately damped case, with the result:

$$[\phi]^T [M] [\phi] \{\ddot{q}\} + [\phi]^T [C] [\phi] \{\dot{q}\} + [\phi]^T [K] [\phi] \{q\} = [\phi]^T \{F\} \quad (8.25)$$

... or ...

$$[M_{gen}] \{\ddot{q}\} + [C_{gen}] \{\dot{q}\} + [K_{gen}] \{q\} = [\phi]^T \{F\} = \{F_{gen}\} \quad (8.25a)$$

If the transforming vectors are orthonormalized vectors, each diagonal element of  $[C_{gen}]$  is transformed to  $2\xi_n\omega_n$ , where  $\xi_n$  is a viscous damping factor ( $0 \leq \xi_n \leq 1$ ).

Applying the LaPlace transform to (8.25) and grouping terms produces a diagonal matrix ...

$$\begin{bmatrix} \ddots & & & \\ & M_n s^2 + C_n s + K_n & & \\ & & \ddots & \end{bmatrix} \begin{Bmatrix} q_1 \\ \vdots \\ q_N \end{Bmatrix} = \begin{Bmatrix} F_{gen\ 1} \\ \vdots \\ F_{gen\ N} \end{Bmatrix} \quad (8.26)$$

... or

$$\begin{bmatrix} \ddots & & \\ & M_n (s^2 + 2\xi_n \omega_n s + \omega_n^2) & \\ & & \ddots \end{bmatrix} \begin{Bmatrix} q_1 \\ \vdots \\ q_N \end{Bmatrix} = \begin{Bmatrix} F_{gen\ 1} \\ \vdots \\ F_{gen\ N} \end{Bmatrix} \quad (8.26a)$$

Inverting solves for the modal participation factors resulting from a generalized forces:

$$\begin{Bmatrix} q_1 \\ \vdots \\ q_N \end{Bmatrix} = \begin{bmatrix} \ddots & & \\ & \frac{1}{M_n (s^2 + 2\xi_n \omega_n s + \omega_n^2)} & \\ & & \ddots \end{bmatrix} \begin{Bmatrix} F_{gen\ 1} \\ \vdots \\ F_{gen\ N} \end{Bmatrix} \quad (8.27)$$

Solving for the displacement at  $b$  resulting from a single force applied at  $a$  ...

$$x_b = \{ \phi_{b1} \dots \phi_{bN} \} \begin{bmatrix} \ddots & & \\ & \frac{1}{M_n (s^2 + 2\xi_n \omega_n s + \omega_n^2)} & \\ & & \ddots \end{bmatrix} \begin{Bmatrix} \phi_{a1} \\ \vdots \\ \phi_{aN} \end{Bmatrix} F_a \quad (8.28)$$

... allows the acceleration/force FRF for the proportionally damped case to be written:

$$\frac{\ddot{x}_b}{F_a} = \sum_{n=1}^N \frac{\phi_{an} \phi_{bn}}{M_n} \frac{\omega^2}{(\omega^2 - 2\xi_n \omega_n s - \omega_n^2)} = \sum_{n=1}^N A_{abn} \frac{\omega^2}{(\omega^2 - 2\xi_n \omega_n s - \omega_n^2)} \quad (8.29)$$

## 8.7 Non-proportional Damping

However, there are many cases where the damping coefficients are not proportional to the mass or stiffness terms. While the three-matrix statement of (8.22) is perfectly valid, no formal method of solution leading to orthogonal vectors has been put forth. However in 1938 Frazer, Duncan and Collar published *Elementary Matrices And Some Applications To Dynamics And Differential Equations* [1] which presented a way to re-express the viscous-damped problem as a two-matrix problem. The method and its application was made far clearer by Walter C. Hurty and Moshe F. Rubinstein, in their classic 1964 *Dynamics of Structures* [3]. In essence, the method exchanged  $N$  second order differential equations for  $2N$  first order equations. This was accomplished by treating the velocities as problem variables independent from the displacements and restricting differentiation by time to a single order. This permitted rewriting (8.22) as:

$$[M] \{\dot{v}\} + [C] \{\dot{x}\} + [K] \{x\} = \{F\} \quad (8.30)$$

They augmented this problem statement with the obvious momentum balance ...

$$[M] \{\dot{x}\} - [M] \{v\} = \{0\} \quad (8.31)$$

... and grouped the two sets of equations together for simultaneous solution:

$$\begin{bmatrix} 0 & M \\ M & C \end{bmatrix} \begin{Bmatrix} \dot{v} \\ \dot{x} \end{Bmatrix} + \begin{bmatrix} -M & 0 \\ 0 & K \end{bmatrix} \begin{Bmatrix} v \\ x \end{Bmatrix} = \begin{Bmatrix} 0 \\ F \end{Bmatrix} \quad (8.32)$$

... sometimes abbreviated as

$$[A] \{\dot{y}\} + [B] \{y\} = \{Y\} \quad (8.33)$$

Note in (8.32) that both matrices have only real-valued elements. Both matrices are symmetric and both are negative-definite. From these equations  $2N$  unique solutions are sought, each involving a complex root or *pole* of the form:

$$p_n = -\sigma_n + j\Omega_n = -\xi_n\omega_n + j\omega_n\sqrt{1 - \xi_n^2} \text{ radian/second} \quad (8.33a)$$

... and an accompanying complex vector of the form:

$$\begin{Bmatrix} v \\ x \end{Bmatrix} = \begin{Bmatrix} p_n\psi_n \\ \psi_n \end{Bmatrix} \quad (8.34)$$

Half of these solutions will be conjugates of the other half. For every pole,  $p_n$ , there will also be another pole:

$$p_n^* = -\sigma_n - j\Omega_n = -\xi_n\omega_n - j\omega_n\sqrt{1 - \xi_n^2} \quad (8.35)$$

... and an accompanying conjugate modal vector of the form:

$$\begin{Bmatrix} v \\ x \end{Bmatrix} = \begin{Bmatrix} p_n^*\psi_n^* \\ \psi_n^* \end{Bmatrix} \quad (8.36)$$

Thus the complete solution will consist of  $2N$  complex vectors, each of length  $2N$ . As with the real modal vectors previously discussed, these can be arranged in a matrix by grouping the  $2N$  solution vectors side-by-side. Equation (8.37) illustrates the matrix format.

$$\begin{bmatrix} p_n\psi_n & p_n^*\psi_n^* \\ \psi_n & \psi_n^* \end{bmatrix} \quad (8.37)$$

Note that these solution vectors reflect a four-fold information redundancy. The upper half of each vector repeats the lower half's elements multiplied by the vector's associated pole. For any given vector there is a conjugate vector, differing only in the sign of its imaginary components. This is important as the complex vectors must be capable of generating real-valued displacement, velocity and acceleration signals. This requires the simultaneous action of conjugate solution vectors. Consider the use of transformation (8.37) to construct real-valued  $v$  and  $x$  signals from a vector of modal participation factors.

$$\begin{Bmatrix} v \\ x \end{Bmatrix} = \begin{bmatrix} p_n\psi_n & p_n^*\psi_n^* \\ \psi_n & \psi_n^* \end{bmatrix} \begin{Bmatrix} q \\ q^* \end{Bmatrix} = \begin{Bmatrix} p_n\psi_nq + p_n^*\psi_n^*q^* \\ \psi_nq + \psi_n^*q^* \end{Bmatrix} = \begin{Bmatrix} 2\text{Re}(p_n\psi_nq) \\ 2\text{Re}(\psi_nq) \end{Bmatrix} \quad (8.38)$$

Observe from (8.38) that real-valued motional signals are generated from complex-valued modal vectors and modal participation factors due to their conjugate interaction. This is a key point to remember; conjugate pairs of poles and modal vectors must cooperate simultaneously to produce real-valued signals.

## 8.8 Orthogonality of Complex Modes

Now our attention turns to the orthogonality properties of the complex modal vectors. Setting  $\{F\} = \{0\}$  and recognizing

$\begin{Bmatrix} \dot{v} \\ \dot{x} \end{Bmatrix} = s \begin{Bmatrix} v \\ x \end{Bmatrix}$  allows us to re-write Eq. (8.32) in the LaPlace domain:

$$s \begin{bmatrix} 0 & M \\ M & C \end{bmatrix} \begin{Bmatrix} v \\ x \end{Bmatrix} = \begin{bmatrix} M & 0 \\ 0 & -K \end{bmatrix} \begin{Bmatrix} v \\ x \end{Bmatrix} \quad (8.39)$$

Substitute  $s = p_n$  and associated modal vector  $\begin{Bmatrix} p_n\psi_n \\ \psi_n \end{Bmatrix}$  in (8.39) and pre-multiply both sides by  $\begin{Bmatrix} p_k\psi_k \\ \psi_k \end{Bmatrix}^T$ , the vector associated with root  $p_k$ , resulting in:

$$p_n \begin{Bmatrix} p_k \psi_k \\ \psi_k \end{Bmatrix}^T \begin{bmatrix} 0 & M \\ M & C \end{bmatrix} \begin{Bmatrix} p_n \psi_n \\ \psi_n \end{Bmatrix} = \begin{Bmatrix} p_k \psi_k \\ \psi_k \end{Bmatrix}^T \begin{bmatrix} M & 0 \\ 0 & -K \end{bmatrix} \begin{Bmatrix} p_n \psi_n \\ \psi_n \end{Bmatrix} \quad (8.40)$$

Transpose both sides of (8.40) yielding:

$$p_n \begin{Bmatrix} p_n \psi_n \\ \psi_n \end{Bmatrix}^T \begin{bmatrix} 0 & M \\ M & C \end{bmatrix} \begin{Bmatrix} p_k \psi_k \\ \psi_k \end{Bmatrix} = \begin{Bmatrix} p_n \psi_n \\ \psi_n \end{Bmatrix}^T \begin{bmatrix} M & 0 \\ 0 & -K \end{bmatrix} \begin{Bmatrix} p_k \psi_k \\ \psi_k \end{Bmatrix} \quad (8.41)$$

Now substitute  $s = p_k$  and  $\begin{Bmatrix} p_k \psi_k \\ \psi_k \end{Bmatrix}$  in (8.39) and pre-multiply both sides by  $\begin{Bmatrix} p_n \psi_n \\ \psi_n \end{Bmatrix}^T$  yielding:

$$p_k \begin{Bmatrix} p_n \psi_n \\ \psi_n \end{Bmatrix}^T \begin{bmatrix} 0 & M \\ M & C \end{bmatrix} \begin{Bmatrix} p_k \psi_k \\ \psi_k \end{Bmatrix} = \begin{Bmatrix} p_n \psi_n \\ \psi_n \end{Bmatrix}^T \begin{bmatrix} M & 0 \\ 0 & -K \end{bmatrix} \begin{Bmatrix} p_k \psi_k \\ \psi_k \end{Bmatrix} \quad (8.42)$$

Subtract (8.42) from (8.41) to discover:

$$(p_n - p_k) \begin{Bmatrix} p_n \psi_n \\ \psi_n \end{Bmatrix}^T \begin{bmatrix} 0 & M \\ M & C \end{bmatrix} \begin{Bmatrix} p_k \psi_k \\ \psi_k \end{Bmatrix} = 0 \quad (8.43)$$

Since the roots are all distinct,  $p_n \neq p_k$  and for (8.43) to be valid requires ...

$$\begin{Bmatrix} p_n \psi_n \\ \psi_n \end{Bmatrix}^T \begin{bmatrix} 0 & M \\ M & C \end{bmatrix} \begin{Bmatrix} p_k \psi_k \\ \psi_k \end{Bmatrix} = 0 \quad (8.44)$$

... establishing that all of the off-diagonal elements of  $[Y]^T[A][Y]$  must be zero. Note that this includes any element formed by two vectors that are conjugates of one another as their poles are distinct. However, the diagonal element is a different story. In specific:

$$\{Y_n\}^T [A] \{Y_n\} = \begin{Bmatrix} p_n \psi_n \\ \psi_n \end{Bmatrix}^T \begin{bmatrix} 0 & M \\ M & C \end{bmatrix} \begin{Bmatrix} p_n \psi_n \\ \psi_n \end{Bmatrix} = \{p_n \psi_n^T \ \psi_n^T\} \begin{Bmatrix} M \psi_n \\ p_n M \psi_n + C \psi_n \end{Bmatrix} = 2p_n \psi_n^T M \psi_n + \psi_n^T C \psi_n = A_n \quad (8.45)$$

Hence the solution vectors are known to exhibit generalized orthogonality with respect to the problem matrix  $[A]$ . Looking again at Eq. (8.40) or (8.42), it is obvious that if  $\{Y\}^T[A]\{Y\}$  is a diagonal matrix,  $\{Y\}^T[B]\{Y\}$  must also be diagonal. Hence the solution vectors also exhibit generalized orthogonality with respect to  $[B]$ . The generalized matrix  $\{Y\}^T[A]\{Y\}$  is sometimes termed “modal A” [4]; it bears the units of viscous damping (Ns/m or lb<sub>f</sub> sec/in). The generalized matrix  $\{Y\}^T[B]\{Y\}$  is similarly called “modal B” and bears stiffness units (N/m or lb<sub>f</sub>/in). For completeness, the diagonal elements of  $\{Y\}^T[B]\{Y\}$  are:

$$\{Y\}^T [B] \{Y\} = \begin{Bmatrix} p_n \psi_n \\ \psi_n \end{Bmatrix}^T \begin{bmatrix} -M & 0 \\ 0 & K \end{bmatrix} \begin{Bmatrix} p_n \psi_n \\ \psi_n \end{Bmatrix} = \{p_n \psi_n^T \ \psi_n^T\} \begin{Bmatrix} -p_n M \psi_n \\ K \psi_n \end{Bmatrix} = -p_n^2 \psi_n^T M \psi_n + \psi_n^T K \psi_n = B_n \quad (8.46)$$

## 8.9 FRFs from a Complex Mode System

Now let's consider the measurable FRFs of such a system. Start with the problem statement (8.32) and apply the Laplace transform.

$$s \begin{bmatrix} 0 & M \\ M & C \end{bmatrix} \begin{Bmatrix} v \\ x \end{Bmatrix} + \begin{bmatrix} -M & 0 \\ 0 & K \end{bmatrix} \begin{Bmatrix} v \\ x \end{Bmatrix} = \begin{Bmatrix} 0 \\ F \end{Bmatrix} \quad (8.47)$$

Now substitute  $\begin{Bmatrix} v \\ x \end{Bmatrix} = \begin{bmatrix} p_n \psi_n & p_n^* \psi_n^* \\ \psi_n & \psi_n^* \end{bmatrix} \begin{Bmatrix} q \\ q^* \end{Bmatrix}$  and pre-multiply the equation by the transpose of the transformation matrix. This results in:

$$\begin{aligned} & s \begin{bmatrix} p_n \psi_n & p_n^* \psi_n^* \\ \psi_n & \psi_n^* \end{bmatrix}^T \begin{bmatrix} 0 & M \\ M & C \end{bmatrix} \begin{bmatrix} p_n \psi_n & p_n^* \psi_n^* \\ \psi_n & \psi_n^* \end{bmatrix} \begin{Bmatrix} q \\ q^* \end{Bmatrix} + \begin{bmatrix} p_n \psi_n & p_n^* \psi_n^* \\ \psi_n & \psi_n^* \end{bmatrix}^T \begin{bmatrix} -M & 0 \\ 0 & K \end{bmatrix} \begin{bmatrix} p_n \psi_n & p_n^* \psi_n^* \\ \psi_n & \psi_n^* \end{bmatrix} \begin{Bmatrix} q \\ q^* \end{Bmatrix} \\ & = \begin{bmatrix} p_n \psi_n & p_n^* \psi_n^* \\ \psi_n & \psi_n^* \end{bmatrix}^T \begin{Bmatrix} 0 \\ F \end{Bmatrix} = \begin{Bmatrix} \psi_n^T F \\ \psi_n^{*T} F \end{Bmatrix} = \begin{Bmatrix} Q \\ Q^* \end{Bmatrix} \end{aligned} \quad (8.48)$$

Note that the application of a real physical force vector results in a complex-valued generalized force with the lower half of the vector equal to the conjugate of the upper half. Hence a real force applies conjugate complex generalized excitation to the model.

$$[A_{gen}] s \begin{Bmatrix} q \\ q^* \end{Bmatrix} + [B_{gen}] \begin{Bmatrix} q \\ q^* \end{Bmatrix} = \begin{bmatrix} A_n & 0 \\ 0 & A_n^* \end{bmatrix} s \begin{Bmatrix} q \\ q^* \end{Bmatrix} + \begin{bmatrix} B_n & 0 \\ 0 & B_n^* \end{bmatrix} \begin{Bmatrix} q \\ q^* \end{Bmatrix} = \begin{Bmatrix} Q \\ Q^* \end{Bmatrix} \quad (8.49)$$

The previously established orthogonality causes the resulting  $[A_{gen}]$  and  $[B_{gen}]$  matrices to be diagonal. Gathering terms lets us write:

$$\begin{bmatrix} A_n s + B_n & 0 \\ 0 & A_n^* s + B_n^* \end{bmatrix} \begin{Bmatrix} q \\ q^* \end{Bmatrix} = \begin{Bmatrix} Q \\ Q^* \end{Bmatrix} \quad (8.50)$$

Inverting the matrix is trivial, owing to its diagonal nature. This inversion provides the modal participation factors resulting from the application of a generalized force.

$$\begin{Bmatrix} q \\ q^* \end{Bmatrix} = \begin{bmatrix} \frac{1}{A_n s + B_n} & 0 \\ 0 & \frac{1}{A_n^* s + B_n^*} \end{bmatrix} \begin{Bmatrix} Q \\ Q^* \end{Bmatrix} \quad (8.51)$$

A single force applied at DOF  $a$  produces a complex-valued generalized force and its conjugate lower half in accordance with (8.52).

$$\begin{Bmatrix} Q \\ Q^* \end{Bmatrix} = \begin{Bmatrix} \psi_{an} \\ \psi_{an}^* \end{Bmatrix} F_a \quad (8.52)$$

The displacement at DOF  $b$  can be found by expanding the  $b$ th row of the general transformation (8.38). Specifically:

$$x_b = \begin{Bmatrix} \psi_{bn} & \psi_{bn}^* \end{Bmatrix} \begin{Bmatrix} q \\ q^* \end{Bmatrix} \quad (8.53)$$

Substitute (8.52) and (8.53) in (8.51) to derive the  $x_b/F_a$  FRF, and multiply by  $s^2$  to obtain the measurable FRF,  $\ddot{x}_b/F_a$ .

$$\ddot{x}_b = \begin{Bmatrix} \psi_{bn} & \psi_{bn}^* \end{Bmatrix} \begin{bmatrix} \frac{s^2}{A_n s + B_n} & 0 \\ 0 & \frac{s^2}{A_n^* s + B_n^*} \end{bmatrix} \begin{Bmatrix} \psi_{an} \\ \psi_{an}^* \end{Bmatrix} F_a \quad (8.54)$$

... or ...

$$\frac{\ddot{x}_b}{F_a} = \sum_{n=1}^N \left[ \frac{\psi_{an} \psi_{bn} s^2}{A_n s + B_n} + \frac{\psi_{an}^* \psi_{bn}^* s^2}{A_n^* s + B_n^*} \right] \quad (8.55)$$

Letting  $s = j\omega$  results in:

$$\begin{aligned}
\frac{\ddot{x}_b}{F_a} &= \sum_{n=1}^N \frac{\psi_{an}\psi_{bn}\omega^2}{B_n + jA_n\omega} - \frac{\psi_{an}^*\psi_{bn}^*\omega^2}{B_n^* + jA_n^*\omega} = \sum_{n=1}^N \frac{-\psi_{an}\psi_{bn}\omega^2 (B_n^* + jA_n^*\omega) - \psi_{an}^*\psi_{bn}^*\omega^2 (B_n + jA_n\omega)}{(B_n + jA_n\omega)(B_n^* + jA_n^*\omega)} \\
&= \sum_{n=1}^N \frac{-\omega^2 (\psi_{an}\psi_{bn}B_n^* + \psi_{an}^*\psi_{bn}^*B_n) - j\omega^3 (\psi_{an}\psi_{bn}A_n^* + \psi_{an}^*\psi_{bn}^*A_n)}{(B_nB_n^* - A_nA_n^*\omega^2) + j\omega (A_nB_n^* + A_n^*B_n)} \\
&= \sum_{n=1}^N \frac{\omega^2 (\psi_{an}\psi_{bn}B_n^* + \psi_{an}^*\psi_{bn}^*B_n) + j\omega^3 (\psi_{an}\psi_{bn}A_n^* + \psi_{an}^*\psi_{bn}^*A_n)}{A_nA_n^* \left[ \left( \omega^2 - \frac{B_nB_n^*}{A_nA_n^*} \right) - j\omega \frac{(A_nB_n^* + A_n^*B_n)}{A_nA_n^*} \right]} \\
&= \sum_{n=1}^N \frac{2Re(\psi_{an}\psi_{bn}B_n^*) + j2\omega Re(\psi_{an}\psi_{bn}A_n^*)}{A_nA_n^*} \frac{\omega^2}{\left[ \omega^2 - j2\omega \frac{Re(A_nB_n^*)}{A_nA_n^*} - \frac{B_nB_n^*}{A_nA_n^*} \right]} \tag{8.56}
\end{aligned}$$

The result of (8.56) is particularly interesting. The algebraically enthusiastic among us might substitute the identities of (8.45) and (8.46) into (8.56) with an aim to proving that  $\frac{B_nB_n^*}{A_nA_n^*} = \omega_n^2$  (radian/second<sup>2</sup>) and  $\frac{Re(A_nB_n^*)}{A_nA_n^*} = \xi_n\omega_n$  (radian/second).

$$\begin{Bmatrix} p_n \psi_n \\ \psi_n \end{Bmatrix}^T \begin{bmatrix} 0 & M \\ M & C \end{bmatrix} \begin{Bmatrix} p_n \psi_n \\ \psi_n \end{Bmatrix} = 2p_n \psi_n^T M \psi_n + \psi_n^T C \psi_n = A_n \tag{8.45 [repeated]}$$

$$\begin{Bmatrix} p_n \psi_n \\ \psi_n \end{Bmatrix}^T \begin{bmatrix} -M & 0 \\ 0 & K \end{bmatrix} \begin{Bmatrix} p_n \psi_n \\ \psi_n \end{Bmatrix} = -p_n^2 \psi_n^T M \psi_n + \psi_n^T K \psi_n = B_n \tag{8.46 [repeated]}$$

Since the poles accompanying  $\begin{Bmatrix} p_n \psi_n \\ \psi_n \end{Bmatrix}$  and its conjugate are  $-\sigma_n \pm j\Omega_n = -\xi_n\omega_n \pm j\omega_n\sqrt{1 - \xi_n^2}$ , I'm willing to accept this foresworn result and simply note that (8.56) is dimensionally consistent with this finding in all regards. The left-hand fraction has the dimensions of 1/mass and the right-hand fraction is dimensionless. Please note that all terms in (8.56) result from ratios of *real numbers*.

## 8.10 An Alternate Complex-Mode FRF Derivation

The result of (8.56) can be more directly found by an alternative tract. Recall from (8.45) and (8.46) that the solution vectors are orthogonal with respect to both [A] and [B]. Note that this does not imply any form of orthogonality with regard to submatrices [M], [K] or [C]. Proof of orthogonality (8.44) identified that applying two different distinct-root solution vectors to either [A] or [B] as a congruence transformation results in a zero. Since a solution vector and its conjugate have different roots, so-transforming a conjugate pair results in zero. However, there is much to be learned by examining *how the zero is formed*. Specifically:

$$\begin{Bmatrix} p_n \psi_n \\ \psi_n \end{Bmatrix}^T \begin{bmatrix} 0 & M \\ M & C \end{bmatrix} \begin{Bmatrix} p_n^* \psi_n^* \\ \psi_n^* \end{Bmatrix} = p_n^* \psi_n^T M \psi_n^* + p_n \psi_n^T M \psi_n^* + \psi_n^T C \psi_n^* = -2\sigma_n \psi_n^T M \psi_n^* + \psi_n^T C \psi_n^* \equiv 0 \tag{8.57}$$

From which we learn:

$$\frac{\psi_n^T C \psi_n^*}{\psi_n^T M \psi_n^*} = 2\sigma_n = 2\xi_n\omega_n \tag{8.58}$$

... and

$$\begin{Bmatrix} p_n \psi_n \\ \psi_n \end{Bmatrix}^T \begin{bmatrix} -M & 0 \\ 0 & K \end{bmatrix} \begin{Bmatrix} p_n^* \psi_n^* \\ \psi_n^* \end{Bmatrix} = -p_n^* p_n \psi_n^T M \psi_n^* + \psi_n^T K \psi_n^* = -(\sigma_n^2 + \Omega_n^2) \psi_n^T M \psi_n^* + \psi_n^T K \psi_n^* \equiv 0 \tag{8.59}$$



From which we find:

$$\frac{\psi_n^T K \psi_n^*}{\psi_n^T M \psi_n^*} = (\sigma_n^2 + \Omega_n^2) = \omega_n^2 \quad (8.60)$$

Our attention now returns to the original problem statement (8.22), which fully retains its validity, though its general solution for free-vibration modal vectors has eluded us.

$$[M] \{\ddot{x}\} + [C] \{\dot{x}\} + [K] \{x\} = \{F\} \quad (8.22 \text{ [repeated]})$$

$$\begin{bmatrix} 0 & M \\ M & C \end{bmatrix} \begin{Bmatrix} \dot{v} \\ \dot{x} \end{Bmatrix} + \begin{bmatrix} -M & 0 \\ 0 & K \end{bmatrix} \begin{Bmatrix} v \\ x \end{Bmatrix} = \begin{Bmatrix} 0 \\ F \end{Bmatrix} \quad (8.32 \text{ [repeated]})$$

While it was necessary to restate the problem as (8.32) in order to find the  $2N$  complex solution vectors,  $\begin{Bmatrix} P_n \psi_n \\ \psi_n \end{Bmatrix}$ , (8.22) provides a simple means to evaluate the acceleration/force FRF,  $\frac{\ddot{x}_b}{F_a}$ . To this end we define the real-valued generalized mass, stiffness and damping matrices associated with the complex mode shape,  $\{\psi_n\}$ . In specific we form:

$$\begin{bmatrix} M_n^{gen} & 0 \\ 0 & \dots \end{bmatrix} = \{\psi_n\}^T [M] \{\psi_n^*\} \quad (8.61)$$

$$\begin{bmatrix} K_n^{gen} & 0 \\ 0 & \dots \end{bmatrix} = \{\psi_n\}^T [K] \{\psi_n^*\} \quad (8.62)$$

$$\begin{bmatrix} C_n^{gen} & 0 \\ 0 & \dots \end{bmatrix} = \{\psi_n\}^T [C] \{\psi_n^*\} \quad (8.63)$$

Note that we cannot define these generalized matrices with a simple pre-and-post matrix multiplication. For example, attempting to form the generalized mass matrix in this fashion results in:

$$[\psi]^T [M] [\psi] = \begin{bmatrix} M_n^{gen} & junk \\ junk & \dots \end{bmatrix} \quad (8.64)$$

The symmetrically arranged complex-valued “junk” terms surrounding the positive real-valued diagonals result from the lack of generalized orthogonality between the  $[\psi]$  vectors and the physical mass matrix,  $[M]$ . Hence, the desired generalized mass, stiffness and damping matrices need to be formed by adding the diagonal elements of (8.63), (8.64) and (8.65) to null matrices, or by forming matrices like that of (8.64) and then zeroing the off-diagonal elements. We can then cast the forced-motion equations in the form of (8.25a).

$$[M_{gen}] \{\ddot{q}\} + [C_{gen}] \{\dot{q}\} + [K_{gen}] \{q\} = [\phi]^T \{F\} = \{F_{gen}\} \quad (8.25a \text{ [repeated]})$$

Using a solution vector and its conjugate to generalize the  $[M]$ ,  $[K]$  and  $[C]$  matrices is the obvious extension of Eq. (8.10). The results of (8.61), (8.62) or (8.63) are positive real scalars. In fact, these equations could be directly applied to the real-mode case without modification. Hence, the real-mode concept of a “modal mass” can be directly applied to the complex-mode case. The modal mass for either a real or complex-mode model is thus:

$$M_n = \{\psi_n\}^T [M] \{\psi_n^*\} = \{\psi_n^*\}^T [M] \{\psi_n\} \quad (8.65)$$

Following the prior derivation described by (8.25)–(8.28), the displacement at DOF  $b$  resulting from a force applied at DOF  $a$  is:

$$x_b = \{ \psi_{b1} \dots \psi_{bN} \} \begin{bmatrix} \ddots & & & \\ & \frac{1}{M_n(s^2 + 2\xi_n \omega_n s + \omega_n^2)} & & \\ & & \ddots & \\ & & & \ddots \end{bmatrix} \begin{Bmatrix} \psi_{a1} \\ \vdots \\ \psi_{aN} \end{Bmatrix} F_a \quad (8.66)$$

Double-differentiating (8.66) by multiplying by  $s^2$  and evaluating for  $s = j\omega$ , allows the corresponding complex-mode acceleration/force FRF to be stated:

$$\begin{aligned} \frac{\ddot{x}_b}{F_a} &= \sum_{n=1}^N \frac{\psi_{an} \psi_{bn}}{M_n} \frac{\omega^2}{(\omega^2 - 2\xi_n \omega_n \omega - \omega_n^2)} = \sum_{n=1}^N A_{abn} \frac{\omega^2}{(\omega^2 - 2\xi_n \omega_n \omega - \omega_n^2)} \\ &= \sum_{n=1}^N \frac{(\psi_{an}^{Re} \psi_{bn}^{Re} - \psi_{an}^{Im} \psi_{bn}^{Im}) + j(\psi_{an}^{Re} \psi_{bn}^{Im} + \psi_{bn}^{Re} \psi_{an}^{Im})}{M_n} \frac{\omega^2}{(\omega^2 - 2\xi_n \omega_n \omega - \omega_n^2)} \end{aligned} \quad (8.67)$$

## 8.11 Related Observations

Finite Element Analysis (FEA) and other analytic modeling tools treat modal analysis as a rather minor sub-set of their capabilities. In general, these programs deal rather superficially with viscous damping, if at all. Complex modes are not commonly modeled; hence their details are largely unfamiliar to the analytic community. However, analysts often calculate normal modes against which test results are to be correlated.

In contrast, virtually all of the commercial modal analysis software currently used in Experimental Modal Analysis (EMA) extracts *complex* mode shapes from acceleration/force FRF measurements. The FRFs are typically measured using the Fast Fourier Transform (FFT) and tri-power averaging. In today's world, these two experimental functions may be provided by separate software vendors while running on common (PC) hardware. It should be noted that commercial modal testing software only retains the lower-left corner  $[\psi]$  of the complex mode matrix; the  $N$  velocity terms and the  $N$  conjugate vectors are neither measured nor retained.

Many analysts say the complex mode model is a bit Shakespearian (i.e. *Much Ado About Nothing*). They prefer to include other damping mechanisms (structural hysteresis, slip-friction, etc.) in addition to viscous damping. But, they fully appreciate Normal Mode models as a starting point for model verification and optimization. To support such cooperative efforts, the experimentalist should be certain his tool kit includes the ability to directly fit Normal Modes to measured FRFs or the facility to convert his complex modal vectors to the best possible approximation of Normal Modes.

Although the closing years of the twentieth century brought great strides in bringing the analytic and experimental communities together, there is still much room for improved communication. Our modern technical Universities and their very hard-working Professors are to be congratulated for closing this communication gap. They deserve real (and financially substantial) rewards and accolades for breaking down the long-standing barriers between previously compartmentalized Engineering disciplines. Today's ME and EE graduates almost understand one-another and the vibration-cognoscente of experimental and analytical bent are beginning to have better conversations; this is wonderful and long overdue. It is my hope this monograph aides that communication.

## 8.12 Conclusions and Confessions

Whether we measure or compute mode shapes, whether those modes are Normal or complex, each modal vector is a list of non-dimensional *displacements*. The elements of a modal vector are always displacements divided by a reference displacement. It doesn't matter if they are computed from acceleration, velocity or displacement measurements, mode shapes are always (normalized) displacement vectors. Since they are normalized shapes, they are always dimensionless.

In a complex-mode model, the elements of the mass, stiffness and damping matrices (and therefore the  $[A]$  and  $[B]$  matrices) are always real-valued. The physical force and response motion signals are likewise real-valued. The generalized force and resulting modal participation factors are (typically) complex-valued; these always appear in conjugate pairs.

The complex-mode solution vectors demonstrate generalized orthogonality with respect to the  $[A]$  and  $[B]$  matrices, not to the  $[M]$ ,  $[K]$  and  $[C]$  matrices. The  $2N$  diagonal complex elements,  $A_n$ , of the generalized  $[A]$  matrix are termed "modal A".

It was previously thought that the ratio between complex vector amplitude and complex modal  $A$  determined the motion/force scaling of measured FRFs. In fact, as shown by Eq. (8.56), it is the ratio between the complex vector amplitude and the real-valued product  $A_n A_n^*$  that determines this scaling. The important ramification of this is that complex modes can be scaled using modal mass, just like real modes. To accomplish this, the modal mass for a complex mode is defined by (8.61) as the result of pre-multiplying the physical mass matrix  $[M]$  by the complex vector and post-multiplying it by the vector's conjugate. This definition also allows the FRFs of a complex mode system to be evaluated from the same Eqs. (8.22) that govern the proportionally damped case, rather than from the special case Eqs. (8.32) required to solve for the vectors.

In prior writings [5–8], I presented flawed results for the FRFs resulting from complex modes. This was the direct result of my misunderstanding the lack of orthogonal behavior between complex modal vectors and the physical  $[M]$ ,  $[K]$  and  $[C]$  matrices. Further, those publications presented inaccurate information about the form of normal-mode vectors retained in a complex mode model. I apologize if these articles mislead you; the errors were unintentional.

**Acknowledgement** Dr. Randall J. Allemang, Contributing Editor of *Sound & Vibration* magazine, Professor of Mechanical Engineering at the University of Cincinnati and Director of its Structural Dynamics Research Laboratory gave generously of his time and specialized knowledge by reviewing and editing this monograph. Like a good flight instructor, he let this novice try to blaze his way through the haze, then brought me back to a more realistic mathematical flight before I could do serious damage. In dynamics and mathematics as in learning to fly, “Good judgment comes with experience; unfortunately, experience is usually gained through bad judgment.” Thank you for the experience!

## References

1. Frazer, B.A., Duncan, W.J., Collar, A.R.: *Elementary Matrices and Some Applications to Dynamics and Differential Equations*, pp. 308–331. The University Press, Cambridge (1950)
2. Wylie Jr., C.R.: *Advanced Engineering Mathematics*, pp. 477–497. McGraw-Hill Book Company (1966)
3. Hurty, W.C., Rubinstein, M.F.: *Dynamics of Structures*, pp. 313–337. Prentice-Hall, Inc. (1964)
4. Allemang, R.J.: *Vibrations: analytical and experimental modal analysis*. UC-SDRL-CN-20-263-662 course notes, University of Cincinnati, August 2013
5. Flannelly, W.G., Lang, G.F.: *Modal analysis for managers*. *Sound Vib.* (1979)
6. Lang, G.F.: *Modal testing principles*. Technical Report Number 023/87, Schlumberger, 1987
7. Lang, G.F.: *Demystifying complex modes*. *Sound Vib.* (1989)
8. Lang, G.F.: *Matrix madness and complex confusion*. *Sound Vib.* (2012)

# Chapter 9

## Best Practices for Using Order-Based Modal Analysis for Industrial Applications

Emilio Di Lorenzo, Simone Manzato, Bart Peeters, Francesco Marulo, and Wim Desmet

**Abstract** The Order-Based Modal Analysis (OBMA) technique shows to be very powerful for identifying the modal parameters in operational conditions in case of rotating machineries during transient operations. The main idea behind the method is that instead of estimating the spectra and apply Operational Modal Analysis (OMA) by using them, the so-called orders can be extracted and used as input for the OMA technique. It can be assumed that the measured responses are mainly caused by the rotational excitation. In this case, run-up and coast-down events can be assimilated to multi-sine sweep excitation in the frequency band of interest. Several studies have been performed to identify the best practice for OBMA both in terms of Order Tracking (OT) techniques and OMA techniques. Based on the boundary conditions, on the structure under-test and on the effective operational conditions a technique can be more powerful than another one. Basically there are two fundamental steps: a very good measurement of the tachometer signal and the correct extraction of the orders, both in amplitude and phase. For the first step several alternatives are possible. The sensors to be used for measuring the rotational speed are depending from both the application and the objective of the study. For this reason, several sensors can be found in the market with a huge variety of costs and performances. The best sensor can then be selected for each individual application based on the type of analysis, the accessibility of the shaft, the ease of instrumentation and the required accuracy or level of detail. For the second step, several techniques are available in commercial software and some others have been implemented in a research environment. Each of them has its own advantages and drawbacks. The final aim of the work is to provide guidelines for the correct use of the OBMA technique in an industrial context. Several cases will be shown: a locomotive cabin and a car during engine run-ups and a 3.2 MW wind turbine gearbox during controlled run-ups on a test rig.

**Keywords** Order tracking • Operational Modal Analysis • Rotating machineries • Wind turbine gearbox • Locomotive • Car engine run-up

### 9.1 Introduction

The dynamic characterization of structures in operating conditions is a challenging step. It becomes more difficult if the structure is composed by several substructures interacting with each other. The situation becomes even more complicated if some parts of the structure under study are rotating with respect to each other. In fact, it is well known that such structures face several complex and non-linear condition during their operating life. On one side, Operational Deflection Shapes are widely used in the industrial domain to visualize the deformation of the structure at certain critical frequencies. On the other side, Operational Modal Analysis is often used for the dynamic characterization of big and complex structures. It is also known as output-only modal analysis because it is based only on measurements of the response of the system without the need of measuring the forces acting on it. In its first development, it was used for civil engineering structures like buildings, bridges

---

E. Di Lorenzo (✉)

Siemens Industry Software, Interleuvenlaan 68, 3001 Leuven, Belgium

University of Naples Federico II, Department of Industrial Engineering, Via Claudio 21, 80125 Naples, Italy

KU Leuven, Division PMA, Celestijnenlaan 300B, 3001 Heverlee, Belgium

S. Manzato • B. Peeters

Siemens Industry Software, Interleuvenlaan 68, 3001 Leuven, Belgium

F. Marulo

University of Naples Federico II, Department of Industrial Engineering, Via Claudio 21, 80125 Naples, Italy

W. Desmet

KU Leuven, Division PMA, Celestijnenlaan 300B, 3001 Heverlee, Belgium

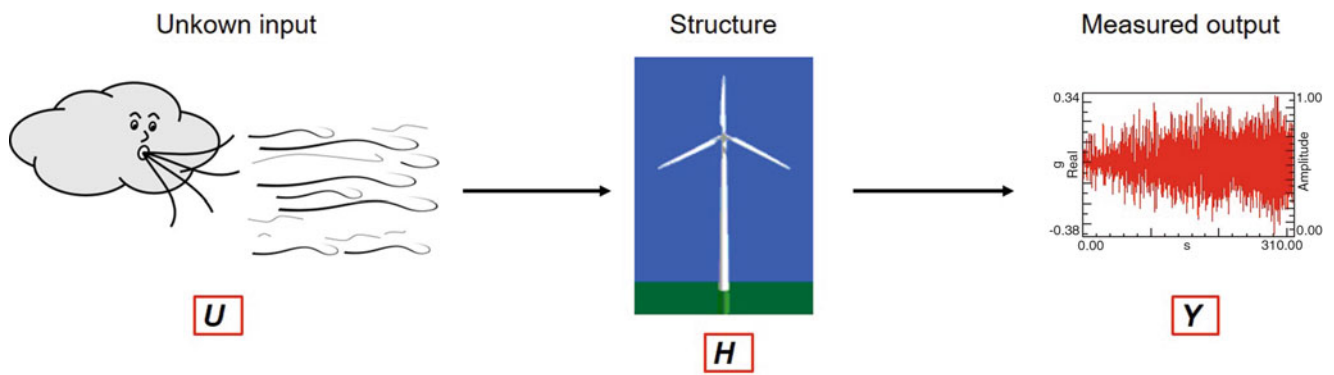


**Fig. 9.1** Source-Receiver-Transfer model:  $U$  = input,  $H$  = structure,  $Y$  = measured output

and wind turbines. Today it is a well-established technique which is widely used for the dynamic identification of all kind of structures such as aircraft, helicopters, vehicles, ships, stadiums, bridges and every kind of industrial machinery. OMA is used instead of classical experimental modal analysis for an accurate modal identification under operating conditions and when it is very difficult to artificially excite the structure. Historically there has always been a distinction between techniques that characterize the dynamic behavior of a structure and the ones that attempt to identify the response signals measured while the same structure is operating [1]. The first category comprises Modal Analysis, whereas the second one includes the Order Tracking procedure. The main distinction between the two categories can be explained by introducing the classical Source-Transfer-Receiver model which is shown in the example of Fig. 9.1. In the Modal Analysis case the scope is to identify the system (Transfer) by measuring the output ( $Y$ ) in all cases and eventually also the input ( $U$ ). The scope of the signature testing, for which the Order Tracking step is usually taken, is the identification of the source of noise and vibration for rotating machinery (gearboxes, engines, drive mechanisms, compressor, pumps, etc.). This technique relies on the fact that the system is well-known and it was already dynamically characterized. This is usually employed in laboratory test facilities, engine test benches, artificial road dynamometers, but also in operational conditions in a real environment. The quality and the performance of both Modal Analysis and Order Tracking are of fundamental industrial importance.

The two categories can be brought together by introducing an Operational Modal Analysis technique based upon the orders extracted by using state-of-the-art order tracking algorithms. Several order tracking techniques will be discussed by identifying their advantages and drawbacks for modal analysis purposes. Then the concept of Order-Based Modal Analysis (OBMA) will be extensively described [2].

## 9.2 Order Tracking Techniques

Order tracking is the estimation of the amplitude and phase of the response of a machine to a referenced rotating components that is allowed to vary in amplitude and frequency over the time. The oldest order tracking techniques were based on analog devices. Vibration signals are fed to a bandpass filter whose center frequency is controlled by a tachometer signal. The output of the filter is then sent to a peak or RMS detector in order to obtain the amplitude of the filtered signal. The amplitude can then be plotted against the rotational speed. With the huge development of digital equipment and software, order tracking techniques have been extensively implemented and studied in the past years. Most of the techniques are very fast and they can be implemented in real time. It can be distinguished among two main categories: non-reconstruction and reconstruction waveform schemes.

The first category includes all the techniques that do not need to reconstruct the time histories of the orders for obtaining the required information. They only extract the amplitude and phase of the orders in the frequency or order domain. The parameters obtained by using these techniques are averaged values over a certain time interval that can be given in terms of constant time interval, angular interval or number of revolutions. The choice of the interval is strictly related with the technique to be used and depends by the test conditions. These techniques are ranging from simple techniques based on Fourier transform to more sophisticated techniques such as resampling based Order Tracking and Time-Variant Discrete Fourier Transform.

On the other hand, the second category, as its name says includes techniques which are based on the reconstruction of the time histories of the orders. Instead of estimating the average amplitude and phase of the orders over a certain blocksize, the time history allows the determination of instantaneous values at any time. They are the most accurate techniques in terms

of resolution, but they also require extensive computations which limit their use in real time cases and for long analysis. Techniques such as the Vold-Kalman filter based order tracking and the Gabor based order tracking are part of this category.

The following methods will be briefly described and then employed in several simulation and test cases in the next sections:

- Time domain sampling based Fast Fourier Transform order tracking (FS);
- Resampling based order tracking in Order Domain (OT or AD);

### 9.2.1 Time Domain Sampling Based Fourier Transform Order Tracking (FS)

The time domain sampling based Fourier transform order tracking require time domain data sampled with constant time intervals. As its name suggests, it is based upon standard Discrete Fourier Transform (DFT) implementation on time domain data. This is the simplest and commonly applied digital order tracking technique. Since the Fast Fourier Transform (FFT) is the most computationally efficient algorithm to perform DFT, the signal is divided into a number of blocks with power of two blocksize. FFT is performed for each block and the results are displayed as FFT waterfall or spectrogram plot. The waterfall plot is a 3D plot in which the FFT spectra are displayed in cascaded form. It is quite useful for detecting the resonances while the machine speed sweeps through a certain frequency range. Another way to show the same kind of data is the so-called spectrogram. It is a 2D plot in which the horizontal axis represents the frequency and the vertical one the time or rotational speed. The amplitudes of the FFT are color coded. Figure 9.2 shows an example of both plots for the same case.

Each of the FFT is calculated by considering an average rpm value over the selected block. The FFTs appear to be horizontal lines in both the colormap and waterfall plot. The rpm step defines the rpm interval between two consecutive FFTs. Of course, Finally, the order, in terms of amplitude and phase, can be extracted from the FFT spectra. The FFT kernel is given in Eq. (9.1).

$$a_m = \frac{1}{N} \sum_{n=1}^N x(n\Delta t) \cos(2\pi \frac{k}{p} n\Delta t)$$

$$b_m = \frac{1}{N} \sum_{n=1}^N x(n\Delta t) \sin(2\pi \frac{k}{p} n\Delta t)$$
(9.1)

$N$  is the number of time blocks and  $n\Delta t$  represents the  $n^{\text{th}}$  time interval. The extracted orders do not normally fall on a single spectral lines. For this reason, often multiple spectral lines are summed together. The main advantage of this method is its

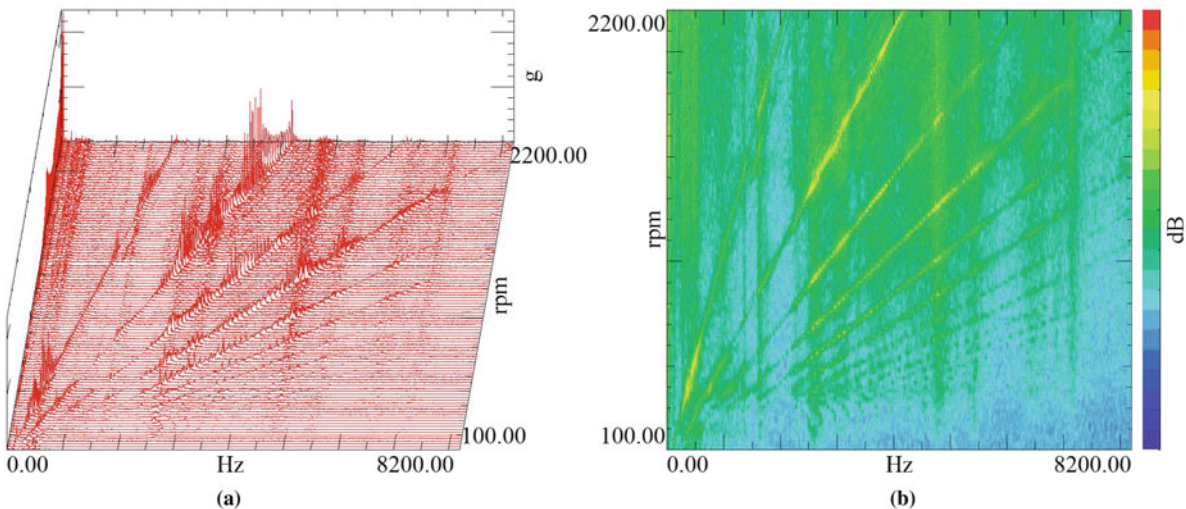


**Fig. 9.2** Fixed sampling order tracking processing. (a) Waterfall plot. (b) Colormap plot



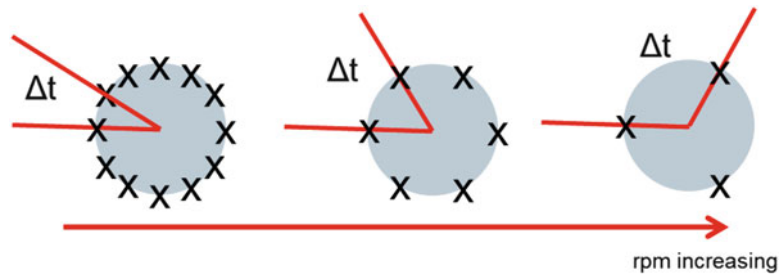


**Fig. 9.3** Time domain sampling based FFT order tracking concept

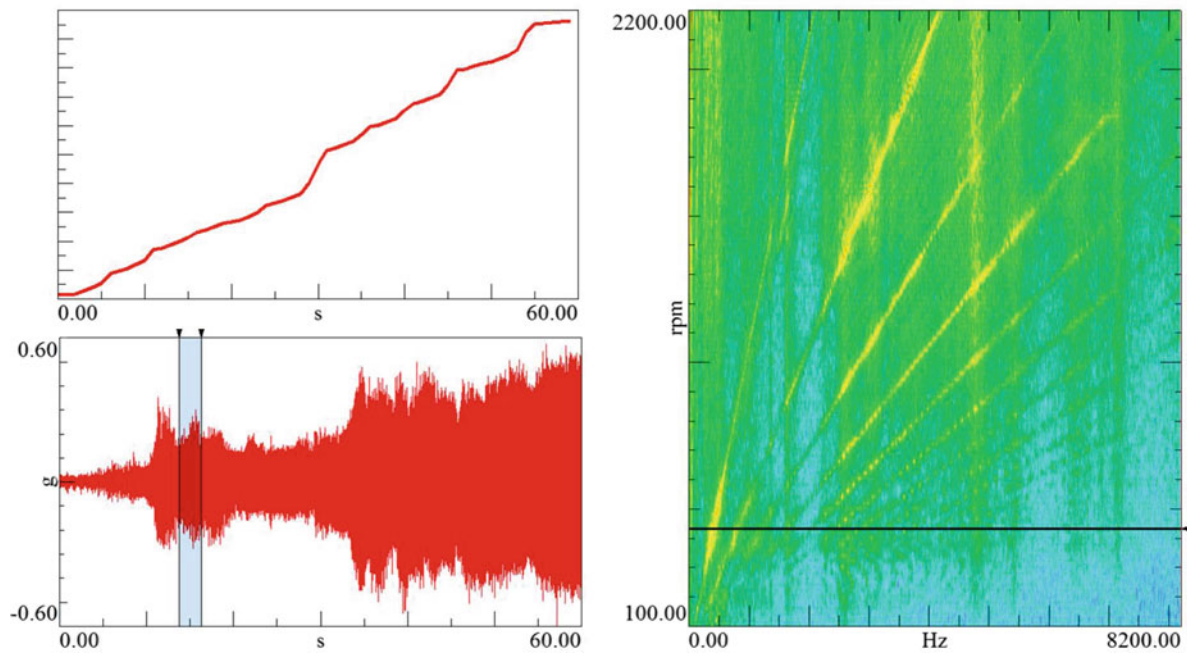


**Fig. 9.4** Angle domain resampling order tracking procedure

computational efficiency. Several drawbacks could be listed. First of all, the blocksize (time interval) is not related to the rpm of the machine. This cause problems both at low and high rotational speed. In fact, at low speeds, the interval is too short to capture the low orders resulting in power leakage (smearing) between closely-spaced orders. At high speeds, the interval is too long to capture rapid variations and spikes in the signal. For minimizing the smearing problem, a Hanning window is typically applied. Figure 9.3 shows that by sampling with a constant time interval, the number of samples per rotation reduces by increasing the rotational speed.

The procedure is shown in Fig. 9.4. On top left there is the tachometer signal which means the measurement of the rotational speed of the machine. The second graph represents the time history recorded by one of the accelerometers placed on the machine under testing. FFT can be performed over a certain time block and the resultant spectrum is placed as an horizontal lined in the colormap on the right side of the figure. By considering all the time blocks the entire colormap can be built.

### 9.2.2 Resampling Based Order Tracking in Order Domain (OT or AD)

In order to solve the listed drawbacks, the analysis time interval should be large enough for low machine speeds and reasonably small for high speeds. One solution to achieve this goal consists of using the constant angle of rotation instead than the constant time interval. Assuming that the blocksize remains constant, this implies that the signal is now sampled at a constant  $\Delta\theta$  rather than at a constant  $\Delta t$ . The computed Order Tracking algorithm was proposed by Potter [3] and it is

based on the angular resampling. The signals are then transformed from the time domain to the angle domain. This technique is widely available in most of the commercial software. The resampling process requires some computational time and it includes two main steps: oversampling and then interpolating in order to get the required  $\Delta\theta$ -spaced samples. As the technique is based on the angle information, a very accurate tachometer signal is needed in this case. In fact, the resampling intervals are calculated by integrating the speed signal. After the resampling step, the variable-frequency order components are converted into regular sinusoidal signals. The DFT (or FFT) can then be used to process the resampled data and to obtain the order components as spectral lines since the transformation is based on angle domain data rather than time domain data. The kernels of the FFT are reformulated from Eq. (9.1) and they are reported in Eq. (9.2).

$$a_m = \frac{1}{N} \sum_{n=1}^N x(n\Delta\theta) \cos(2\pi \frac{k}{p} n\Delta\theta)$$

$$b_m = \frac{1}{N} \sum_{n=1}^N x(n\Delta\theta) \sin(2\pi \frac{k}{p} n\Delta\theta)$$
(9.2)

In this case,  $n\Delta\theta$  represents the  $n^{\text{th}}$  angular interval. The order resolution  $\Delta o$  can be found in a similar way to the frequency resolution  $\Delta f$  as the reciprocal of the total angle of rotation of the machine [Eq. (9.3)].

$$\Delta o = \frac{1}{N\Delta\theta}$$
(9.3)

An equivalent Nyquist-Shannon sampling theorem can be stated in the order domain [Eq. (9.4)].

$$o_{Nyq} = o_s = \frac{1}{2\Delta\theta}$$
(9.4)

$o_s$  is the angular sampling rate and  $o_{Nyq}$  stands for the angular Nyquist rate which corresponds to the maximum order which can be processed. It must be noticed that by choosing  $N$  such that an integer number of revolutions is described, then the smearing problem is minimized even without using any window. On the other hand, if non-harmonic components are present, then a smoothing window is required. For FFT algorithm that needs a power of 2 as blocksize, the zero-padding can be used in order to provide extra samples beyond the integer number of revolutions. Figure 9.5 shows a waterfall and a colormap for the same case analyzed in Fig. 9.2 in the previous section.

The key property of angle domain data is that an order which changed frequency as a function of time if the machine was operating during a run-up or coast-down conditions becomes constant in frequency relative to the sample rate. In other words, the order now falls on a single spectral line for all time values. Several drawbacks are still present. In fact, orders can only be tracked with reference to one rotating shaft and it is quite complicated to distinguish among crossing orders.

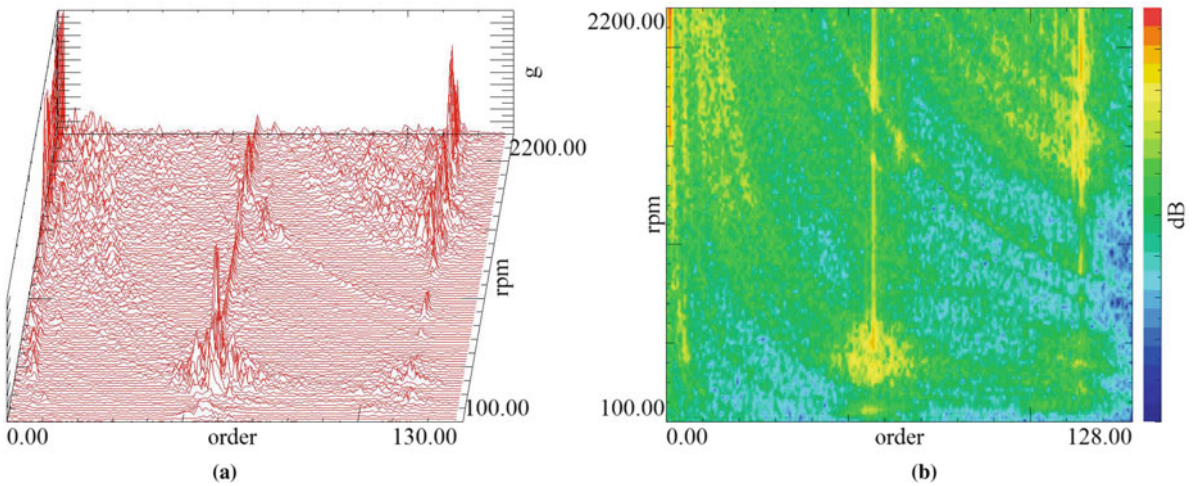


**Fig. 9.5** Resampled order tracking processing. (a) Waterfall plot. (b) Colormap plot



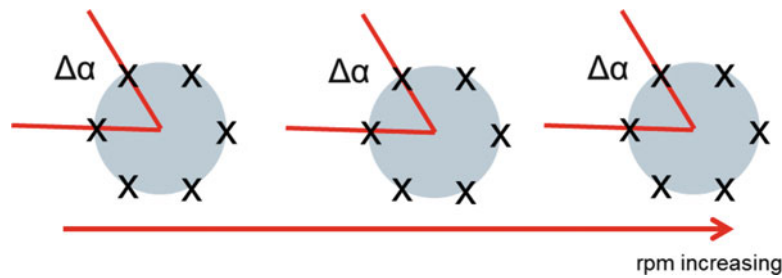


Fig. 9.6 Angle domain resampling order tracking concept

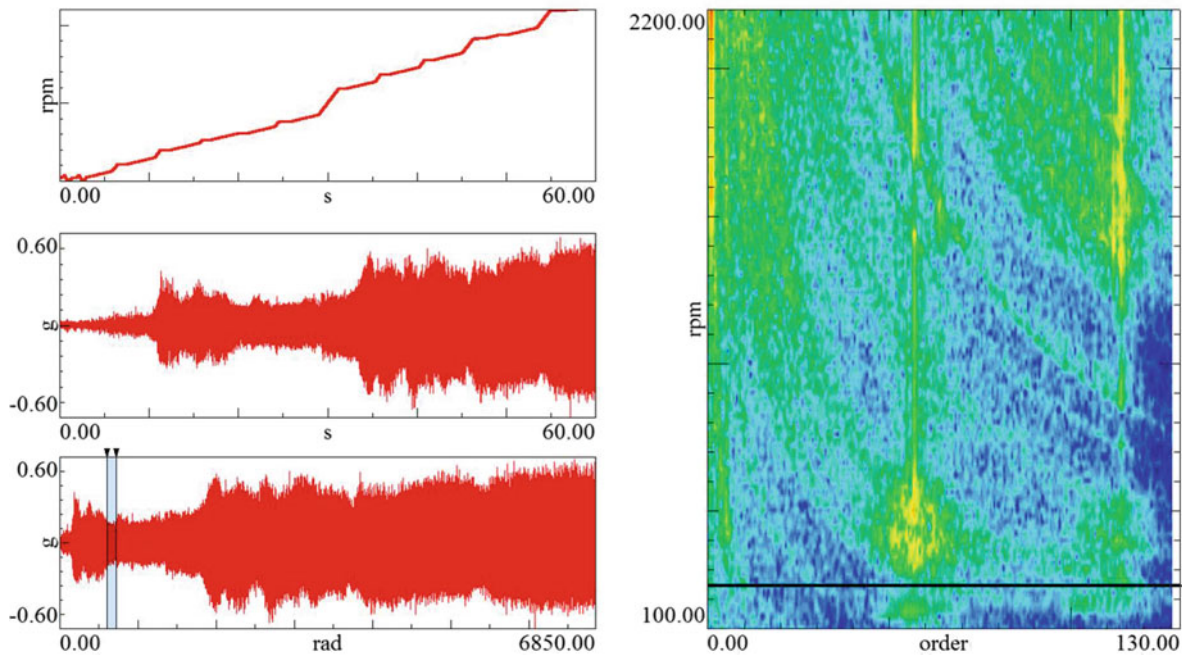


Fig. 9.7 Angle domain resampling order tracking procedure

Another limitation is due to the finite order resolution which makes the analysis of orders which do not fall on a spectral line very difficult. Furthermore, the resampling step can be quite time consuming in some cases.

By using the angular resampling procedure, the same number of samples per rotation for all the rotational speeds can be obtained, as shown in Fig. 9.6.

The procedure is shown in Fig. 9.7. On top left there is the tachometer signal which means the measurement of the rotational speed of the machine. The second graph represents the time history recorded by one of the accelerometers placed on the machine under testing. The resampling to the angle domain yields the bottom curve. FFT can be performed over a certain angular block and the resultant spectrum is placed as an horizontal lined in the colormap on the right side of the figure. By considering all the angular blocks the entire colormap can be built.

### 9.2.3 Other Methods

Several more methods are available in the literature. One of the most computationally efficient is the so-called Time Variant Discrete Fourier Transform (TVDFFT) method which was proposed by Blough [4]. It is defined as a discrete Fourier transform with a kernel that allows the frequency to vary in time, but amplitude of the data is assumed to remain constant across the data block. Also TVDFFT allows a leakage free estimates of orders, but there is no need to resample the data from time to angle domain which allows the technique to be much less computational demanding and suitable for real-time processing. Borghesani [5] proposed the velocity synchronous discrete Fourier transform (VSDFT) for order tracking in the field of rotating machinery and compared its performances with the ones of TVDFFT underlining advantages and drawbacks of the

two methods. A method developed as a post-processing technique has been named Vold-Kalman filter since it was developed by Vold and Leuridan as an extension of the classical Kalman filter [6]. It requires information about “future” data points when estimating an order and it allows extracting close and crossing orders. Another method developed for post-processing purposes is the Gabor transform which has been compared to the Vold-Kalman filter and to other techniques as well [7].

### 9.3 Order-Based Modal Analysis

Operational Modal Analysis (OMA) algorithms, such as Operational Polymax [8], allows the identification of the modal parameters of a structure by taking into account only operational measurements. Previous studies have demonstrated that the classical OMA has some drawbacks when it has to be applied in the rotating machinery field. Some of the peaks in the overall spectrum are originated from order components that suddenly stop at the maximum rpm. These components are identified as poles, while they are not physically present in the system. They have been named “end-of-order” related poles. Order-Based Modal Analysis (OBMA) estimates the modal parameters of a structure during a run-up or a run-down test by applying the curve fitting algorithms to the extracted orders instead than to the overall spectra. It can be assumed that the measured responses are mainly caused by the rotational excitation. Run-up and run-down can be assimilated to multi-sine sweep excitation in the frequency band of interest. Several observations need to be taken into account for applying the same OMA algorithms to the orders:

1. Displacement orders are proportional to the squared rotation speed and acceleration orders are proportional to the forth power of the same rotation speed. The main difference is that in the classical modal analysis the acceleration FRFs are proportional to the squared frequency axis.
2. Complex upper and lower residuals, while in classical modal analysis they are real.
3. Complex participation factor both in classical modal analysis and in order-based modal analysis.

Methods such as Operational Polymax are robust again these observations and they can be employed for estimating the modal parameters in case of rotating machineries by looking at the orders rather than at the spectra. Compared to other applications of order tracking, OBMA requires that the orders are calculated with respect to a reference signal  $\Theta(t)$  which is synchronous with the excitation coming from the rotating source. This signal has been chosen as a sine sweep with frequency equal to the instantaneous rotational speed  $\omega(t)$  of the machine multiplied by the order  $o_m$  which is being extracted, as shown in Eq. (9.5).

$$\Theta(t) = \cos \left( \int_0^T o_m * \omega(t) dt \right) \quad (9.5)$$

In all cases, the following steps need to be taken for applying with success the OBMA technique:

- Measure the tachometer signal during run-up or run-down conditions:  
Several alternatives are possible. The sensors to be used are depending from both the application and the objective of the study. For this reason, several sensors can be found in the market with a huge variety of costs and performances. The best sensor can then be selected for each individual application based on the type of analysis, the accessibility of the shaft, the ease of instrumentation and the required accuracy or level of detail. Some example of sensors are the magnetic pickups, zebra tapes, laser interferometers, low and high resolution encoders.
- Select the measurement points and the measurement sensors to be put on the structure:  
Several alternatives also in terms of sensors are available in the market. The most used ones are the accelerometers, but also velocity or displacement sensors or strain gauges could be used for modal analysis purposes.
- Use order tracking techniques for extracting the orders and select the proper phase reference channel:  
The best compromise in terms of resolution and noise has to be found. Both phase and amplitude are important. A very good phase reference channel synchronous with the rotational speed is needed. AD allows to get an absolute reference channel, while with the other techniques some formulas are needed for creating the sine sweep channel to be used as reference.
- Use Operational Polymax to estimate the modal parameters:  
An estimation of natural frequencies, damping ratios and mode shapes can be obtained by using as input functions the orders instead than the spectra. Inputs remain unknown and the main assumption is that the input force is mainly due to the rotation.

## 9.4 Best Practice for Tachometer Measurement and Order Estimation

### 9.4.1 Tachometer Measurement

Several sensors for an accurate measurement of the tachometer signal are normally employed by test engineers. Among them surely the coder-based techniques are the most used in an industrial environment. Depending on the application, it could be enough to instrument the rotating shaft with a zebra tape and using an optical sensor to detect the rotational speed. For some other applications a high number of pulses per revolution could be needed. In this case an incremental encoder built for the particular application could give better results. The use of accelerometers or strain gauges has many drawbacks and it is not suggested for demanding cases. In our applications, we mainly used coder-based techniques. Both the use of a zebra tape and of incremental encoders has been tested for different application cases. In both cases it must be considered that each pulse detection moment corresponds to a known increase in angular position. In other words, at each tacho moment, the angular position is known with respect to the first tacho moment. This means that interpolation techniques are needed to estimate the position or the speed between two tacho moments and to generate time-equidistant rpm trace at the desired sampling frequency. Digital reconstruction filters are also needed to avoid aliasing. Another point which must be taken into account is that the quality of coder-based measurements is affected by the correct selection of a minimum number of pulses per rotation. In case too few markers per revolution are present, an error named angle-domain aliasing will be added. Three main principles can be used for identifying the minimum coder resolution:

- Nyquist-Shannon sampling theorem: The required number of samples per revolution  $M$  is obtained by applying the Nyquist theorem to an angle domain acquisition. It states that the number of samples per rotation  $M$  must be at least two times higher than the maximum order  $O_{max}$ .

$$M > 2O_{max} \quad (9.6)$$

- Relation order bandwidth for rotating machinery: The maximum order observed  $O_{max}$  is a function of the bandwidth  $bw$  of the system and the rotational speed  $rpm$ . For varying speeds such as in case of runups, rundowns, etc., the  $rpm_{min}$  determines the maximum observed order.

$$O_{max} = 60 \frac{bw}{rpm_{min}} \quad (9.7)$$

- Optimal number of pulses per rotation: Based on the previous principles, the optimal coder resolution can be estimated as in Eq. (9.8).

$$M = 2O_{max} = 120 \frac{bw}{rpm_{min}} \quad (9.8)$$

In many cases, test engineers are not free to choose the optimal coder for the test. For example, in cases in which the teeth of a gear in a gearbox are used as coders, it is fundamental to estimate the error made by using few pulses. The reversed Eq. (9.9) is used to estimate the bandwidth of the coder for specific  $rpm$  conditions.

$$bw = M \frac{rpm_{min}}{120} \quad (9.9)$$

### 9.4.2 Practical Order Estimation

The Order Based Modal Analysis technique requires a very good order estimation which can only be obtained if an accurate tachometer measurement took place. There are several parameters and considerations which must be taken into account when choosing the order tracking technique to apply to the acquired data. Next Section will show several industrial examples to clarify these concepts, but the main considerations can already be listed at this point and then discussed during the application cases analysis:

- **Purpose of the order tracking step**

It is important to know which is the reason why an order tracking step is going to be performed. For instance, if the aim is the dynamic analysis of the rotating system by means of OBMA technique, then a particular care need to be reserved to the phase of the orders. In fact it is an essential part of the signal especially for modal analysis. If the main scope is just to analyze at which frequencies orders are facing a resonance or at which frequency the highest order amplitude is obtained, then most of the listed techniques will be able to give these kind of information.

- **Computational time**

The choice of the order tracking technique is always a compromise between the computational effort and the good quality of the results. For example, the FS technique allows to get a good approximation of the orders in a simple and numerically efficient way even if it does not take into account the fact that the frequencies of orders are changing with the time. It suffers from the problems due to the limited sweep rate. On the other hand, OT and AD need a higher computational time but they provide leakage free estimates of orders. Furthermore, TVDFT estimates orders which closely match those of the resampling based methods with much less computational load. In fact, this technique is essentially resampling the kernel of the Fourier transform instead of resampling the data. The VK filter is able to extract the time histories of the orders and for this reason it is quite computationally demanding.

- **Presence of close/crossing orders**

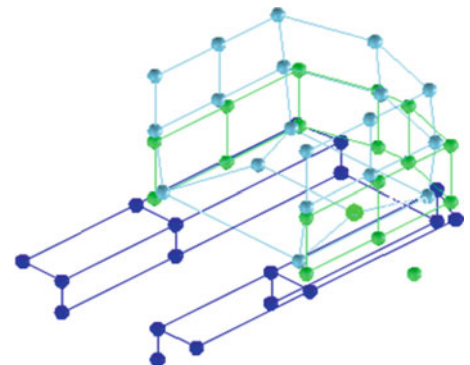
The presence of close/crossing orders can be known in advance and it is important for choosing the best technique for the analysis. In fact, only TVDFT (with OCM compensation) and VK are able to separate close/crossing orders. All the other techniques will have some troubles in these cases.

## 9.5 Validation Cases

### 9.5.1 Locomotive

A first application where OBMA shows some clear advantages against standard Experimental or Operational Modal Analysis is the characterization of the operational response of vehicle cabins during operations. For tracks and locomotives, cabin comfort is a crucial design parameters, as drivers are subjected to vibrations for extended time. As a consequence, an accurate characterization of the operational frequencies and damping is crucial to improve the design of the vibration isolation systems and the controls. Testing these systems in the lab with hammers (or rather sledges) or shaker can be very difficult and expensive, and the results may not be completely representative of the real conditions. On the other hand, relying on operational accelerations acquired during engine run ups or coast down will provide reliable operational boundary conditions and excitation and response levels. In this way, beside extracting operational modal parameters, the engineers will understand how the sources and the structure contribute to the response, identifying most excited modes and most critical frequencies. The case analyzed here includes both hammer excitation and run up/coast down with response measured both on the locomotive frame and cabin shown in Fig. 9.8. The objective is to demonstrate that reliable information on the dynamic response of the structure can also be retrieved relying on the operational excitation only. The first step is also in this case the identification of the dominant orders which are the number 1, 2 and 4 as in most of the cases in which a diesel engine is involved, as it can be seen in Fig. 9.9. The colormap has been plotted in the frequency domain. In this case, the orders are lines which are increasing with the frequency and the rotational speed.

**Fig. 9.8** Locomotive frame and cabin measurement points



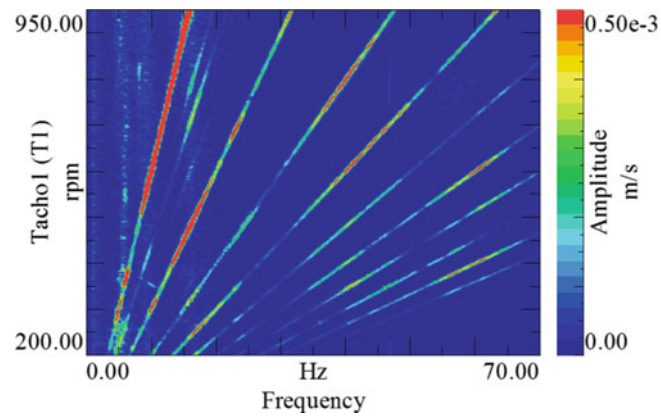


**Fig. 9.9** Colormap in the frequency domain for a run-up case

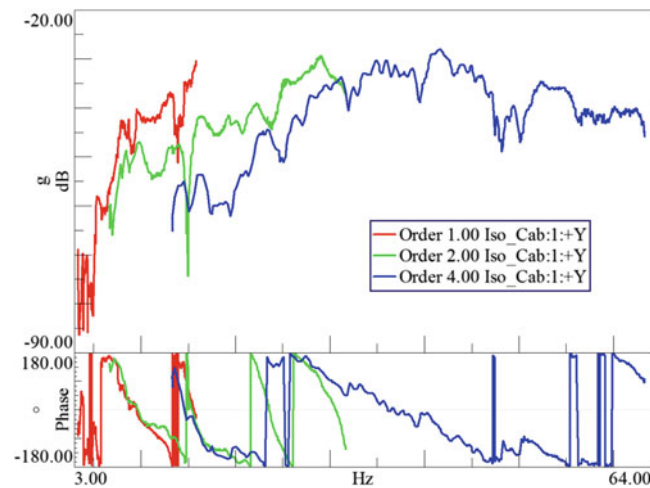


**Fig. 9.10** Orders 1, 2 and 4 obtained by using AD technique during a run-up

Before analyzing the orders, classical Experimental Modal Analysis (EMA) was performed by using the hammer around the cabin structure. Although the FRFs were quite noisy, they helped to better understand which modes could be expected in the frequency range spanned by the mentioned orders. Afterwards the operational case has been analyzed and the dominant modes have been identified by considering each order separately. The modes which fall in the same frequency band have been found by considering any of the orders (1, 2 and 4) as shown in Fig. 9.10. This confirms their presence and the fact that the OBMA technique is able to identify them with success in most cases. Not all modes can be identified, but only the ones which are excited by the rotational excitation. Most of those modes can be found back in the colormap analyzed in the beginning. Also in this case, a comparison between the orders extracted by using the three techniques has been performed and Fig. 9.11 shows that AD is the technique which allows to get the best results.

Finally, the modes have been compared by estimating them from the 2<sup>nd</sup> orders obtained by using the three different techniques (FS, OT and AD). Figure 9.12 shows the comparison between two modesets obtained by using FS and OT. Figure 9.13 compares OT and AD results. By using OT and AD some more modes can be obtained in the same frequency band spanned by order 2 (7–30 Hz). Finally, in Table 9.1 the natural frequencies obtained by using OBMA are compared to the ones obtained in case of EMA.

### 9.5.2 Wind Turbine Gearbox

A second application case is a wind turbine gearbox in a test-rig configuration. The measurement campaign took place on the 13.2 MW dynamic test-rig at ZF Wind Power in Lommel where two prototype gearboxes were placed in a back-to-back



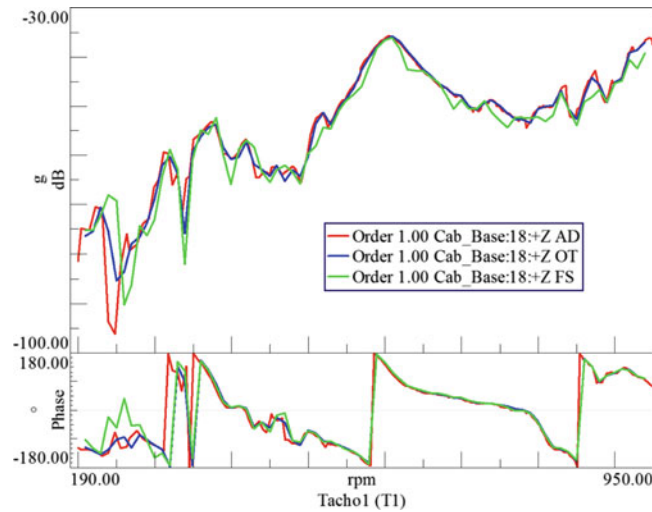


Fig. 9.11 Comparison between orders 2 extracted by using FS, OT and AD techniques

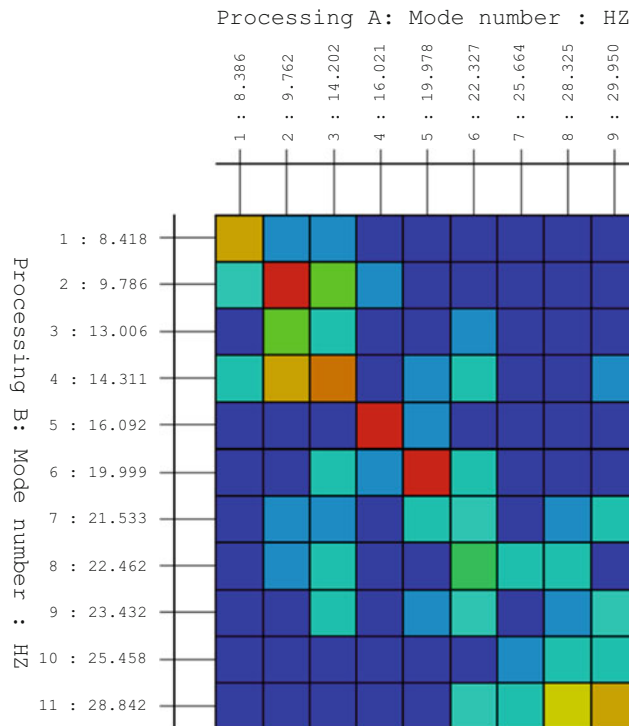
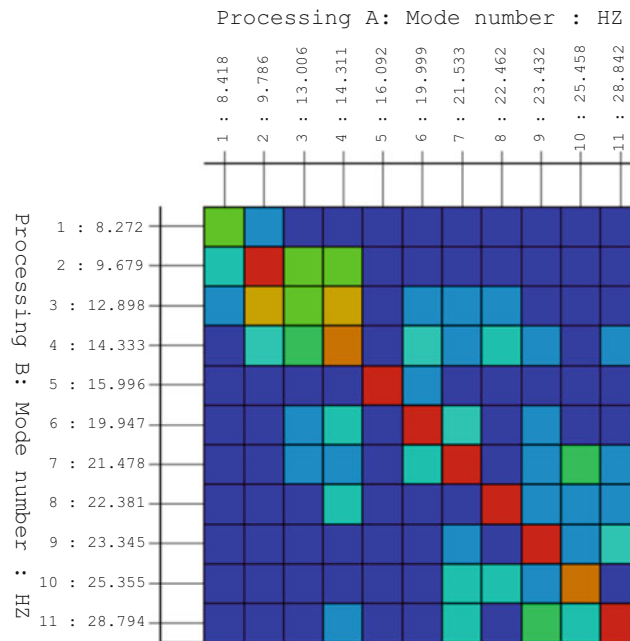


Fig. 9.12 Modal Assurance Criterion (MAC) between the modes obtained by applying OBMA to the orders extracted by using FS (Processing A) and OT (Processing B)

configuration, as shown in Fig. 9.14. This is a typical configuration used for testing gearboxes: a gearbox (named P3) is operating as in the wind turbine, while the second one (named P2) is operating in the so-called motor mode. They have a slightly different gear ratio which allow only one of the two gearboxes to run at its nominal speed.

More than 250 measurement points have been defined for this analysis and, in order to cover all of them, several batches needed to be done. Standstill conditions, run-ups and constant speed at different torque levels were performed for each batch. The results were then merged together by considering the common points along the entire measurement campaign [9] (Fig. 9.15).

Figure 9.16 shows a comparison between the same order (Order 25 in this case) extracted by using the three different techniques. The rotational speed has been measured by means of a high resolution encoder (1024 ppr). In this case OT and



**Fig. 9.13** Modal Assurance Criterion (MAC) between the modes obtained by applying OBMA to the orders extracted by using OT (Processing A) and AD (Processing B)

**Table 9.1** Natural frequencies and damping ratios comparison between EMA and OBMA (by using both OT and AD)

No.	EMA		OBMA (OT)		OBMA (AD)	
	Natural frequency [Hz]	Damping ratio [%]	Natural frequency [Hz]	Damping ratio [%]	Natural frequency [Hz]	Damping ratio [%]
1	-	-	8.42	3.44	8.27	4.03
2	9.16	1.04	9.79	2.91	9.68	3.49
3	-	-	13.01	1.00	12.90	1.68
4	14.87	3.08	14.31	3.78	14.33	4.11
5	16.68	2.74	16.09	3.66	15.99	3.70
6	20.57	11.58	19.99	3.40	19.95	3.40
7	-	-	21.53	1.04	21.48	1.65
8	-	-	22.46	1.20	22.38	1.32
9	-	-	23.43	1.39	23.34	1.85
10	-	-	25.46	2.50	25.35	2.52
11	28.23	2.47	28.84	2.53	28.79	2.66

AD give very similar results, while FS is noisier both in amplitude and phase. The MAC comparison between OT and AD is shown in Fig. 9.17. AD orders allow to get one more mode at higher frequencies which is not identified if OT or FS orders are taken into account.

### 9.5.3 Car Engine Run-up

A third example of industrial case in which the use of OBMA can help to better understand the dynamic of the system in operational conditions is an automotive case. In fact also in this case an engine run-up can be exploited to go through a certain number of resonance frequencies and identify them. In most cases, data obtained for other purposes could still be used also for operational identification without any need of instrumenting again the car or, more in general, the structure. Of course, also in this case, regardless of the method used for the extraction of the orders, a high-quality measurement of the rotational



**Fig. 9.14** Measurement setup for the wind turbine gearbox in the test rig configuration

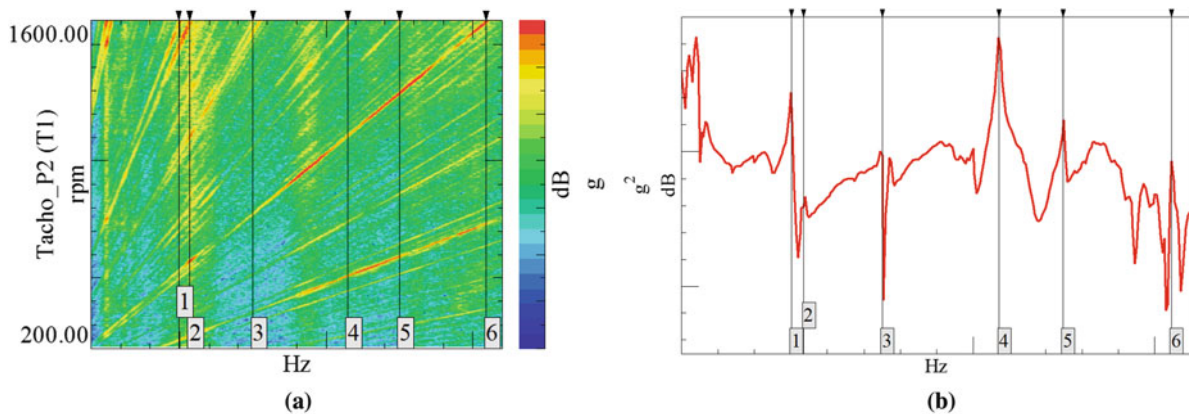


**Fig. 9.15** “End of order” effect. (a) Colormap for a wind turbine gearbox acceleration channel. (b) Crosspower for the same wind turbine gearbox acceleration channel

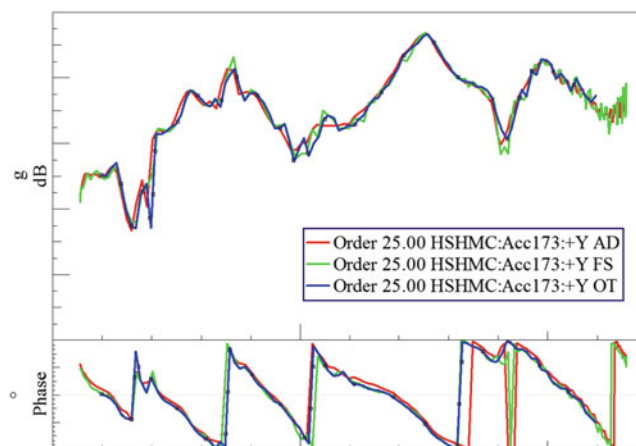


**Fig. 9.16** Orders comparison by using the three different order tracking techniques (FS, OT and AD)

speed is needed. The applicability of the method in the automotive field has been tested by acquiring data during several engine run-ups on a roller bench on different gears. The data were collected by using tri-axial accelerometers to measure operational response levels on the chassis and front subframe of a car during operation. The advantages of OBMA approach against the classical ones used in the industrial environment such as Operational Deflection Shapes (ODS) and Operational Modal Analysis (OMA) have been shown in terms of accuracy and reliability of the achieved results. The measurement



**Fig. 9.17** Correlation between OBMA by using OT orders and OBMA by using AD orders

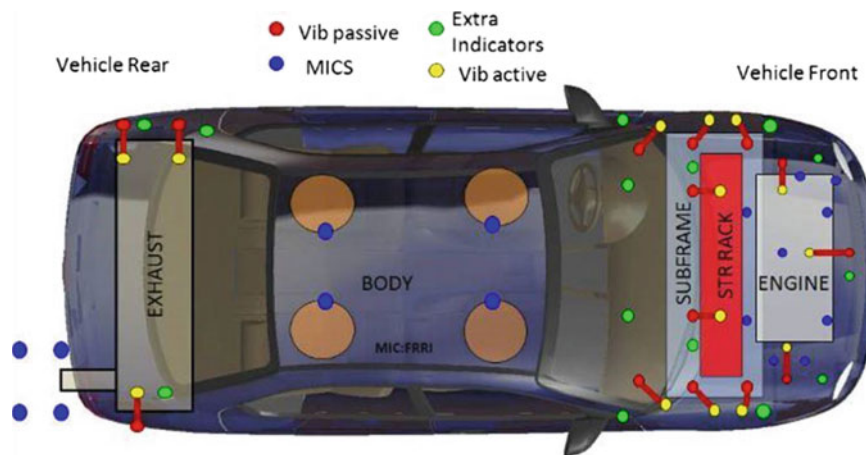
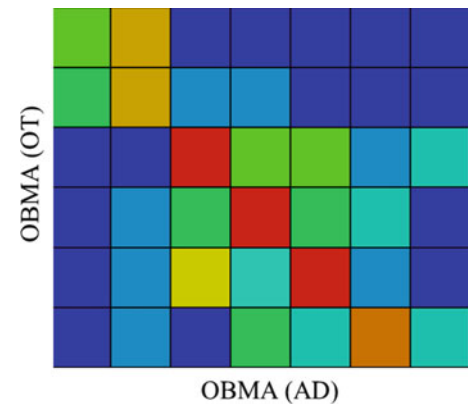


**Fig. 9.18** Measurement setup for the car during an engine run-up

setup is shown in Fig. 9.18: 36 points on the car body and 12 on the subframe have been considered for this analysis for a total of 144 measured channels. For the locomotive case presented in the previous section, a validation of the technique was performed against the EMA results obtained by hammering the structure. In this case it was meaningless to do the same mainly because the hammer excitation was performed for practical reasons after removing the engine and the front wheels. Hence, EMA and operational measurements were performed in two different configurations. On the other hand, OBMA results could be compared to the ODS and the OMA ones in order to underline differences and similarities between the techniques. As usual, the first step is the identification of the dominant orders from the colormap shown in Fig. 9.19.

The rotational speed increase from 900 to 4600 rpm in almost one minute. This is a fast and linear run-up with a sweep rate of roughly 70 rpm/s. The selected orders are the number 2, 4 and 6 which means to consider a frequency range from 30 to 400 Hz. The dynamics obtained by considering the different orders are very consistent with each others in the overlapping frequency band. The Operational Deflection Shapes (ODS) have been calculated by manually selecting the peaks in the crosspower spectra. These results can be compared to the ones obtained by applying OMA to the same crosspowers and, then, in a second step to the ones given by using the OBMA technique after having extracted the dominant orders (2, 4 and 6). In Fig. 9.20 the so-called “end-of-order” effect can be highlighted. On top two crosspowers from two different channels are shown. OMA has been performed and among several natural frequencies identified by Operational Polymax, three frequencies are evidenced on the x axis. They do not actually correspond to physical poles of the system, but they are due to the fact that at these frequencies an order is ending at the maximum rpm. This is quite evident by looking at the bottom picture in which a colormap obtained by using one of the two channels is shown. This is a drawback of applying classical OMA in presence of run-ups. The same considerations could be done regarding run-downs. These frequencies could also be wrongly identified when manually picking the peaks for ODS purposes. Figures 9.21 and 9.22 shows the MAC comparison between ODS and OMA and between OMA and OBMA.

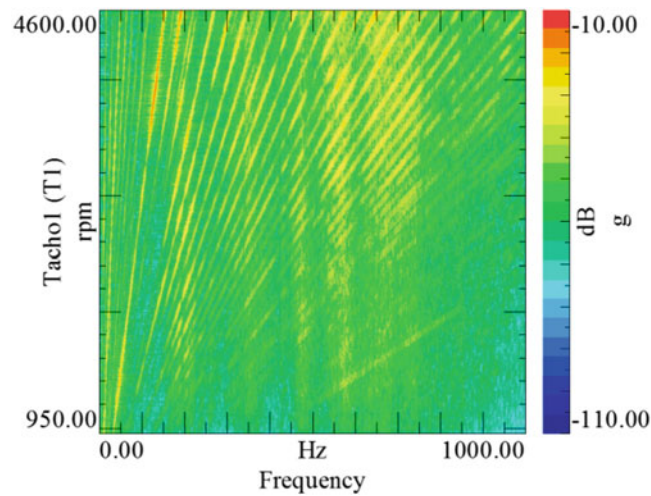


Fig. 9.19 Colormap in the frequency domain for a run-up case

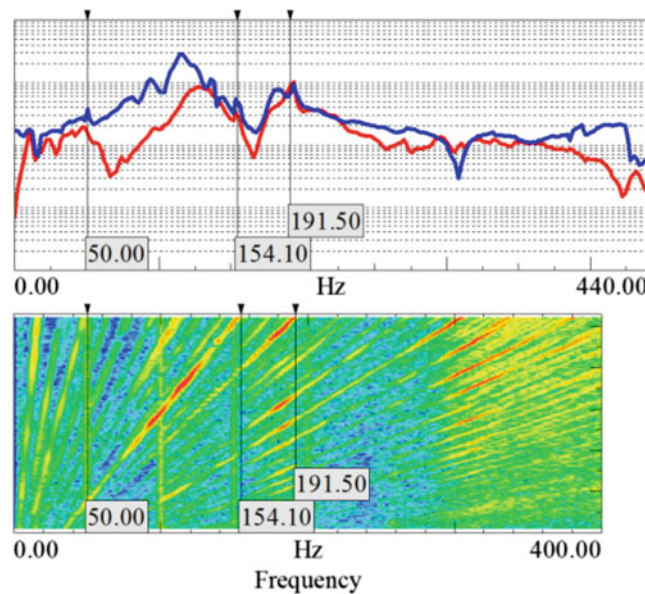
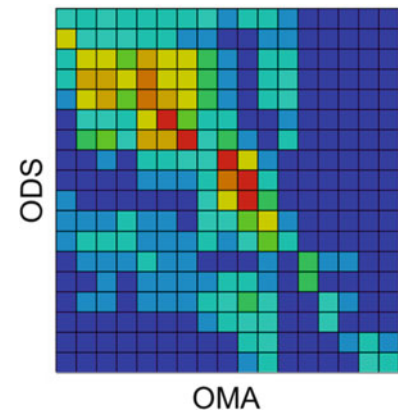


Fig. 9.20 “End of order” frequencies show clear peaks in the spectra

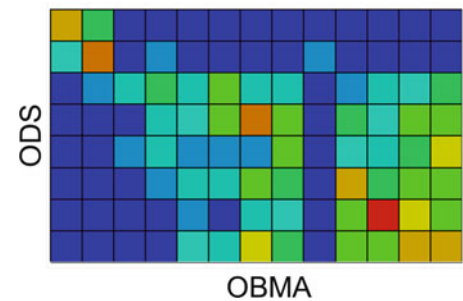
## 9.6 Conclusions

Several techniques for analyzing the dynamic behavior of a structure with one or more rotating parts have been described. Normally, OMA and ODS are a standard in the industrial field, but both techniques show some limitations in case of rotating machines. These limitations have been highlighted making use of several industrial cases such as a locomotive cabin, a car on a roller test bench and a wind turbine gearbox in a test rig configuration. ODS technique is not able to identify the modal parameters, but shows only the deformation pattern of the structure at a certain frequency line. OMA, on the other hand, allows to identify the modal parameters, but requires the strict hypothesis for which the input force can be represented by a white noise spectrum. The technique named Order Based Modal Analysis allows the modal characterization of rotating structures by considering the hypothesis for which the excitation is mainly due to the rotation of the system. Its advantages have been underlined and its application cases discussed in details. It has also been applied in other fields, such as for jet engines, turbines and so on. In general, it can be stated that each time that the dominant excitation is due to the rotation of some parts and the rotational speed can be measured, OBMA can be successfully applied to identify the modal model of the structure under test.

**Fig. 9.21** Correlation between OMA modes and ODS from crosspowers



**Fig. 9.22** Correlation between ODS and OBMA shapes identified from Order 2



## References

1. Blough, J.: Improving the analysis of operating data on rotating automotive components. PhD thesis, University of Cincinnati (1998)
2. Janssens, K., Kollar, Z., Peeters, B., Pauwels, S., Van der Auweraer, H.: Order-based resonance identification using operational polymax. In: Proceedings of 24<sup>th</sup> International Modal Analysis Conference (IMAC), Saint Louis, MO (2006)
3. Potter, R.: A new order tracking method for rotating machinery. *Sound Vib.* **24**(9) (1990)
4. Blough, J., Brown, D.L., Vold, H.: The time variant discrete fourier transform as an order tracking method. In: Proceedings of Society of Automotive Engineers Noise and Vibration Conference, SAE paper number 972006 (1997)
5. Borghesani, P., Pennacchi, P., Chatterton, S., Ricci, R.: The velocity synchronous discrete fourier transform for order tracking in the field of rotating machinery. *Mech. Syst. Signal Process.* **44**, 118–133 (2014)
6. Vold, H., Leuridan, J.: High resolution order tracking at extreme slew rates, using kalman tracking filters. In: Proceedings of Society of Automotive Engineers Noise and Vibration Conference, SAE paper number 931288 (1993)
7. Qian, S.: Application of gabor expansion for order analysis. In: LabVIEW application notes. National Instruments, Austin, TX (2003)
8. Peeters, B., Van der Auweraer, H., Vanhollebeke, F., Guillaume, P.: Operational modal analysis for estimating the dynamic properties of a stadium during a football game. *Shock Vib.* **11**, 395–409 (2004)
9. Di Lorenzo, E., Manzato, S., Vanhollebeke, F., Goris, S., Peeters, B., Desmet, W., Marulo, F.: Dynamic characterization of wind turbine gearboxes using order-based modal analysis. In: Proceedings of 26th International Conference on Noise and Vibration Engineering (ISMA), Leuven (2014)

# Chapter 10

## Could the Veering Phenomenon be a Mechanical Design Instrument?

Carlo Rosso, Elvio Bonisoli, and Fabio Bruzzone

**Abstract** During the design process, especially in systems where dynamic characteristics are crucial, modal analysis is an instrument to understand the response of systems subject to external loads. The presence of a resonance into the component operative range usually sounds like an alarm bell, and modal analysis highlights this. But modal analysis gives just an indication, only the calculation of a forced response provides the actual behaviour of the analyzed system. This is principally due to the fact that resonances are excited only if the mode displacements are directed along the exciting force direction. So, in particular conditions, modal analysis highlights possible resonances, but in actual situations they do not occur. Setting a particular geometry, veering phenomenon between mode shapes can arise, related to a design parameter. Mode shapes can deeply interact and change the response of the system. As a matter of fact, two mode shapes affected by veering can be in the operating range, but just one of them can be excited by the external force. So, changing geometry and selecting the non-excitable mode, the component can be however used in the resonance conditions. On the basis of this considerations, in this paper, the possibility to use veering as a design instrument is investigated and this procedure is applied to high speed gears. As a principal result, the possibility to set a geometrical parameter in order to switch between two different mode shapes is underlined and potentials of the technique are explored.

**Keywords** Thin-webbed helical gears • Veering • Design criterion • Geometric optimization

### 10.1 Introduction

It is generally well understood that when a dynamic system undergoes a parameter variation the resulting eigenvalues related to different eigenvectors can be affected by crossing, remaining otherwise unaffected, can veer away from each other, or can be subject to lock-in as pointed out by Mace and Manconi [1] and also by Giannini and Sestieri [2]. The scenario of veering is more curious, because during this parametric variation process a swap in modal properties can be observed through a rapid variation in the eigenvectors, and also the frequency curves diverge from each other. One of the first observers of this phenomenon in the field of structural dynamics was Leissa [3] whom argued that this behaviour could be caused by numerical artefacts and demonstrated that it could be artificially induced through inadequate approximations and discretisations. However, Kuttler and Sigillito [4], showed that this phenomenon is not an aberration, but a correct representation of the physical reality, through the application of accurate mathematical models of fixed membranes. Furthermore Perkins and Mote [5] presented an exact solution of the elementary eigenvalue problem to confirm the existence of curve veering, introducing also the concept of coupling factors that are able to quantify the eigenfunctions coupling. Pierre [6] further differentiated between physical coupling between components and structures and the modal coupling through parameter perturbations. Balmès [7] showed instead that modal crossing can take place only in structures that allow truly multiple modes at the same frequency, such as symmetric or cyclic structures, multi-dimensional substructures such as plates with uncoupled bending and torsional behaviour, or structures with fully uncoupled substructures. Veering has been studied mainly mathematically or numerically. Du Bois et al. [8], then Bonisoli et al. [9] and finally Giannini et al. [2] focused researches on detailed experimental test-rigs, their experimental variation of natural frequencies and mode-shapes of veering phenomena and corresponding models. In particular, Du Bois et al. analysed a redundant truss, whose transverse stiffness is influenced by the axial pre-load. Experimental results have been then compared with a numerical model confirming the counterintuitive variations of the mode shapes and also showing that the analysis of mode shapes variations in terms of eigenvectors rotations is a valuable tool to study those phenomena. Akay et al. [10] studied the brake squeal phenomenon,

---

C. Rosso (✉) • E. Bonisoli • F. Bruzzone

Department of Mechanical and Aerospace Engineering, Politecnico di Torino, Corso Duca degli Abruzzi 24, 10129, Torino, Italy  
e-mail: [carlo.rosso@polito.it](mailto:carlo.rosso@polito.it)

that is the simultaneous excitation of different vibration modes that coexist at the same frequency, which shows similarities to the crossing phenomena. Chan and Ewins showed the influence of parameters [11] and tolerances [12] in the design process of arrays of mistuned blades and blisks using models of increasing complexity. The small mistuning masses are shown to split the coincident eigenvalues, typical of cyclically-symmetric structures, but in doing so they also highlighted the important role played by the levels of interblade coupling on the natural frequencies of the system for mode shapes with varying nodal diameters, which, in some of the discussed examples, induced veering. However until this point the veering phenomenon has only been regarded as curiosity of modal interactions varying a parametric structure. Purpose and scope of this paper is hence to show that veering can be used to substitute in the stationary operative range an excitable mode shape with a non-excitable one or at least less sensitive, by simply adjusting some geometrical parameters, with a considerable reduction in the dynamic response and thus also improving fatigue life and noise levels. In the specific case the application of this methodology to thin-webbed helical gears will be investigated and the parameters variations will induce a veering towards modes that are not excitable by the meshing interaction.

## 10.2 The Idea

In some mechanical fields and in particular in gearboxes, normal modes of a component can be excited by the exchanged forces and these normal modes can be present in the working frequency band. Usually modal analysis is a check made after having designed the component, so if some normal modes are close to the working frequency band, some adjustments on the component design are done. In the authors opinion, this is not the right approach to component design, because dynamic behaviour should be a design constraint. In trying to investigate the possibility to insert into the design process also the dynamic behaviour of the component, the authors have investigated a lot of techniques and strategies. During the process of understanding the relationship between the main geometrical features of the component and its dynamic behaviour, the authors tried different configurations of a component. During that phase, the authors experienced that some particular geometrical parameters of the component can deeply change the dynamic response and so they decided to investigate the possibility to use the veering phenomenon as a way to change the dynamic response of a component.

In order to demonstrate that, a gear with a traditional shape is considered (see Fig. 10.1). Some parameters are varied in order to change the gear dynamic behaviour. Gears were selected because they are the classical example of a component that has a design procedure that only sometimes considers dynamic behaviour. Moreover gears have to operate typically in a precise frequency band, that usually is defined by the application and cannot be changed arbitrarily. As test case, a thin-webbed helical gear is used and its dynamic behaviour is analysed. This choice is driven by the possibility to have high density of normal modes, potentially dangerous, in the operative range of the gear.

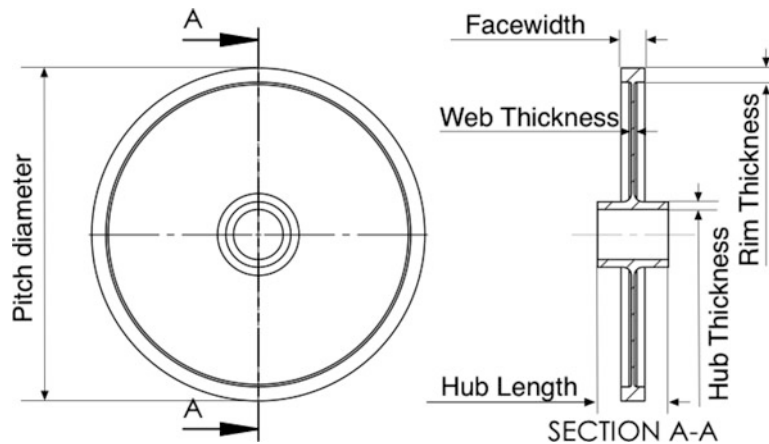


Fig. 10.1 Gear geometry



### 10.3 Model Description

In order to highlight the possible occurrence of veering, a parametric model has been built using the Ansys Parametric Design Language (APDL) Finite Element solver suite. The gear geometry used for this example is visible in Fig. 10.1. The hub length is 60 mm, while its thickness is 7.5 mm. To simplify the geometry generation and the meshing procedures the crown of teeth has not been modelled, but it has been cut at the pitch circle which has a diameter of 281.94 mm, which corresponds to a gear with module  $m = 2.54$  mm with  $z = 111$  teeth. The web thickness is 2.54 mm, while the thickness of the rim is 12 mm. The parameter that varies for each different case is the face width, which has values ranging from 8 to 30 mm, with a step-by-step increase of 2 mm. The generation of the parametric geometry is tasked to a Matlab script, which writes an input file for Ansys APDL. Each model cross-section has been initially meshed with 4-node MESH200 element type, with a mesh size of 2 mm. Then the 2D mesh has been revolved forming 72 sectors of  $5^\circ$  each and creating 8-node SOLID185 solid elements. The number of 3D elements ranges from 18,360, for the case with the lowest value of face width, to 21,456, for the highest one. The inner surface of the hub has been constrained in the axial and tangential directions. Then a modal analysis has been issued, using the Lanczos algorithm solver. Using specifically created macros the resulting eigenvalues and eigenvectors of each case were written for further processing and analysis. In order to easily observe the evolution of the different mode shapes, a hybrid Matlab-Ansys mode tracking algorithm is integrated in the process, whose flowchart is visible in Fig. 10.2. This algorithm uses the Modal Assurance Criterion (MAC) to compare the mode shapes of the different gear models, categorising them by the number of Nodal Diameters (ND) and by the number of Nodal Circumferences (NC).

Due to the definition of MAC [13]

$$MAC_{r,s} = \frac{(\Phi_r^T \Phi_s)^2}{(\Phi_r^T \Phi_r) (\Phi_s^T \Phi_s)} \quad (10.1)$$

this index is suitable to measure the likeness of two eigenvectors (mode shapes)  $r$  and  $s$  of the same model or of two different gears according to a corresponding nodes pattern and their degrees of freedom.

Firstly Matlab generates the input files changing the face width parameter at each iteration. This input file is read and processed by Ansys, which builds the model, performs the modal analysis and stores the obtained results, which are fed back to Matlab. Then the eigenvectors are compared to those obtained through an analogue process for a starting geometry allowing to visualize the mode shapes variation and their correlation to each other at each iteration step.

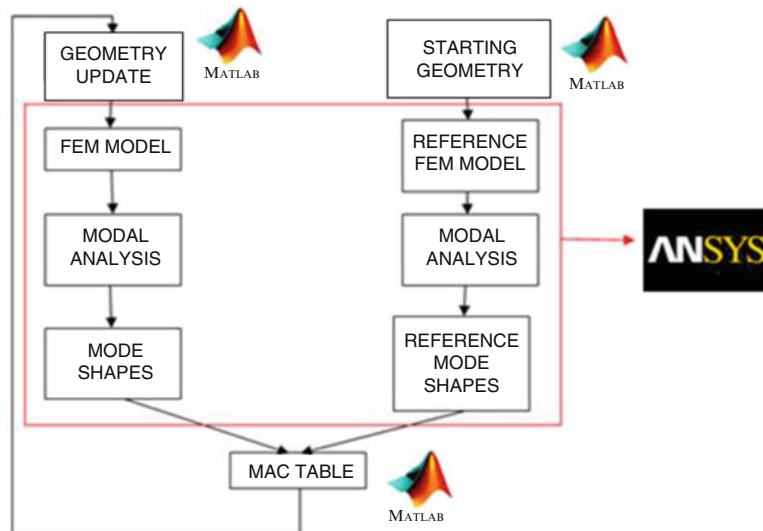


**Fig. 10.2** Parametric modal analysis and mode tracking algorithm flowchart

## 10.4 Mode Veering and MAC

As stated before, in order to keep track of the evolution of the different mode shapes and to highlight veering or crossing phenomena, a MAC table was created for each different model. This tool greatly helps in visualising and differentiating the different phenomena involved as the geometry changes. Since the face width has a broad range of values, also the number of degrees of freedom in the FE model changes. Therefore, in order for the MAC tables created to be consistent, a selection of the most influent nodes was made at each iteration: mainly were selected the nodes on the surface of the web, that are greatly influenced by the number of nodal circumferences, and also the ones on the crown of the gear, which instead are influenced mainly by the number of nodal diameters. The full sets of nodes that make up the FE models, and the nodes selected for this purpose are visible in Figs. 10.8 and 10.15. Once this process was completed, the lines corresponding to the degrees of freedom associated with the selected nodes were extracted from the resulting eigenvectors to form a subset of reduced eigenvectors. Those were finally used for the calculation of the MAC tables. If a model is not affected at all by veering or crossing phenomena, only the bars on the diagonal should have values different from 0. If instead there are bars with values different from 0 outside the main diagonal, it means that something is happening. A crossing is easily identified in a cross-MAC, that is a MAC calculated between two sets of eigenvectors not belonging to the same model, because the bars located on the diagonal will have values close to 0, while the bars outside of it will have values close, if not equal, to one. If a veering is happening instead, the bars on the main diagonal will have values still close to 1, but those outside of it will also be different from 0. This is visible equally in auto-MAC or cross-MAC and the higher those values will be, the more similar the mode shapes, and therefore it also means that the exchange of modal information is at its maximum at that configuration. Crossing phenomena can only happen for modes completely uncoupled, such an axial mode crossing a torsional one. In the other cases, when there is not a complete uncoupling, a veering is happening. Sometimes those veerings are misinterpreted as crossings because they happen suddenly and the modal exchange is localized in a very narrow zone. However, if the modal exchange zone is investigated in finer detail, it will appear evident that it shows the classic telltale signs of a veering: the modal exchange will not be sudden and full, but gradual.

## 10.5 Discussion and Design Criterion

As results of the previous procedure, a series of graphs that depict the component dynamic properties in relationship with the face width variation have been produced. By tracking one mode shape with a target natural frequency, veering phenomena can be highlighted. As an example, let consider the two mode shapes of Fig. 10.3. By varying the gear face width, the natural frequencies change as shown in Fig. 10.7. In particular, with a face width of 8 mm, the two analysed mode shapes are so far in frequency and they are excitable in a very different frequency range. As the face width increases, the two natural frequencies approach and the exciting frequency band is narrowing. When the face width reaches 20 mm, veering occurs, and the two mode shapes interchange. As depicted in the succession of Figs. 10.3–10.6, the two mode shapes share modal information. The most important result is that the veering phenomenon creates a modification of the mode shape and an interchange of them. If the excitation band is always around 3200 Hz, if the face width of the gear is equal to 8 mm, the excited mode is the ND = 4, if the face width is 25 mm, the excited mode is the ND = 4, NC = 1. So at the precise excitation band, by varying one geometrical feature of the gear, the system response can be significantly different.

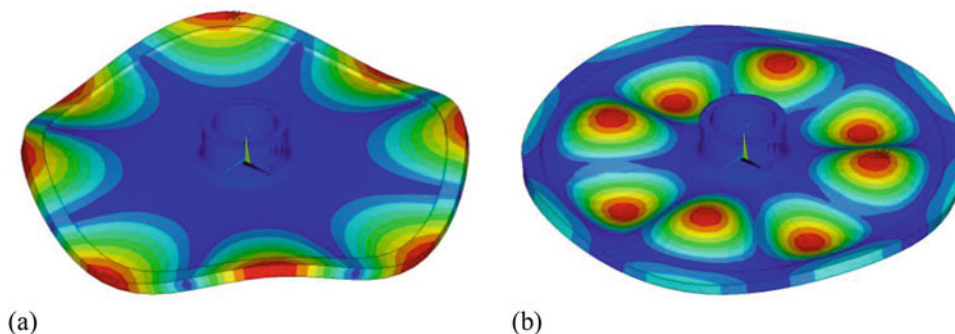


**Fig. 10.3** Mode shapes for (a) ND = 4 at 1876 Hz and (b) ND = 4, NC = 1 at 3193 Hz for face width = 8 mm

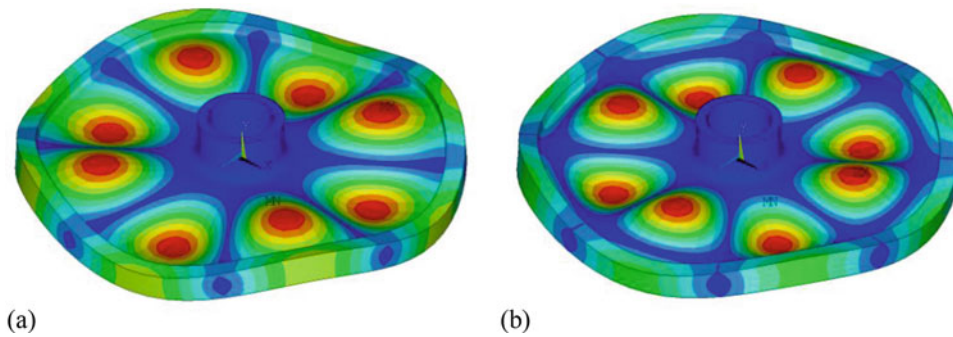


**Fig. 10.4** Veering mode shapes for (a)  $ND = 4$  at 3043 Hz and (b)  $ND = 4, NC = 1$  at 3366 Hz for face width = 18 mm

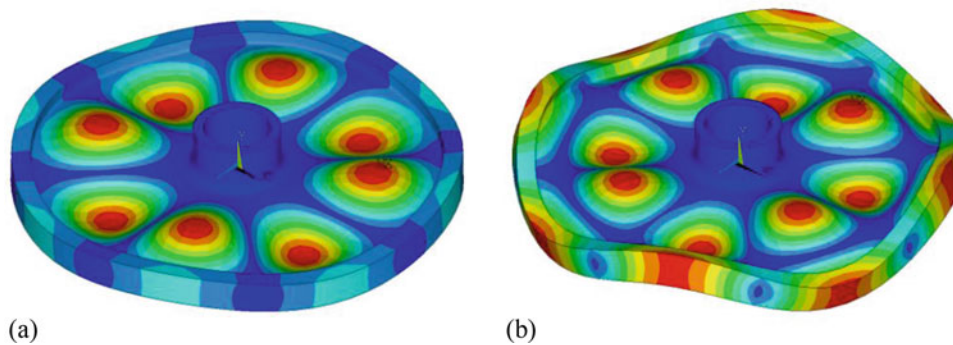


**Fig. 10.5** Veering mode shapes for (a)  $ND = 4, NC = 1$  at 3153 Hz and (b)  $ND = 4$  at 3501 Hz for face width = 20 mm

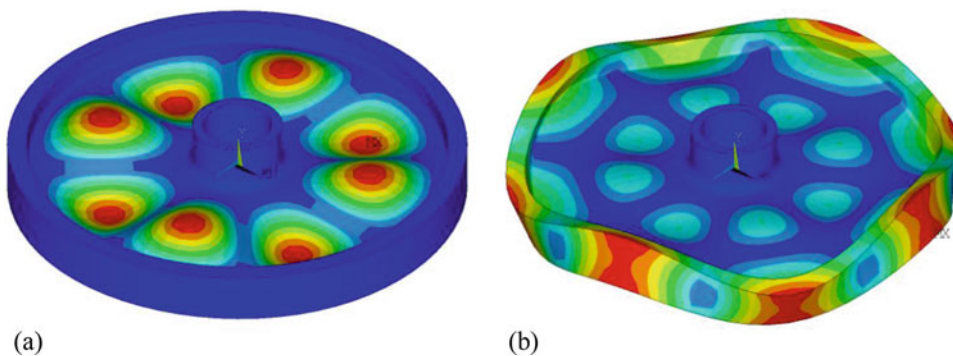


**Fig. 10.6** Mode shapes for (a)  $ND = 4, NC = 1$  at 3247 Hz and (b)  $ND = 4$  at 4416 Hz for face width = 30 mm

The external force due to meshing actions interacts with the gear in a precise way, and in particular along the line of action, so the excitation energy is inserted in the system with a precise direction. This means that only the mode shape that are more compliant in that direction can be excited by this force. Let now consider a helical gear, the excitation force can be decomposed in three forces, one radial, one tangential and one axial. If the  $ND = 4, NC = 1$  mode is considered, neither the radial nor the axial components of the meshing force can excite this mode shape, whereas the axial force can induce vibration by considering the  $ND = 4$ . Following that reasoning, the  $ND = 4, NC = 1$  mode shape does not respond to the meshing force with a high magnitude, whereas the  $ND = 4$  does. Now, imagine to use this kind of gear in the range of frequency near 3200 Hz. If the face width is 8 mm, the gear response to the meshing force is influenced by the mode shape  $ND = 4$  and a great amplitude of response is expected, whereas if the face width is 25 mm, the gear answers following  $ND = 4, NC = 1$  mode shape, so the answer amplitude is expected to be very low.

By considering that behaviour and what happens in the neighbourhood of face width value of 20 mm, it can be concluded that a little change of a geometrical parameter can deeply affect the system response. So by moving just one parameter, it is possible to change the answer of the same component. This could be an interesting design approach because gears have some geometrical features that are rigidly defined by the functional design, thus the operative range is defined. Having the



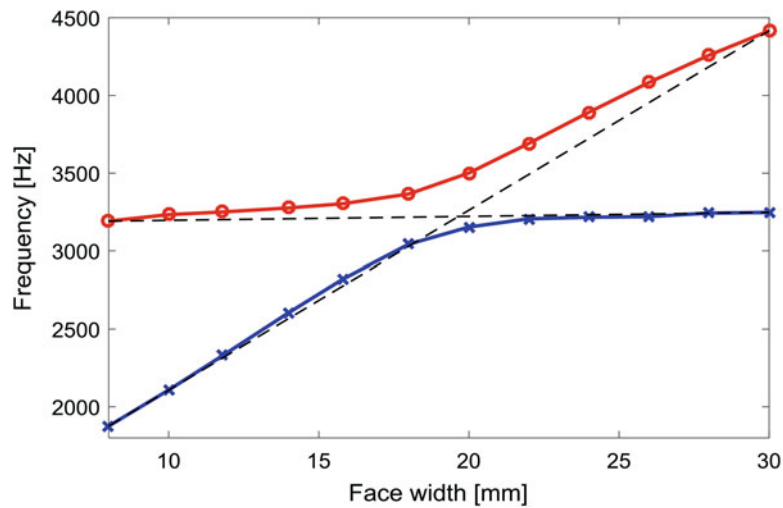


**Fig. 10.7** Veering occurrence between mode shapes  $ND = 4$  and  $ND = 4$ ,  $NC = 1$

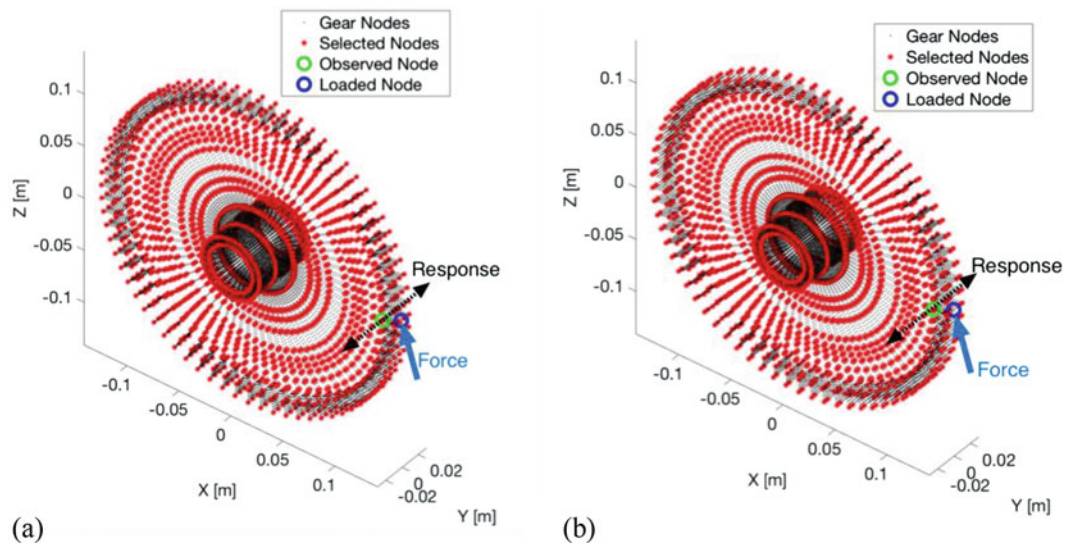


**Fig. 10.8** Gear nodes for face width values of 18 mm (a) and 20 mm (b) and the selected nodes for MAC calculation

possibility to change the answer of the gear only by changing an easy parameter, in that case a parameter that cannot be functional, arises a great importance in the design process.

Taking into account  $ND = 4$  and  $NC = 1$ , Figs. 10.3–10.6 show the transition of mode shapes interacting in the first veering case. In particular, comparing Figs. 10.4 and 10.5, it can be underlined the abrupt transformation of mode shapes. Fig. 10.7 shows the veering phenomenon concerning the natural frequencies. Based on Fig. 10.8 for the node comparison of the FE models, Figs. 10.9–10.11 show the auto-MAC and the cross-MAC during the veering phenomenon.

Multiple cases are simulated, also with veering interactions between three mode shapes. Taking into account  $ND = 6$  and  $NC = 1$  or  $NC = 2$ , Figs. 10.12 and 10.13 show the mode shapes interacting in the most coupled configurations. Figure 10.14 shows the multiple veering phenomena concerning the natural frequencies. Based on Fig. 10.15 for the node comparison of the FE models, Figs. 10.16 and 10.17 show the cross-MAC during the veering phenomenon.

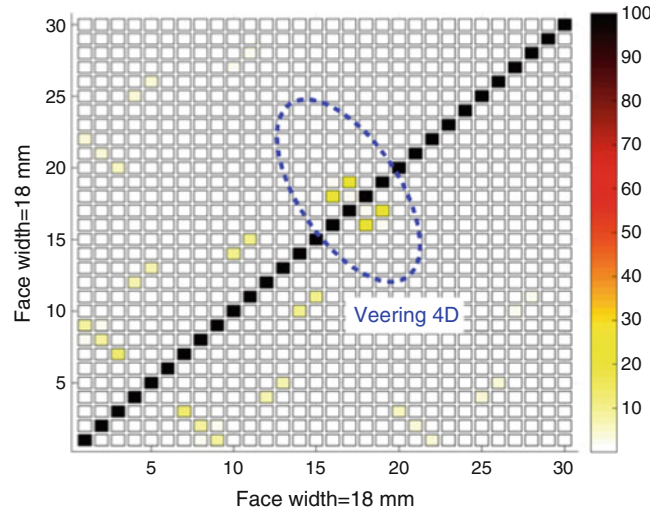


Fig. 10.9 Auto-MAC for face width = 18

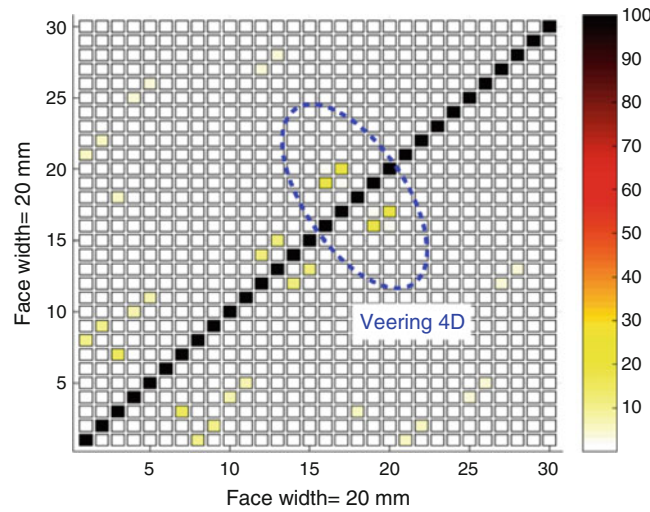


Fig. 10.10 Auto-MAC for face width = 20

## 10.6 Design to Reduce Dynamic Interactions

In order to demonstrate the idea of using veering for design improvements, the modal superposition is taken into account to analyse the steady state condition of a dynamic excitation. According to a proportional light viscous damping model, the inertance in a node  $j$ , due to a dynamic force in node  $k$ , results:

$$A_{j,k}(\omega) = \frac{\ddot{x}_j}{F_k} = \sum_{r=1}^N \frac{-\omega^2 \varphi_j^{(r)} \varphi_k^{(r)}}{\omega_r^2 + 2i \zeta_r \omega \omega_r - \omega^2} \quad (10.2)$$

by varying one geometrical feature of the gear, the system response can be significantly different and the weights of the interacting veering modes can be emphasised by neglecting them progressively from the complete modal superposition. Figure 10.18 shows the effect on the four configurations of Figs. 10.3–10.6. If a dynamic excitation is set in the range around 3000 and 3500 Hz and it is acting on the meshing direction  $z$ , the inertances in direction  $y$  of nodes on  $x$  axis at the pitch diameter should be as lower as possible (see Fig. 10.8). Paying attention to the case (b) and (c) of Fig. 10.12, it can be seen of how the two modes that are exchanging their shapes can have a benefit in the inertance modulus.

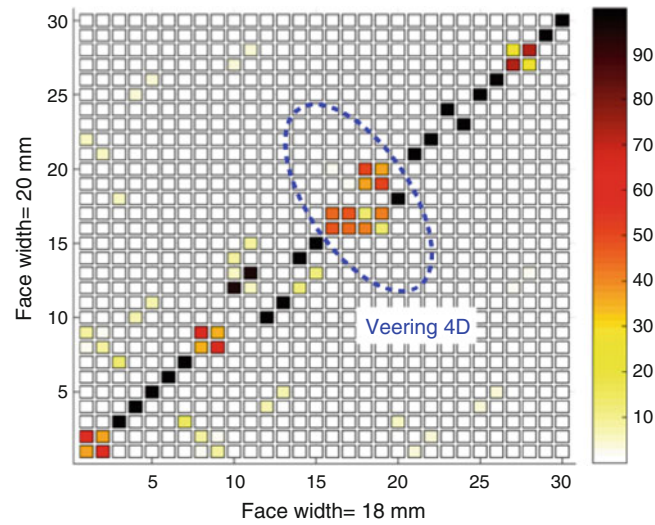


**Fig. 10.11** Cross-MAC between face width = 18 and face width = 20

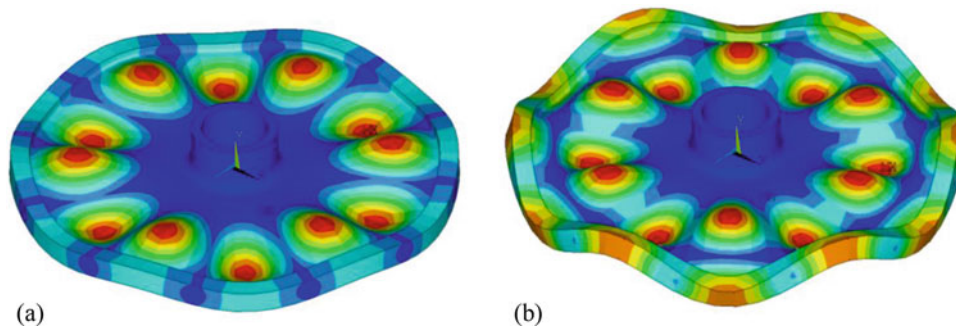


**Fig. 10.12** Veering mode shapes with  $ND = 6$ ,  $NC = 1$  for face width = 14 mm in veering zone 1: 5863 Hz (a), 6486 Hz (b)

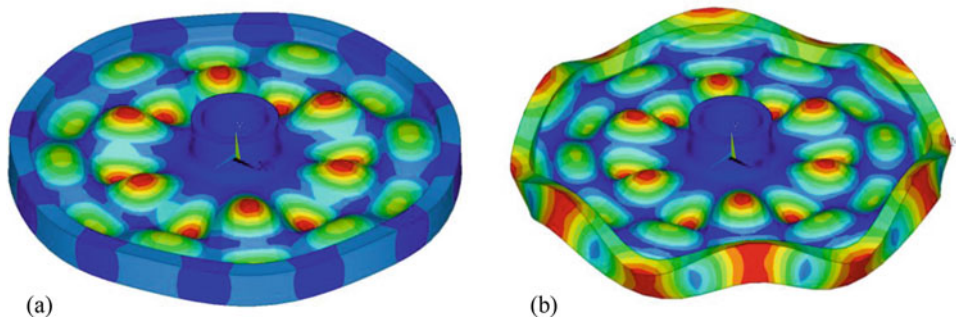


**Fig. 10.13** Veering mode shapes with  $ND = 6$ ,  $NC = 2$  for face width = 24 mm in veering zone 2: 8459 Hz (a), 9443 Hz (b)

## 10.7 Conclusions

Taking into account the example of improve the dynamic performance in steady state conditions of thin-webbed helical gears, a proposal of using veering phenomena between coupled mode shapes has been proposed. During the design process, especially in these kind of systems where dynamic characteristics are crucial, the effects of resonances can be tuned according to mode displacements and exciting force directions. This idea is under evaluation for high speed gear design in order to optimise a set of geometrical parameters in order to switch between two different mode shapes and improve the system performance.

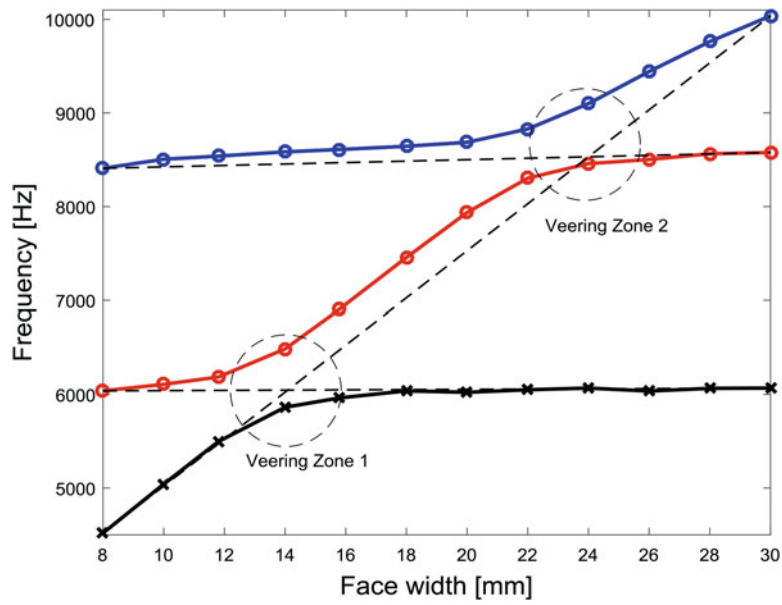


Fig. 10.14 Veering zones for mode shapes with six nodal diameters

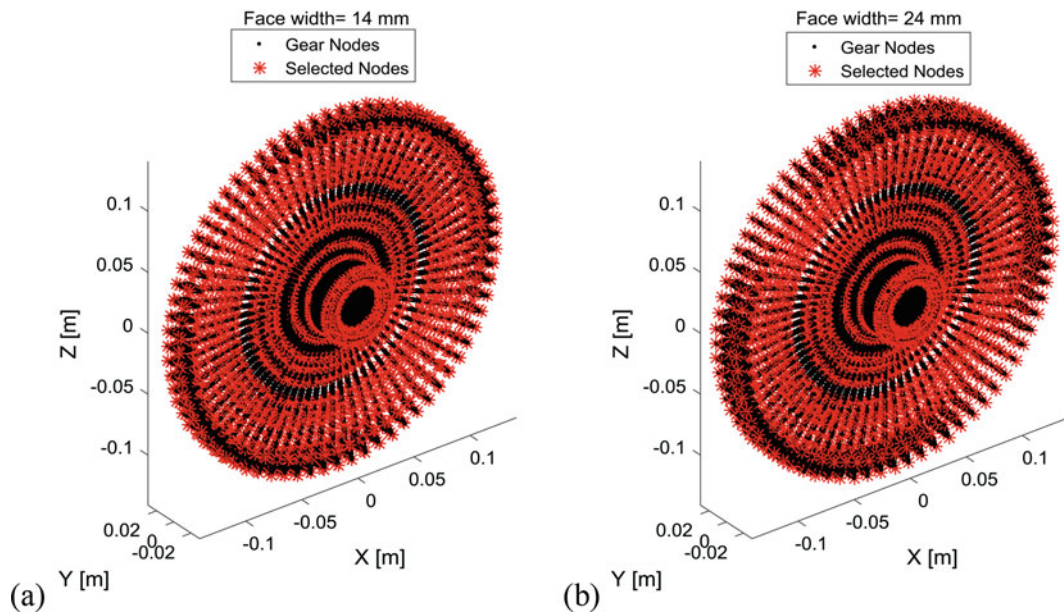
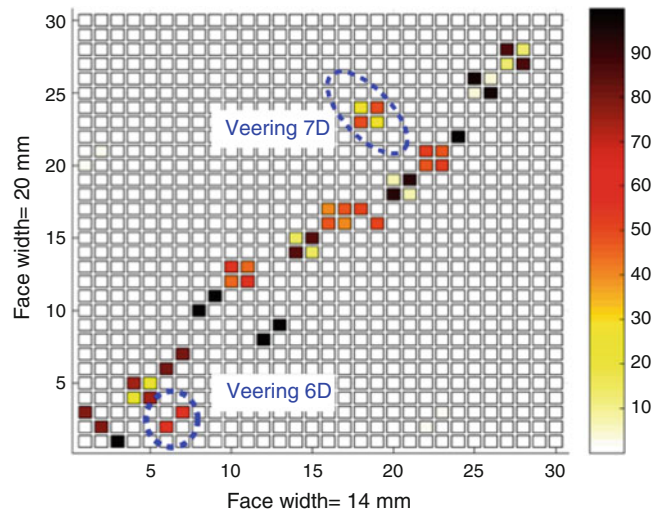
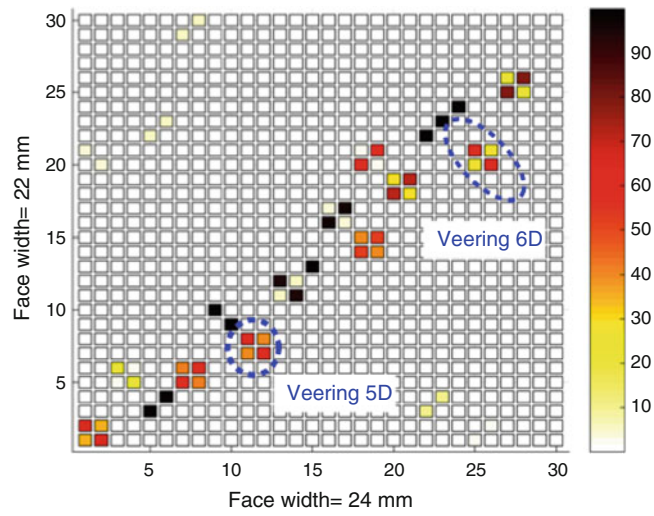


Fig. 10.15 Gear nodes for face width values of 14 mm (a) and 24 mm (b) and the selected nodes for MAC calculation





**Fig. 10.16** Cross-MAC for face width = 14 and 12 mm



**Fig. 10.17** Cross-MAC for face width = 24 and 22 mm

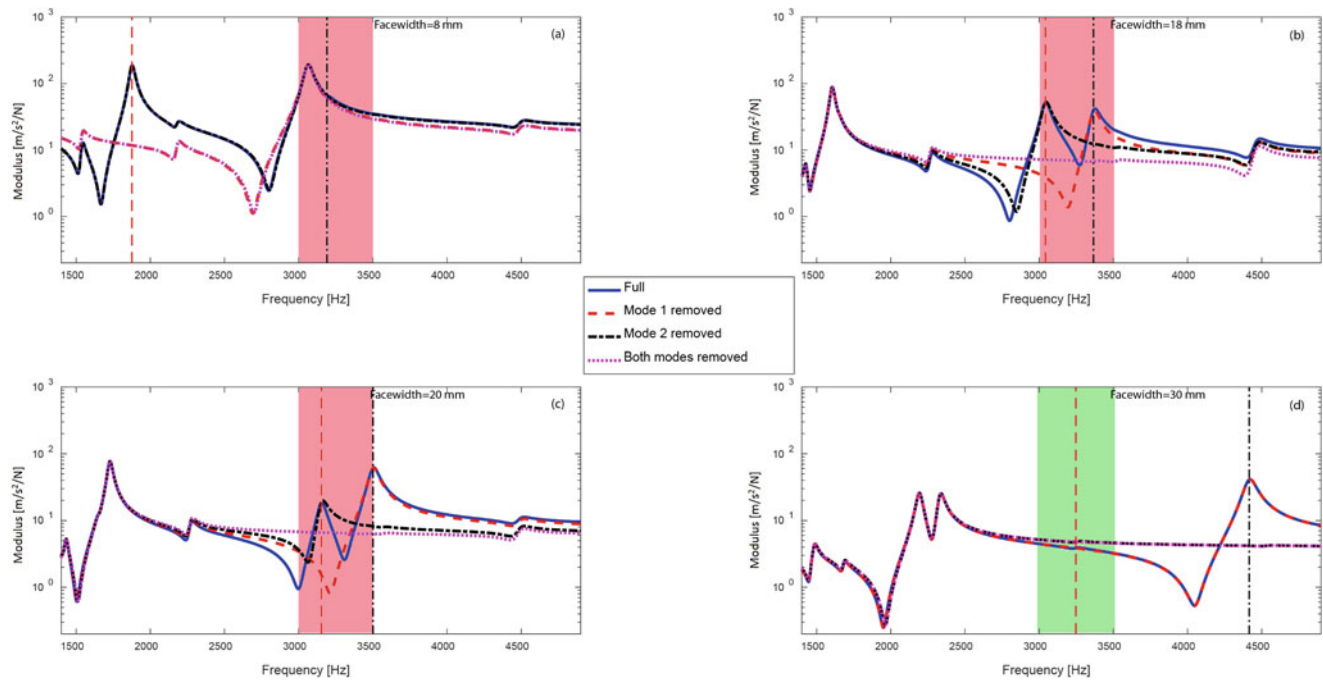


**Fig. 10.18** Computed transfer functions for different face width values and their modal participation factors

## References

1. Mace, B.R., Manconi, E.: Wave motion and dispersion phenomena: veering, locking and strong coupling effects. *J. Acoust. Soc. Am.* **131**, 1015–1028 (2012)
2. Giannini, O., Sestieri, A.: Experimental characterization of veering crossing and lock-in in simple mechanical systems. *Mech. Syst. Signal Process.* **72-73**, 846–864 (2012)
3. Leissa, W.: On a curve veering aberration. *J. Appl. Math. Phys.* **25**, 99–111 (1974)
4. Kutter, J.R., Sigillito, V.G.: On curve veering. *J. Sound Vib.* **75**, 585–588 (1981)
5. Perkins, N.C., Mote Jr., C.D.: Comments on curve veering in eigenvalue problems. *J. Sound Vib.* **106**(3), 451–463 (1986)
6. Pierre, C.: Mode localization and eigenvalue loci veering phenomena in disordered structures. *J. Sound Vib.* **126**(3), 485–502 (1988)
7. Balmès, E.: High modal density, curve veering, localization: a different perspective on the structural response. *J. Sound Vib.* **161**(2), 358–363 (1993)
8. Du Bois, J.L., Adhikari, S., Lieven, N.A.J.: Eigenvalue curve veering in stressed structures: an experimental study. *J. Sound Vib.* **322**, 1117–1124 (2009)
9. Bonisoli, E., Delprete, C., Esposito, M., Mottershead, J.E.: Structural dynamics with coincident eigenvalues: modelling and testing. Proceedings of the 29th IMAC, a conference on structural dynamics (2011)
10. Akay, A., Giannini, O., Massi, F., Sestieri, A.: Disc brake squeal characterization through simplified test rigs. *Mech. Syst. Signal Process.* **23**, 2590–2607 (2009)
11. Chan, Y.J., Ewins, D.J.: Management of the variability of vibration response levels in mistuned bladed discs using robust design concepts. Part 1: parameter design. *Mech. Syst. Signal Process.* **24**, 2777–2791 (2010)
12. Chan, Y.J., Ewins, D.J.: Management of the variability of vibration response levels in mistuned bladed discs using robust design concepts. Part 2: tolerance design. *Mech. Syst. Signal Process.* **24**, 2792–2806 (2010)
13. Allemang, R.J., Brown, D.L.: A correlation coefficient for modal vector analysis. Proceeding of the IMAC, pp. 110–116 (1982)

# Chapter 11

## Impulse Excitation of Piezoelectric Patch Actuators for Modal Analysis

V. Ruffini, T. Nauman, and C. W. Schwingshackl

**Abstract** Impact hammer testing is a fundamental technique in experimental modal analysis, allowing a fast estimation of the dynamic properties of a structure in its linear range. However, human error can limit the accuracy of the measured frequency response functions when the tests are conducted manually, as the FRFs are influenced by the locations and orientation of the hits, as well as the magnitude of the impact if the test piece is nonlinear. Piezoelectric patch actuators can be permanently attached to a structure and provide a controllable means of excitation, thus reducing the uncertainties introduced by manual testing, and allowing testing on structures in operation. This paper therefore investigates the possibility of using piezoelectric patches to simulate impact testing, and of their use as a minimally intrusive on-board monitoring system allowing to extract the natural frequencies, damping, and mode shapes of flexible structures. The methodology has been verified on a free-free beam, and validated against standard testing methods and analytical results, demonstrating its viability. It was then applied to the modal analysis of an academic blade disk, and led to the successful extraction of its resonance frequencies and damping values.

**Keywords** Experimental modal analysis • Piezoelectric actuator • Frequency response function • Impulse testing • Bladed disk

### 11.1 Introduction

Piezoelectric laminar, or patch, actuators have been steadily gaining popularity over the past 20 years. They consist of flat patches of encapsulated piezoelectric material, and are characterized by low weight, low cost, and good achievable forcing levels, and low cost. Piezoelectric patches can be driven by arbitrary control voltages, and attached to the structure directly at the input locations of choice, even ones that would be inaccessible to standard shakers or magnet arrays (e.g. the side of a blade in a staggered cascade), without significantly altering the intrinsic dynamic properties of the underlying structures, making them particularly suited to experimental modal analysis (EMA) applications.

The actuation characteristics come from the coupled electromechanical properties of piezoelectric materials: an applied voltage is able to produce a strain in the material, which can elongate and compress, and transmit a bending moment to the underlying structure through the bond interface [1]. Piezoelectric actuators can thus be incorporated into “smart” structures for active vibration control [2, 3], energy harvesting [4], and structural health monitoring (SHM) [5].

As modal-based SHM techniques are reaching maturity [6], the possibility of using embedded piezoelectric actuators to generate Frequency Response Functions (FRFs) is attractive, as it would allow to do modal analysis on a structure in operation, while using the time-proven methods of experimental modal analysis. The possibility of generating FRFs through piezoelectric actuation has been proven through several studies, initially based on simple cantilever beam models to derive experimental validation data [7, 8]. Applications to ultra-lightweight [9] or complex structures, like bladed disks [10–13] or robots [14], have proved the versatility and reliability of these actuators in identifying modal parameters.

However, the modal tests tend to rely on techniques like sinusoidal [12, 15], or random excitation [16], which, while reliable, can be time-consuming. Hammer tests, on the other hand, are a staple of EMA as they provide FRFs over large frequency ranges and with good resolutions in a short amount of time. However, human error can limit the accuracy of the measured frequency response functions when the tests are conducted manually, as the FRFs are influenced by the

---

V. Ruffini (✉) • C.W. Schwingshackl

Department of Mechanical Engineering, Imperial College London, Exhibition Road, London, SW7 2AZ, UK  
e-mail: [v.ruffini@imperial.ac.uk](mailto:v.ruffini@imperial.ac.uk)

T. Nauman

Department of Mechanical Engineering, Boston University, One Silber Way, Boston., MA 02215, USA

locations and orientation of the hits, as well as the magnitude of the impact if the test piece is nonlinear. In addition, hammer tests cannot, in general, be performed on structures in operation. This paper investigates the possibility of reproducing the characteristics of a hammer test with piezoelectric actuators, to deliver a fast experimental method that yields broadband excitation while ensuring a high level of repeatability.

## 11.2 Characterization of Piezoelectric Impulse Excitation

The concept of the proposed method is illustrated in Fig. 11.1a. A piezoelectric patch actuator is attached directly to the structure under test (SUT). An analog-output DAQ card is used to generate a low-amplitude voltage pulse. The pulse is then sent to a power amplifier, to increase the voltage amplitude and exploit the working range of piezoelectric actuators, which usually spans hundreds of volts. This high-amplitude voltage drives the piezoelectric actuator, which reacts with an impulsive strain transmitted directly to the SUT. If a high-impedance channel is present on the output side of the amplifier, providing a low-voltage measurement of the actual output signal to the actuator, the impulse excitation can be monitored for distortions introduced by the amplifier, and this signal used as reference input for standard Frequency Response Function (FRF) calculations.

### 11.2.1 Experimental Set-up

To verify the viability of the approach, a simple test rig (Fig. 11.1b) was set up to reduce uncertainties in the results. The SUT is a rectangular cross-section mild steel beam ( $500 \times 70 \times 3$  mm), suspended vertically by fishing wires in a free-free configuration. Two Macro-Fiber Composite (MFC) patch actuators (Smart Material M-5628 P2), operating in the d31 mode, are attached longitudinally at 80 mm from the short edges of the beam. Only one patch was used for the tests presented in this article, and was connected to a power amplifier (PI E-835 piezo-driver module), with a fixed gain of 25, and an output voltage range of  $-50$  to  $250$  V. A high-impedance monitor channel divided the high-amplitude output voltage by a factor of 100, allowing its measurement after passage through the amplifier. The input drive signal to the amplifier was generated by an analog output card (NI 9264), with a maximum sampling frequency of 51,200 Hz, and an output of  $\pm 10$  V, which was controlled from a PC through a LabView interface. The response of the beam was measured by an IEPE accelerometer (PCB 352B10), attached with wax at the tip of the beam. Both the acceleration and the monitor signal from the piezo-amplifier were acquired by a Data Physics Quattro DAQ system, and the two signals used to calculate the FRFs.

The dedicated LabView interface allowed to set the amplitude and duration of the impulse voltage signal, and therefore to control both the intensity and bandwidth of the excitation. Figure 11.2 shows the spectra of the excitation signal at different pulse durations, while the maximum voltage amplitude was kept at 150 V. As expected, the bandwidth of the excitation

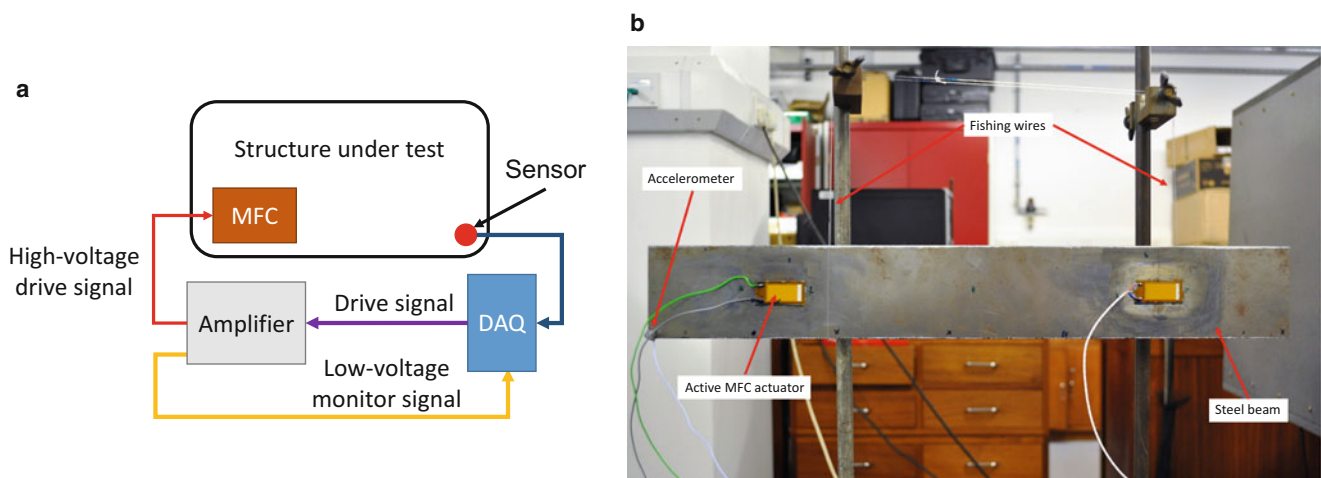
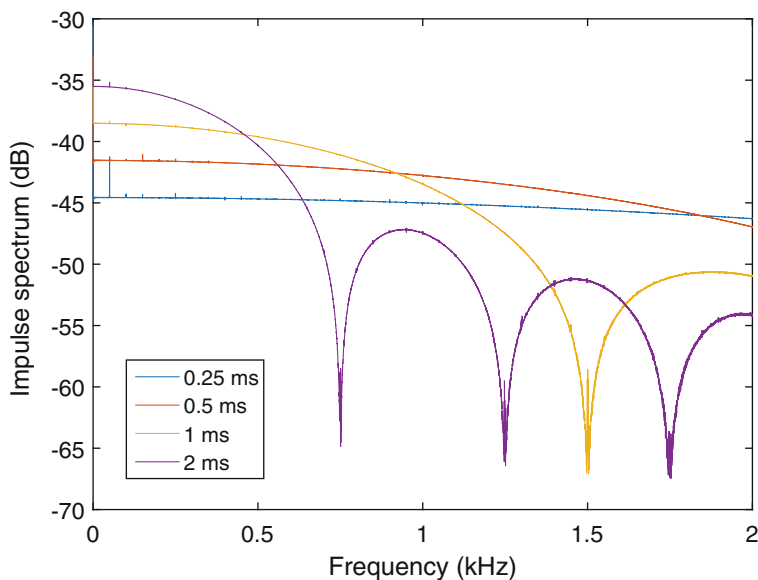


Fig. 11.1 (a) Lay-out of the measurement chain; (b) experimental set-up





**Fig. 11.2** Input spectra of the piezoelectric impulse at different pulse durations

decreases as the pulse duration increases, with the 0.25 ms pulse resulting in a nearly flat spectrum over the whole 2-kHz frequency range of interest, and the main lobe of the 2 ms pulse covering less than half of the same span. Longer pulses introduce higher energy levels at the lower frequencies (the 2 ms pulse is 5–10 dB larger than the 0.25 ms pulse in the 500-Hz range), thus making it possible to enhance excitation quality in the desired ranges, just as, in a traditional hammer test, hammer tips with different stiffness levels would be chosen. Isolated peaks were also found at harmonics of the mains frequency (50 Hz), indicating a small amount of electrical noise.

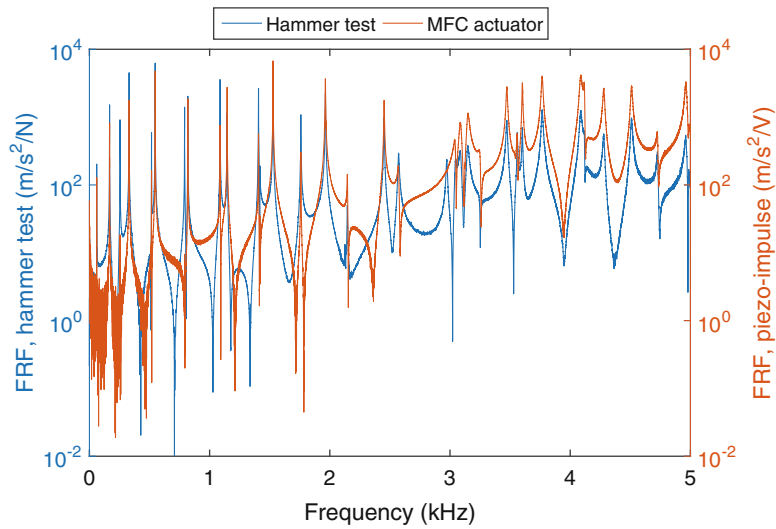
### 11.2.2 Frequency Response Functions Characteristics

Figure 11.3 shows a representative FRF obtained by piezoelectric impulse excitation. A FRF from a standard hammer test is used as reference. It can be seen that both methods yield very similar FRFs, and that all peaks match. The different distribution of minima and anti-resonances is predictable, due to the different physical means of forcing the structure: a concentrated force for the hammer, a concentrated moment pair for the MFC patch [1].

It can be seen that the piezo-FRF is characterized by very low noise levels, except at frequencies below 200 Hz. To further explore the dynamic characteristics of the piezo-impulse excitation, the effects of the pulse duration on the FRF itself were investigated, and the coherence function was chosen as quality measure. Ten tests were performed at 0.25, 1, and 2 ms each, and their coherence calculated. Fig. 11.4a shows that a lower pulse duration increases dramatically the coherence at higher frequencies, with levels equal to one except at anti-resonances.

The influence of the pulse amplitude was then varied, to assess the voltage range within which noiseless response could be expected, without exciting nonlinearities. Five different values of the peak voltage (25–200 V) were tested, while the pulse duration was kept constant at 0.5 ms. Ten tests were performed at each level, and the resulting coherence functions are shown in Fig. 11.4b. It is clear that higher voltages yield higher coherence levels, as the larger response improves the signal-to-noise ratio. The fact that the coherence is constant over large ranges (except, again, at anti-resonances), and very close to unity, is also an indication that no non-linearities were activated, either in the structure, or in the piezo-amplifier, confirming the linearity of the proposed method.

Figure 11.4 shows that the coherence did not improve significantly below 100 Hz, regardless of pulse duration or amplitude levels. It is possible that further increasing the pulse duration would boost the excitation of the lower frequency range, but it should also be remarked that, as the first bending mode of the beam used for these tests is at 60 Hz, the low frequencies are dominated by rigid body motion. This is readily excited by a hammer hit, but not by the patch actuator, which relies on the flexibility of the SUT. This can have a beneficial effect, as rigid body modes can interfere with the identification of the flexible ones.



**Fig. 11.3** FRFs from standard hammer test and piezoelectric impulse

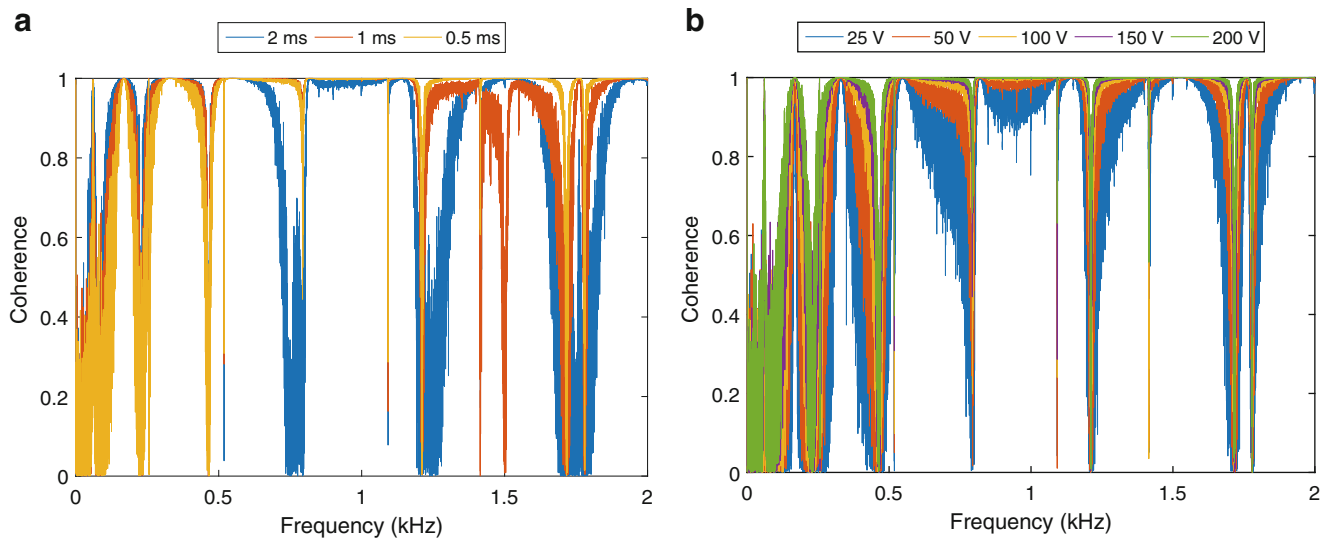


**Fig. 11.4** Coherence function at (a) different pulse durations, peak voltage of 200 V, and (b) different peak amplitudes, pulse duration of 0.5 ms

To test the behaviour at the high-end of the spectrum, the pulse peak voltage was increased to 240 V, and the duration reduced to 0.1 ms. A hammer test (with the hammer equipped with a steel tip) was also performed to provide a reference. For the piezo-impulse test, the main lobe of the input spectrum covered more than 10 kHz, and the resulting coherence (Fig. 11.5) remained close to one over the whole 2–10 kHz range. For the hammer test, on the other hand, where the pulse duration was dictated by the physics of the impact, and resulted in 0.2 ms, the coherence started dropping after 7 kHz.

### 11.2.3 Modal Parameter Identification

To investigate the validity of the proposed method for modal analysis purposes, the natural frequencies and damping ratio values were extracted from the FRFs measured at the five peak voltage levels and three pulse duration shown in Sect. 11.2.2 using an implementation of the poly-reference Least Squares Complex Frequency algorithm (pLSCF) [17]. For the sake of brevity, the comparison will be shown solely on the first three bending modes of the beam, which are located in the range of minimum coherence for the piezoelectric impulse method, and thus potentially the most problematic. In addition, as the

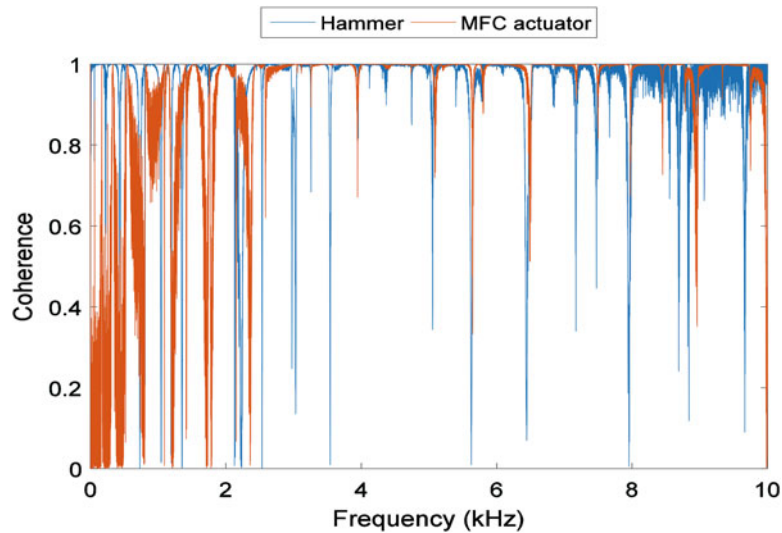


**Fig. 11.5** Coherence function over a frequency range of 10 kHz from a standard hammer test and the piezoelectric impulse test (240 V peak amplitude, 0.1 ms pulse duration)

**Table 11.1** Damping ratio for the first three bending modes of the test beam, at different combinations of peak amplitude and pulse duration

	25 V	50 V	100 V	150 V	200 V
Damping ratio (%) for 1st bending mode (60.7 Hz)					
0.25 ms	0.05	0.06	0.07	0.08	0.08
0.5 ms	0.05	0.09	0.08	0.09	0.09
1 ms	0.03	0.05	0.08	0.11	0.12
Damping ratio (%) for 2nd bending mode (167.9 Hz)					
0.25 ms	0.03	0.02	0.03	0.04	0.04
0.5 ms	0.02	0.03	0.04	0.04	0.04
1 ms	0.03	0.04	0.04	0.04	0.04
Damping ratio (%) for 3rd bending mode (329.9 Hz)					
0.25 ms	0.04	0.04	0.04	0.04	0.04
0.5 ms	0.04	0.04	0.04	0.04	0.04
1 ms	0.07	0.04	0.04	0.04	0.04

**Table 11.2** Comparison between the extracted resonance frequencies and damping ratios from a standard hammer test and the piezoelectric impulse

Hammer test		MFC actuator	
Frequency (Hz)	Damping ratio (%)	Frequency (Hz)	Damping ratio (%)
60.72	0.07	60.69	0.08
167.96	0.04	167.96	0.04
329.96	0.05	329.99	0.04

resonance frequencies showed a maximum range of variation of 0.03 Hz over all the test configurations, only their final values are shown in Table 11.1, which shows the damping ratio values for the different combinations of pulse amplitude/duration.

The damping ratio for the first bending mode at 60.7 Hz shows the most variability, ranging from 0.03 to 0.12%. This is compatible with the narrow range of high coherence around the 60.7-Hz peak observed in Fig. 11.4, as the MFC patch was not optimally placed for the first bending mode. Both the second and third mode shapes, however, show remarkably low variations of the extracted damping. The results of the identification process were then compared to the results of a standard hammer test (Table 11.2), and the excellent agreement between them confirmed the repeatability and linearity of the approach.

The piezo-impulse data was also used to extract the mode shapes of the beam. Ten measurement points were taken along the lower edge of the beam at intervals of 50 mm. To avoid a roving accelerometer configuration, that would affect the FRFs due to the moving mass of the sensor from test to test, a laser Doppler vibrometer (LDV) was used for these tests to measure velocity in the out-of-plane direction. The resulting ten FRFs were processed simultaneously using the pLSCF

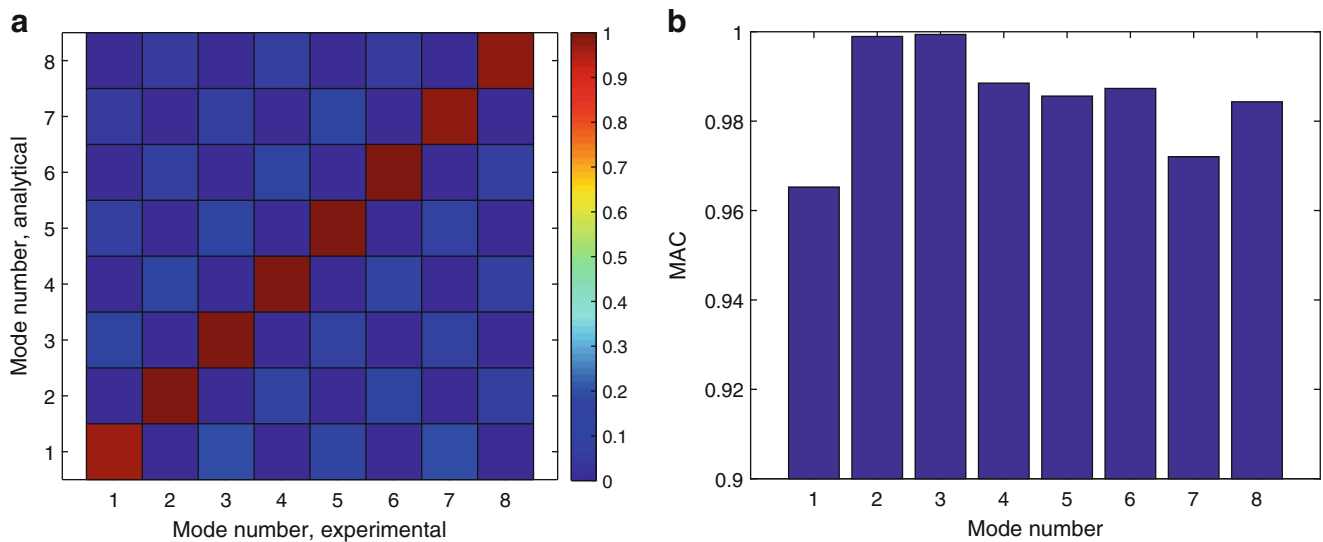


**Fig. 11.6** MAC between the first eight analytical and experimental modes of the test beam: (a) MAC matrix, and (b) values on the MAC diagonal

algorithm, and the first eight bending modes of the beam were compared to the analytical modes from classic beam theory. The resulting MAC is shown in Fig. 11.6. The dominant diagonal visible in Fig. 11.6a shows that the ten degrees of freedom (d.o.f.s) provided sufficient spatial resolution to identify the modes correctly.

The numerical values of the diagonal of the MAC matrix are displayed in Fig. 11.6b. A good agreement exists between the experimental and analytical data, as the lowest MAC value is 0.96 for the first bending mode. To better verify the match between the two sets of modes, the modal amplitudes at the measured d.o.f.s for the first four modes are plotted in Fig. 11.7. Both mode sets were separately scaled to unity. It can be seen that there is an excellent correspondence between the experimental and analytical values, with the exception of the first bending mode (Fig. 11.7a). While the experimental data follow the analytical mode shape, the scaling is not consistent: this is likely due to the noisier quality of the FRFs around the first peak, which has been shown above as affecting the modal parameters.

### 11.3 Application to the Modal Analysis of Bladed Disks

Section 11.2 showed that the piezoelectric impulse approach can be as reliable as standard EMA methods. To prove its applicability to more complex structures, and prepare the ground for tests on rotating machinery in particular, the method was used on a bladed disk (blisk, see Fig. 11.8a). A detailed description of the test rig can be found in [18], and only the relevant information is provided here. The blisk has eight sectors, it has a diameter of 200 mm, and a thickness of 2 mm. It is equipped with eight identical MFC actuators attached to its rear face with epoxy, one per sector (Fig. 11.8b).

The actuators (Smart Material M-0714-P2) have an active area of only  $7 \times 14$  mm, to minimize any mass loading and added stiffness and damping effects. Due to the light weight and flexibility of the blisk, the effect of the application of the actuators on its dynamics were assessed, by performing a hammer test before and after instrumenting it. To eliminate any interference from the assembly, the blisk was suspended in free-free configuration, and the response was measured with a LDV. The results for the first five nodal diameter (ND) modes are reported in Table 11.3, along with the natural frequencies predicted by finite element modelling. It can be seen that the resonances are unaffected by the addition of the MFC actuators, with a maximum change of 0.11%, and a negligible increase in mistuning. Variation in damping is more noticeable, with the first three modes in particular showing a one order of magnitude increase, although it can still be classified as lightly damped. It should also be noted that, in addition to the actuators, 16 strain gauges with their wires were also installed on the blisk [16]. It can therefore be concluded that the actuators have limited impact on the measurable dynamic properties of the SUT.

The blisk was then mounted in its final configuration on a shaft via a flanged joint and a Trantorque bushing. For the impulse test, the same power amplifiers described in Sect. 11.2.1 were used. Only the actuator on the reference sector was activated, and fed with a pulse of 200 V peak amplitude. The frequency range of interest, where the first five ND modes of

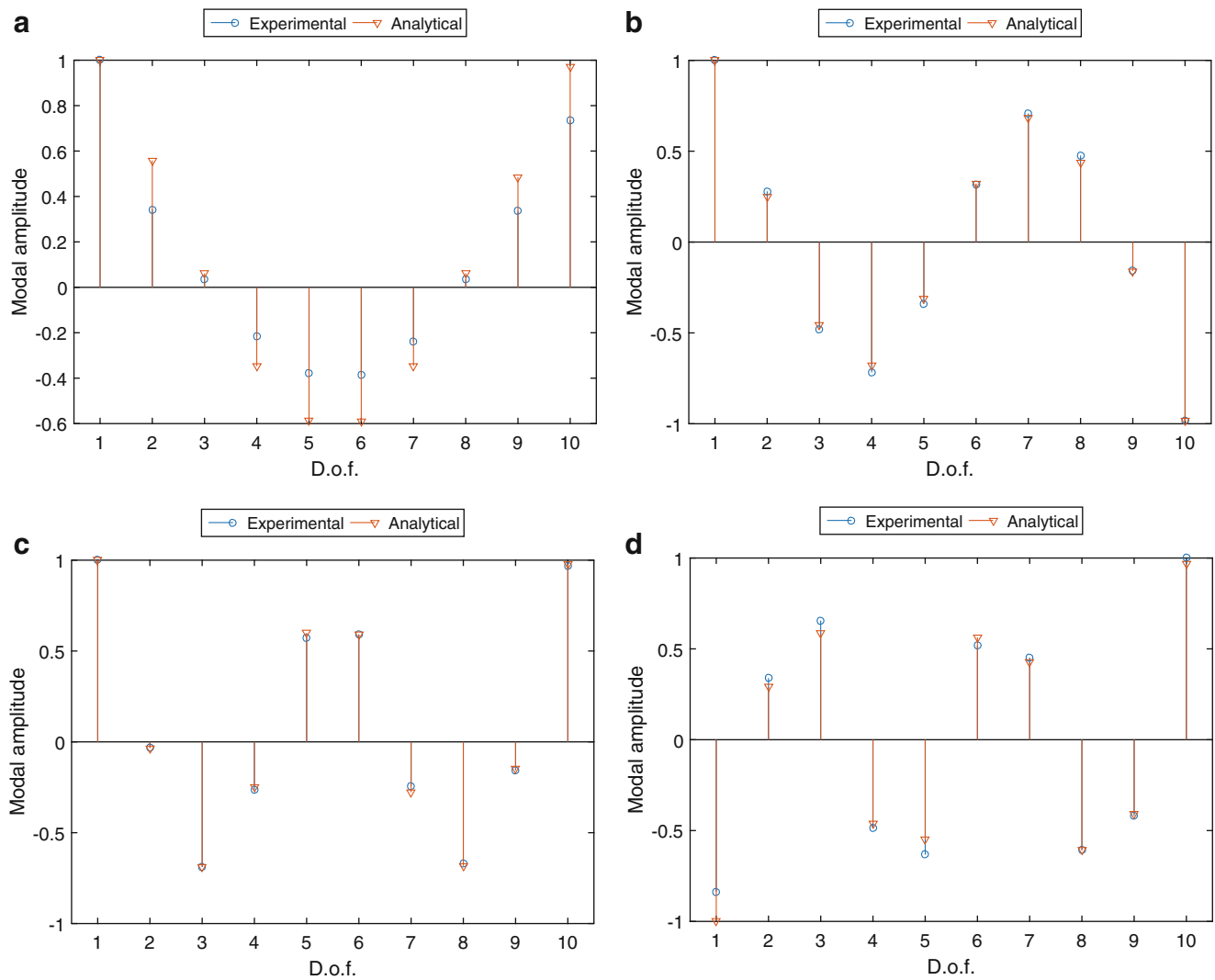


**Fig. 11.7** First four modes of the test beam: comparison between the analytical and experimental modal amplitudes for the measured d.o.f.s

the blisk were expected to be, was 160–320 Hz. The duration of the pulse was thus fixed at 4 ms. The response was measured at a point on the reference sector, close to the outer edge of the blisk (Fig. 11.8a), with a LDV.

The resulting FRF can be seen in Fig. 11.9. All the peaks associated to the ND modes are clearly visible, and other FRF features like anti-resonances and minima are well discriminated. Double peaks at the 1ND and 2ND modes appear due to mistuning, while the 3ND mode is unaffected by it. The pLSCF algorithm correctly fits the experimental FRF, and ignores the spurious peaks corresponding to mains noise.

Natural frequencies and damping ratio values were extracted, and compared to the results from a standard hammer test (Table 11.4). The frequencies from the methods show excellent agreement, with a maximum difference of 1% at the first 1ND peak. It is important to note that, for this test, it was necessary to carefully limit the force imparted by the hammer, as it could easily excite coupled disc-shaft-bearing modes. The discrepancy between the results for this mode, which is notable not for its absolute value, but because it is notably larger than all the rest of the results, could then be explained by the fact that the MFC actuator is much more capable of delivering repeatable low-level excitation, thus potentially providing the correct, blisk-only resonance value. This could prove valuable in single component testing, i.e. in separating the dynamic characteristics of a single component from the rest of the assembly.

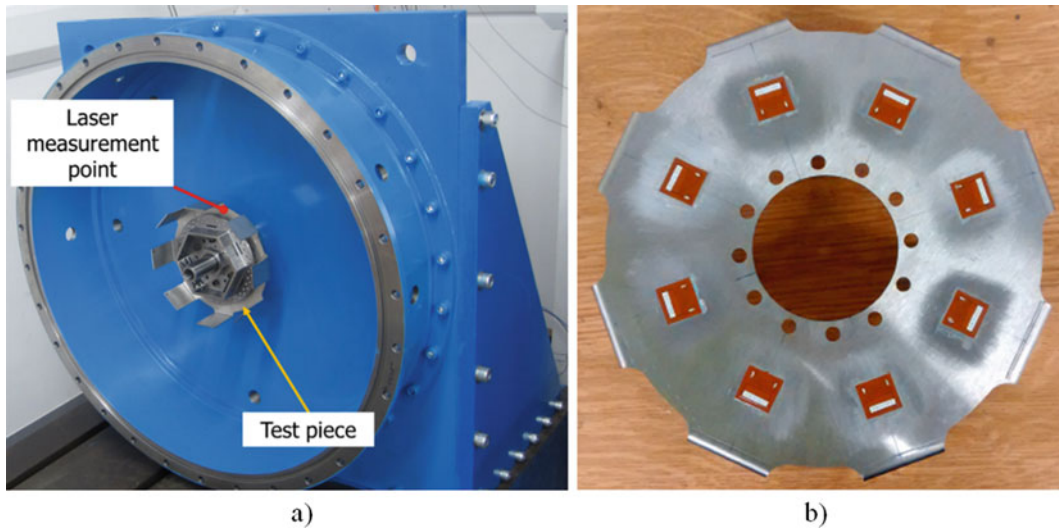


**Fig. 11.8** Bladed disk (a) Test piece mounted on its shaft, and (b) piezoelectric actuators

**Table 11.3** Comparison of the frequency and loss factors of the blisk before and after the installation of the MFC actuators

Mode	f FE (Hz)	f original blisk (Hz)	f after instrumenting (Hz)	$\eta$ original blisk (%)	$\eta$ after instrumenting (%)	$\Delta f$ (%)	Mistuning original blisk (%)	Mistuning after instrumenting (%)
2ND	119.4	111.0	111.0	0.04	0.19	-0.01	3.16	3.18
		114.6	114.6	0.03	0.11	0.02		
0ND	180.5	190.6	190.8	0.02	0.35	0.11	0	0
3ND	239.1	236.7	236.6	0.02	0.05	-0.04	0	0.12
			236.9		0.09	0.10		
4ND	302.1	300.1	300.3	0.02	0.03	0.10	0	0

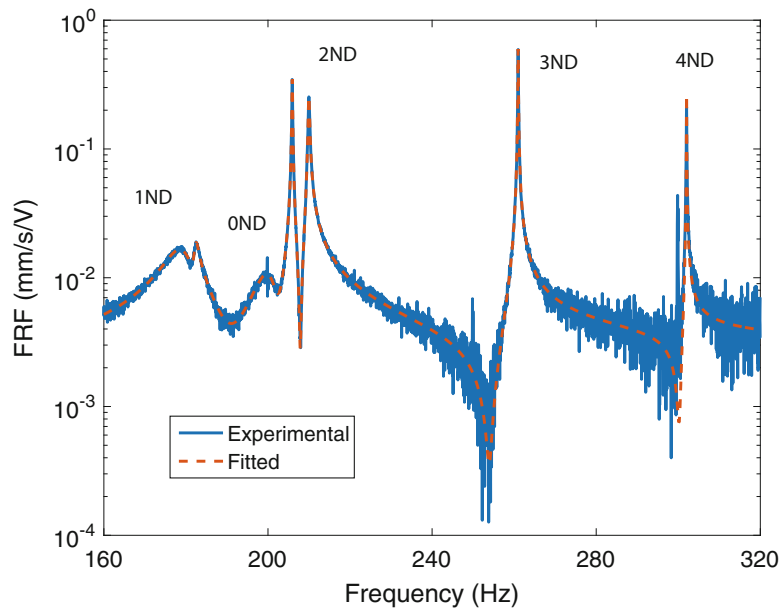


**Fig. 11.9** FRF of the blisk from the piezoelectric impulse test: experimental data and curve-fit

**Table 11.4** Comparison between the extracted resonance frequencies and damping ratios of the blisk from a standard hammer test and the piezoelectric impulse

	Hammer test		MFC impulse	
	Frequency (Hz)	Damping ratio (%)	Frequency (Hz)	Damping ratio (%)
1ND	177.5	2.45	179.4	2.26
	182.6	0.16	182.3	0.34
0ND	199.6	1.16	200.6	1.55
2ND	205.8	0.04	205.9	0.03
	209.8	0.08	210.0	0.08
3ND	260.7	0.02	261.0	0.01
4ND	301.9	0.01	302.0	0.01

## 11.4 Conclusions

A novel application of piezoelectric impulse testing to experimental modal analysis was presented. It is based on the use of piezoelectric patch actuators attached directly to the structure under test, and excited by a voltage pulse that can be controlled in both amplitude and duration to adjust the desired frequency range. It thus provides a broadband, fast testing method that is virtually applicable to structures that are not easily accessible, like rotating machinery, and is virtually unaffected by human error, unlike hammer tests in a standard lab environment.

The method was applied to a simple steel beam to assess its characteristics, and was shown to produce high-quality FRFs over a frequency range of at least 10 kHz. Low coherence was found at frequencies dominated by rigid body motion, showing that the new method can successfully filter them out. The high values of coherence over the rest of the excited bandwidth indicated the linearity and repeatability of the method. The resulting modal parameters of the beam compared very well to data obtained from a standard hammer test and analytical results. Resonance frequencies and damping values showed excellent agreement with the hammer test, and proved relatively independent from voltage levels and pulse duration. The extracted mode shapes matched the analytical ones very closely, and confirmed the reliability of the proposed approach.

The method was then applied to a blisk mounted on a shaft at rest, and yielded clear FRFs and natural frequency and damping values very close to the ones extracted from a hammer test. This, together with the little impact of the addition of the actuators on the dynamic properties of the structure, shows the viability of the method for the experimental modal analysis of complex structures, and promise for EMA-based condition monitoring purposes.

## References

1. Crawley, E.F., De Luis, J.: Use of piezoelectric actuators as elements of intelligent structures. *AIAA J.* **25**(10), 1373–1385 (1987)
2. Leo, D.J.: *Engineering Analysis of Smart Material Systems*. Wiley (2008)
3. Jalili, N.: *Piezoelectric-Based Vibration Control: From Macro to Micro/Nano Scale Systems*. Springer (2010)
4. Erturk, A., Inman, D.J.: *Piezoelectric Energy Harvesting*. Wiley (2011)
5. Park, G., Farrar, C.R., Rutherford, A.C., Robertson, A.N.: Piezoelectric active sensor self-diagnostics using electrical admittance measurements. *J. Vib. Acoust.* **128**(4), 469–476 (2006)
6. Doebling, S.W., Farrar, C.R., Prime, M.B.: A summary review of vibration-based damage identification methods. *Shock Vib. Dig.* **30**, 91–105 (1998)
7. Charette, F., Guigou, C., Berry, A., Plantier, G.: Asymmetric actuation and sensing of a beam using piezoelectric materials. *J. Acoust. Soc. Am.* **96**(4), 2272–2283 (1994)
8. Maurini, C., Porfiri, M., Pouget, J.: Numerical methods for modal analysis of stepped piezoelectric beams. *J. Sound Vib.* **298**, 918–933 (2006)
9. Park, G., Sausse, M., Inman, D.J., Main, J.A.: Vibration testing and finite element analysis of an inflatable structure. *AIAA J.* **41**(8), 1556–1563 (2003)
10. Hollkamp, J. J., Gordon, R. W.: Modal testing of a bladed disk. In: *Proceedings of IMAC XVII: 17th International Modal Analysis Conference*, pp. 826–832, Society of Photo-Optical Instrumentation Engineers (1999)
11. Jeffers, T., Kielb, J., Abhari, R.: A novel technique for the measurement of blade damping using piezoelectric actuators. In: *ASME Turbo Expo 2000: Power for Land, Sea, and Air* (2000)
12. Kammerer, A., Abhari, R.S.: Experimental study on impeller blade vibration during resonance—part II: blade damping. *J. Eng. Gas Turbines Power.* **131**(2), 022509 (2009)
13. Belz, J., May, M., Siemann, J., Seume, J. R., Voigt, C., Bohmer, H., Gruber, B.: Excited blade vibration for aeroelastic investigations of a rotating blisk using piezoelectric macro fiber composites. In: *ASME Turbo Expo 2013: Turbine Technical Conference and Exposition*. American Society of Mechanical Engineers (2013)



14. Wang, X., Mills, J.: Experimental modal identification of configuration-dependent vibration using smart material transducers with application to a planar parallel robot. In: *Robotics and Biomimetics (ROBIO)*. 2005 IEEE International Conference, pp. 234–239 (2005)
15. Gibert, C., Kharyton, V., Thouverez, F., Jean, P.: On forced response of a rotating integrally bladed disk: Predictions and experiments. In: *ASME Turbo Expo 2010: Power for Land, Sea, and Air*, pp. 1103–1116. American Society of Mechanical Engineers (2010)
16. Ruffini, V., Schwingshackl, C.W., Green, J. S.: Modal analysis of rotating structures under MIMO random excitation. In: *VIRM11-Vibrations in Rotating Machinery*, Institution of Mechanical Engineers (2016)
17. Guillaume, P., Verboven, P., Vanlanduit, S., Van Der Auweraer, H., Peeters, B.: A poly-reference implementation of the least-squares complex frequency-domain estimator. In: *Proceedings of IMAC*, vol. 21, pp. 183–192 (2003)
18. Ruffini, V., Schwingshackl, C.W., Green, J. S.: Experimental and analytical study of Coriolis effects in bladed disk. In: *ASME 2015 International Design Engineering Technical Conferences and Computers and Information in Engineering Conference*, vol. 8: 27th Conference on Mechanical Vibration and Noise. American Society of Mechanical Engineers (2015)

# Chapter 12

## Modal Parameter Estimation in Multi-Patch Operational Modal Analysis: Perspectives and Approaches

D. Mironovs and S. Chauhan

**Abstract** A general scenario in Operational Modal Analysis (OMA) is that of performing measurements in several patches instead of performing all the measurements over the structure simultaneously. This scenario might arise due to various factors, such as availability of limited number of sensors, partial access to the structure etc. In these circumstances, the task is to patch together the data obtained from various patches so that modal parameters, representative of the entire structure, can be estimated. Two general approaches exist to accomplish this. First approach requires modal parameters to be estimated individually for each patch and then patching together the results. The other approach is to combine together the data from individual patches such that parameter estimation algorithms can be applied on the combined data resulting in global modal parameters directly.

This paper studies the multi-patch OMA techniques and aims at providing useful insights and perspectives. The work presented in this paper lays down fundamental mathematical foundations of patching techniques in scenarios where data from different patches is first combined before applying parameter estimation algorithms. Further, a new Singular Value Decomposition (SVD) based approach is suggested in the paper for carrying out the patching procedure in the Pre-patching framework. The SVD based technique introduced in the paper also provides the basis of several other tools that help in evaluating overall effectiveness of the patching procedure, such as quality of acquired data, patch compatibility, validation of OMA assumptions regarding input excitation and time-invariance of the structure, etc. The concepts developed in this work are demonstrated by means of studies conducted on analytical and experimental systems.

**Keywords** Operational modal analysis • Multi-patch OMA • Modal parameter estimation • Singular value decomposition • Modal assurance criteria

### Nomenclature

$x$	Response vector
$\mathbf{G}_{XX}$	Output power spectra matrix
$\mathbf{H}$	Frequency response function
$\mathbf{X}$	Fourier transform of response vector matrix $\mathbf{x}$
$\mathbf{F}$	Fourier transform of force vector matrix $\mathbf{f}$
$\mathbf{U}$	Singular vector matrix
$\mathbf{S}$	Singular value diagonal matrix
$\mathbf{V}$	Orthonormal singular vector matrix
$s$	Separate singular values
$N_{ref}$	Number of reference channels

---

D. Mironovs  
Electrical Engineering, Acoustic Technology, Denmark Technical University, Copenhagen, Denmark  
e-mail: [den.alex.mironov@gmail.com](mailto:den.alex.mironov@gmail.com)

S. Chauhan (✉)  
Buel & Kjaer Sound and Vibration Measurement A/S, Skodsborgvej 307, DK, 2850, Naerum, Denmark  
e-mail: [schauhan@bksv.com](mailto:schauhan@bksv.com)

## Abbreviations

DOF	Degrees of Freedom
EM	Spatially Evenly distributed Modulated (Colored) noise
EW	Spatially Evenly distributed White noise
FFT	Fast Fourier Transform
FRF	Frequency Response Function
MAC	Modal Assurance Criterion
OMA	Operational Modal Analysis
PoGER	Post Global Estimation Rescaling
PreGER	Pre Global Estimation Rescaling
SDEC	Stability Diagram Evaluation Coefficient
SNR	Signal to Noise Ratio
SSI	Stochastic Subspace Identification
SSI-Cov	Covariance-driven SSI
SVD	Singular Value Decomposition
UM	Spatially Unevenly distributed Modulated (Colored) noise
UW	Spatially Unevenly distributed White noise

## 12.1 Introduction

Structural dynamics plays a vital role in design and development of variety of structures including civil infrastructure such as buildings and bridges, automotive and aerospace structures, industrial machines etc. Knowledge of dynamic properties of a structure allows for its better design by being able to predict its behavior while in operation. Typically, dynamic characteristics of a structure are described using modal parameters—modal frequency, damping and associated mode shapes.

Operational Modal Analysis is an extension of Experimental Modal Analysis (EMA) [1], the key difference between the two being the fact that OMA does not require input force to be measured. Thus, only output responses are measured and used for modal parameters estimation purposes. The unavailability of knowledge about excitation forces is taken care by a key assumption regarding the nature of these excitation forces. It is assumed that the excitation forces are random in the frequency range of interest and also randomly distributed on the structure in spatial sense [2].

Due to assumptions regarding the excitation force, OMA is best performed in one measurement. However, for many cases, when the structure is large or complex, it becomes too hard to measure all responses simultaneously. In such situations, instead of performing simultaneous measurements, a series of measurements are performed. Each measurement then forms a patch. The task here is to estimate modal parameters of the complete structure from measurements done by means of numerous patches. An engineer is then faced with two options—(1) perform modal parameter estimation on each patch, then combine parameters estimated for individual patches to obtain global parameters, representing the dynamics of the structure (for e.g. Classical approach, PoGER [2, 3]), or (2) combine data from patches and then obtain global modal parameters in one step by performing parameter estimation on patched, or combined, data (for e.g. PreGER [2, 3]).

This paper proposes a Singular Value Decomposition based approach to multi-patch OMA that aims at estimating global modal parameters after combining the data from various patches. The paper is arranged in the following manner: Sect. 12.2 discusses multi-patch OMA in general, along with mathematical fundamentals. Section 12.3 is devoted to the proposed SVD based method and its application is demonstrated by means of analytical and experimental studies in Sect. 12.4. Section 12.5 highlights other useful aspects of this method before concluding the paper with overall perspectives and conclusions.

## 12.2 Multi-Patch OMA

Multi-patch OMA is a scenario where a set of measurement setups (patches) is established and an engineer measures each patch separately until all DOFs are covered. This typically occurs when one is dealing with a large or complex structure, requires high spatial resolution, has limited number of transducers, etc. All multi-patch methods rely on presence of reference sensors during measurements, which are kept at the same location for all patches. These reference sensors provide the basis

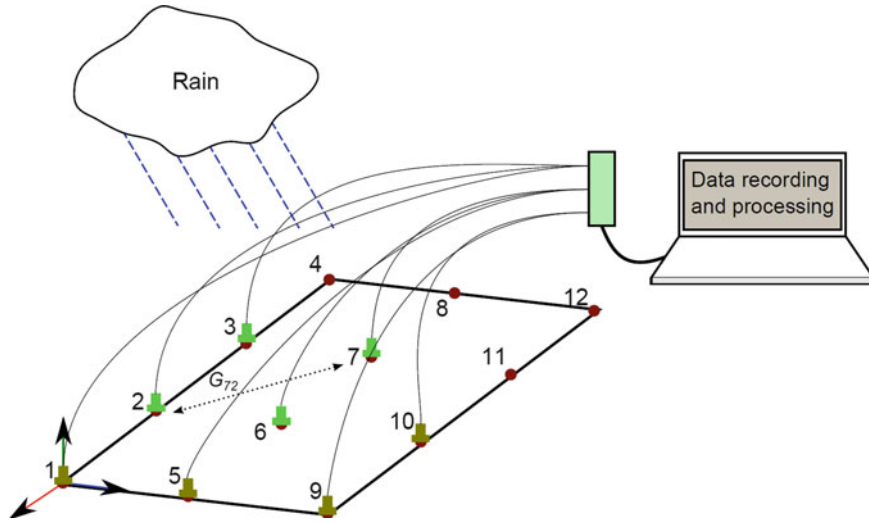


**Fig. 12.1** Schematic of a multi-patch OMA measurement with two patches

for scaling (normalizing) measurements from one patch with respect to another, as they are the common aspect shared by all patches. Another set of sensors, called moving or roving sensors, are moved from one patch to another. Fig. 12.1 shows a multi-patch scenario. The structure is measured in two stages by means of two patches, patch one comprising locations 1, 2, 3, 5, 6, 7, 9 and 10 and another comprising locations 2, 3, 4, 6, 7, 8, 11 and 12. The four sensors in common to each patch (locations 2, 3, 6 and 7) are reference sensors. It should be noted that set up depicted in Fig. 12.1 corresponds to measurement for first patch.

To summarize, the steps for performing multi-patch OMA are as follows:

1. choose reference locations and attach sensors to these locations,
2. attach roving sensors to the patch 1 location,
3. record vibration data,
4. move roving sensors to the next patch location,
5. repeat steps 2–4 until data from all DOFs is recorded.

### 12.2.1 Theoretical Foundations

This section lays down the fundamentals of merging the data acquired in various patches. It also provides the basis of SVD based method explained in Sect. 12.3. In the process, a formal derivation of PreGER method is also developed, which is yet another original contribution of this work.

Equation (12.1) forms the fundamental basis of OMA and allows for output response power spectra to be used for modal parameter estimation purposes [4].

$$\mathbf{G}_{\mathbf{X}\mathbf{X}}(\omega) = \mathbf{H}(\omega) \mathbf{G}_{\mathbf{F}\mathbf{F}}(\omega) \mathbf{H}(\omega)^H \quad (12.1)$$

where  $\mathbf{H}(\omega)$  is FRF matrix of the system, i.e. matrix of individual FRFs for each DOF,  $\mathbf{G}_{\mathbf{X}\mathbf{X}}(\omega)$  is output response power spectra and  $\mathbf{G}_{\mathbf{F}\mathbf{F}}(\omega)$  is the power spectra matrix of the excitation forces, which is unknown. Instead of computing complete power spectra matrix, output power spectra can be computed with respect to only reference sensors. This is given as

$$\mathbf{G}_{\mathbf{X}\mathbf{X}^r}(\omega) = \mathbf{X}(\omega) [\mathbf{X}^{ref}(\omega)]^H \quad (12.2)$$

where  $\mathbf{X}(\omega)$  is the FFT of output response vector  $x(t)$  and  $\mathbf{X}^{ref}$  is the FFT of only reference DOFs output response vector. In case of multi-patch OMA, measurements can be obtained as a set of power spectra matrices  $\mathbf{G}_{\mathbf{X}\mathbf{X}^r}(\omega) \Big|_j$  and  $\mathbf{G}_{\mathbf{X}\mathbf{X}^r}(\omega) \Big|_k$  for

patch  $j$  and  $k$  correspondingly. Note that number of columns of these matrices will be the same, as the same reference DOFs are used. Number of rows, though, can be different, if the amount of sensors in patches  $j$  and  $k$  differ.

Let the FFT of output response vector  $\mathbf{X}_j$  (where  $(\omega)$  is suppressed for conciseness) for patch  $j$  be given by

$$\mathbf{X}_j = \mathbf{H}_j \mathbf{F}_j \quad (12.3)$$

where  $\mathbf{F}_j$  is the FFT of force matrix for patch  $j$ . Similarly, the output response of reference sensors in patch  $j$  can be expressed as

$$\mathbf{X}_j^{ref} = \mathbf{H}_j^{ref} \mathbf{F}_j^{ref} \quad (12.4)$$

where  $\mathbf{H}_j^{ref}$  is FRF matrix for reference DOFs of patch  $j$ . The cross-spectra is calculated as

$$\mathbf{X}_j [\mathbf{X}_j^{ref}]^H = \mathbf{H}_j \mathbf{F}_j [\mathbf{F}_j^{ref}]^H [\mathbf{H}_j^{ref}]^H \quad (12.5)$$

$$\mathbf{G}_{\mathbf{X}\mathbf{X}^r} \Big|_j = \mathbf{H}_j \mathbf{G}_{\mathbf{F}\mathbf{F}^r} \Big|_j [\mathbf{H}_j^{ref}]^H \quad (12.6)$$

which is power spectra of patch  $j$  with respect to reference sensors. In the same way, auto power spectra matrix for reference sensors in patch  $j$  is given by

$$\mathbf{G}_{\mathbf{X}^r\mathbf{X}^r} \Big|_j = \mathbf{H}_j^{ref} \mathbf{G}_{\mathbf{F}^r\mathbf{F}^r} \Big|_j [\mathbf{H}_j^{ref}]^H \quad (12.7)$$

In order to scale  $\mathbf{G}_{\mathbf{X}\mathbf{X}^r} \Big|_j$  to  $\mathbf{G}_{\mathbf{X}\mathbf{X}^r} \Big|_k$  one can imagine that force in patch  $k$  is applied to the patch  $j$ , thus the scaled version of  $\mathbf{G}_{\mathbf{X}\mathbf{X}^r} \Big|_j$  is defined as (Note the change in notation for force power spectra from  $j$  to  $k$ , indicating that applied forces now correspond to those exciting patch  $k$ )

$$\mathbf{G}_{\mathbf{X}\mathbf{X}^r} \Big|_{j \rightarrow k} = \mathbf{H}_{j \rightarrow k} \mathbf{G}_{\mathbf{F}\mathbf{F}^r} \Big|_k [\mathbf{H}_{j \rightarrow k}^{ref}]^H \quad (12.8)$$

and similarly to Eq. (12.7), the reference auto spectra matrix is defined as

$$\mathbf{G}_{\mathbf{X}^r\mathbf{X}^r} \Big|_{j \rightarrow k} = \mathbf{H}_{j \rightarrow k}^{ref} \mathbf{G}_{\mathbf{F}^r\mathbf{F}^r} \Big|_k [\mathbf{H}_{j \rightarrow k}^{ref}]^H \quad (12.9)$$

Assuming time-invariant system, one concludes that  $\mathbf{H}_{j \rightarrow k} = \mathbf{H}_j$  and  $\mathbf{H}_{j \rightarrow k}^{ref} = \mathbf{H}_j^{ref} = \mathbf{H}_k^{ref}$ , i.e. systems dynamic characteristics do not change. With this understanding, it is easy to see that  $\mathbf{G}_{\mathbf{X}\mathbf{X}^r} \Big|_{j \rightarrow k}$  and  $\mathbf{G}_{\mathbf{X}\mathbf{X}^r} \Big|_j$  differ only in the force spectra term (Eqs. (12.6) and (12.8)). The same is also true for the auto spectra of references (Eqs. (12.7) and (12.9)). Note that  $\mathbf{H}_j \neq \mathbf{H}_k$ , because these are FRFs for different DOFs and hence  $\mathbf{H}_{j \rightarrow k} \neq \mathbf{H}_k$ , instead it is same as  $\mathbf{H}_j$  as mentioned before.

If the forces acting on the structure adhere to OMA assumptions, it is valid to assume that the ratio of forces applied to a patch and those applied to the reference DOFs of that patch is constant irrespective of the patch and scale of forcing, and hence remains same.

Using Eqs. (12.6) and (12.7), this ratio is expressed and expanded as

$$\mathbf{G}_{\mathbf{X}\mathbf{X}^r} \Big|_j (\mathbf{G}_{\mathbf{X}^r\mathbf{X}^r} \Big|_j)^{-1} = \mathbf{H}_j \mathbf{F}_j [\mathbf{F}_j^{ref}]^H [\mathbf{H}_j^{ref}]^H \left( [\mathbf{H}_j^{ref}]^H \right)^{-1} \left( [\mathbf{F}_j^{ref}]^H \right)^{-1} (\mathbf{F}_j^{ref})^{-1} (\mathbf{H}_j^{ref})^{-1} = \mathbf{H}_j \mathbf{F}_j (\mathbf{F}_j^{ref})^{-1} (\mathbf{H}_j^{ref})^{-1} \quad (12.10)$$

Similarly, using Eqs. (12.8) and (12.9) for the scaled version of patch  $j$

$$\mathbf{G}_{\mathbf{X}\mathbf{X}^r} \Big|_{j \rightarrow k} (\mathbf{G}_{\mathbf{X}^r\mathbf{X}^r} \Big|_{j \rightarrow k})^{-1} = \mathbf{H}_{j \rightarrow k} \mathbf{F}_{j \rightarrow k} (\mathbf{F}_{j \rightarrow k}^{ref})^{-1} (\mathbf{H}_{j \rightarrow k}^{ref})^{-1} \quad (12.11)$$

Since  $\mathbf{H}_{j \rightarrow k} = \mathbf{H}_j$  and  $\mathbf{H}_{j \rightarrow k}^{ref} = \mathbf{H}_j^{ref}$ , the only difference in Eqs. (12.10) and (12.11) is due to different forcing terms. However, as explained, the ratio between forces acting on the structure and those acting at reference DOFs should remain constant and hence Eqs. (12.10) and (12.11) are equal. This can be explained mathematically as follows.

Let the relationship between forces acting on patch  $j$  and patch  $k$  be expressed by means of a scaling factor  $c$ , such that

$$\mathbf{F}_{j \rightarrow k} = c\mathbf{F}_j \text{ and } \mathbf{F}_{j \rightarrow k}^{ref} = c\mathbf{F}_j^{ref} \quad (12.12)$$

If such a relationship exists, Eqs. (12.10) and (12.11) are equal, as

$$\mathbf{F}_{j \rightarrow k} \left( \mathbf{F}_{j \rightarrow k}^{ref} \right)^{-1} = c\mathbf{F}_j \left( c\mathbf{F}_j^{ref} \right)^{-1} = \mathbf{F}_j \left( \mathbf{F}_j^{ref} \right)^{-1} \quad (12.13)$$

Note that constant  $c$  may not be scalar, it can also be a matrix and in most cases a function of frequency. For simplicity, though,  $c$  is regarded as a scalar here. This relationship between excitation forces acting on various patches provide the inspiration for estimating the scaling factor describing this relationship in different ways. This is the basis of different scaling approaches suggested in this work and explained in Sect. 12.3.2.

Remembering that  $\mathbf{H}_{j \rightarrow k}^{ref} = \mathbf{H}_k^{ref}$ , from Eq. (12.8) one makes a conclusion that

$$\mathbf{G}_{\mathbf{X}^r \mathbf{X}^r} \Big|_{j \rightarrow k} = \mathbf{H}_k^{ref} \mathbf{G}_{\mathbf{F}^r \mathbf{F}^r} \Big|_k \left( \mathbf{H}_k^{ref} \right)^H = \mathbf{G}_{\mathbf{X}^r \mathbf{X}^r} \Big|_k \quad (12.14)$$

Once again using Eqs. (12.10) and (12.11) and replacing  $\mathbf{G}_{\mathbf{X}^r \mathbf{X}^r} \Big|_{j \rightarrow k}$  with  $\mathbf{G}_{\mathbf{X}^r \mathbf{X}^r} \Big|_k$  one obtains

$$\mathbf{G}_{\mathbf{X} \mathbf{X}^r} \Big|_j \left( \mathbf{G}_{\mathbf{X}^r \mathbf{X}^r} \Big|_j \right)^{-1} = \mathbf{G}_{\mathbf{X} \mathbf{X}^r} \Big|_{j \rightarrow k} \left( \mathbf{G}_{\mathbf{X}^r \mathbf{X}^r} \Big|_k \right)^{-1} \quad (12.15)$$

Since  $\mathbf{G}_{\mathbf{X} \mathbf{X}^r} \Big|_j$ ,  $\mathbf{G}_{\mathbf{X}^r \mathbf{X}^r} \Big|_j$  and  $\mathbf{G}_{\mathbf{X}^r \mathbf{X}^r} \Big|_k$  are power spectra calculated directly from the data measured in patches  $j$  and  $k$ , one can now calculate  $\mathbf{G}_{\mathbf{X} \mathbf{X}^r} \Big|_{j \rightarrow k}$  i.e. scaled version of patch  $j$  with respect to forcing conditions in patch  $k$  using following equation.

$$\mathbf{G}_{\mathbf{X} \mathbf{X}^r} \Big|_{j \rightarrow k} = \mathbf{G}_{\mathbf{X} \mathbf{X}^r} \Big|_j \left( \mathbf{G}_{\mathbf{X}^r \mathbf{X}^r} \Big|_j \right)^{-1} \mathbf{G}_{\mathbf{X}^r \mathbf{X}^r} \Big|_k \quad (12.16)$$

Above discussion and derivation provides theoretical basis of the SVD based method developed in this paper, and is discussed in next section. Further, it turns out Eq. (12.16) is an equivalent expression for PreGER patching method. Reference [3], which mentions PreGER, only provides the Eq. (12.16) without any formal derivation of the same and to authors knowledge, such derivation is not available elsewhere either. In this sense, the derivation provided here provides a concrete proof and basis of PreGER based global scaling approach for OMA and is an original contribution of this work.

## 12.3 Singular Value Decomposition Based Patching Methodology

Based on mathematical understanding developed in Sect. 12.2.1, a singular value decomposition (SVD) based approach for combining various patches in a multi-patch OMA scenario is introduced in this section. First the mathematical details of this method are presented and then various scaling approaches that this method enables are discussed.

### 12.3.1 Mathematical Formulation

The power spectra terms in Eq. (12.16) can be decomposed using SVD in following manner

$$\mathbf{U} \Big|_{j \rightarrow k} \mathbf{S} \Big|_{j \rightarrow k} \mathbf{V}' \Big|_{j \rightarrow k} = \mathbf{U}_j \mathbf{S}_j \mathbf{V}_j' \left( \mathbf{U}_j^{ref} \mathbf{S}_j^{ref} \left( \mathbf{V}_j^{ref} \right)' \right)^{-1} \mathbf{U}_k^{ref} \mathbf{S}_k^{ref} \left( \mathbf{V}_k^{ref} \right)' \quad (12.17)$$

which gives

$$U|_{j \rightarrow k} S|_{j \rightarrow k} V'|_{j \rightarrow k} = U_j S_j V_j' \left( (V_j^{ref})' \right)^{-1} (S_j^{ref})^{-1} (U_j^{ref})^{-1} U_k^{ref} S_k^{ref} (V_k^{ref})' \quad (12.18)$$

At this point it is possible to assume that  $U_j^{ref} = U_k^{ref}$ ,  $V_j^{ref} = V_k^{ref}$  and also  $V_j = V_j^{ref}$  and  $V_k = V_k^{ref}$ , due to orthonormal nature of these matrices. Physically it can be explained by the fact that system characteristics do not change between measurement setups. This is similar to the assumption made in Sect. 12.2.1 that  $\mathbf{H}_{j \rightarrow k} = \mathbf{H}_j$  and so on. In light of this, Eq. (12.18) simplifies to

$$U|_{j \rightarrow k} S|_{j \rightarrow k} V'|_{j \rightarrow k} = U_j S_j (S_j^{ref})^{-1} S_k^{ref} V_j' \quad (12.19)$$

where  $(S_j^{ref})^{-1} S_k^{ref} \equiv k$ —scaling factor as diagonal square matrix. Thus scaled version of patch  $j$  can be written in terms of its singular values and vectors and a scaling matrix  $k$  as:

$$\mathbf{G}_{XX^r}|_{j \rightarrow k} = U_j k S_j V_j' \quad (12.20)$$

Due to various factors such as measurement noise etc., it is possible that singular vectors  $U$  in practice might not be the same between patches, at least not for all frequencies. However, it is expected that this method will help minimizing the associated errors by calculating an optimal scaling matrix.

### 12.3.2 Scaling Approaches

Before discussing the scaling approaches, it is important to restate that equations developed in Sects. 12.2.1 and 12.3.1 are functions of frequency  $\omega$ . One can perform scaling for each frequency (locally) or obtain a single scaling factor for all frequencies (globally). As discussed in previous section, the scaling approaches described here seek to explain the relationship between excitation forces acting on the two patches. Discussions regarding Eqs. (12.10)–(12.15) suggest that a scaling factor varying with frequency might be a good approach. This forms the basis for the first scaling approach, termed as local scaling. It is also possible to identify a single scaling factor representing the entire frequency range, because if the excitation forces adhere to OMA assumptions, being random and flat in frequency range of interest, they should only differ in magnitude. This difference can be accounted for by a single scaling factor and this reasoning forms the basis of second scaling approach suggested here and termed as global scaling. The third approach suggested here is another version of global scaling, where instead of using information coming from entire frequency range, only a subset of frequencies is chosen. This approach is termed as global filtered scaling. Thus, the three different scaling approaches explored in this paper are

1. Local scaling ( $k_1(\omega)$ )—Scaling factor for each frequency
2. Global scaling ( $k_2$ )—A common scaling factor for all frequencies
3. Global filtered scaling ( $k_3$ )—Scaling factor based on all frequencies where first singular vectors of the two patches are similar. The similarity is calculated by means of Modal Assurance Criteria (MAC) [1].

It should be noted that in the discussion to follow, the singular value matrix  $S$  is represented as a vector of its diagonal values.

#### (a) Local scaling ( $k_1(\omega)$ )

The most straightforward way to re-scale  $S_j$  to fit  $S_k$  is to find a scaling factor  $k$  for each frequency. Factor  $k$  is found as a vector  $1 \times N^{ref}$  for each frequency by

$$k_1(\omega) = S_k(\omega) \bullet (S_j(\omega))^{-1} \quad (12.21)$$

where  $\bullet$  means element-wise operation, i.e. vector  $S_k$  is being divided by  $S_j$  element by element for each frequency.



(b) Global scaling ( $k_2$ )

For calculating  $k_2$ , the Least Squares approach is utilized and the scaling factor is calculated as

$$s_{[k,n]}(\omega) = k_{2,n} s_{[j,n]}(\omega) + \varepsilon(\omega) \quad (12.22)$$

where  $n$  is the index for singular value and  $j$  denotes the measurement index (patch);  $s$  is a single singular value from  $S$ . To find one scalar  $k$  that satisfies this equation by minimizing the error term, a pseudo-inverse for vector  $s_{[j,n]}$  is used, so

$$k_2 = s_{[j,n]}(\omega)^+ s_{[k,n]}(\omega) \quad (12.23)$$

which results in a scalar vector  $N^{ref} \times 1$ . Scaling vector  $k_2$  is constant for all frequencies and individual for each singular value line in vector  $S(\omega)$ . It should be noted that the reasoning behind this scaling approach might not hold in practice due to noise and other factors, but it is hoped that finding this global scaling factor in a least squares manner might provide an optimal estimate in such cases. Yet another aspect worth pointing out is that computation wise, it is faster to compute global scaling factor than local scaling factor and hence it is felt that it is worth developing this idea and compare its performance with local scaling approach.

(c) Global filtered scaling ( $k_3$ )

The final approach described in this section is also based on Eq. (12.23). However, a frequency filtering technique is used to select those frequencies that will theoretically provide the most accurate scaling factor  $k$ . Instead of arrays that are of size  $N_f$  (number of frequency lines), as the result of filtering the size of arrays will be  $N_{ff}$  values long, where  $N_{ff}$  denotes number of filtered frequency lines.

This approach is similar to global scaling approach, but instead of using all frequencies  $\omega$  only those  $\omega_f$  are selected, where singular vectors are similar between patches. Physically this means that the algorithm is looking for matching operational deflection shapes, or mode shapes, in reference DOFs between different patches. The expression for third scaling method is given by

$$k_3 = s_{[j,n]}(\omega_f)^+ s_{[k,n]}(\omega_f) \quad (12.24)$$

The procedure for selecting  $\omega_f$  is following. One takes singular vectors of the two patches,  $U_j^{ref}$  and  $U_k^{ref}$  and checks their similarity for each frequency by using Modal Assurance Criterion (MAC) [1]:

$$\text{MAC} \left( U_j^{ref}, U_k^{ref} \right)_\omega = \frac{\left| U_j^{ref} (U_k^{ref})^* \right|^2}{\left( U_j^{ref} (U_j^{ref})^* \right) \left( U_k^{ref} (U_k^{ref})^* \right)} \quad (12.25)$$

The result is a matrix of MAC values, representing similarity between all singular vectors. It is more important to have first singular vectors, i.e. first column vector of  $U^{ref}$  being similar than others, because these are the ones represented with the most energy, as their corresponding singular values  $s$  have the highest value in  $S$  matrix. So only the first MAC value is looked at. Those frequencies  $\omega$  that have MAC value higher than 0.95 are selected and stored as a new frequency vector  $\omega_f$ . The value 0.95 is selected based on empirical common sense and experience of engineers from the field of modal analysis.

### 12.3.3 Method Summary

To recap, here is an overview of the overall procedure. In order to patch together two measurements  $j$  and  $k$ , having the same reference DOFs, one obtains power spectra matrices for these patches— $\mathbf{G}_{\text{XX}^r}|_j$  and  $\mathbf{G}_{\text{XX}^r}|_k$ . These matrices are decomposed using singular value decomposition to get singular values  $S_j$  and  $S_k$ , which are then used for calculating one of the three scaling factors. Now Eq. (12.20) can be used to obtain a scaled version of patch  $j$   $\mathbf{G}_{\text{XX}^r}|_{j \rightarrow k}$ . After that, one simply builds a new matrix  $\mathbf{G}_{\text{XX}^r}$  that represents the whole system by combining  $\mathbf{G}_{\text{XX}^r}|_{j \rightarrow k}$  with  $\mathbf{G}_{\text{XX}^r}|_k$ . With  $\mathbf{G}_{\text{XX}^r}$ , it is possible to estimate modal parameters using any desired technique. Figure 12.2 gives a visual overview of the SVD based method.

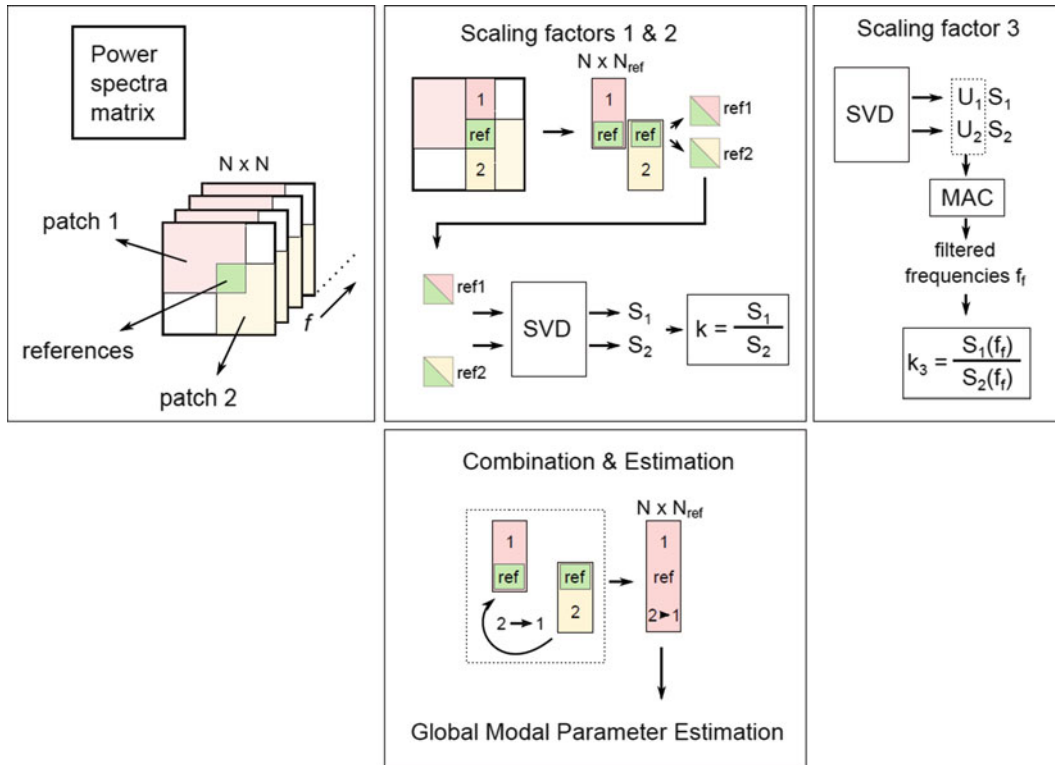


Fig. 12.2 Flow chart for SVD based patching method

## 12.4 Experiments

The performance of suggested SVD based method is studied by means of an analytical and an experimental system. Each system is excited and measured completely twice, using uncorrelated forces. One of the two obtained full power spectra is chosen to be baseline. From these measurements, two patches are formed. The patches are rescaled and combined. Finally, modal parameters are estimated using SSI-covariance [5, 6] algorithm for both baseline and rescaled power spectra matrix. The results are presented in terms of stability diagram [7] and table of estimated modal parameters. To evaluate and compare the stability diagrams, a criteria termed as *Stability Diagram Evaluation Coefficient* is developed, whose details are also explained in this section.

### 12.4.1 Studies on Analytical System

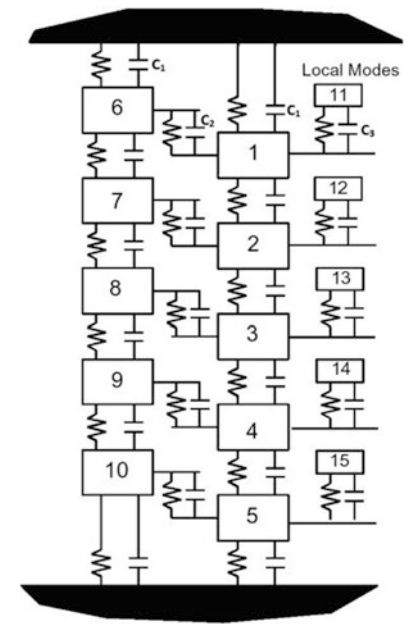
#### 12.4.1.1 Description of the System and Simulations

A 15 DOF system, as shown in the Fig. 12.3, is used for this study and four different forcing scenarios are explored as listed below.

- evenly spatially distributed white noise (even white—EW),
- unevenly spatially distributed white noise (uneven white—UW),
- evenly distributed frequency modulated (colored) noise (even modulated—EM),
- unevenly distributed frequency modulated (colored) noise (uneven modulated—UM)

Additionally, the robustness of the method is examined by means of noise related studies. For this, noise is added to evenly distributed white noise (EW) case using SNR values of  $-10$ ,  $0$ ,  $10$ ,  $20$ ,  $30$  and  $40$  dB. Thus, a total of ten forcing scenarios are considered. It is worth noting that only EW case is the one that fully satisfies OMA assumptions with respect to unmeasured input excitation. Further, in all these studies, DOFs 9, 10, 11 and 12 are chosen as reference DOFs.

**Fig. 12.3** 15 DOF analytical system



The sampling rate of output responses is 1024 Hz. The power spectra matrices are formed using periodogram approach, with Hanning windows and 66% overlap, window width being 1 s. Power spectra matrices are rescaled if needed and then transformed into covariance matrices  $R$ , which are used in SSI-Cov estimation algorithm.

#### 12.4.1.2 Results and Discussion

This section showcases interesting results from the studies carried out on the analytical system. For complete results, the reader is advised to refer [8].

##### Even White (EW) Case

In order to examine and compare the suggested scaling approaches in the EW case, the system is excited two times, each time with different force magnitudes. The collected output responses are processed to obtain complete  $(15 \times 15)$  power spectra matrices. Since 4 DOFs are chosen as reference DOFs, these two matrices are segregated such that one obtains a  $12 \times 4$  power spectra matrix,  $G_{XX}^r|_1$  corresponding to first force excitation and  $7 \times 4$  power spectra matrix,  $G_{XX}^r|_2$  for second. Matrices  $G_{XX}^r|_1$  and  $G_{XX}^r|_2$  represent the measurements from two different patches having four reference DOFs (DOFs 9–12) in common. Note that first patch has DOFs 1–12 and second patch comprises of DOFs 9–15.

Figure 12.4 shows comparison of first singular vectors corresponding to reference DOFs by means of MAC. This plot is obtained by performing SVD on  $4 \times 4$  power spectra matrices of reference DOFs corresponding to two patches and comparing first singular vectors using MAC. The SVD is performed on frequency by frequency basis to obtain the variation across the entire range. Additionally, the variation of all four singular values for one of the patches is also shown in background, as it helps in identifying the location of potential modes (peaks in the singular value plot). For clear representation, frequencies, where MAC value is higher than 0.95, are highlighted with red vertical lines. From Fig. 12.4, it is seen that red vertical lines practically cover the frequencies where modes have sufficient energy. This implies that for even white case with no added noise, similarity between first singular column vectors from two patches is high.

Scaling factors  $k_1$ ,  $k_2$  and  $k_3$  are plotted together in Fig. 12.5. It should be noted that by definition only  $k_1$  is a function of frequency, others are constant. All scaling factors for all SVD lines are approximately 120 dB, which is the squared difference between two applied forces in this case. In some sense, this provides a good validation of the suggested approach as one expects the scaling factor to be related to the ratio of the magnitude of the forces acting on the two patches. The deviation of  $k_1$  is quite small, not exceeding 1 dB. Global scaling factors  $k_2$  and  $k_3$  are almost identical. Due to this reason, stability diagrams of power spectra matrices obtained using global scaling are almost the same, as well as their modal parameters (see Table 12.1 for estimated modal parameters). It is rather challenging to objectively evaluate the difference

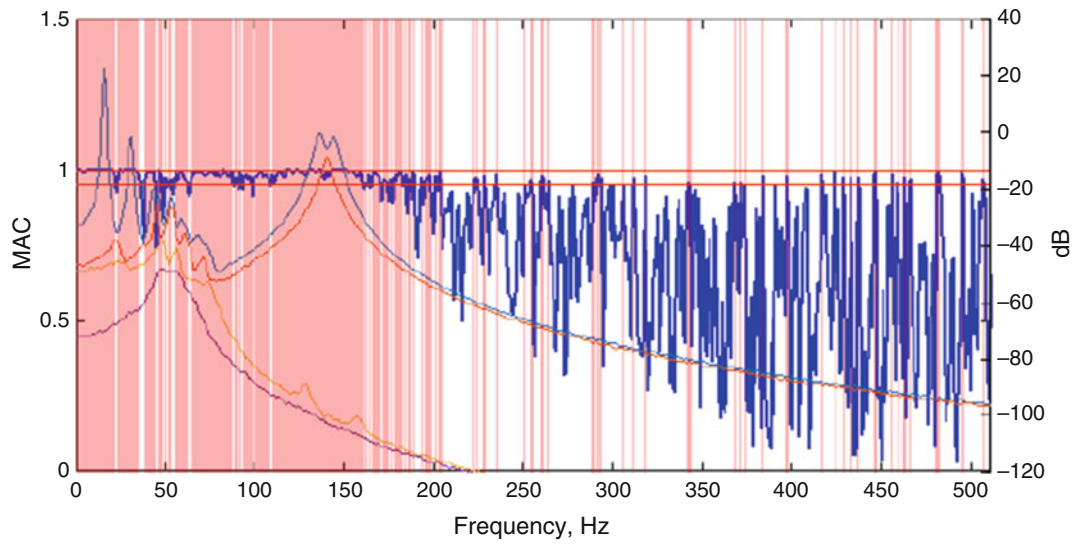


Fig. 12.4 MAC plot for EW case

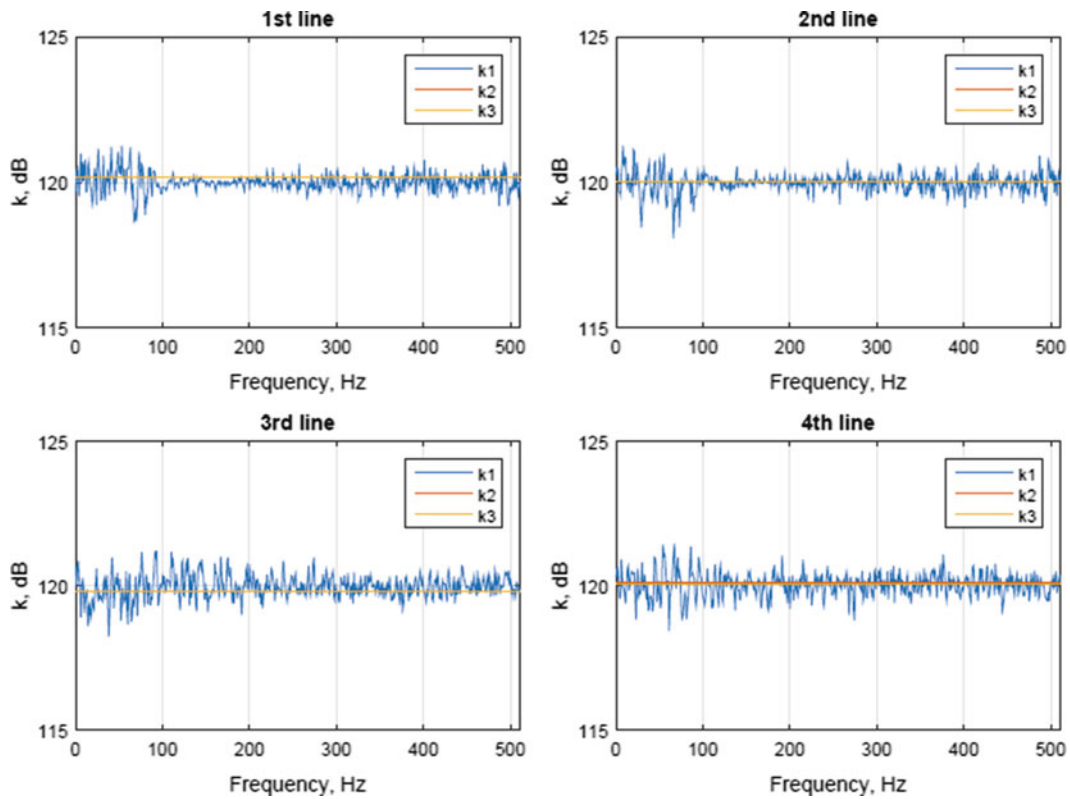


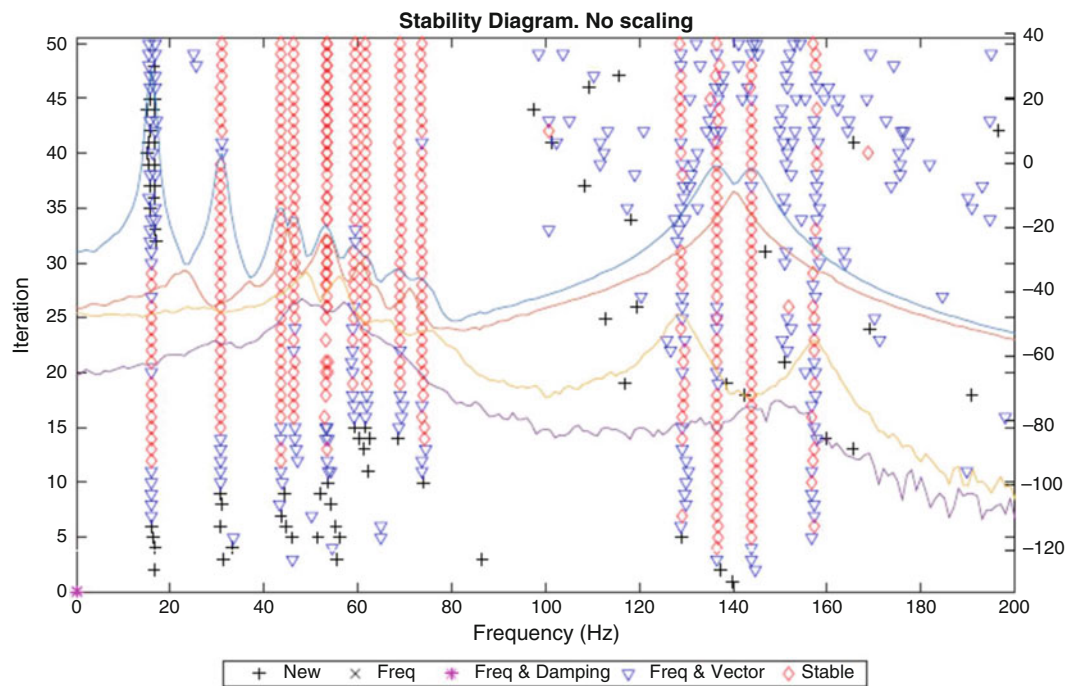
Fig. 12.5 Scaling factors for each SVD line

in estimation quality between baseline and rescaled matrices from table of modal parameters, so a measure termed Stability Diagram Evaluation Coefficient (SDEC) is developed and introduced later for comparison of modal parameter estimation quality.

Figure 12.6, shows the baseline stability diagram corresponding to one of the force excitations. As mentioned earlier, the system is excited completely by two different force realizations and hence it is possible to choose any one of the scenarios and draw a stabilization diagram using  $15 \times 4$  power spectra matrix (power spectra of all DOFs with respect to four reference

**Table 12.1** Modal parameters estimated for patched power spectra matrices using different scaling methods

No.	Baseline		$k_1$		$k_2$		$k_3$	
	f (Hz)	$\zeta$ (%)	f (Hz)	$\zeta$ (%)	f (Hz)	$\zeta$ (%)	f (Hz)	$\zeta$ (%)
1	15.99	1.14	15.99	1.12	16	1.14	16	1.13
2	30.84	2.19	30.8	2.16	30.77	2.18	30.77	2.18
3	43.59	2.71	43.54	2.9	43.55	2.87	43.55	2.87
4	46.37	3.19	46.59	2.86	46.61	2.91	46.61	2.91
5	53.51	3.52	53.4	3.7	53.4	3.72	53.4	3.72
6	53.51	3.52	53.4	3.7	53.4	3.72	53.4	3.72
7	59.2	3.89	59.27	3.85	59.21	3.92	59.21	3.92
8	61.7	3.89	61.8	4.04	61.79	4.17	61.79	4.17
9	68.96	4.87	69.16	4.57	69.18	4.78	69.18	4.77
10	73.78	4.34	73.53	4.49	73.46	4.57	73.46	4.57
11	128.81	2.82	128.88	2.69	128.91	2.75	128.91	2.75
12	136.48	2.45	136.51	2.48	136.55	2.47	136.55	2.47
13	143.88	2.36	143.84	2.35	143.88	2.35	143.88	2.35
14								
15	157.91	2.19	157.64	2.26	157.44	2.25	157.44	2.25

**Fig. 12.6** Stability diagram for baseline matrix for EW case

DOFs). The stability diagram for the patched  $15 \times 4$  power spectra matrix using local scaling factor  $k_1$  is shown in Fig. 12.7. As can be seen, overall estimation result is quite close to baseline stability diagram of Fig. 12.6.

### Uneven Modulated (UM) Case

Next the case of spatially uneven modulated white noise excitation (UM) scenario is considered. In this scenario, the OMA assumptions regarding the nature of excitation are violated in both temporal and spatial sense. Excitation is modulated in frequency and is unevenly distributed in spatial sense instead of being uniformly distributed. The modulated nature of a force spectrum is shown in Fig. 12.8, which shows the force modulation used while exciting the two patches. With regards

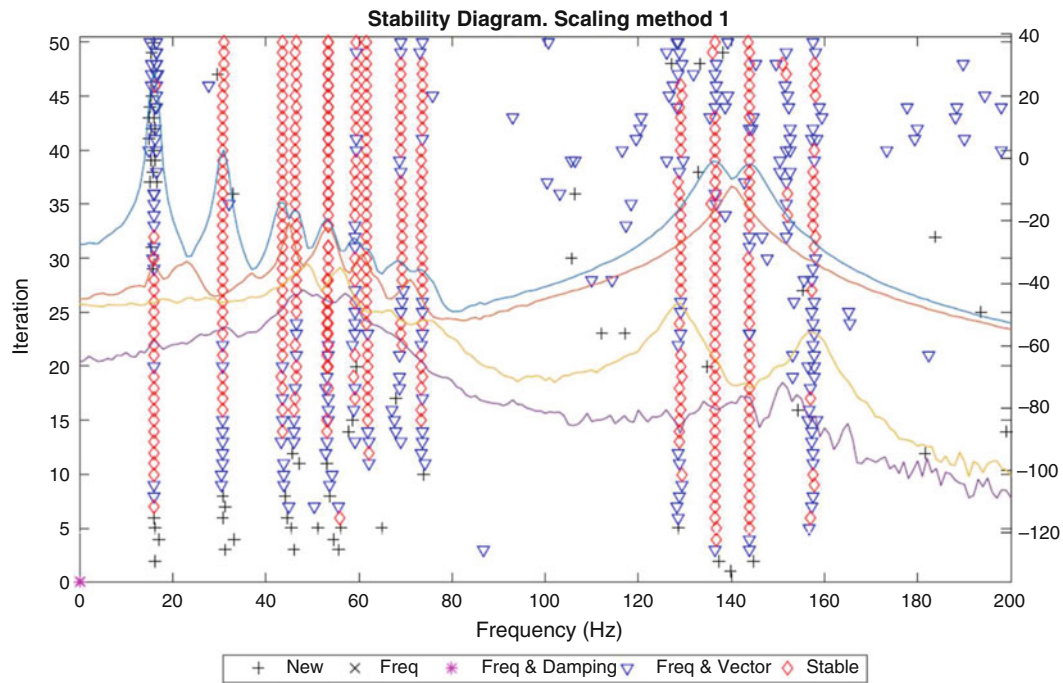


**Fig. 12.7** Stability diagram for multi-patch matrix using first scaling approach

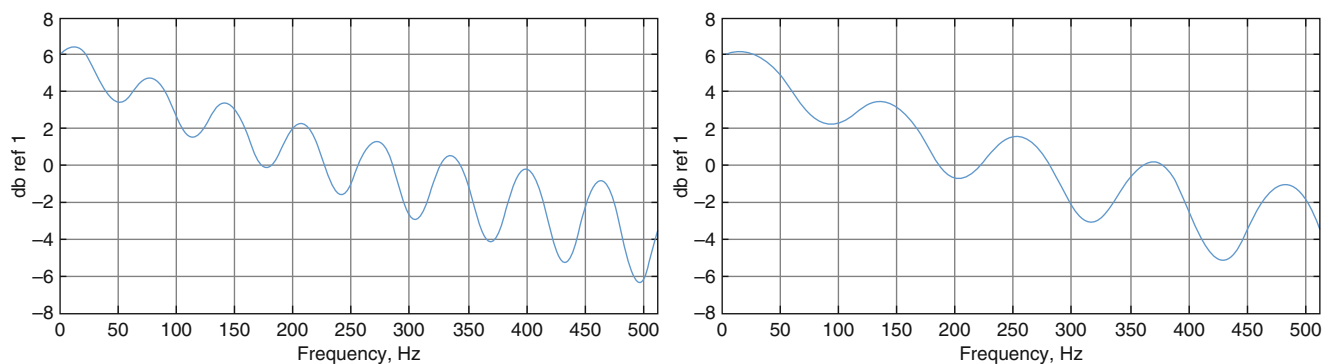


**Fig. 12.8** Force spectra envelope,  $-10$  dB decay over full frequency region, with sine shape modulation of 1–5 dB

to spatial distribution of forces, a force strength factor is introduced, which is a number between 0.2 and 1 indicating the strength of the force signal. This factor is multiplied to the force signal before using it for exciting the system. In EW case the forces act with full strength on all DOFs, thus force strength is one. In UM and UW case however, the force strength factor varies between 0.2 and 1 in random manner. This creates a scenario where all DOFs are not being excited evenly or equally and hence the forcing is labeled uneven.

As can be seen from MAC plot in Fig. 12.9, the  $U$  vectors from the two patches match only for certain frequencies, not even covering all the modes indicated by the SVD plot. This can be due to several reasons such as changes in the system (not the case here) or modes not getting sufficiently excited (more likely the case here). In this scenario, Fig. 12.9 provides a very good indication that the measurements across the reference DOFs in two patches are not correlated enough to do patching in a satisfactory manner. In this sense, the MAC plot proves to be a valuable tool to investigate whether excitations in various patches are adhering to OMA assumptions or not, a fact that is very critical from modal parameter estimation perspective.

Figure 12.10, plot of scaling factors, indirectly shows the difference in forces between two patches. It deviates with a range of up to 20 dB for different frequencies (ideally, like EW case, should be constant throughout the spectrum). As a result, modal parameter estimation quality from patched power spectra matrix suffers. Typically, it is not known beforehand, whether the excitation follows OMA assumptions or not and hence it is difficult to analyze the performance of modal parameter estimation procedure from the excitation conditions point of view. The local scaling method thus provides a way



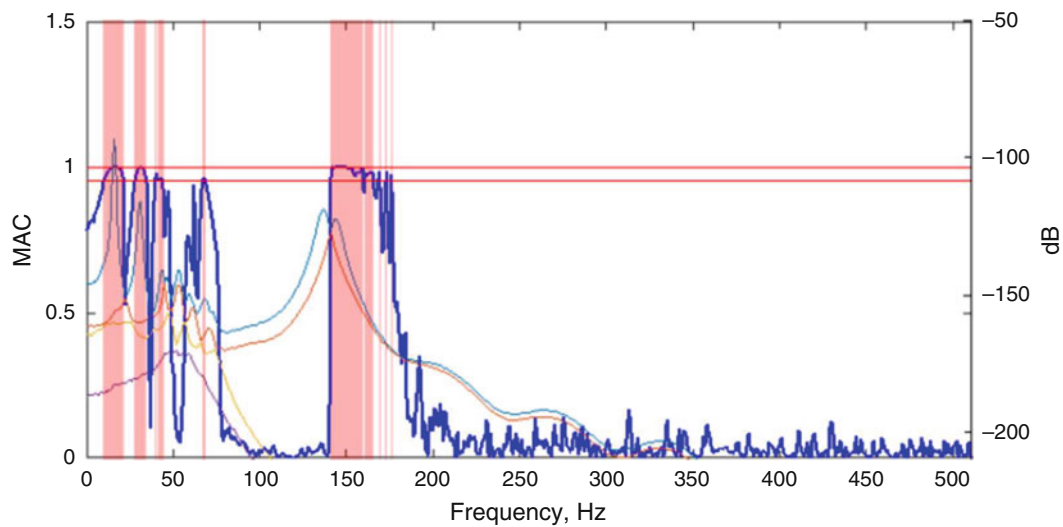


Fig. 12.9 Plot of MAC values as a function of frequency for UM case

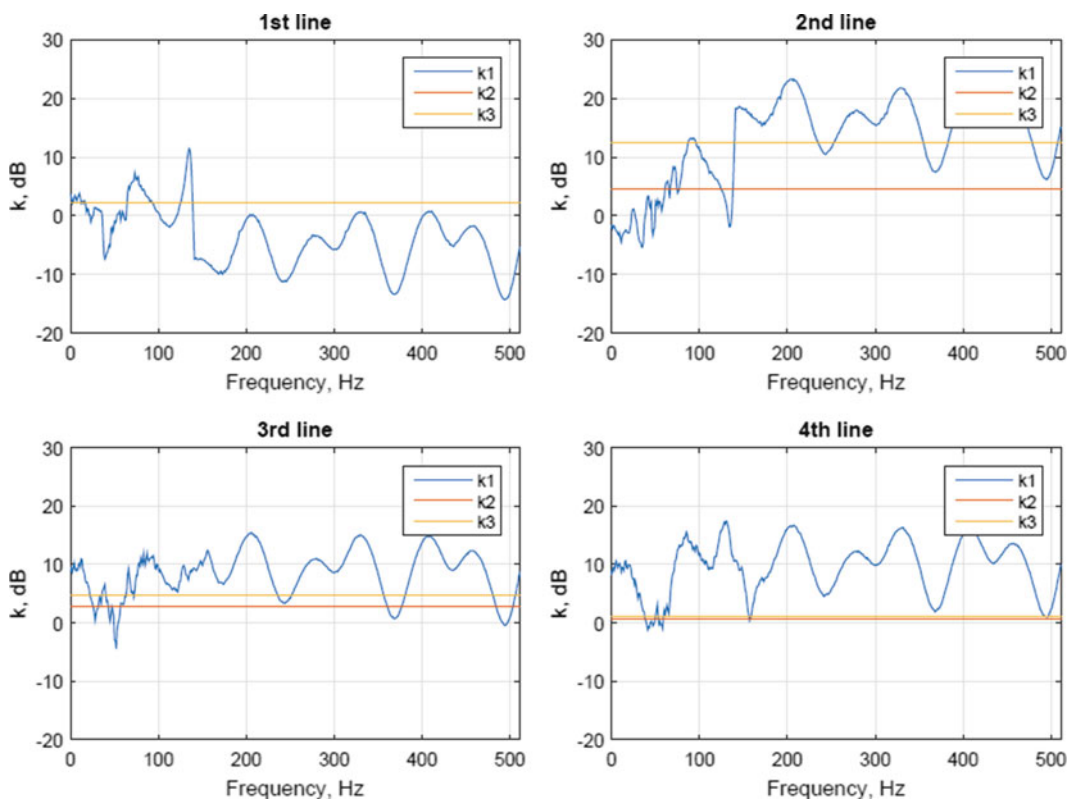


Fig. 12.10 Scaling factors between  $G_{XX^r}|_1$  and  $G_{XX^r}|_2$  for UM case

to indirectly analyze the excitation conditions and helps in evaluating the same in terms of whether the excitation related basic OMA assumptions are being fulfilled or not. This, of course would require user experience and reason to evaluate, whether the excitation difference is satisfactory, or whether the measurement for a patch should be redone. Perhaps, it might be a good idea in these situations to use classical approach of merging the patches, i.e. obtain modal parameters for individual patches and combine them later.

Finally, Figs. 12.11 and 12.12 show stability diagrams for the baseline and patched scenario using local scaling factor  $k_1$ . As one can see, the quality of modal parameter estimation for baseline is higher than for patched matrix.



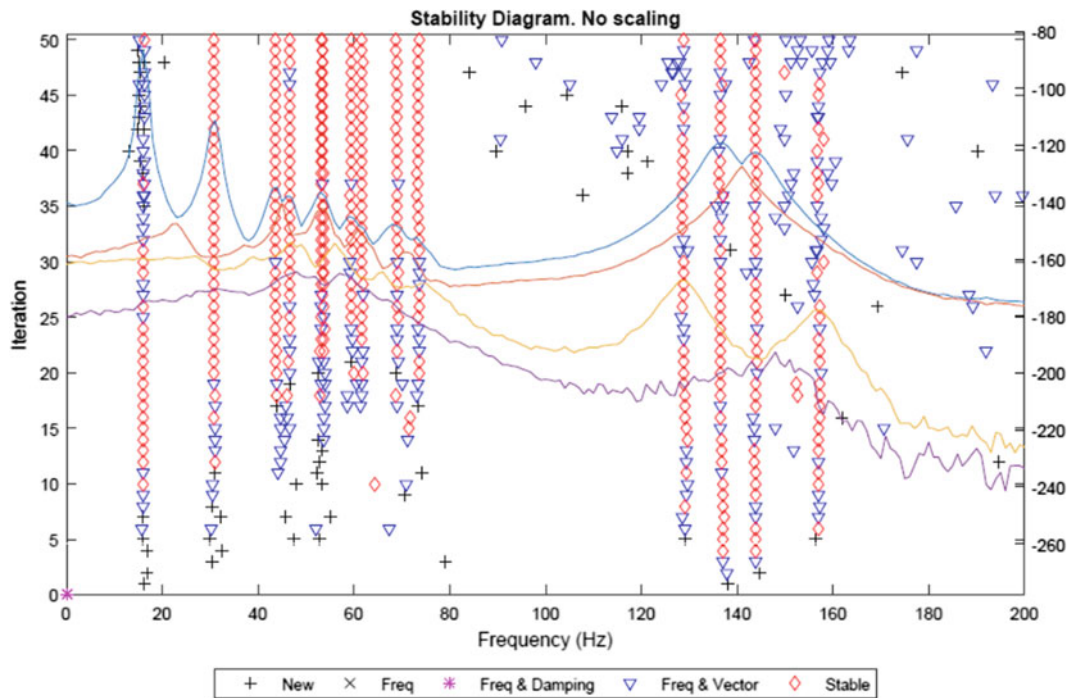


Fig. 12.11 Stability diagram for baseline matrix for Uneven Modulated case

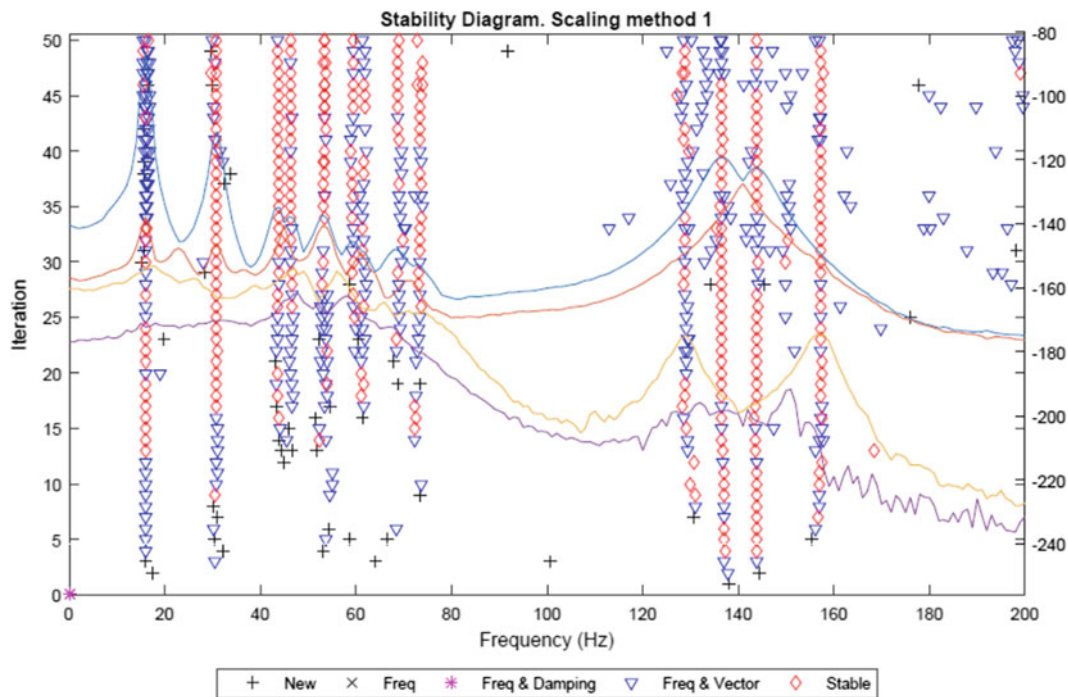


Fig. 12.12 Stability diagram for multi-patch matrix using first scaling approach for Uneven Modulated case

Stability Diagram Evaluation Coefficient (SDEC)

The comparison done in previous section is subjective in nature. In order to develop an objective assessment of the performance of SVD based patching procedure a tool called Stability Diagram Evaluation Coefficient (SDEC) is developed. This tool also provides a means to compare various scaling approaches under all ten scenarios (various excitation conditions and added noise).

In order to calculate SDEC for a given Stability Diagram, one takes the normalized number of stable modes  $\bar{N}_{tot}$ , standard deviation of frequency  $\sigma_f$  and damping  $\sigma_\xi$  and combines these parameters using the following expression

$$\text{SDEC}_g = \bar{N}_{tot} (1 - \sigma_f) \left(1 - \frac{\sigma_\xi}{100}\right) \quad (12.26)$$

which gives us single number from 0 to 1 that indicates how well the estimation is performed. This number can be obtained for the whole stability diagram (global SDEC<sub>g</sub>) or for individual modes (local SDEC<sub>l</sub>). Normalized number of stable modes is obtained by counting the total number of estimated stable modes for all model orders and then normalizing it to the maximum possible number of estimated modes for given stability diagram. This obviously requires prior knowledge about how many modes are there in the system.

The estimated frequency and damping differs between estimated modal models in stability diagram. This difference is expressed in standard deviation in percent and used for SDEC calculation. There should be a reference value for frequency and damping, around which the deviation is happening. This reference value can be for e.g. average value between all stable modal models. Frequency standard deviation is limited by 1%, because if it is more than 1% than the estimated models can be considered rather different and might not be estimating the same physical mode. That is why models with frequency deviating more than 1% from a reference value are not taken into account when calculating SDEC. The damping standard deviation is not limited and can be any value expressed in percent, which is then normalized by 100 as shown in Eq. (12.26). Damping deviation between models higher than 100% will result in a negative SDEC which will imply low quality of estimation of the given mode.

Figure 12.13 shows a comparison of SDEC for different scaling approaches with baseline reference. Several important observations can be inferred from this plot as listed below.

- The SDEC for patched and baseline is comparable for spatially even excitation cases irrespective of whether excitation is white or modulated. There is an understandable decrease in overall quality for the modulated case but it is similar to that observed in baseline scenario.
- Patching suffers greatly when OMA assumptions are not adhered. This is evident in case of both uneven excitation scenarios where SDEC for patched data is significantly lower than baseline reference.

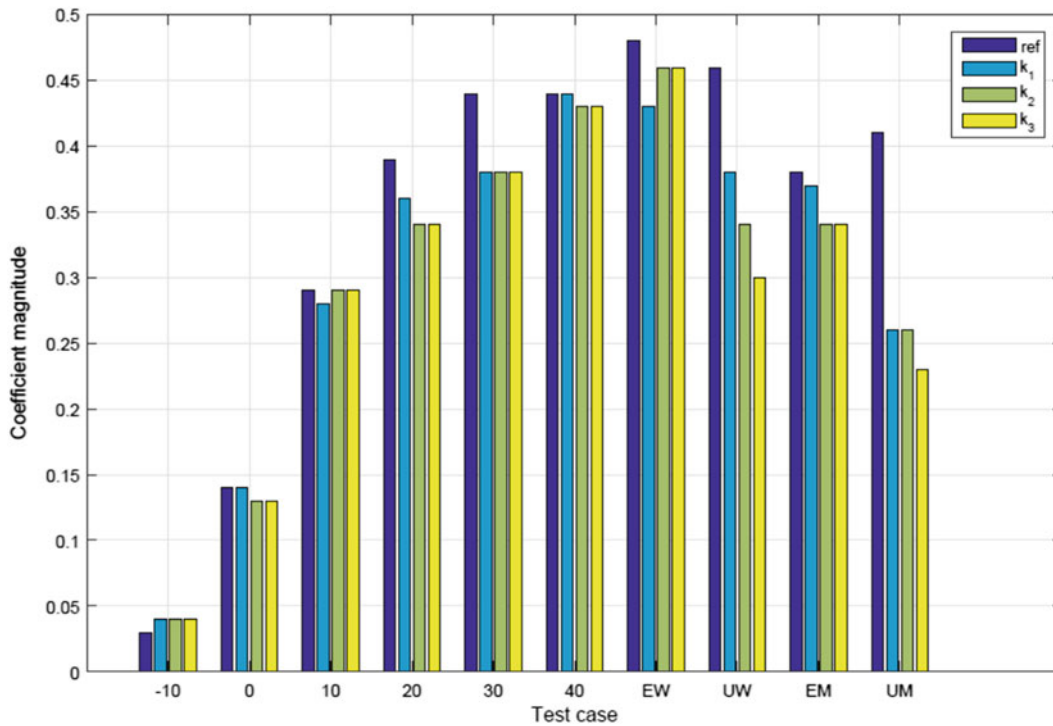


Fig. 12.13 Total SDEC values of stability diagrams for all test cases

**Table 12.2** Averaged total SDEC values between all ten cases

Method	Baseline	$k_1$	$k_2$	$k_3$
SDEC	0.35	0.31	0.30	0.29

- c. Quality of modal parameter estimation suffers, in general, when OMA assumptions are not adhered. SDEC for all excitation cases where OMA assumptions are violated (all scenarios except EW) is lower in comparison, even for baseline. This signifies an overall decrease in terms of quality of parameter estimation procedure.
- d. Results from noise related study on EW scenario are on expected line. The quality of parameter estimation procedure decreases as SNR is reduced. However, a good agreement between SDEC for baseline and patched data shows that when OMA assumptions are adhered, the suggested SVD based patching approach works satisfactorily.

By looking at the Table 12.2 one can see that first scaling approach  $k_1$  (local scaling) gives slightly higher SDEC value than global or global filtered scaling. In general, the performance of local scaling approach has been better in comparison to the other two approaches. As mentioned in Sect. 12.3.2, this is on expected lines and it can be suggested on the basis of these results that local scaling approach should be preferred over other two approaches.

## 12.4.2 Studies on a Steel Plate

### 12.4.2.1 Experiment Design

This section presents the results from experiments on a real steel plate, shown in Fig. 12.14. The plate is 60 cm long, 36 cm wide and 2 mm thick. It rests on soft pads that are in contact with the bottom side of the plate. The contact area is only around 10% of the plates area, so the plate is lightly damped. The soft pads further rest on a soft slab to damp vibration from the table and floor.

#### Excitation

Forces in OMA are assumed to be uncorrelated white noise. To simulate this, the plate is excited by hitting the plate randomly in vertical direction (perpendicular to the surface of the plate). Two excitation cases are considered for this study. First excitation method involves hitting the plate with pens for both patches. This case is an attempt to reproduce similar forces between patches and is referred as the case 1. Excitation case 2 involves hitting the plate with plastic spoons for the first patch and then with fingernails for the second, which theoretically should give rather different forces between patches. This case is expected to be closer to real life scenario where the two patches, not measured simultaneously, are most likely excited by different type of forces.

#### Measurements and Signal Processing

For the first case, data is collected for approximately 11 min, which is divided into two time histories, one time history for each patch. For second case, data is acquired for around 2 min for each patch using excitations as explained previously. The frequency range is limited to 400 Hz with 1024 Hz sampling frequency. A total of 12 DOFs are chosen as shown in Fig. 12.14 uniaxial accelerometers are placed to measure the response at these DOFs and hence complete power spectra matrix is  $12 \times 12$ . Just like in the numerical study section, the baseline power spectra matrix is chosen to be reduced  $12 \times 4$  matrix, where four projection channels are reference DOFs 2, 3, 6 and 7 (see Fig. 12.14). Patches are formed as follows: patch 1—DOFs [1–3, 5–7, 9, 10]; patch 2—DOFs [2–4, 6–8, 11, 12]. The modal parameter estimation technique used is again SSI-Cov.

### 12.4.2.2 Results and Discussion

Figure 12.15 shows SDEC values obtained for various scaling approaches for the two excitation cases. For the first case there is observable, but insignificant decrease of SDEC value. Also, as observed with analytical system, local scaling  $k_1$

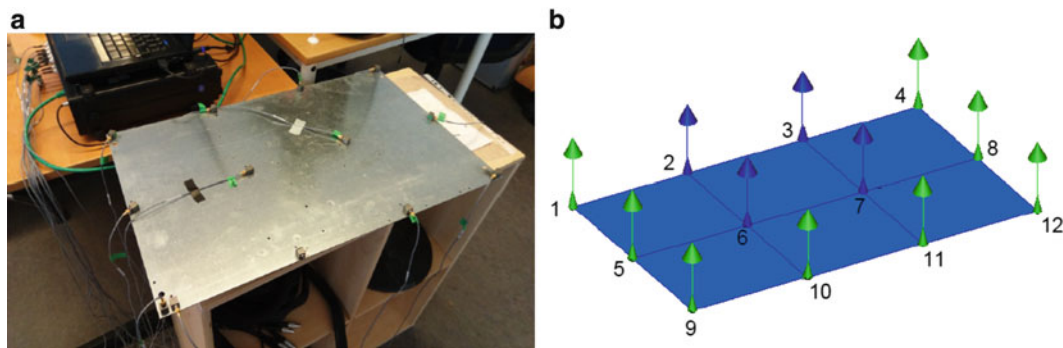


**Fig. 12.14** (a) Steel plate with 12 accelerometers and, (b) their measuring directions (*blue arrows* show reference sensors)

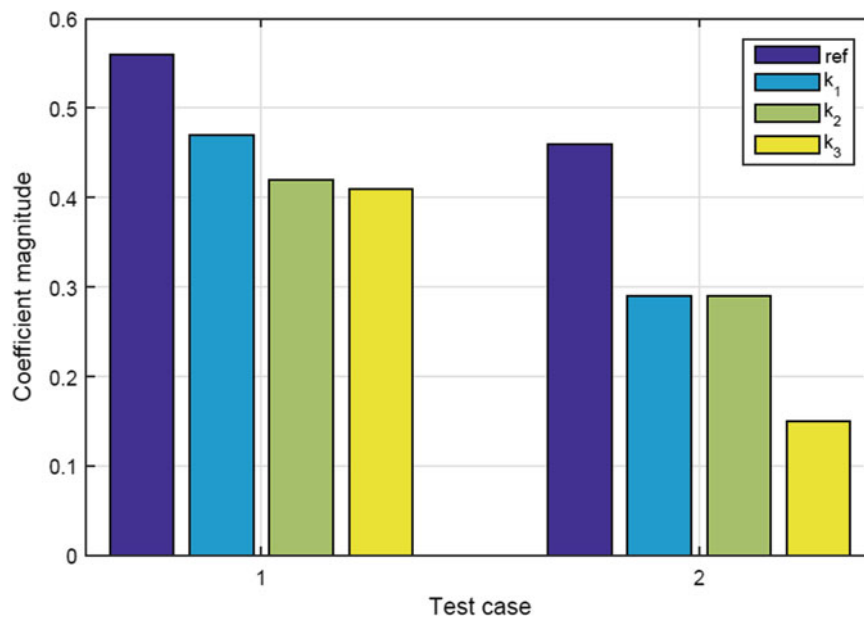


**Fig. 12.15** Global SDEC values for SVD based patching method

performs better than global scaling factors. The drop in SDEC value, in comparison to baseline reference, is much more significant in second case. One highlight of SVD based patching method suggested in this paper, as mentioned in Sect. 12.4.1 as well, is that it also gives an indication about the difference in excitation between the two patches in addition to whether the excitations is adhering to OMA assumptions or not. The MAC plot in Fig. 12.16, clearly shows that while first singular vector corresponding to SVD of  $4 \times 4$  reference power spectra matrix matches very well for the two patches for first case, the same is not true at all for the second case. This is bit unexpected as one would expect the first singular vector to match, since data pertaining to only the reference DOFs is considered, which are common to both patches and hence should yield similar singular vectors. Since the OMA assumptions are adhered in both cases, this observation for second case cannot be attributed to that. A more probable reason, in second case, is that perhaps the system has changed slightly between the measurements carried out for the two patches (for e.g. the boundary conditions can change if plate is disturbed even slightly). It should be remembered that unlike the first case, where a long measurement is carried out, and the acquired data is divided into two, one for each patch, in second case two separate measurements are performed pertaining to the two patches. Further, unlike the first case, the manner of exciting the plate for the two patches is different in second case. Considering the fact that the plate is very light, it could also be that this might lead to different mass loading resulting in the observed behavior.

Variation in scaling factors for the two cases also provide a hint with regards to quality of patching procedure. For the first case, the local scaling factor function (Fig. 12.17a) deviates within a range of approximately 5 dB, which is tolerable. Also global scaling factors are located somewhere around the mean value of the local scaling function. These observations indicate good similarity between forces applied on the two patches and also that forces adhere to OMA conditions of being

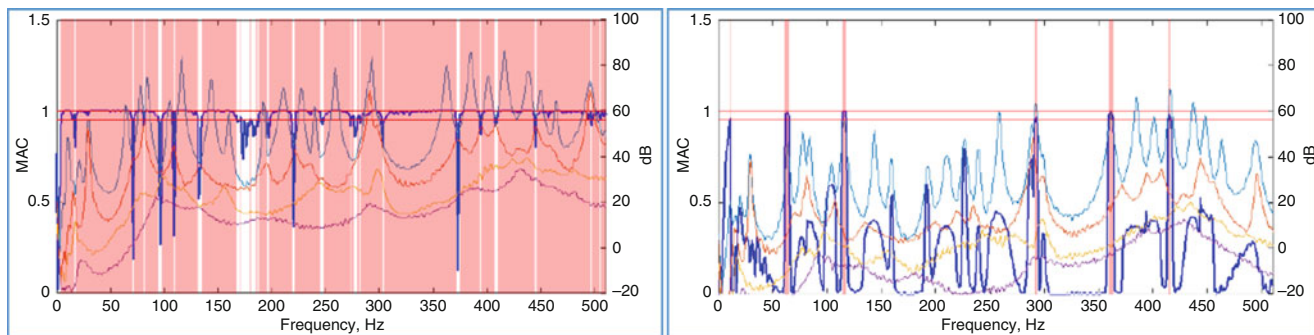


Fig. 12.16 MAC plots for first (left) and second (right) test cases

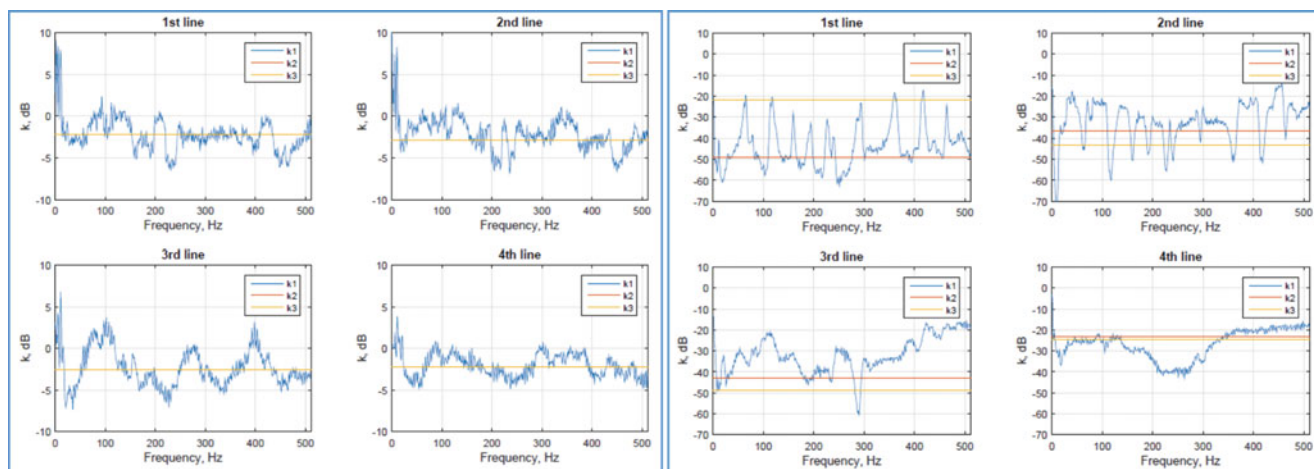


Fig. 12.17 Scaling factors for (a) 1st case, (b) 2nd case

Gaussian in nature throughout the frequency range of interest. This similarity allows to perform effective patching that results in stable and better estimation of modal parameters. In contrast, the variation in local scaling factor is quite large (up to 40 dB) for the second case (Fig. 12.17b), which could be attributed to reasons listed before.

## 12.5 Further Perspectives on SVD Based Methodology

The SVD based patching methodology suggested in this paper works towards combining the data from various patches so that global modal parameters, characterizing the entire structure, can be obtained in one go. The method works on output response power spectra matrices and hence is not specific to any OMA modal parameter estimation algorithm, although it should be noted that this approach will not work with algorithms that operate directly on raw time histories instead of power spectra or covariance/correlation functions.

In addition to performing its intended task of patching the measurements from different patches together, the approach also provide tools that not only give valuable insights into the patching procedure but also facilitate in assessing whether underlying assumptions (both OMA and EMA) are held or not. The plot of local scaling factor  $k_l$ , which is a function of frequency, is a useful tool for monitoring the difference in forces between patches. By evaluating the dynamic nature of local scaling factor engineer can identify whether the excitation for a set of patches meets OMA assumptions, i.e. force is distributed randomly on a system in spatial sense and has a white noise spectrum. In ideal circumstances, when OMA assumptions are met, the variation in local scaling factor will be low and it will be mostly flat, indicating that one can expect good patching results. On the contrary, a situation similar to that described in Sect. 12.4.1.2 pertaining to uneven modulated case, will result in significantly varying local scaling factor (Fig. 12.10), highlighting the fact that OMA assumptions are not adhered and hence patching is suboptimal.

The MAC plot comparing the first singular vectors associated with reference sensors (DOFs) of the two patches, obtained after decomposing the power spectra matrix associated with reference sensors (DOFs), is yet another tool in this regard. Since



the reference sensors are common to both patches and SVD results in singular vectors that are orthonormal, it is expected that singular vectors for the two patches should be same. In reality, this might not be true due to noise but it is still expected that first singular vectors will match as most of the energy is associated with first singular value, especially in vicinity of a resonance, and it is safe to assume that it is noise free (noise being accounted in lower singular values). Further, MAC is a measure of similarity and not exactitude and hence it is expected that MAC will be high in general. If this is not that case, it is an indication of violation of general modal analysis assumption that the system is time-invariant and observable. Low MAC value in this regard is either an indication of the fact that somehow the structure has undergone a change between measuring the patches or boundary conditions changed or excitation forces for the two patches differ in their nature such that some modes are not excited in one or the other patch and are hence not observable. Thus, MAC plot provides a useful assessment with regards to basic modal assumptions, violation of whom can adversely affect the patching procedure.

The theory developed in this paper (Sect. 12.2.1), which forms the basis of this method, also explains in general the principle of Pre Global Rescaling or PreGER. As far as authors knowledge, the mathematical framework of PreGER has not been explained this way. [9] proposes a method for merging data from various patches before estimating modal parameters. This is similar to the scheme adopted in this paper, except that the suggested method is centered around subspace based time domain methods. This is also the case with [10], which describes a merging technique in context of SSI-Cov algorithm. Finally, [3] only lists Eq. (12.16) without any formal derivation of the same. Thus, developed theory not only sets the basis for SVD based patching methodology but also provides a formal derivation of PreGER. It provides a thorough and complete explanation of the method and the reasons why it is expected to perform the patching task as intended.

It should be noted that during the studies made in this paper, the SVD based approach is found to be comparable to original PreGER (i.e. using Eq. (12.16) directly) in its performance, though not really outperforming it. In fact, in certain cases, PreGER might still be preferred as it turned out to be slightly more robust. This can be attributed to the fact that SVD based methodology is based on the assumption that left and right singular vectors of reference power spectra matrix do not change from one patch to another. This however, may not be true in real situations due to presence of noise. It was expected that SVD based method might be able to deal better with such scenarios, due to inherent properties of SVD with regards to separating signal and noise subspaces, but seemingly PreGER's simple approach, of taking all information and scaling it accordingly, is more effective in handling such situations. Nonetheless, one can still combine the two methods and utilize the positive aspects of SVD based approach, such as local scaling factor plot and MAC plot between first singular vectors, with PreGER, to further improve the patching procedure in multi-patch OMA.

## 12.6 Conclusions

The work presented in this paper explores methods of estimating global modal parameters of a structure that has been measured in series of patches. The paper presents theoretical background in such a case and introduces a SVD based method for combining the data before application of parameter estimation algorithms. The method uses SVD as the basis of scaling data pertaining to one patch with respect to other. In essence, this amounts to scaling the data of one patch in such a way that it simulates the excitation conditions of the other patch with respect to whom the data is being scaled. Three different scaling approaches are suggested in this paper for this purpose and it is shown, by means of comparisons with baseline measurements, that local scaling method works satisfactorily in most cases.

It is also illustrated in the paper that the suggested method not only aids in patching the data together but also provides useful insights about the quality of the acquired data, measurement setup and conditions; factors that affect the quality of the patching procedure. It is shown how plots of local scaling factor and MAC plot between first singular vectors of reference DOFs power spectra, from the two patches, can assist in assessing the quality of patching. Also, a measure called Stability Diagram Evaluation Coefficient is introduced in the paper that provides a way to quantitatively compare estimation quality of various patching methods by evaluating overall quality of stability diagrams.

The theory developed in this paper also provides a formal derivation of PreGER approach of merging data in multi-patch OMA, thereby giving a solid mathematical foundation to the methods developed around this hypothesis of patching the data before estimating modal parameters. This, along with positive results as shown in paper, make proposed method a promising technique for multi-patch OMA.

## References

1. Maia, N.M.M., Silva, J.M.M., et al.: Theoretical and Experimental Modal Analysis. Research Studies Press, Taunton (1997)
2. Brincker, R., Ventura, C.: Introduction to Operational Modal Analysis. Wiley, Chichester (2015)
3. Parloo, E.: Application of frequency-domain system identification techniques in the field of operational modal analysis. PhD thesis, Vrije Universiteit Brussel (2003)
4. Chauhan, S.: Parameter estimation algorithms in operational modal analysis: a review. Sixth International Operational Modal Analysis Conference (2015)
5. Peeters, B., De Roeck, G.: Stochastic system identification for operational modal analysis: a review. *J. Dyn. Syst. Meas. Contr.* **123**, 659–667 (2001)
6. Brincker, R., Andersen, P.: Understanding stochastic subspace identification. In: Proceedings of 24th International Modal Analysis Conference (IMAC), St. Louis (2006)
7. Allemang, R.J.: Vibrations: experimental modal analysis, Structural Dynamics Research Laboratory, Department of Mechanical, Industrial and Nuclear Engineering, University of Cincinnati, UC-SDRL-CN-20-263-662 (1999)
8. Mironovs, D.: Estimation of global modal parameters in multi-patch operational modal analysis. Master thesis. Denmark Technical University (2016)
9. Mevel, L., Basseville, M., Benveniste, A., Goursat, M.: Merging sensor data from multiple measurement set-ups for non-stationary subspace-based modal analysis. *J. Sound Vib.* **249**, 719–741 (2002)
10. Döhler, M., Reynders, E., Magalhaes, F., Mevel, L., De Roeck, G., Cunha, A.: Pre- and post-identification merging for multi-setup OMA with covariance-driven SSI. Proceedings of the IMAC-XXVIII, 1–4 Feb 2010



# Chapter 13

## Modeling and Nonlinear Parameter Identification of an Electric-Power Steering System

Cassio T. Faria, Giorgio Pulvirenti, and Theo Geluk

**Abstract** The electrification of auxiliary systems in the next generation of automobiles complies with the regulatory and customer requirements to increase the overall system efficiency and reduce the carbon footprint of the product. For the power steering system its electrification also attends another important demand of the industry: the actuation of the vehicle for autonomous driving function. The development of advanced model-based controllers increase the requirements for model accuracy which are met by incorporating nonlinearities in the model and also by carrying out advanced parameter identification in those systems. This paper illustrates a modeling and testing procedure for a C-class electric power steering (EPS) system, following a model-based system testing (MBST) approach and presents results from a test campaign. A comparison it is drawn on the model prediction capabilities when compared to collected experimental data.

**Keywords** Electric power steering • Parameter identification • Nonlinearity • Multiphysics • Model based system testing

### 13.1 Introduction

Electrical power steering has several advantages when compared to hydraulic actuation, it is more compact, more efficient and reliable [1]. Simultaneously, noise and vibration are an issue for this type of electromechanical system and the control strategy plays an important role into addressing this issue while alleviating the required torque from the driver [2, 3]. An undesirable consequence of a poorly designed control law for the EPS is to isolate the feedback to the driver (reducing the driving connectivity feeling to the road), which is an important sensorial feedback to the driver to allow for safe vehicle handling [2].

Advance control strategies, in particular model-based ones often prove to be an appropriate solution for EPS systems; nevertheless they require high-fidelity models, which are by nature very complex, nonlinear and multiphysical. Good controllers and hence good models must include these nonlinear physical properties to improve their prediction capabilities and allow for the model-based controller to properly drive the system [4].

A significant portion of the mismatch between model and system behaviors lies on poor characterization of the nonlinearities. Experience from engineering projects within Siemens Industry Software dictates that the nonlinear behavior of the individual components is not the same as the behavior observed when they are interconnected. Therefore the parameter identification procedure needs to be carried out at a system level testing and not by a series of isolated component measurements. A measurement campaign of an entire electromechanical system poses several challenges, in particular to isolate and determine the influence of individual parameter on the overall system behavior.

Experimental methodologies have recently shifted from test-only routines to simulation-aided methods [5]. As test campaigns and their objectives grow in complexity, more virtual models are used to increase the knowledge of system behavior prior to the (usually expensive) test campaign. Moreover, testing is no longer solely related to troubleshooting analysis and the model parameter identification, as they can also be used for other purposes, such as force and load estimation, in the so-called virtual sensing applications [6].

With the purpose of supporting the new paradigm that combines test and simulation, the model based system testing (MBST) framework was created [5]. The main purpose of MBST and its underlying methodologies is to support and improve testing and validation techniques, by using and/or combining test and simulation, with the aim to study, identify and validate multiphysical and mechatronic systems.

---

C.T. Faria (✉) • G. Pulvirenti • T. Geluk  
Siemens Industry Software N.V., Interleuvenlaan 68, B-3001, Leuven, Belgium  
e-mail: [cassio.faria@siemens.com](mailto:cassio.faria@siemens.com); [cassioharry@hotmail.com](mailto:cassioharry@hotmail.com)

## 13.2 Electric Power Steering (EPS) and Its Functional Model

Electric power steering (EPS) assistance systems provide auxiliary power to the steering mechanism of the vehicle to aid the driver in performing a desired maneuver, where part of the effort is frontloaded by an electric drive combined to the steering column of the mechanism. Figure 13.1a gives a generic schematic representation of the EPS mechatronic system and main components are shown: a steering wheel (where drivers apply inputs—angular position and torque); an electric motor and drive to provide the assistance power; a reduction mechanism to transmit the electric motor power into the steering column; an electronic control unit (ECU) that commands the electric motor to assist the driver (reduce the torque required to perform a maneuver); a steering column that transmits torque to the rack and pinion; the rack and pinion that converts the rotary movement into a translation one; the tie-rods (left and right) which carry the translation motion and loads to the wheels and lead to the rotation of a rotation motion around their axis.

The challenge, from a modeling perspective, is to idealize the system and define its fundamental dynamics for each component such that one can adequately represent the behavior of the real system. A starting point is a simple electro-mechanical representation of the system by a combination of mechanical converters (gears and leverages), springs, masses, dampers, and electromechanical motors and drives to accomplish a functional iteration of the model (called the linear model). As previously established, for disturbance rejection/control purposes a high fidelity model is desired, which imposes the inclusion of the nonlinear behavior present on the real system. One possible solution (followed in this paper) is to lump the nonlinearities at each component, meaning a set of specific nonlinear behavior are assigned for the: steering column, electric motor, gear reduction, rack-pinion and wheel.

A multi-physical model is constructed using LMS.Imagine AMESIM software, which is a block diagram physical programming language, the sketch of the model is shown at Fig. 13.1b together with a general classification used for the different subsystems considered. Each of the groups has a friction component assigned (this is not the case for the control strategy—ECU) to lump all the kinetic nonlinear effects. The model takes the driver's steering wheel angular motion as input and calculates the torque perceived by the driver (the model is also a function of the vehicle speed to take into account variable rolling friction and the assistance tables at the ECU). If the control strategy is turned off (e.g. zero PI gains), the electrical drive reacts as a passive inertial component and the driver's action is cascaded down to the tie-rods which push against the tire friction to create an angular motion at the spindle. From a practical testing perspective it is interesting to characterize the EPS dynamics when the electric drive and control strategy is not activated, to define the response of the passive mechanical system, and also considering zero vehicle speed so the tire friction can be defined at its maximum (pure tire slip).

Some parameters in the model can be easily identifies a-priori and by doing so the number of unknown parameters is drastically reduced and the uncertainty of the model can be associated in its majority to the nonlinearities of the subsystems. Geometrical and mechanical characteristics (i.e. mass and stiffness) can be determined beforehand by executing component

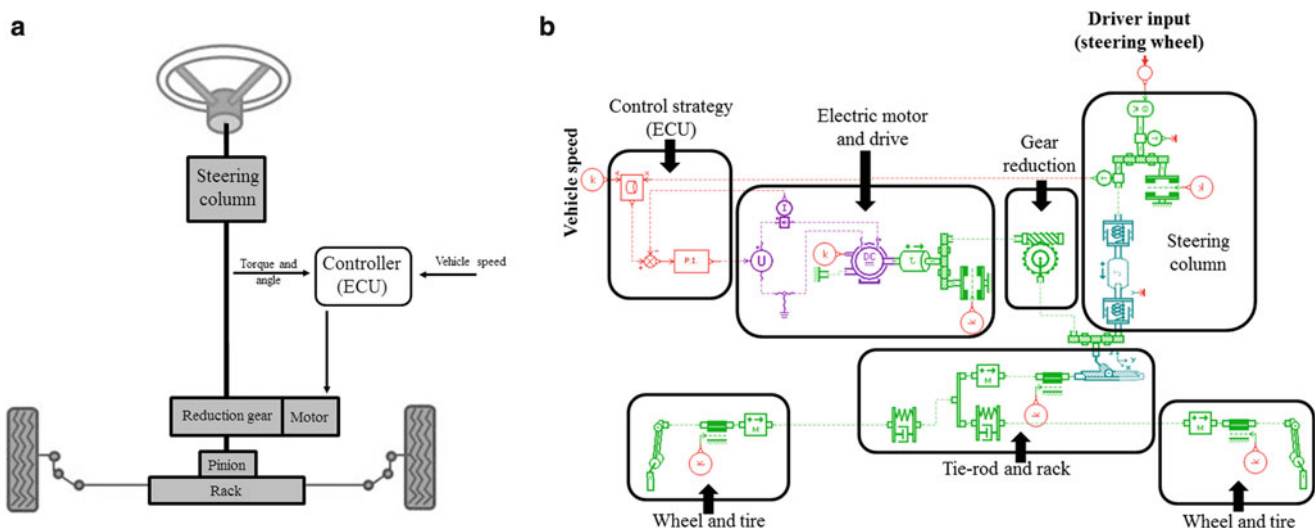


**Fig. 13.1** (a) Sketch of the working principle of an EPS system and (b) EPS model realization in AMESIM

inspection and simple tests. Electrical quantities can also be directly measured at the electric motor and drive. Although, the largest uncertainty must be assigned to the nonlinear parameters of the model, a certain level of confidence can also be assigned to the linear parameter previously identified to allow for model fine tuning by the identification procedure.

### 13.3 Experimental Setup and Implementation of the MBST Approach

The deployment of Model-Based System Testing (MBST) concepts to this problem [5] can generate a lot of insight on the testing activity being planned and can be accomplished by performing a series of exploratory simulations to evaluate the system response and help define testing configurations and methodologies that expose critical and key parameters of the EPS. To exemplify this concept, MBST is applied to the electric power steering (EPS) system in order to develop a testing procedure that allows for the high fidelity modeling that is needed for control purposes.

The basic structure of the EPS model under consideration is the one introduced on Fig. 13.1b. This model can be used in a variety of ways to explore different aspects of the tests that will be carried out and to evaluate configurations and boundary conditions that would favor the later identification of the model parameters. It is important to note that this model already has reasonable values for the linear dynamics components, such as masses, dimensions, transmission ratios and stiffness. The challenge on developing an accurate model for this particular physical system lies on the characterization of the nonlinearities and viscous damping terms used.

Firstly, the system is split into smaller assemblies, called cut-outs, which could encompass multiple EPS subsystems. Simulations are carried out to explore the cut-outs behavior under different inputs and boundary condition to allow for the testing engineer to isolate the nonlinearities on a given component and precisely characterize it. Naturally, not all possible cut-outs of the model can be executed in practice, furthermore imposing certain boundary condition might be unfeasible or too costly, therefore a subset of all the possibilities are explored as an intersection of three different factors: utility of such a cut-out, the effort to implement it and the cost to execute it. Figure 13.2 exemplifies three possible EPS cut-outs exploring the behavior of a section of the system under a particular boundary condition, for example, on the left-hand side figure, the goal is to isolate the behavior of the steering column by blocking the shaft at its base and identify the friction at this component. The use of simulation of such a subset of the original developed model can help the test engineer evaluate if this cut-out can be useful or not for parameter identification procedure, i.e. if unique information can be extracted from a given test condition.

A combination of six different cut-outs and boundary conditions scenarios were investigated for this paper, five where the e-motor was a passive element in the system (blocked steering column, free tie-rods, blocked spindle, full system without

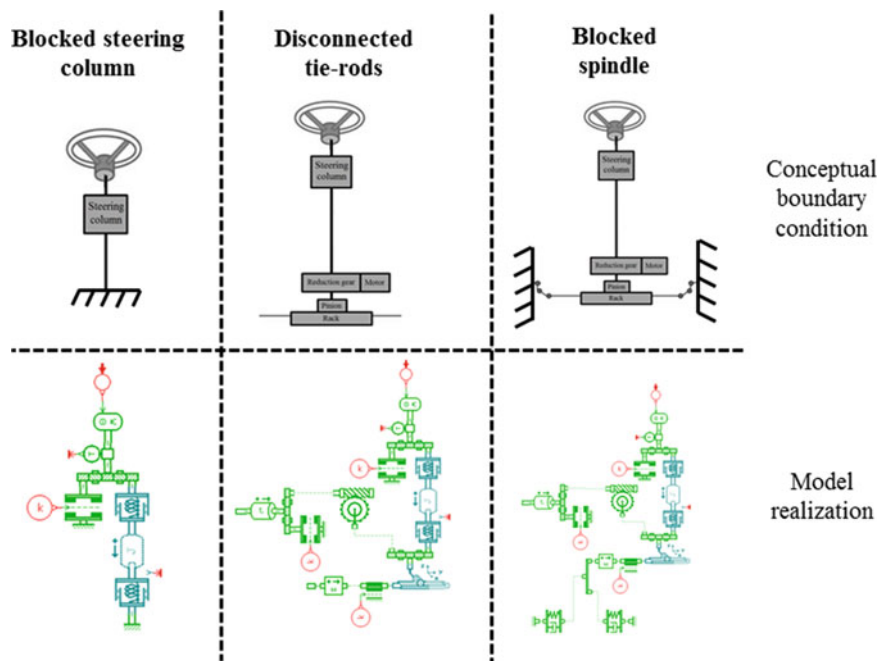


Fig. 13.2 Different possible boundary condition for the EPS mechanism and its AMESIM model realization

tire friction—suspended vehicle—and full system with tires on the ground) and one scenario where the motor was actuated with a constant supply (free tie-rod). Based on the simulation results, three of these scenarios were chosen: (1) blocked steering column; (2) free tie-rods and; (3) full system with tires on the ground. These would, according to simulation results, enable the identification of all the unknown model parameters and were a good compromise between quality of the results and time/cost of the campaign.

As previously mentioned, the virtual representation of the EPS system can also be used to evaluate the sensitivity to different inputs and how they would affect the response and therefore the excitation of nonlinear behaviors. Typical input profiles evaluated are: harmonic inputs (sine waves or sine sweep), used to evaluate cyclic behaviors; impact inputs (sharp or wide impacts), used to evaluate linear dynamic behavior; and also ramp inputs, used to identify transition points in the system dynamics. Moreover, a combination of these inputs or different levels of the same input can be used to exploit the dominance of a given parameter in the response of the system. By developing this knowledge over several simulations, a set of unique input profiles can be derived such that the parameters are identified more accurately. For example, different responses can be observed between the two inputs applied to the system, where on the higher frequency sine input more inertial forces have to be overcome in order to start the motion and to reverse its direction, also the higher velocities make the viscous losses in the system more prominent.

The MBST approach is also used in this case to evaluate how candidate sensor positions can help (or not) to detection of nonlinearities. In this situation, it is not feasible to carry out an exhaustive search of all the sensor locations given that many of these locations and physical quantities cannot be instrumented due to several issues, e.g. effort, feasibility, cost, etc. In this paper, simulations were carried with ten candidate position of sensor locations, chosen based on the accessibility of the location and cost/time-to-instrument. The responses of the sensors were examined and three were selected as the minimal set of sensors needed to fully capture the system behavior. The driver steering angle was selected as the input to the system (to also be used in the simulations) and a sensor was also placed in that location.

Figure 13.3 is a schematic representation of the sensor positions selected for the test campaign, where a potentiometer is used to capture the angular input from the driver, a full-bridge of strain-gauges (062AK\_350 from micro measurements) is used to measure the driver input torque and also to measure the force transmitted by the tie-rod to the wheel. A wire-draw displacement sensor (WDS-250-MPM-C-P\_HG from micro-epsilon) records the displacement of the rack/tie-rod. A second force measurement of the force in the tie-rod is also done to verify the system symmetry. Data was collected by a SCADAS mobile hardware using VB8 family modules and the acquisition and post-processing using LMS Test.Lab software (Signature

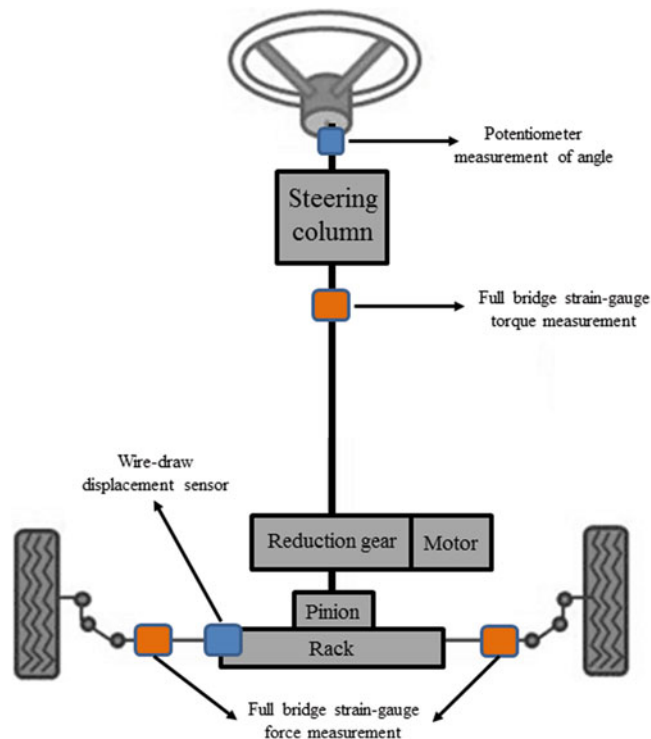


**Fig. 13.3** Schematic representation of the test setup and instrumentation used

Acquisition module). Exponential filtering was used on the collected data to eliminate high frequency noise content of the data. It is important to note that the specifics on the EPS under test, such as model, brand, etc., cannot be provided due to data confidentiality issues.

### 13.4 Parameter Identification and Results

The parameter identification process was carried out by a gradient-based optimization process that minimizes the accumulated error between experimental and simulated data (called here cost function). For each of the tests the function is adapted to relate to a particular quantity of importance (error on the steering torque, rack displacement and tie-rod force, or a linear combination of these three). Due to the nonlinear nature of the dynamic system under analysis an NLPQL (Non-Linear Programming by Quadratic Lagrangian) algorithm [7] is chosen, and it uses the simulation of the system at a central point and apply disturbances to each model parameter to calculate its derivatives and form a gradient vector used in the search for optimum values for the system parameters that minimizes the cost function.

Some of the model parameter can directly be measured and therefore they are taken as constants and are not subjected to the optimization process to fit the model to the obtained test data. These parameters are described by Table 13.1 below. Given that the direct measurement of these quantities are also subjected to uncertainties one could also subject them to the same optimization process under a more strict constrain, e.g. allow a 10% change in the parameter value. Although this is what is done in practice, this paper will focus only on the fitting of the nonlinear parameters and therefore will keep these parameters constant throughout the following optimization routines.

The nonlinear parameter identification procedure was carried out at a model cut-out representing the test scenario 1 (blocked steering column), followed by scenario 2 (free tie-rods) and finally scenario 3 (full system with tires on the ground). The parameters identified in the previous scenario were cascaded to the subsequent identification step and they were taken as constant to allow the algorithm to focus on the fitting based only on a subset of the model parameters. This approach allows for the attribution of nonlinearities to each of the subsystems and prevents the optimization process to lump all the nonlinear effects at a single nonlinear block of the system.

For the scenario 1 the following cost function was applied:

$$e(f_{column}, v_{damping}) = \int_t (T_{sim} - T_{exp})^2 dt \quad (13.1)$$

where  $f_{column}$  correspond to the friction parameters at the steering column,  $v_{damping}$  the damping coefficients and  $T$  the steering wheel torque (SWT) for the simulation (*sim*) and experimental data (*exp*). The results of the parameter identification procedure (NLPQL algorithm) are shown in Fig. 13.4 and the final accumulated error was 1.894 for the section under analysis.

**Table 13.1** Parameters of the model identified a priory

Name	Quantity	Unit
Steering column stiffness	7	Nm/degree
Worm gear ratio	26	–
Worm wheel diameter	200	mm
Worm diameter	40	mm
Electric motor inertia	1.20E-04	kg m <sup>2</sup>
Electric motor supply	12	V
Electric motor resistance	0.1	Ohms
Electric motor inductance	7.50E-05	H
Torque constant	0.05	Nm/A
Radius of the pinion	8.5	mm
Mass of the rack	7	kg
Tie-rod and bushings stiffness	3000	N/m
Mass of the wheels	60	kg
Lever arm at wheels	120	mm

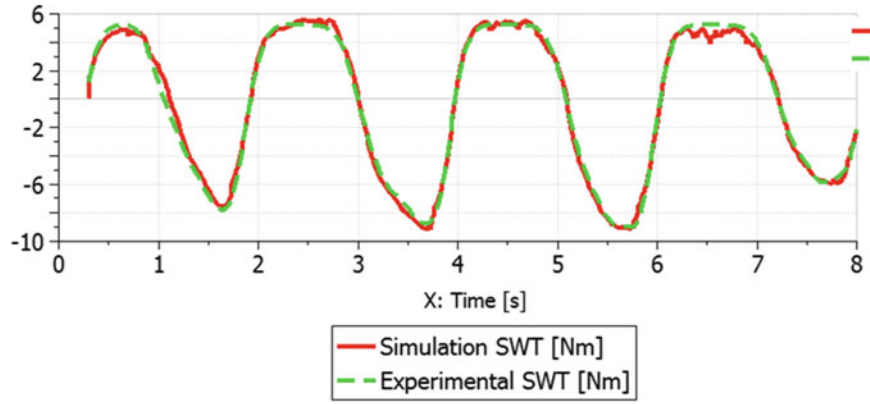


**Fig. 13.4** Blocked steering column results for the experimentally measured and simulated results after parameter identification is carried out

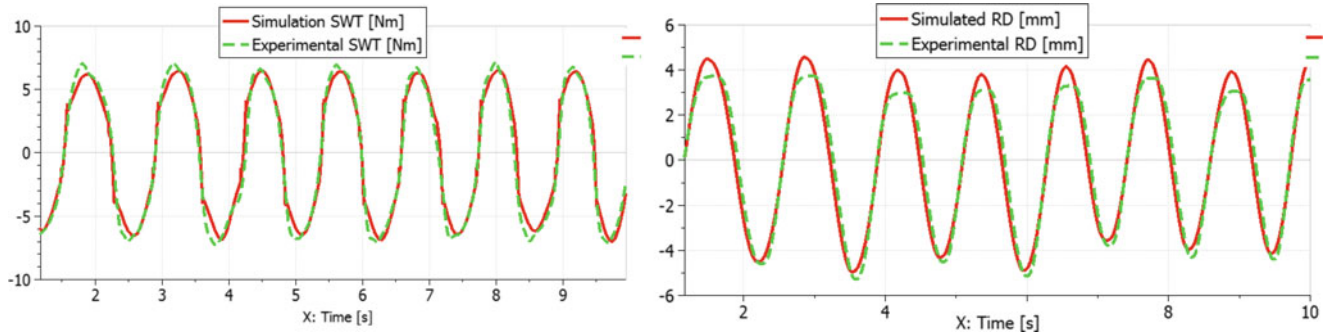


**Fig. 13.5** Disconnected tie-rods results for the experimentally measured and simulated results after parameter identification is carried out

Qualitatively these results are very good, as the simulation is able to accurately represent the experimental data. Some small simulation discrepancies can still be observed at the extremities of the SWT curve, in particular the presence of “noise” in the simulation, this effect is caused by the discontinuities in the solution and can be filtered out in a post-processing step.

For cut-out 2 another function was used, one that took into account also the rack displacement and for a different set of parameter to be determined:

$$e(f_{rack}, f_{e-motor}, f_{worm}) = \int_t \left[ (T_{sim} - T_{exp})^2 + (X_{sim} - X_{exp})^2 \right] dt \quad (13.2)$$

where  $f$  is associated with friction parameters for the rack-pinion, electric motor and worm gear, indicated by the subscripts, *rack*, *e-motor* and *worm*, respectively. The quantity  $X$  expresses the rack displacement (RD). The final accumulated error for this parameter identification was 7.884 and the results are presented by Fig. 13.5.

In comparison to the results presented by Fig. 13.4, there is a drop in quality of the fitting between experimental data and simulation (also observable in the larger accumulated error), this is expected given the large increase of model complexity in this step, nevertheless the model is still capable of represent in a very good fashion the main physical phenomena present at the experimental data.

Finally, for the third scenario tested and modeled where the system is fully assembled and the tire friction is present the cost function utilized in the parameter identification procedure is given below:

$$e(f_{tire}, k_{tire}, c_{tire}) = \int_t \left[ (T_{sim} - T_{exp})^2 + (X_{sim} - X_{exp})^2 + (F_{sim} - F_{exp})^2 \right] dt \quad (13.3)$$

where the tire friction ( $f_{tire}$ ) and stiffness ( $k_{tire}$ ) are the parameters to be identified given the addition of the rack force ( $F$ ) in the cost function. The results for the parameter identification for the complete system are shown in Fig. 13.6.



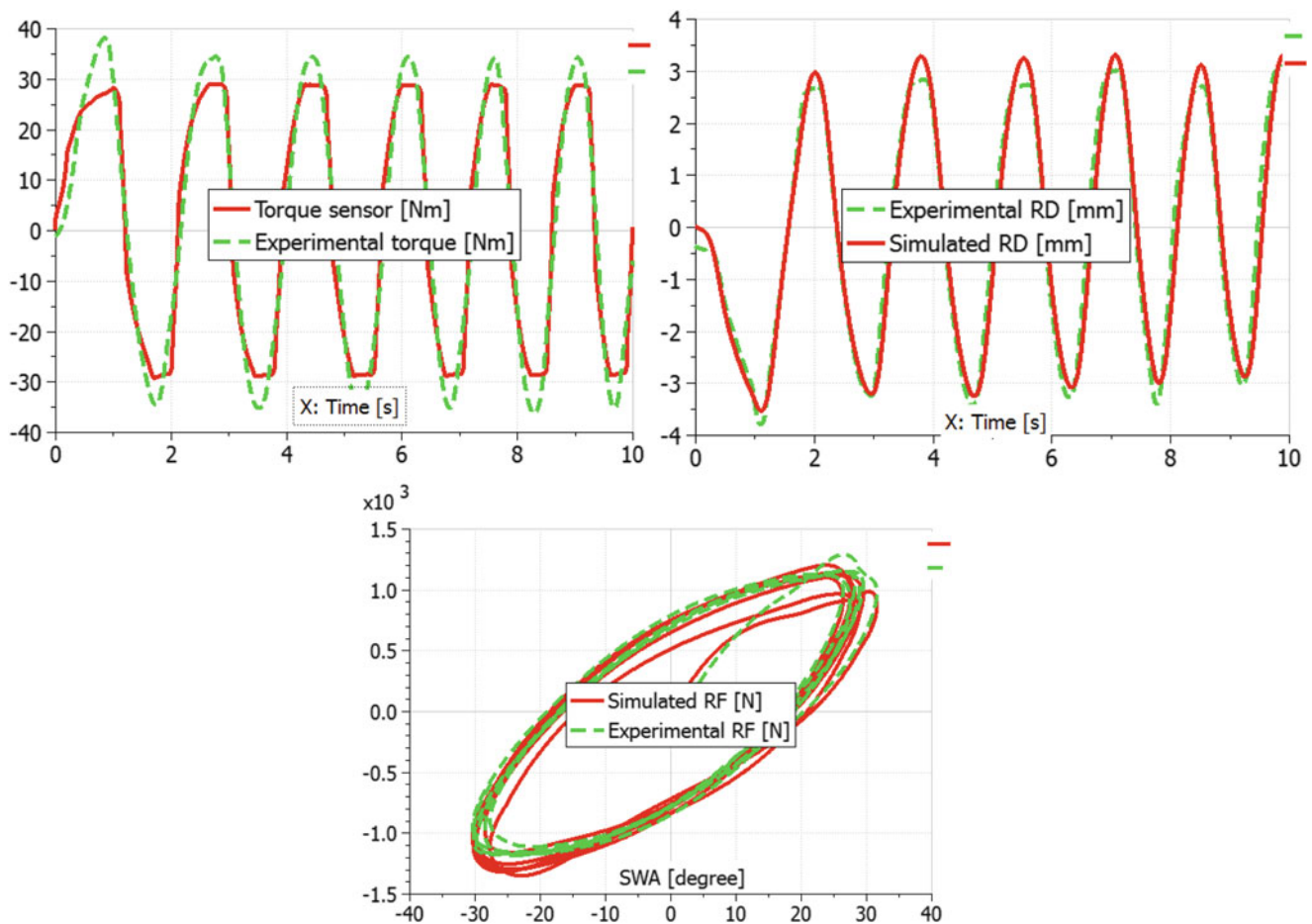


**Fig. 13.6** Wheels on the ground results for the experimentally measured and simulated results after parameter identification is carried out

Similar to what occurred in the previous identification step, the increase in model complexity lead to a not so precise identification of the model parameter after a series of optimization steps, for example, one can note a consistent underestimation of the driver's steering torque. This issue can be addressed by assigning weights to the different sources of error in the cost function; this approach was not followed in this paper given that these results already provided a very good dynamic model for the system. With the parameter identification procedure completed the final compilation of results are at table taking into account the parameters identified in all three scenario (Table 13.2). It is important to note that the focus of this paper is the definition and demonstration of a process for steering system identification using a limited number of responses that are acquired on a full vehicle assembly. As multiple steering system parameters are identified together in the identification procedure steps, this can imply that individual parameters are not yet accurately identified but are lumped with other system parameters. Further investigation will aim at refinement of both the test and system identification procedure to enhance the estimation of the individual system parameters.

### 13.5 Discussion and Conclusions

This article presented the use of model based system testing applied to an electric power steering system. For that purpose, the concept of MBST was introduced and deployed to mechatronic system of interest, where simulation and virtual models are used to aid in the testing procedure. Then, it was shown how it is possible to obtain a high fidelity model of an EPS system by breaking it down into different functional subsystems and lumping the nonlinearities accordingly. A full model was used prior to the execution of the test campaign to explore possible subdivision of the system (called in this paper cut-outs), to



**Table 13.2** Equivalent identified parameters for the nonlinearities (approximated values given)

Name	Quantity	Unit
Static friction on rack	330	N
Dynamic friction on rack	270	N/(m/s)
Static friction on steering column	0.5	Nm
Dynamic friction on steering column	30	Nm/(rad/s)
Viscous damping on steering column	7.5	Nm/(rad/s)
Static friction on electric motor	0.000001	Nm
Dynamic friction on electric motor	0.01	Nm/(rad/s)
Static friction on worm gear	0.05	Nm
Dynamic friction on worm gear	0.05	Nm/(rad/s)
Tire stiffness	370	N/mm
Tire viscous friction	54,000	N/(m/s)
Tire dry friction	2000	N

clearly isolate the effects of nonlinearities and moreover to explore boundary conditions that could be used for the upcoming tests. Moreover, sensor locations were evaluated taking into account ease of access, instrumentation efforts and observability.

Subsequently, a test campaign was carried out based on the insights obtained through the simulations in order to validate the proposed MBST methodology. The results obtained at this stage were used in combination with simple geometrical and material properties to create a first model iteration and allow for the deployment of a NLPQL optimization algorithm to identify the model parameter, such that a high fidelity representation of the physical system could be obtained. The executed test effort did not required a specialized test rig or highly specialized devices to carry out the measurements, but it rather combined the expertise of a test engineer and the simulations to identify relevant test scenarios that would enrich the overall data collected to the purpose of a later correlation to the original model. Simultaneously, the fact that the mechanism was tested while installed on the vehicle guarantees that significance of the identified model when it is applied to a realistic condition of the vehicle.

One of the key advantages of such approach is not only the identification of the input-output behavior of the system but rather a subcomponent characterization that allows for specific targeting of a component or a section of the mechanism for further design improvements. The results presented on the previous section demonstrate how powerful the approach proposed in this paper can be as it was able to accurately identify a model with a reduced effort in terms of instrumentation, testing effort and optimization/parameter fitting. The ease of deployment of such approach indicate a future application of online parameter estimation during the tests, a capability that would allow the test engineer to judge immediately the quality of the data being collected and asses if the more tests need to be executed or not.

Regarding the values identified, their magnitude is in accordance with other values reported in literature [4] and a closer examination of each indeed indicates that the optimizer converged to values that are physically acceptable and possible to such a complex physical system. A better agreement between model and experiments can be obtained in case a more exhaustive parameter search is carried out taking into account different weighting functions to each of the terms in the cost function and more strict convergence parameters to the NLPQL optimizer.

In conclusion, it was observed that the combination of simulation and test (the MBST framework) can be very beneficial to aid in testing and parameter identification of complex systems. By using a model of the EPS system, it was possible to speed-up the testing procedure, reduce the number of used sensors and improve accuracy of the results.

**Acknowledgments** The research presented in this paper was partly performed in the context of the ITEA2 project I1004 MODRIO. The authors gratefully acknowledge the support of VLAIO, The Flemish agency for Innovation & Entrepreneurship.

## References

1. Badawy, A., Zuraski, J., Bolourchi, F., Chandy, A.: Modeling and analysis of an electric power steering system. In: Proceedings of the Symposium on Steering and Suspension Technology, No. 1991-01-0399, 1999
2. Zaremba, A.T., Liubakka, M.K., Stuntz, R.M.: Control and steering feel issues in the design of an electric power steering systems. Proc. Am. Control Conf. **1**, 36–40 (1998)

3. Li, X., Zhao, X.-P., Chen, J.: Controller design for electric power steering system using T-S fuzzy model approach. *Int. J. Autom. Comput.* **6**(2), 198–203 (2009)
4. Data, S., Pesce, M., Reccia, L.: Identification of steering system parameters by experimental measurements processing. *J. Automob. Eng.* **218**, 783–792 (2004)
5. dos Santos, F.L.M., Pastorino, R., Peeters, B., Faria, C.T., Desmet, W., Góes, L.C.S., Van Der Auweraer, H.: Model based system testing: bringing testing and simulation close together. In: *Damage Detection and Mechatronics: In Structural Health Monitoring*, vol. 7, pp. 91–97 (2016)
6. Lourens, E., Reynders, E., De Roeck, G., Degrande, G., Lombaert, G.: An augmented Kalman filter for force identification in structural dynamics. *J. Mech. Syst. Signal Process.* **27**, 446–460 (2012)
7. Farhat, N., Mata, V., Page, A., Valero, F.: Identification of dynamic parameters of a 3-DOF RPS parallel manipulator. *Mech. Mach. Theory.* **43**(1), 1–17 (2008)

# Chapter 14

## A Framework for Additive Manufacturing Process Monitoring & Control

Ian T. Cummings, Megan E. Bax, Ivan J. Fuller, Adam J. Wachtor, and John D. Bernardin

**Abstract** Fused deposition modelling, like other additive manufacturing methods, has largely remained an open loop process in the absence of rigorous process monitoring and diagnostic functionality. By creating a framework that integrates quantitative diagnostic tools whose measurements are coordinated with the printing process and the system which commands the printer hardware, this paper demonstrates the feasibility of closing the loop in additive manufacturing systems. Specifically, this paper introduces the use of ultrasonic excitation as a means of detecting filament bonding failures introduced by manipulating the print bed temperature during the fused deposition modelling build process. Furthermore, this work demonstrates the capability of correcting these filament bonding failures using a correction mechanism introduced through tunable control of another process parameter of the printer. By demonstrating the detection and correction of filament bonding failures in situ, this work has demonstrated the progress toward fully closed loop control for fused deposition modeling processes.

**Keywords** Additive manufacturing • Fused deposition modeling • Nondestructive evaluation • Process monitoring

### 14.1 Introduction

Recent advances in additive manufacturing (AM) capabilities have propelled its application to many exciting and complex manufacturing problems. Yet the AM process has largely remained an open loop in the absence of process feedback mechanisms. In traditional manufacturing, the absence of in-process part qualification was acceptable due to the wealth of information on the mechanical characteristics of the stock materials, which enabled part qualification through sampled destructive testing. Yet, one of the major advantages of AM is its ability to produce incredibly complex geometries with rapid turnaround for low production volumes. Because additive manufacturing processes produce structures with bulk properties which are often anisotropic and difficult to characterize, post-process qualification becomes considerably less feasible. Therefore, a framework to integrate data acquisition, signal processing, and control feedback into the print process has become necessary. Such a system would close the loop in AM systems, providing greater levels of confidence in AM products, by increasing part quality quantification and providing part defect correction. In this research, we demonstrate progress toward a novel fault detection data acquisition system (DAQ) and integrated control feedback for fault correction in fused deposition modeling.

Previous work in additive manufacturing research has explored a wide range of diagnostic sensors, including acoustic emissions sensors [1–3], accelerometers, temperature sensors, and cameras [4]. Post-process vibration-based inspection techniques have also been investigated [5]. Furthermore, in-process ultrasonic part characterization has been attempted via build plate piezoelectric transducers [6] and laser Doppler vibrometer measurements [7].

---

I.T. Cummings

Electrical and Computer Engineering Department, Michigan Technological University, 1400 Townsend Dr, Houghton, MI 49931, USA

Applied Engineering and Technology Division, Los Alamos National Laboratory, P.O. Box 1663, Los Alamos, NM 87545, USA

M.E. Bax

Mechanical and Aerospace Engineering Department, Missouri University of Science and Technology, 1201 N State St, Rolla, MO 65409, USA

Applied Engineering and Technology Division, Los Alamos National Laboratory, P.O. Box 1663, Los Alamos, NM 87545, USA

I.J. Fuller • A.J. Wachtor (✉) • J.D. Bernardin

Applied Engineering and Technology Division, Los Alamos National Laboratory, P.O. Box 1663, Los Alamos, NM 87545, USA

e-mail: [ajw@lanl.gov](mailto:ajw@lanl.gov)

As AM techniques increase in popularity and application, control feedback is becoming more crucial to creating parts that meet mechanical properties specifications, as well as meet dimensional tolerances required to be effectively used in industry. Since material properties are determined from the build history in AM processes, and hence geometry dependent, qualification of AM parts will require control over process parameters most greatly affecting the material properties [8]. Several methods of detection and correction of faults in AM parts have been explored, such as correcting the part based off of discrepancies found by measuring height differences [9], and using scans of the geometry [10]. This work approaches the problem using ultrasonic sensors and a control feedback loop to adjust certain parameters in the print process in order to correct part failure. In order to accomplish this, a unified DAQ and control framework was developed to integrate real-time diagnostics with 3D printer commands. A repeatable fault mechanism was identified and a robust corrective mechanism was found to test the unified framework. Lastly, an experimental setup for full integration of the developed unified framework and data acquisition techniques for fault detection are discussed.

## 14.2 Unified DAQ and Control Framework

This work began from the perspective that both the issues of process monitoring and control should be simultaneously addressed in a unified system. This governed that the system responsible for controlling the printer must also communicate with the software running online diagnostics during the print process such that any detected failures of the print could be corrected or compensated for by sending additional commands to the printer or by modifying the commands in the queue. Because there are a multitude of AM platforms and a variety of diagnostic tools under development, the framework should be constructed in a manner that would allow quick adaptation to new printers and incorporation of multiple diagnostic tools.

The developed architecture is shown in Fig. 14.1, which demonstrates the flow of data and control in the system. At the beginning of a print, the G-code machine language instructions for the 3D printer are loaded into the print control software and the contents of each field are parsed and stored. The Print Control & Feedback software sends its commands to the printer over a USB (Serial) link—a common interface for open source, FDM 3D printers. The printer responds by executing the commands it was sent, while simultaneously a set of diagnostic sensors observe the print process resulting from each command. The Data Acquisition & Processing Software takes the data from those sensors and informs the Control Feedback Software about the status of the print via statistics from each process monitoring sensor. The Control Feedback Software would then use these statistics to make decisions about whether or not it needs to modify the instructions to be sent to the printer, and how to do so.

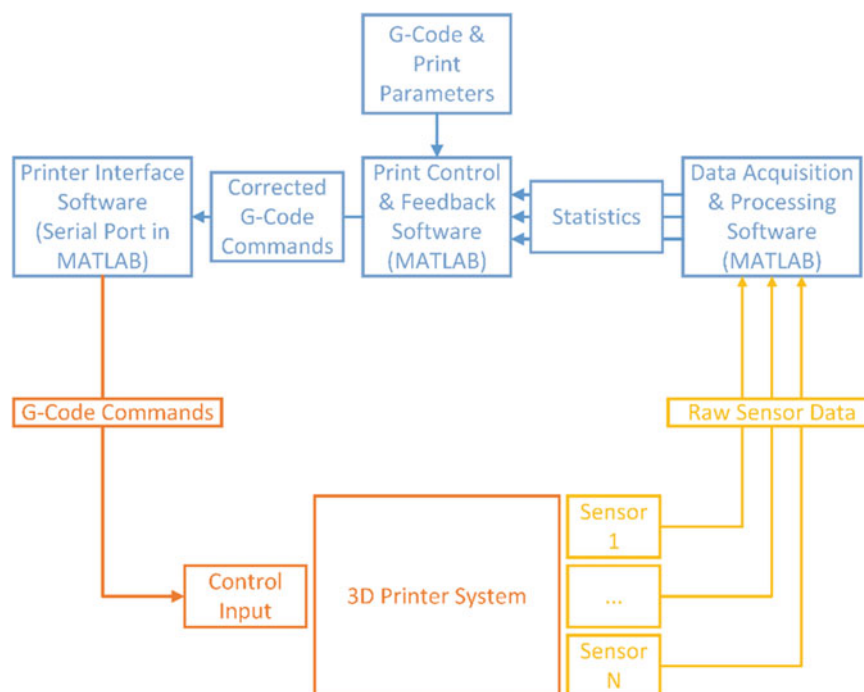


Fig. 14.1 Additive manufacturing unified DAQ and control system architecture

The system developed in this work was a code set written in MATLAB that interfaced with a Lulzbot Taz 6 3D printer and a National Instruments PXI-6250 M-Series Multifunction DAQ. Like any other print control software, it accepted G-code generated from a CAD model using toolpath-planning (“slicer”) software. In this work, Cura Lulzbot Edition configured for the Lulzbot Taz 6 3D printer was used to slice the test geometry. The G-code was parsed and stored by the MATLAB code, referred to as the Print Control & Feedback Software in Fig. 14.1. This software was responsible for interfacing with the printer via a serial port opened in MATLAB. The printer accepted ASCII G-code commands via the serial port, with a line number prepended and a checksum appended. The printer responded by completing the commands it had been sent and notifying the print control software when they were finished. This setup allowed the Print Control Software to send G-code line-by-line to the printer, allowing the software to synchronize data acquisition to the start and end of each command. Once the DAQ was integrated with the control of the printer and began taking data, that data was able to be mapped back to the position where it was taken. With this mapping ability, three-dimensional visualizations of the diagnostic data were able to be created in the form of MATLAB plots.

### 14.3 Part Failure and Correction Methods

To test this idea of a unified data acquisition and control feedback system, a test part geometry had to be selected. The approach taken was to induce a fault in the part by changing one of the printing parameters and then having the control feedback system change a different printing parameter to correct the induced fault. In addition to being able to induce a repeatable fault, it was also desired to restrict print times to less than 30 min, so that experimental design iterations could be done quickly. Ultimately, a single shell thick, hollow square box was chosen having dimension of 40 mm × 40 mm × 20 mm, Fig. 14.2.

Debonding is a common fault occurring in FDM parts, especially in larger parts in which thermal stresses and differential cooling rates can cause debonding great enough for complete print failure. Even small debonding events can significantly reduce the strength and integrity of the part when deployed in service. Therefore, a debonding type fault was targeted as the fault to be studied. In order to introduce a fault in the printing of the test geometry, several experiments varying extrusion speed, the print head temperature, and the print bed temperature outside the range of the manufacturer recommended settings for these parameters were conducted. It was discovered that increasing the print bed temperature from 25 °C to 60–80 °C and disabling the cooling fan on the print head resulted in a repeatable fault for this geometry. By keeping the bed temperature raised for the duration of the print, temperatures in regions of the part remained above the glass transition temperature for PLA (60–65 °C). Resultantly, the plastic did not solidify enough to support the layers being printed on top of it. This caused the part to slump away from the print head, resulting in a visually detectable fault in which sections of the walls were not bonded together, Fig. 14.2.

Since the fault is induced by temperature variation, a temperature control mechanism needed to be identified to correct the faults. As such, it was found this fault can be statically corrected by enabling the cooling fan for the duration of the print with the elevated print bed temperature. The fan actively cooled the extruded PLA layer to below its glass transition temperature and solidified the plastic layer to create a rigid foundation for the next layer to be printed on. The healthy part, the faulted part, and the statically corrected part are shown in Fig. 14.2.

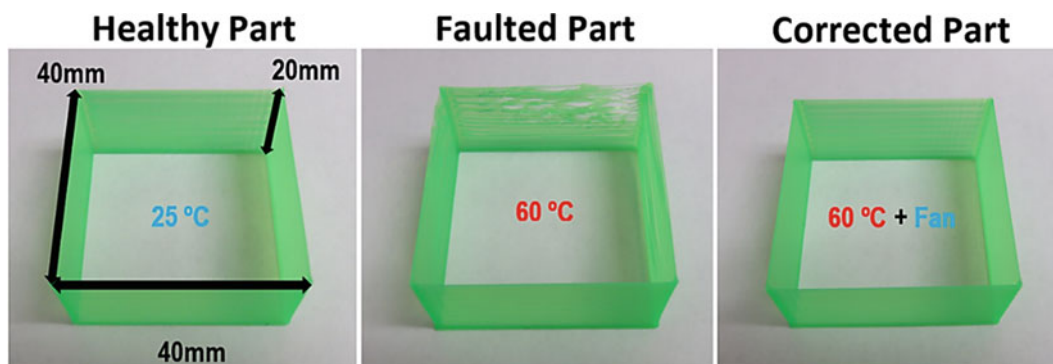


Fig. 14.2 (left to right) Healthy, faulted, and control corrected prints

## 14.4 Control Feedback Demonstration

The logic flow to be executed during the printing of the test geometry is shown in Fig. 14.3. A characteristic signal is collected during the print and compared to a known acceptance value from healthy prints. If the characteristic value is determined to be too far outside the acceptance range, the print will be aborted to save material and machine time being wasted on a failed print. Between the acceptance range and the abort value, the characteristic can be used to determine the control action - in this case, either tune the fan speed to control the level of cooling or simply turn the fan on/off using its max speed.

To clearly demonstrate a simplified version of this process, a 40 mm × 40 mm × 20 mm single shell thick, hollow square box was built. A pause command was inserted into the G-code to temporarily stop the print once the print reached the 20 mm height and move the print bed forward. An excitation transducer (APC 90-4050) attached to the print bed was then driven at 50 kHz, and an acoustic emission sensor (APC PK15I) was placed on the print bed on the opposite side of the part from the excitation transducer. The sensor then collected fifty RMS values of the received signal based on 1.25 million samples each. This was done for twenty healthy prints with the bed temperature at 25 °C to determine the distribution of this characteristic signal. The acceptance range for the characteristic was set to be two standard deviations from the mean of the characteristic.

After this acceptance criteria was determined, the control logic could then be implemented. In this case, the same characteristic signal gathering procedure was used, then the average of the fifty RMS values was compared against the acceptance limit. Simple logic to turn the fan on to its maximum speed and continue building another 20 mm of box height was used for values which fell outside of the acceptance window, and the build proceeded with no fan cooling if it fell within. To exaggerate the level of fault previously discussed, the print bed temperature was increased to 80 °C for five prints with the control turned on. In Fig. 14.4, it is seen that the print was able to largely recover the desired geometrical shape of the part once the control is initiated. For reference the cubic, hollow structure was also printed with the elevated bed temperature and no control (Fig. 14.4, middle) and the structure continued to see deformation and unbonded layers. The diagnostic used to test the control logic was not meant to be robust, but rather to give a quick validation of the performance of fan control concept when implemented into a build. In doing so, this test also demonstrated the capability of the build to meet its prescribed shape at the top of the build when printing on a largely deformed base.

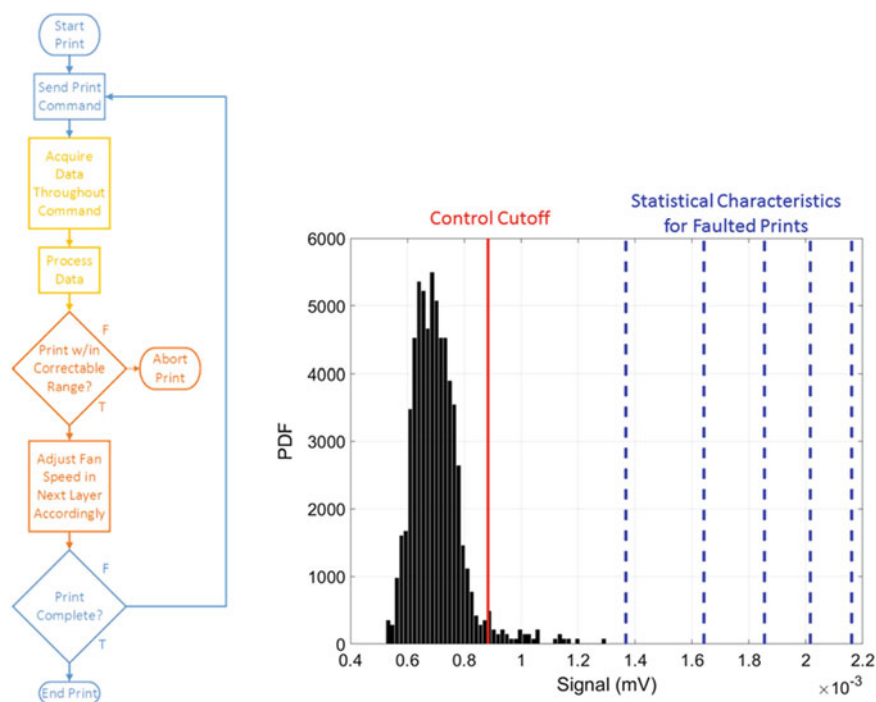


**Fig. 14.3** (left) Control logic flow to correct part failures due to high print bed temperature using cooling fan. (right) PDF of RMS signal strength of transducer at 20 mm test height location with cutoff used for fan control (red) and statistical values of the faulted parts at 20 mm test height location (blue)





**Fig. 14.4** (left to right) Healthy, faulted, and pseudo-static control corrected parts

## 14.5 Process Monitoring System

Previous experimental investigations have used ultrasonic inspection techniques to monitor FDM builds [6, 7]. It was the intention of this work to build off the lessons learned from those studies to design a more robust system of measurement. The methodology explored in [6] involved ultrasonic transducers mounted to the build plate of the printer. One transducer pitched an excitation signal into the build plate that transmitted up into the part and the resulting vibrations were caught by three transducers on the far side of the part. Data analysis from that study indicated that either the sensors themselves or the adhesive used to bond them to the build plate degraded with repeated heat cycling, suggesting that a more robust set of sensors and sensor attachment methods would be appropriate.

A few items were identified to potentially improve on the setup used in [6] (1) improve the power of an ultrasonic excitation source, (2) use of the print head itself as a sensing location would allow automatic localization of the data and easily allow reconstruction 3D diagnostic information of the build process [11], (3) a simpler base measurement might lead to more reliable results and worthwhile statistics. To accommodate these proposed changes, the excitation source used in [7], namely the APC 90-4050, was acquired and attached to the build plate. The simpler base measurement chosen was the energy of a single frequency sinusoid excitation transmitted from the build plate up through the part into the print head. The choice of single frequency excitation tone was also informed by the success of LDV measurements of AM parts in [7], and because a single frequency would be an easy distinguishable signal in the frequency domain. The expectation was that gaps, voids, and debonding would attenuate the transmitted energy of the signal significantly, as shown in Fig. 14.5.

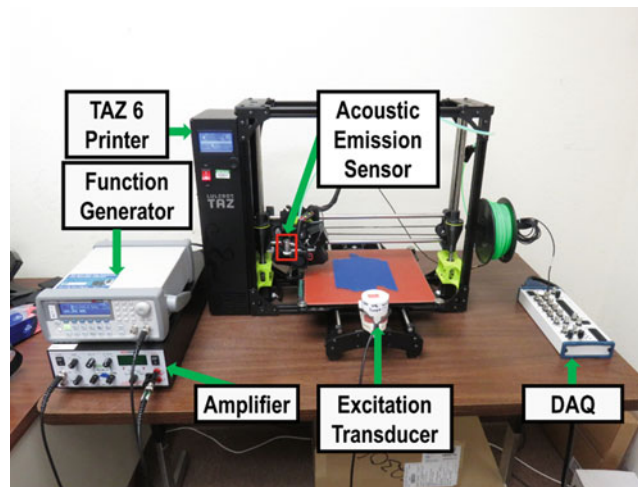
During each extruding command, the build plate was excited with a 40 kHz sinusoidal tone via a power ultrasonic transducer, shown in Fig. 14.6. This vibration propagated through the build plate and up into the part, which then excited the print head. An ultrasonic acoustic emissions sensor was mounted on a modified hot end mounting plate made of ABS plastic with the intention that it would convert the vibrations it experienced into a measurable voltage waveform. It was hypothesized that the strength of the measured 40 kHz tone would be strongly reduced in areas where the extruded filament did not properly bond with the layer beneath it, and that by adaptively estimating the distribution of the magnitude of the 40 kHz component of the measured signal, the integrated framework could be used to estimate the probability of the occurrence of a bond failure event and take action to turn on the cooling fan if necessary.

Figure 14.7 shows the 3D visualization for a healthy print with the setup described, including the printer head movement from its home location to start printing, and the skirt which was printed along with the test part geometry. It was found that this setup needs improvement to make this sensing technique robust. First, the ABS mounting plate for the sensor was susceptible to cracking and should be replaced by a machined aluminum plate instead. Also, the exciter/sensor pair used was not ideal. Excitation from the transducer through air was easily picked up by the sensor and washed out the expected differences in signal strength that were intended to be used to implement the feedback control continuously during the print. This aspect was actually taken advantage of in the previous section for the control logic demonstration, but is not desired in continuous inspection of the part. A more robust exciter/sensor pair for this experiment is currently being researched.





**Fig. 14.5** Schematic concept for healthy (*left*) vs faulted (*right*) signal energy transmission



**Fig. 14.6** Initial experimental setup for in-process ultrasonic inspection

## 14.6 Fault Detection Discussion

Although the diagnostics for the experimental setup were not robust enough to demonstrate the full capability of the integrated DAQ and control framework, ultrasonic techniques show great promise at detecting and localizing faults in the printed parts. To further demonstrate this point, a new analysis of the data collected for [6] is presented here. The previous work mainly focused on the FRF behavior. However, if excitation energy is transferred into the printed part, then a unique signature of the pulse reflecting off the top surface of the part should be present at the receiver transducer locations. In order to identify this signature, cross-correlations of the transmitted signal with the one of the time series data samples from each measurement were computed. To highlight time dependent trends, the temporal average of the computed correlations is removed.

$$\text{Cross - Correlation} : \sum_{n=-N}^N m(x) \cdot h(x - n)$$

Where:  $m(x)$  is the measured signal,  $h(x)$  is the excitation waveform, and  $N$  is the length of  $m(x)$

To give a sense of scale for the correlation plots, the pulse sent during the experiment was 0.1 s long and consisted of a sine chirp from 50–100 kHz, but the scale of the temporal separation which is plotted is 0–0.0005 s, and therefore largely describes only the front edge of the pulse.

Figure 14.8 is the plot of the correlation described above for an “empty” print, i.e. the G-code commands for the desired geometry (a square column) were executed, but no filament was extruded. The plot demonstrates relatively constant behavior across the samples. The data in this study was not integrated with the 3D printer, so sample size index was used instead of

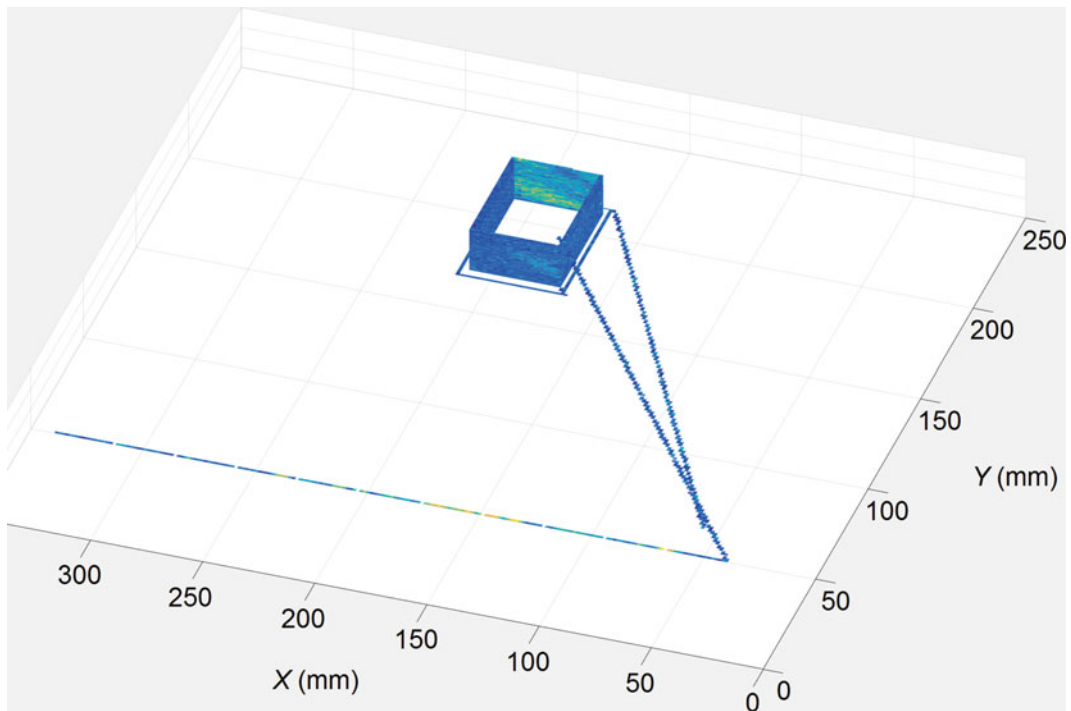


**Fig. 14.7** Example of 3D data visualization of received signal energy collected for test build geometry

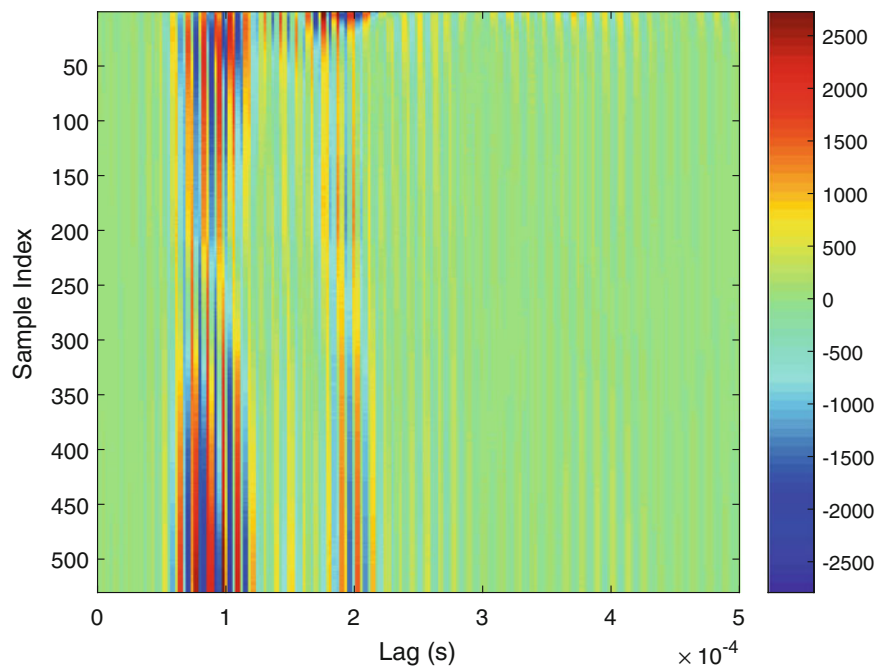


**Fig. 14.8** Demeaned cross-correlations of a print without any filament (empty)

build height. A linear relationship existed between build height and sample index, as the area of each layer in the column was constant, but it has not been computed directly. The vertical lines seen in the cross-correlation plot correspond to where the transmitted signal correlates well with the measured signal. This happened repeatedly, because the pulse is long and its frequency did not change rapidly, meaning the first few sinusoidal cycles align well. These lines suggest the pulse traveled straight from the transmitter to the sensor. Theoretically, any stationary behavior like that seen above should have been removed by the demeaning process, but the data was not exactly stationary during the build possibly caused by the samples being taken while the print bed was in different locations.

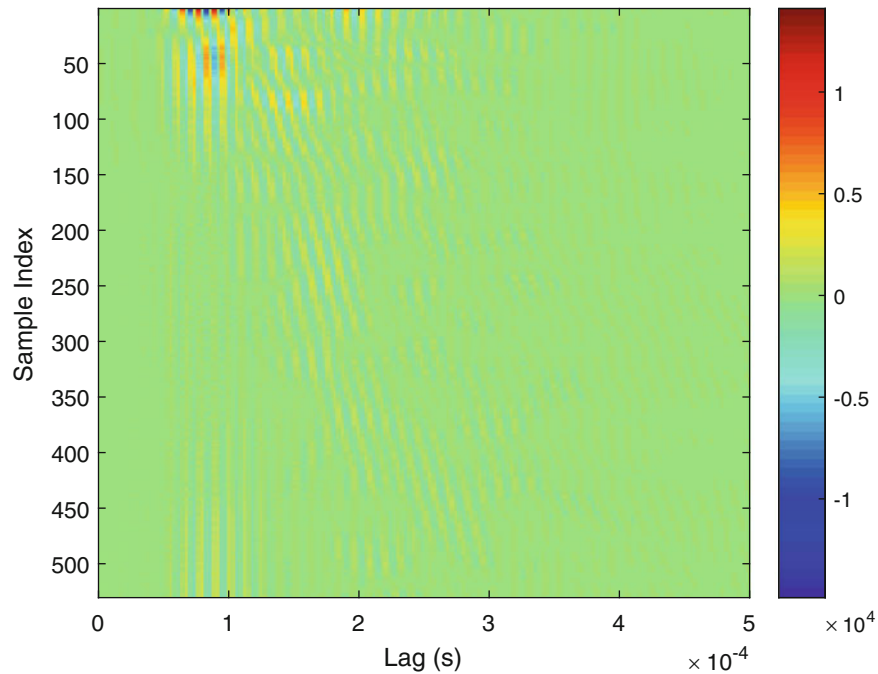


**Fig. 14.9** Demeaned cross-correlations of a healthy print

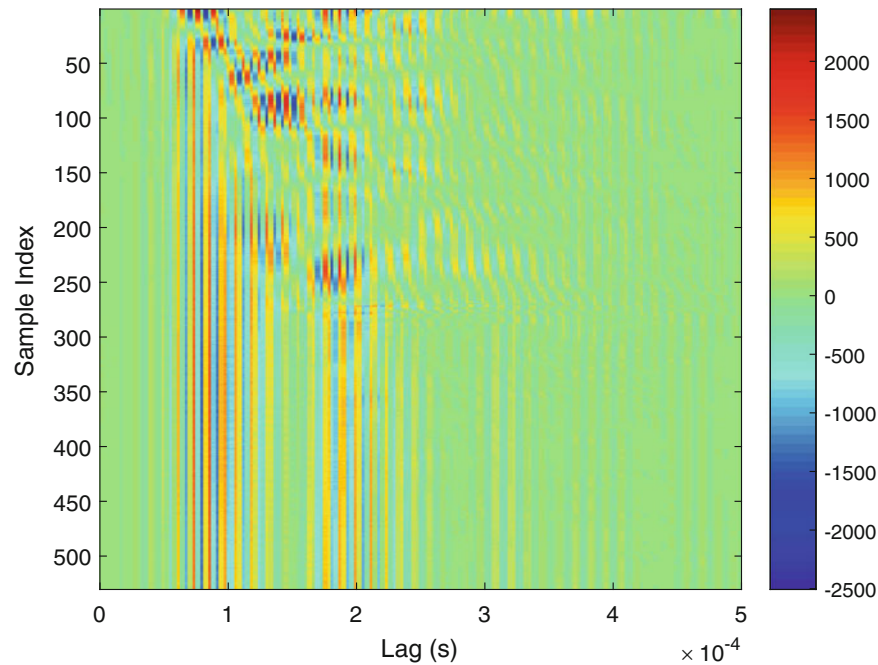


**Fig. 14.10** Demeaned cross-correlations of debonded part (debond near Sample 260–280)

When filament was included and a healthy part was built, Fig. 14.9, in addition to the artifacts of the pulse passing straight through the build plate, a diagonal trend was also observed, indicating a pulse whose arrival was becoming more and more delayed as the part grew. This trend appears to be nearly linear as well, suggesting this second pulse return corresponds to the reflection off of the top of the part as it was being built up and its height grew linearly with time.

The cross-correlation for an intentionally faulted part is shown in Fig. 14.10. The fault was induced by increasing the z-step height at layer 300 for only that layer, introducing a debonding event at that layer. In the plot above, this event

corresponds roughly to sample index 280. The near linearly delayed return is seen in the cross-correlation up until the point in which this debonding event was introduced. The pulse continued to be reflected off of the fault in the part, and did not appear to propagate strongly further into the top section of the part.

These results suggest that the pulse transmitted into the plate travelled up into the part, was reflected off the top surface or the defect layer, and traveled back into the plate, where it was picked up at a later time than the signal that took the direct route to the sensors through the build plate. This phenomenon could also help explain the strange “start-up” behaviors with the general magnitudes of the FRF data presented in [6]. The constructive and destructive interference of shifted pulses could have caused strange behavior in the magnitude of the FRFs.

This data validates the idea that an ultrasonic pulse can travel through a part being built on a 3D printer and be measured by sensors on the build plate. It also validates that a fault can stop the excitation signal from propagating into layers further above the fault, which is fundamental idea proposed in the previous section for fault identification. Future work could improve the clarity of these plots by using a much shorter ultrasonic pulse with characteristics that would create a much sharper cross-correlation profiles, e.g. a random burst. This could allow an algorithm to track the delay of the peak corresponding to the reflected pulse, and compare it with the expected time of arrival for the current height of the part/print head. A stronger excitation source, such as the one used in the experiment presented in this paper and in [7], and a more sensitive transducer than the ones used in [6] may also improve the results.

## 14.7 Conclusions

This work demonstrates the progress toward the development of a closed loop feedback control framework in an FDM application. A repeatable fault and correction mechanism was found to introduce slump and debonding in the parts and fix them. The control logic for this test case was demonstrated in a pseudo-static application of the correction control and can easily be altered in the MATLAB code once the excitation and sensing diagnostics are improved. Although the in-process measurement attempted did not successfully detect part debonding or slumping, it was shown that the unified framework is capable of visualizing detailed 3D data collected during the build process. As this tool matures, it will enable the identification of in process diagnostics for material characterization applications and part testing. Furthermore, new analysis of data from ultrasonic inspection of FDM builds showed that the hypothesis behind the proposed setup has a large chance of success, once a better exciter/sensor combination is acquired, because excitation energy is reflected off of the debonded layer back down into the build plate and should not be received at the printer head. Eventually, the developed unified DAQ and control framework could be applied to closed loop control across a variety of AM processes, not just FDM. However, meaningful diagnostics need to drive the control and may need to be developed for the particular AM technique of interest. Further development may include incorporation of process simulation databases to use for control when diagnostic information for a healthy dataset of built parts is not available.

**Acknowledgements** The authors would like to extend their gratitude to Eric B. Flynn, Eliseanne C. Koskelo, and Niall O’Dowd for their thoughtful discussions on this work. This work was performed at Los Alamos National Laboratory (LANL). LANL is operated by the Los Alamos National Security, LLC for the U.S. Department of Energy NNSA under Contract No. DE-AC52-06NA25396.

## References

1. Wu, H., et al.: In situ monitoring of FDM machine condition via acoustic emission. *Int. J Adv. Manuf. Technol.* (84), 1483–1495 (2016)
2. Strantz, M., et al.: Evaluation of SHM system produced by additive manufacturing via acoustic emission and other NDT methods. *Sensors* (15), 26709–26725 (2015)
3. Clavette, et al.: Chapter 4: Real time NDE of cold spray processing using acoustic emission. In: *Structural Health Monitoring and Damage Detection, Volume 7, Proceedings of the 33rd IMAC, A Conference and Exposition on Structural Dynamics, 2015*
4. Rao, P.K., et al.: Online real-time quality monitoring in additive manufacturing processes using heterogeneous sensors. *J. Manuf. Sci. Eng.* **137** (2015)
5. Sbriglia, L.R., et al.: Embedding sensors in FDM plastic parts during additive manufacturing. In: *International Modal Analysis Conference XXXIV, Orlando, FL, 2016*, pp. 205–214
6. Cummings, I.T., et al.: In-process ultrasonic inspection of additive manufactured parts. In: *International Modal Analysis Conference XXXIV, Orlando, FL, 2016*, pp. 235–247
7. Koskelo, E.C., Flynn, E.B.: Scanning laser ultrasound and wavenumber spectroscopy for in-process inspection of additively manufactured parts. In: *SPIE Smart Structures/NDE 2016, Las Vegas, NV, 2016*

8. Gao, W., et al.: The status, challenges, and future of additive manufacturing in engineering. *Comput. Aided Des.* **69**, 65–89 (2015). doi:[10.1016/j.cad.2015.04.001](https://doi.org/10.1016/j.cad.2015.04.001)
9. Politics & Government Week. Patents; Researchers Submit Patent Application, “Additive Manufacturing with Virtual Planarization Control”, for Approval (USPTO 20150266242) [Online]. Available: <http://search.proquest.com/docview/1719986055?accountid=27865>
10. Cohen, D.L.: Additive manufacturing of functional constructs under process uncertainty. Ph.D. dissertation, Cornell Univ., Ithaca, NY (2010)
11. Flynn, E.B.: Personal correspondence (2016, May)

# Chapter 15

## Reliability of Using Stereo Photogrammetry to Estimate Modal Parameters

Danilo Damasceno Sabino, Peyman Poozesh, Joao Antonio Pereira, and Christopher Niezrecki

**Abstract** Stereophotogrammetry is a three-dimensional full-field measurement technique that has gained more importance in the area of modal analysis in the past few years. In this technique, full-field data can be taken in a single snapshot, which can be considered a great advantage over conventional measurement techniques such as laser vibrometer and accelerometer. However, it is not clear whether the stereophotogrammetry data can provide accurate modal parameters for output-only systems identification applications. This work presents a study that integrates stereophotogrammetry with output-only systems identification aiming at evaluate the use of optical measurement data (stereophotogrammetry) to estimate the modal parameters. A comparative study of two output-only systems identification (Operational PolyMAX and Stochastic Subspace Identification) and ordinary input-output based method (PolyMAX) was carried out to verify the capability of output-only methods to work with stereophotogrammetry data. The Operational PolyMAX provided more clear stability diagram and accurate damping ratio when compared with the reference parameters, however, it missed some modes in the analysis, while SSI has been shown more robust to identify the whole modes in the analyzed frequency range.

**Keywords** Operating modal analysis • Digital image correlation • Operating deflection shapes • Stereophotogrammetry

### 15.1 Introduction

Stereophotogrammetry is an optical non-contact measurement technique that provides some additional measurement capabilities compared to accelerometers and lasers sensors. In the stereophotogrammetry, images captured from a stereo pair of charge-coupled device (CCD) or complementary metal–oxide–semiconductor (CMOS) cameras over a period of time are processed using three dimensional point tracking (3DPT) technique to determine the position of discrete points on the geometry's surface and displacement of the structure subjected to a static or dynamic load [1–5]. The characteristics of this technique show its potential use to Operational Modal Analysis (OMA). Within this work, two output only system identification methods, Stochastic Subspace Identification (SSI) and Operational PolyMAX were employed to estimate modal parameters of a vibrating cantilevered aluminum beam. The beam contains a handful of optical targets and the response of the structure in the target points were captured using a pair of high-speed cameras. The comparative study evaluates the capability of the two output only system identification to deal with optical measurement.

### 15.2 Experimental Modal Analysis Test

The experimental modal analysis test consisted in the mounting the structure and the measuring setup to obtain the responses of a cantilevered aluminum beam using an optical system (cameras) and a set of accelerometers (Fig. 15.1). The accelerometers data were used as reference data for comparison.

---

D.D. Sabino (✉) • J.A. Pereira  
Department of Mechanical Engineering, UNESP – Univ Estadual Paulista, Ilha Solteira, SP, Brazil  
e-mail: [danielosabino@hotmail.com](mailto:danielosabino@hotmail.com)

P. Poozesh • C. Niezrecki  
Structural Dynamics and Acoustic Systems Laboratory, University of Massachusetts Lowell, One University Avenue,  
Lowell, MA 01854, USA



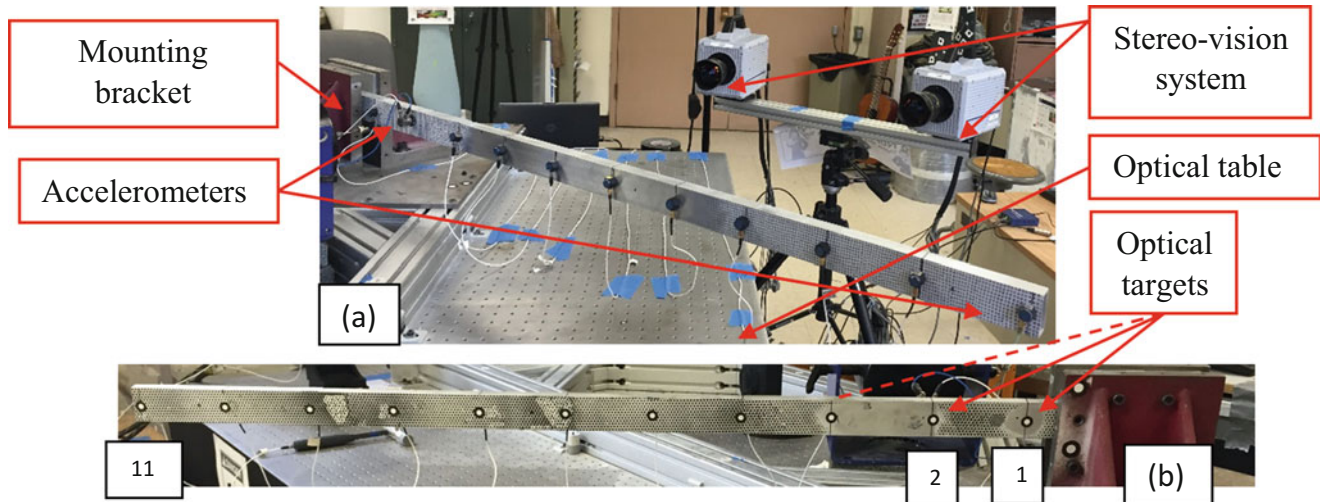


**Fig. 15.1** Test bed is composed of the optical table, structure with the optical targets placed, mounting bracket, stereo-vision measurement systems and the set of accelerometers

**Table 15.1** Estimated frequencies and damping ratios from accelerometer data using the input-output PolyMAX method

Modes	Freq. (Hz)	Damping ratio
1	14.34	0.17
2	89.28	0.15
3	247.07	0.24
4	471.88	0.20

The modal parameters of the structure used as reference to compare with the output-only data were estimated using the PolyMAX method in the LMS™ software. The choice of the PolyMAX method was defined since it is considered an accurate and accepted method for modal analysis [6–8]. In the Table 15.1 is shown the values of the estimated parameters (frequency, damping ratio and modal shapes) used as reference parameters for comparisons.

## 15.3 Operational Modal Analysis

### 15.3.1 Operational Modal Analysis Using Accelerometers Data

The parameters of the model in this FRF analysis were estimated from the only responses measured with the accelerometers. The Operational PolyMAX method from the LMS commercial software and the SSI method from a proper software, denominated Operational and Experimental Modal Analysis System (OEMASys) [9] were used to the analysis. A comparison among the estimated parameters obtained with the Operational PolyMAX and SSI methods are shown in the Table 15.2. The difference in the frequencies and damping ratios values are related to the parameters estimated with the PolyMAX method from the reference data (FRFs). The correlation of the estimated modes with the reference ones (input-output based modes) was calculated using the modes correlation (MAC values matrix) between reference and estimated mode shapes and is shown in the Table 15.3.

The comparison confirms that both output-only systems identification can estimate well the modal parameters of the model using the responses measured with accelerometers in the frequency range analyzed. The result presents almost no discrepancies, confirming the capability of the two methods to estimate the parameters of the model.



**Table 15.2** Frequencies and damping ratios comparison, Operational PolyMAX and SSI method

Modes	Operational PolyMAX				SSI			
	Freq. (Hz)	Damping ratio	Diff. (%)		Freq. (Hz)	Damping ratio	Diff. (%)	
			Freq.	Damp. ratio			Freq.	Damp. ratio
1	14.33	0.13	0.07	23.53	14.32	0.20	0.14	17.65
2	89.24	0.15	0.04	0	89.22	0.22	0.07	46.67
3	247.1	0.25	0.01	4.17	246.90	0.30	0.07	25
4	471.75	0.21	0.03	5	471.62	0.22	0.06	10

**Table 15.3** The modes correlation (MAC values matrix) between reference and estimated mode shapes

	Operational PolyMAX				SSI			
Accelerometer Data								
	1.000	0.016	0.017	0.021	1.000	0.018	0.018	0.006
	0.016	1.000	0.020	0.016	0.016	1.000	0.025	0.008
	0.016	0.020	1.000	0.028	0.017	0.019	0.999	0.025
	0.019	0.016	0.027	1.000	0.020	0.017	0.025	0.976

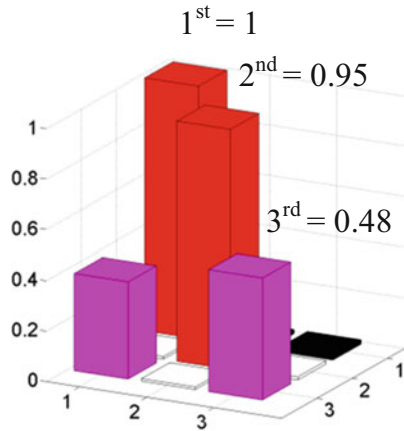
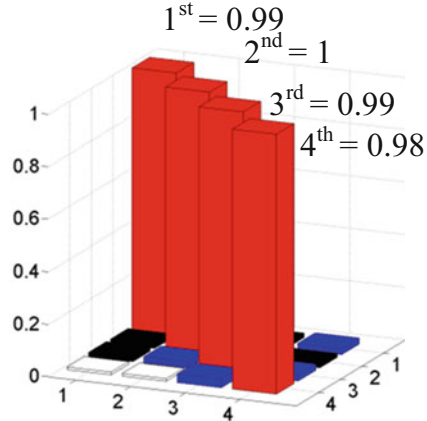
**Table 15.4** Estimated frequencies and damping ratios from stereo-vision data

Modes	Operational PolyMAX				SSI			
	Freq. (Hz)	Damping ratio	Diff. (%)		Freq. (Hz)	Damping ratio	Diff. (%)	
			Freq.	Damp. ratio			Freq.	Damp. ratio
1	14.24	0.48	0.70	182.35	14.19	0.52	1.05	205.88
2	88.13	0.47	1.29	213.33	88.14	0.50	1.28	233.33
3	245.00	0.61	0.84	154.17	244.69	0.80	0.96	233.33
4	X	X	X	X	467.53	0.50	0.92	150

**15.3.2 Operational Modal Analysis Using Optically Measured Data**

In this section the parameters of the model were estimated directly from the displacement data obtained with the stereophotogrammetry system in conjunction with 3DPT technique. In the Table 15.4 are shown the estimated natural frequencies and damping ratios obtained with Operational PolyMAX and SSI methods and their respective differences in relation to the reference parameters.

**Table 15.5** The modes correlation (MAC values matrix) between reference and estimated mode shapes

	<b>Operational PolyMAX</b>	<b>SSI</b>																									
Stereovision Data	 <table border="1" style="margin-left: auto; margin-right: auto;"> <tr><td>1.000</td><td>0.010</td><td>0.385</td></tr> <tr><td>0.017</td><td>0.949</td><td>0.001</td></tr> <tr><td>0.017</td><td>0.012</td><td>0.483</td></tr> </table>	1.000	0.010	0.385	0.017	0.949	0.001	0.017	0.012	0.483	 <table border="1" style="margin-left: auto; margin-right: auto;"> <tr><td>0.998</td><td>0.016</td><td>0.016</td><td>0.010</td></tr> <tr><td>0.028</td><td>1.000</td><td>0.024</td><td>0.009</td></tr> <tr><td>0.017</td><td>0.021</td><td>0.999</td><td>0.034</td></tr> <tr><td>0.023</td><td>0.015</td><td>0.024</td><td>0.989</td></tr> </table>	0.998	0.016	0.016	0.010	0.028	1.000	0.024	0.009	0.017	0.021	0.999	0.034	0.023	0.015	0.024	0.989
1.000	0.010	0.385																									
0.017	0.949	0.001																									
0.017	0.012	0.483																									
0.998	0.016	0.016	0.010																								
0.028	1.000	0.024	0.009																								
0.017	0.021	0.999	0.034																								
0.023	0.015	0.024	0.989																								

The correlation of the estimated modes for each output-only system identification was calculated and is shown in the Table 15.5. In the case of using the accelerometers data, the correlation of the modes of both methods were almost perfect. However, for the optically measured displacement data the Operational PolyMAX did not identified the whole modes in the analyzed frequency range.

This difficulty probably is related with the noise level in the measurement as argued in [6] to explain the variability of the identified modal parameters. The presence of the noise in the measurement makes the estimating of modal parameters from response-based system identification more challenging. It seemed that Operational PolyMAX is more sensitive to the measurement noise than SSI method. It seems that the two output-only systems identification would operate well with optically measured data.

### 15.4 Final Remarks

In this paper, it has been discussed the capability of the output-only systems identification operate with optically measured data (stereophotogrammetry) to estimate the modal parameters of a cantilevered beam. Two output-only systems identification, Operational PolyMAX and Stochastic Subspace Identification, were used. The compatibility of the two systems estimate the parameters of the model was initially investigated using accelerometers measured data. For the estimating of using the optically measured displacements it is more challenging due to the measurement noise level. The SSI method has shown more robust, the Operational PolyMAX did not identified the whole modes in the frequency range analyzed. The presence of the noise in the measurement could be a key factor to estimate the parameters of the model. So, a systematic investigation needs to be carried out to demonstrate the effect of measurement noise on the uncertainty of modal parameters estimated using different output-only systems identification.

## References

1. Helfrick, M.N., Niezrecki, C., Avitabile, P., Schmidt, T.: 3d digital image correlation methods for full-field vibration measurement. *Mech. Syst. Signal Process.* **25**, 917–927 (2011)
2. Baqersad, J., Poozesh, P., Niezrecki, C., Avitabile, P.: Photogrammetry and optical methods in structural dynamics—a review. *Mech. Syst. Signal Process.* **86**, Part B, 17–34 (2017)
3. Poozesh, P., Baqersad, J., Niezrecki, C., Avitabile, P., Harvey, E., Yarala, R.: Large-area photogrammetry based testing of wind turbine blades. *Mech. Syst. Signal Process.* **86**, Part B, 98–115 (2017)
4. Poozesh, P., Sabino, D.D., Baqersad, J., Avitabile, P., Niezrecki, C.: Practical techniques for scaling of optically measured operating deflection shapes. In: *Rotating Machinery, Hybrid Test Methods, Vibro-Acoustics & Laser Vibrometry*, vol. 8, pp. 1–17. Springer (2016)
5. Baqersad, J., Poozesh, P., Niezrecki, C., Avitabile, P.: Full-field strain monitoring of a wind turbine using very limited set of displacements measured with three-dimensional point tracking. In: *ASME 2015 International Design Engineering Technical Conferences and Computers and Information in Engineering Conference*, pp. V008T13A100-V008T13A100 (2015)
6. Peeters, B., Van der Auweraer, H., Guillaume, P., Leuridan, J.: The polymax frequency-domain method: a new standard for modal parameter estimation? *Shock. Vib.* **11**(3–4), 395–409 (2004)
7. Peeters, B., Van der Auweraer, H.: Polymax: A revolution in operational modal analysis. In: *1st International Operational Modal Analysis Conference* (2005)
8. Poozesh, P., Baqersad, J., Niezrecki, C., Avitabile, P.: A multi-camera stereo dic system for extracting operating mode shapes of large scale structures. In: *Advancement of optical methods in experimental mechanics*, vol. 3, pp. 225–238. Springer (2016)
9. Pereira, J.A.: Oemasys—Operational & Experimental Modal Analysis System Developed at the Department of Mechanical Engineering, UNESP- Univ Estadual Paulista, Ilha Solteira

# Chapter 16

## Constant Mass Metastructure with Vibration Absorbers of Linearly Varying Natural Frequencies

Katherine K. Reichl and Daniel J. Inman

**Abstract** This work looks at the effectiveness of constant weight metastructures for vibration suppression. A *metastructure* is a structure with distributed vibration absorbers. The metastructures are compared to a baseline structure of equal mass. The equal mass constraint shows that any increase in performance is due to the addition of the vibration absorbers and not due to adding additional mass to the structure. In this paper, two different metastructure designs are compared. These structures are designed to suppress longitudinal vibrations traveling along the length of the bar. The metastructures have ten vibration absorbers distributed on the length of the bar and the ratio of mass of the absorbers to mass of the host structure is 0.26. One metastructure has all the absorbers tuned to the natural frequency of the host structure and the other metastructure uses absorbers that are tuned to frequencies that have linearly varying natural frequencies. These structures were modeled using two different methods, a one-dimensional (1D) finite element method with lumped mass vibration absorbers and a fully three-dimensional (3D) finite element model. The results show that the metastructure with linearly varying natural frequencies outperforms that metastructure with vibration absorbers tuned to a single natural frequency.

**Keywords** Metastructure • Additive manufacturing • Passive damping

### 16.1 Introduction

Metastructures are a metamaterial inspired concept. Metamaterial research began with the investigation of electromagnetic metamaterials which exhibit a negative permittivity and or permeability [1, 2]. Inspired by the electromagnetic metamaterials, the concepts were extended to acoustic metamaterials [3]. Milton and Willis were the first to conceive the idea of using local absorbers to create structures with negative effective mass that varies with frequency [4]. Liu et al. created the first physical metastructure using local vibration absorbers. This structure is designed to suppress acoustic waves above 300 Hz. Their acoustic metamaterial contains lead spheres coated in a silicone rubber within an epoxy matrix. The lead balls in the rubber are referred to as local resonators. The local resonator mechanism is the same mechanism used for vibration suppression [5]. The research reported here emulates the concept of repeated elements from metamaterials' research to devise a structure with repeated inserts consisting of vibration absorbers. A *metastructure* is defined as a structure with distributed vibration absorbers. Previous research often considers two structures with equal stiffness and compares the response of the structure [6, 7]. The addition of the distributed vibration absorbers leads to an increase in mass of the structure. For aerospace applications, the additional mass is undesirable. This work takes the alternative approach and keeps the mass constant between the baseline structure and the metastructure by redistributing the mass.

In this paper, three different structures are compared. These structures are designed to examine longitudinal vibrations traveling along the length of the bar. All three structures have the same weight. The baseline structure has no vibration absorbers and is used as a baseline to see the improved performance of the metastructures. The other two structures are both metastructures with ten absorbers distributed along the length of the bar. One structure has all the absorbers tuned to the natural frequency of the host structure and the other metastructure uses absorbers that are tuned to frequencies that have linearly varying natural frequencies. These structures were modeled using two different methods, a one-dimensional (1D) finite element method with lumped mass vibration absorbers and a fully three-dimensional (3D) finite element model.

---

K.K. Reichl (✉) • D.J. Inman  
Department of Aerospace Engineering, University of Michigan, François-Xavier Bagnoud Building,  
1320 Beal Avenue, Ann Arbor, MI 48109, USA  
e-mail: [reichl@umich.edu](mailto:reichl@umich.edu)

## 16.2 Metastructure Design

The metastructures are designed to suppression vibrations in the longitudinal direction. The metastructures are composed of the host mass and the distributed absorbers. The host structure is the part of the structure not consisting of the vibration absorbers. The aim is to minimize the vibrations in the host structure. The host structure is a hollow square bar as seen in Fig. 16.1 with  $w = 50$  mm and  $t = 5$  mm. The length of the bar is 45 cm. There are ten vibration absorbers with in the hollow section distributed throughout the length of the bar. The vibration absorbers consist of a bar and a tip mass. The cantilever configuration is arranged such that the bending motion of the beam and tip mass suppress vibrations along the length of the bar. The specific geometry of the absorbers is modified to tune the natural frequency of the absorber. The mass ratio,  $\mu$  of the metastructure is defined as the ratio of mass in the absorbers over the mass in the host structure. For this configuration, the mass ratio utilized is  $\mu = 0.26$ . The host structure has a mass of 473 g leading to the mass of the absorbers to be 123 g. This gives the structure a total mass of 600 g. These parameters are used for both metastructures analyzed in this paper.

The baseline structure is used as a comparison to quantify the improved performance of the metastructure. The baseline structure has no vibration absorbers and consists of just the hollow square cross-section. The dimensions of the baseline bar are  $w = 50$  mm and  $t = 6.5$  mm. The length is also 45 cm. Since the baseline structure and the metastructure are the same weight, 600 g, the baseline structure has a slightly larger thickness to account for the lack of vibration absorbers. 3D CAD models of the metastructure and the baseline structure are shown in Fig. 16.2. The material properties for all structures utilized are those from the Objet Connex 3D printer by Stratasys, specifically the DM8430 digital material. The Young's modulus and density of the material are 1.97 GPa and 1168 kg/m<sup>3</sup> respectively. The 3D printer will be used for the fabrication of an experimental prototype in future work.

**Fig. 16.1** Cross sectional area of bar

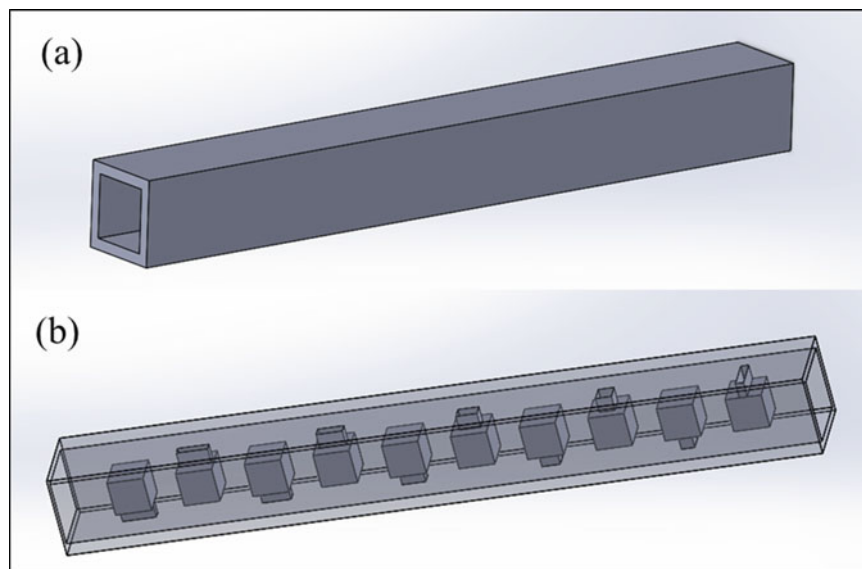
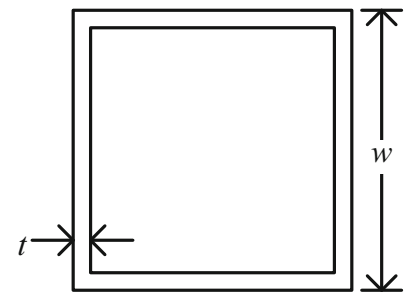


**Fig. 16.2** 3D models of (a) baseline structure and (b) metastructure with vibration absorbers with linearly varying natural frequencies

## 16.3 Modeling

Two different modeling methods were utilized. A 1D model and a fully 3D finite element model. The 1D finite element was created in MATLAB. Because of the simplicity of the 1D model, the simulation runs quickly and can be optimized relatively easily in order to find the ideal range of natural frequencies for the absorbers. The 3D finite element model was created in Abaqus using 3D tetrahedral elements. The 3D modeling allows us to capture the 3D effects present in all systems leading to a more accurate model. For both modeling procedures, we are interested in the frequency response function (FRF) of the structures. The frequency range of interest for these structures is 0–1500 Hz. As a performance measure, the area under the FRF within this frequency range is utilized. A smaller area corresponds to lower vibration response from the structure. Three different structures are analyzed, a baseline structure and two metastructures. The first metastructure has all the vibration absorbers tuned to the same natural frequency while the second one has the absorbers tuned to a range of frequencies. Previous work has shown that varying these frequencies is beneficial [8] and this work seeks to confirm this using a 3D finite element model.

### 16.3.1 1D Finite Element Model

This 1D finite element model is depicted in Fig. 16.3. The host structure is discretized into 100 elements along the length of the bar and a simple bar 2-noded bar element is utilized. The vibration absorbers are modeled as lumped masses and springs and are distributed evenly throughout the length of the bar. The mass of the vibration absorbers is chosen such that the mass ratio,  $\mu = 0.26$  is achieved and the stiffness of the absorbers varies such that specific natural frequencies can be achieved. The baseline structure is modeled using 100 bar elements. The finite element model allows us to determine the mass and stiffness matrices for this model. Using these matrices, the system can be transformed into state space and the frequency response function of the structure is calculated.

The simplicity of this model allows an optimization procedure to easily be implemented. Varying the stiffness of the vibration absorbers results in different natural frequencies of the absorbers leading to a different response in the structure. All other parameters are kept constant and the stiffness values are varied. The stiffness values are constrained to vary in a linear fashion thus the minimum and maximum values characterize these values. The objective function of the optimization is the area under frequency response function as described above. The optimization is done in MATLAB using a constrained non-linear interior point algorithm (`fmincon`). The results of the optimization show that the natural frequencies of the absorbers should vary from 450 Hz to 1100 Hz in order to achieve the best performance. The natural frequency of the host structure is 721 Hz.

### 16.3.2 3D Finite Element Model

The 3D finite element modeling is done in Abaqus. This allows us to capture the 3D effects of the structure which do not appear in a 1D model. Also, the 3D modeling allows for a realistic vibration absorber geometry to be determined which has a natural frequency that matches the desired frequency. The vibration absorbers utilized consist of a cantilever beam with a large tip mass. This design is the same design utilized by other researchers [9]. To vary the natural frequency of the absorber, the cross-sectional area of the beam is varied. A larger thickness of the beam leads to a stiffer absorber which raises the natural frequency. To keep the mass of all the vibration absorbers constant, the cross-sectional area of the beam is

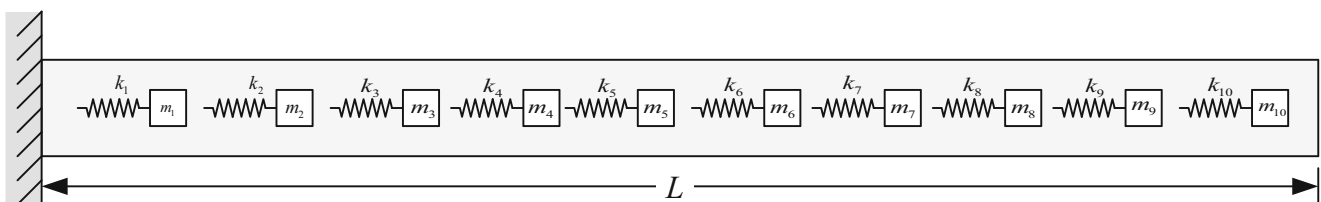
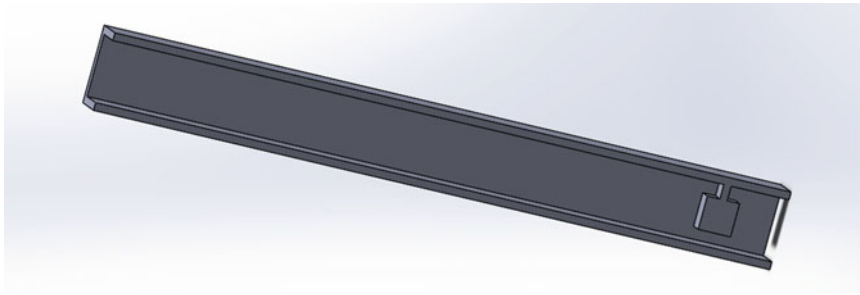


Fig. 16.3 1D finite element model with lumped mass vibration absorbers



**Fig. 16.4** 3D model used to determine the natural frequency of the absorbers

**Table 16.1** Geometry properties of the vibration absorbers and the resulting natural frequency

Absorber	Thickness [mm]	Width [mm]	Area [mm <sup>2</sup> ]	Distance from root [cm]	Finite element frequency [Hz]
1	20.3	4.93	100.1	40.9	939.8
2	18.7	5.3	99.1	36.8	913.9
3	17.2	5.81	99.9	32.7	875.4
4	15.6	6.38	99.5	28.6	839.2
5	14.1	7.07	99.7	24.5	794.8
6	12.59	7.94	100.0	20.5	764.0
7	11.05	9.05	100.0	16.4	648.3
8	9.51	10.5	99.9	12.3	610.6
9	7.97	12.6	100.4	8.2	564.2
10	4.88	20.5	100.0	4.1	426.5

restricted to be constant throughout the entire structure. Thus, an increased thickness of the beam will result in a decrease in the width of the beam. To tune the natural frequencies of the vibration absorber, a 3D finite element model was necessary. The stiffness of the host structure contributes significantly to the natural frequency of the absorber thus must be accounted for in the modeling. To achieve this each absorber was modeled by itself attached to the host structure as seen in Fig. 16.4 and a modal analysis is performed. This allows the stiffness of the host structure to be accounted for while eliminating the interactions between the various vibration absorbers. The results of this modeling are shown in Table 16.1. The entire range of frequencies from the optimization procedure described above was not able to be achieved. The optimization called for frequencies ranging from 450 Hz to 1100 Hz. In order to reach frequencies above 940 Hz, the thickness of the beam needed to be greater than 21 mm. The absorber mass is 21 mm in length on each side, thus the dimensions of the beam must be less than 21 mm. The dimensions shown in Table 16.1 are used for the final design of the metastructure with varying frequencies. The metastructure with vibration absorbers having a single frequency used absorber seven for all ten of the vibration absorbers which has a natural frequency closest to that of the host structure, 721 Hz.

## 16.4 Results

For each of the three designs, (1) the baseline structure, (2) the metastructure with linearly varying natural frequencies and (3) the metastructure with vibrations absorbers with a single frequency both models were used to create the resulting FRF. All three of these structures have equal mass so any increase in performance is due to the addition of the vibration absorbers and not due the addition of mass to the structure. The results for the various structures and models are shown in Fig. 16.5. The FRF plotted is the response of the tip mass due to a loading at the tip mass. All the FRFs plotted are normalized with respect to the static response of the baseline structure.

As mentioned previously, the performance of the structure is characterized by the area under the FRF from 0 Hz to 1500 Hz and is compared to the response of the baseline structure. These results are shown Table 16.2. In both cases the metastructure with linearly varying natural frequencies performs better that the baseline structure but that is not the case for the metastructure with all the absorbers tuned to the same natural frequency. The 3D finite element model shows better performance but the 1D model does not. This discrepancy is likely due to damping of the structure not being modeled effectively. Even though the results for the two models do not match up very well, both models show the same trends.



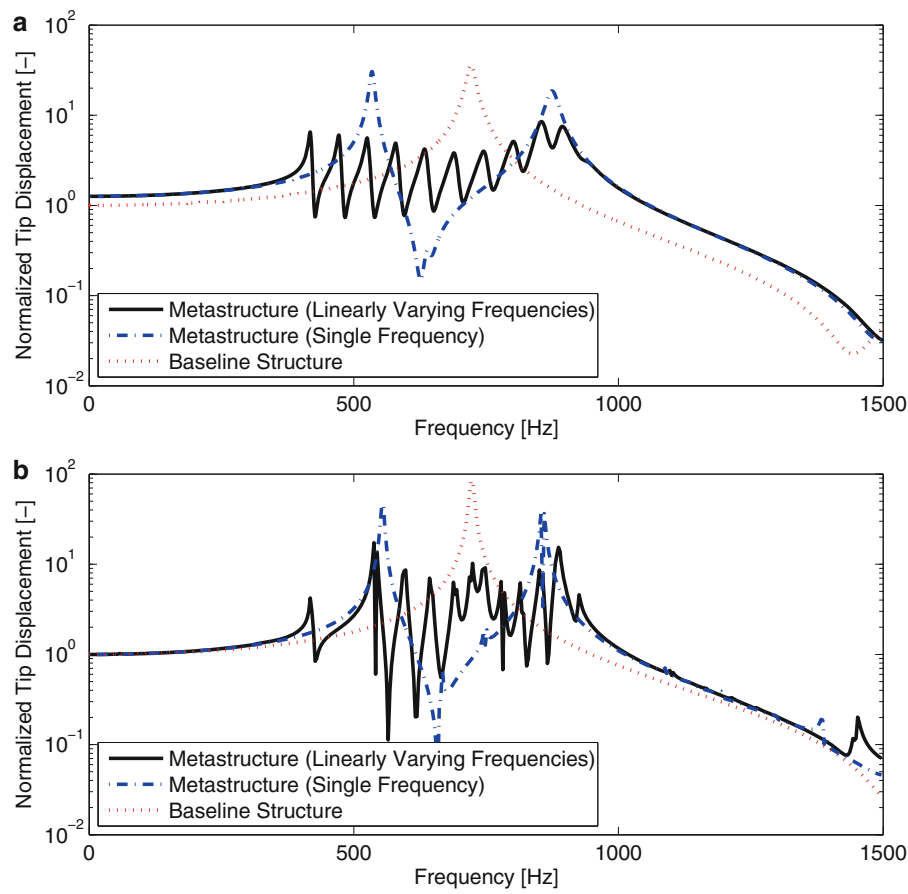


**Fig. 16.5** FRF of the metastructure and baseline structure for the (a) 1D finite element model and (b) 3D finite element model

**Table 16.2** Performance measure results for both metastructures and both models

	Single absorber frequency		Multiple absorber frequencies	
	Absorber natural frequency [Hz]	Decrease in area from baseline structure	Absorber natural frequency range [Hz]	Decrease in area from baseline structure
1D finite element model	648.3	-8.32%	426.5–939.8 Hz	14.8%
3D finite element model		16.2%		29.6%

For the metastructure with a single vibration absorber, there are clearly two peaks on either side of the natural frequency of the baseline structure. The metastructure with multiple frequencies, many small peaks can be seen throughout the range of frequencies of interest. Both models show that the metastructure with absorbers tuned to multiple natural frequencies has better performance than the metastructure with the absorbers tuned to a single frequency. When using a model, it is hard to capture the true effects of damping. This shows the necessity of conducting experimental tests to better quantify how the damping contributes to the results.

**Acknowledgements** This work is supported in part by the US Air Force Office of Scientific Research under the grant number FA9550-14-1-0246 “Electronic Damping in Multifunctional Material Systems” monitored by Dr. BL Lee and in part by the University of Michigan.

## References

- Engheta, N., Ziolkowski, R.W.: *Metamaterials: Physics and Engineering Explorations*, IEEE (2006)
- Laszlo, S., Shamonina, E.: A historical review. In: *Waves in Metamaterials*, pp. 315–324 (2009)
- Cummer, S.A., Christensen, J., Alù, A.: Controlling sound with acoustic metamaterials. *Nat. Rev. Mater.* **1**(3), 16001 (2016)
- Milton, G.W., Willis, J.R.: On modifications of Newton’s second law and linear continuum elastodynamics. *Proc. R. Soc. A Math. Phys. Eng. Sci.* **463**(August 2006), 855–880 (2007)

5. Liu, Z., Zhang, X., Mao, Y., Zhu, Y.Y., Yang, Z., Chan, C.T., Sheng, P.: Locally resonant sonic materials. *Science*. **289**(5485), 1734–1736 (2000)
6. Baravelli, E., Ruzzene, M.: Internally resonating lattices for bandgap generation and low-frequency vibration control. *J. Sound Vib.* **332**(25), 6562–6579 (2013)
7. Yu, T., Lesieutre, G.A.: Damping of sandwich panels via acoustic metamaterials. In: *AIAA SciTech, 57th AIAA/ASCE/AHS/ASC Structures, Structural Dynamics and Materials Conference* (2016)
8. Reichl, K.K., Inman, D.J.: Modelling of low-frequency broadband vibration mitigation for a bar experiencing longitudinal vibrations using distributed vibration absorbers. In: *20th International Conference on Composite Materials* (2015)
9. Hobeck, J.D., Laurant, C.M.V, Inman, D.J.: 3D printing of metastructures for passive broadband vibration suppression. In: *20th International Conference on Composite Materials* (2015)

# Chapter 17

## Study on Random Decrement Signature Under Different Triggering Level and Length of Time History

Jinzhi Wu, Xiujuan Zheng, Jie Hu, Yigang Zhang, and Fuh-Gwo Yuan

**Abstract** Random Decrement Technique (RDT) is a widely used method to extract free decay response data by averaging time segments obtained under certain triggering condition from structural vibration response. And thus, different triggering condition will inevitably lead to different Random Decrement Signature (RDS) and different modal parameters. The quality of RDS has significant influence on the modal parameter identification results. Based on three assessments criteria for RDS's quality, statistical analysis of change law of RDS with different triggering level and length of time history are carried out by a SDOF system and a 6-DOF system. A multi-triggering method is proposed, by which a better RDS can be obtained. Numerical simulation and the practical engineering application verified the recommended method and values.

**Keywords** Random decrement technique • Triggering level • Length of time history • Modal parameters • Space truss

### 17.1 Introduction

In order to transform a random time series into a free decay of the structure, instead of estimating the Power Spectral Density (PSD) and the auto correlation function, Random Decrement Technology (RDT) was introduced by Cole at NASA during the late 1960s and early 1970s based on a conceptual illustration of primary statistics of the Random Decrement Signature (RDS) [1, 2]. In 1977, Ibrahim extended auto RDS to cross RDS by multi-point measurements method and identified the structure's model shape [3]. In 1982, Vandiver presented the mathematical basis for RDT [4]. In the particular case of a linear, time invariant system excited by a zero mean, stationary, Gaussian random process, Vandiver obtained that a RDS is proportional to the correlation function and limited subsample number of RDS estimation is unbiased estimation of theoretical RDS. In 1986, Bedewi expanded Vandiver's mathematical proof into multiple degrees of freedom system [5]. In 1991, Brincker calculated and compared the RDT and frequency response function as two kinds of estimate of the correlation function, results show that RDT is more accurate and rapid than FFT [6]. Due to its simple and clear physical meaning, RDT has been widely used in structural modal parameter identification under environmental excitation [7–9].

There are so many triggering condition choices during using RDT. Cole used the level crossing triggering condition [1]. Based on level triggering condition, Asmussen proposed local extremum triggering condition, positive point triggering condition, zero crossing triggering condition, general triggering condition, and put forward the vector triggering conditions to reduce the computation of RDS matrix [10]. In practice, the most widely used is still the level crossing triggering condition [7–9], but triggering level has not been determined under a certain sampling length. Cole discussed and recommended the level crossing triggering condition from  $1.2 \sigma_x$  to  $1.4 \sigma_x$ , the standard deviation of the measured time history, for better damping ratio identification and shorter testing time [1]. Brincker suggested from  $1.0 \sigma_x$  to  $2.0 \sigma_x$  based on the comparison with correlation function [11]. Asmussen pointed that the shape invariance criteria (SIC) can be used to check the shape invariance of the RDSs, and  $\sqrt{2}\sigma_x$  is recommended [10].

The aim of this paper is to find the appropriate triggering level value and the appropriate length of time history, so that better modal parameters can be extracted from the RDSs. The work will be carried out based on four aspects: (1) Study on the assessment criterion of RDS's quality. (2) Statistical analysis of the characteristics of RDSs under different triggering levels and different lengths of time history of a single degree of freedom model. (3) Investigation to the modal parameters

---

J. Wu (✉) • X. Zheng • J. Hu • Y. Zhang  
Space Structures Research Center, Beijing University of Technology, Beijing 100124, China  
e-mail: iassjzwu@vip.sina.com

F.-G. Yuan  
Department of Mechanical and Aerospace Engineering, North Carolina State University, Raleigh, NC, USA

identified by Ibrahim Time Domain method (ITD) [12] and Eigensystem Realization Algorithm (ERA) [13] based on the RDSs under different triggering levels to find the appropriate triggering level. and (4) Numerical simulation and the practical engineering application to confirm the validity of selected values.

## 17.2 Theoretical Basis

### 17.2.1 RDS and Its Variance

RDS of a random response process is given by

$$\delta(\tau) = E[x(t_i + \tau) | x(t_i) = x_s] \tag{17.1}$$

where  $\delta(\tau)$  denotes RDS,  $t_i$  is the triggering time,  $\tau$  is time delay,  $x_s$  is triggering level [4]. The basic concept of RDT is shown in Fig. 17.1.

In practical engineering, the sampling data of a random process is limited, and the RDS can be estimated as the average of the time segments  $x(t_i + \tau)$  of the response.

$$\hat{\delta}(\tau) = \frac{1}{N} \sum_{i=1}^N (x(t_i + \tau) | x(t_i) = x_s) \tag{17.2}$$

where  $N$  is the number of triggering points, i.e. the subsample number.

According to Vandiver [4] and Huang [14], when subsamples are independent, zero-mean Gaussian stationary process, the estimation of RDS is unbiased. The mean value and variance of the estimate are

$$E[\hat{\delta}(\tau)] = \delta(\tau) \tag{17.3}$$

$$\text{Var}[\hat{\delta}(\tau)] = \frac{R_x(0)}{N} \left( 1 - \frac{R_x^2(\tau)}{R_x^2(0)} \right) \tag{17.4}$$

where  $R_x(\tau)$  is correlation function,  $R_x(0) = \sigma_x^2$ ,  $\sigma_x^2$  is variance of the zero-mean Gaussian stationary process.

According to Rice formula [15],

$$N = 2f_n T e^{-\frac{x_s^2}{2\sigma_x^2}} \tag{17.5}$$

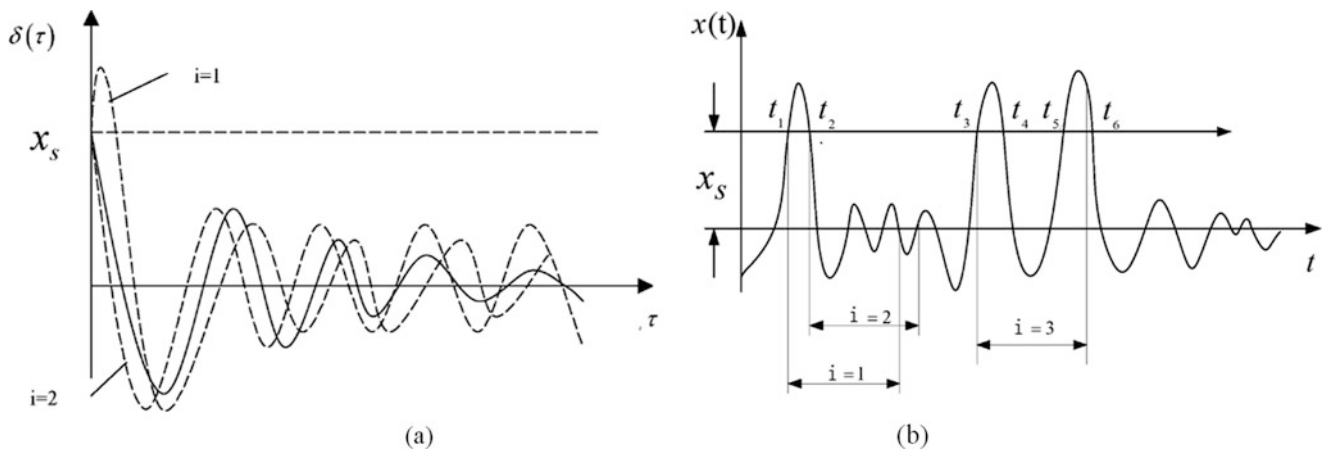


Fig. 17.1 RDT's basic principle

where  $f_n$  is first frequency, T is the length of time history. Equation (17.4) becomes

$$\text{Var} [\widehat{\delta}(\tau)] = \frac{\sigma_x^2}{2f_n T} \left( 1 - \left( \frac{R_x(\tau)}{\sigma_x^2} \right)^2 \right) e^{\frac{-x_s^2}{2\sigma_x^2}} \quad (17.6)$$

It can be seen obviously that triggering level and length of time history have influence on RDS's variance. These will be studied in the following sections.

### 17.2.2 Quality Assessment of RDS

In order to assess the quality of RDS, three indexes are used.

(1) The sum of square error of RDS to random response can be defined as

$$SSE_1 = \sum_{n=1}^N \varepsilon_1^2(n) \quad (17.7)$$

$$\varepsilon_1(n) = \frac{\delta(n) - y_f(n)}{y_f(0)} \quad (17.8)$$

where  $\varepsilon_1$  is the difference between RDS and free response, as shown in Eq. (17.8),  $y_f$  is the free response of the system, n is the data point;  $y_f(0)$  represents the initial displacement of the free response. If RDS is obtained from displacement response of the structure under triggering level  $x_s$ , then  $y_f$  is scaled by setting  $y_f(0)$  to  $x_s$ .

(2) The sum of square error of RDS to correlation function

$$SSE_2 = \sum_{n=1}^N \varepsilon_2^2(n) \quad (17.9)$$

$$\varepsilon_2(n) = \frac{\delta(n) - y_c(n)}{y_c(0)} \quad (17.10)$$

where  $y_c$  is the correlation function. If RDS is obtained from displacement response of the structure under triggering level  $x_s$ , then  $y_c$  is scaled by setting  $y_c(0)$  to  $x_s$ .

(3) Shape Variance Criteria (SVC). With reference to Asmussen's Shape Invariance Criteria (SIC) of the RDS [10], SVC can be defined as

$$SVC = 1 - \frac{(y_{rds_1} \cdot y_{rds_2})^2}{y_{rds_1}^2 \cdot y_{rds_2}^2} \quad (17.11)$$

where  $y_{rds_1}$  and  $y_{rds_2}$  are two RDSs of a random process under different triggering level. The greater the value of SVC is, the higher the shape variance degree will be.

## 17.3 Simulation Analysis of a SDOF System

A SDOF system is used as shown in Fig. 17.2, where the mass is  $m = 1$  kg, the stiffness is  $k = 64$  N/s, and the damping is  $0.06$  N·s/m, so the damping ratio is  $0.03$  and the undamped natural frequency is  $8$  rad/s, the basic period is  $0.785$  s. The exciting load  $F(t)$  is a zero-mean Gaussian stationary random process, the sampling frequency is  $100$  Hz, and the output signal contains  $20\%$  of noise.

(1) Change of RDS's quality with triggering level

The triggering level  $x_s$  ranges from  $0.1 \sigma_x$  to  $3.0 \sigma_x$ , with the increment step of  $0.1 \sigma_x$ . When the length of time history is longer than  $100$  s, the quality of RDSs tends to be stable. The quality of RDS is shown in Fig. 17.3. It can be seen that better quality of RDS appears under triggering level rang of  $(0.5-2.0) \sigma_x$ . The three assessment indexes show the same law.

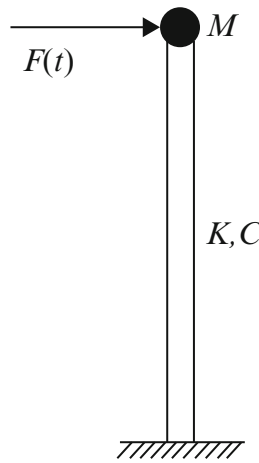


Fig. 17.2 Single degree of freedom model

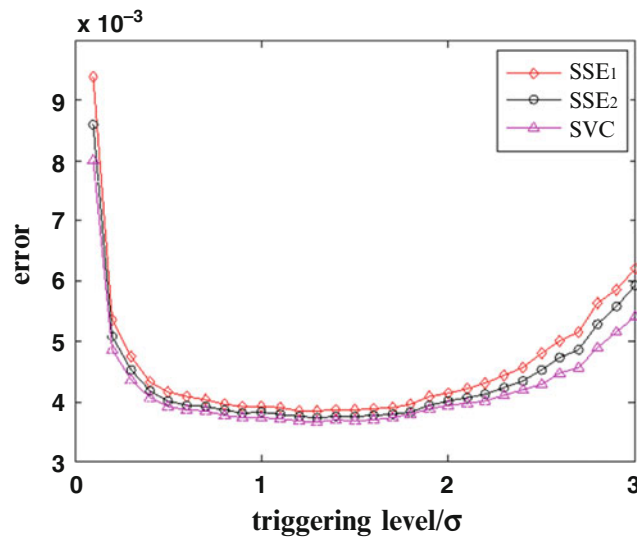


Fig. 17.3 RDS quality changes with triggering level

When the sample size is large enough, different triggering level values within the interval of  $(0.5-2.0) \sigma_x$  have not much influence on RDS's quality. 100 samples are simulated in this paper. However, in practical engineering application, RDS's quality will fluctuate when different triggering level values are taken within the interval of  $(0.5-2.0) \sigma_x$  due to the deficiency of sample size. As shown in Fig. 17.4, the change law of RDS's quality with triggering level value during single sampling is not remarkable.

Therefore, multi-triggering method is used to obtain the RDS. The value of triggering levels are taken from  $x_{s1}$  to  $x_{s2}$ , with the increment step of  $\Delta x_s$ . There are  $m$  groups in total, so

$$m = \frac{x_{s2} - x_{s1}}{\Delta x_s} + 1 \tag{17.12}$$

RDS corresponding to every triggering level value is adjusted into  $\delta'$  proportionally by setting the initial value as  $x_{s1}$ , and then the new RDS is obtained through weighted averaging, which can be called averaged random signature (ARDS). It is defined as follows:

$$\delta = \frac{1}{m} \sum_{i=1}^m q_i \delta'_i \tag{17.13}$$

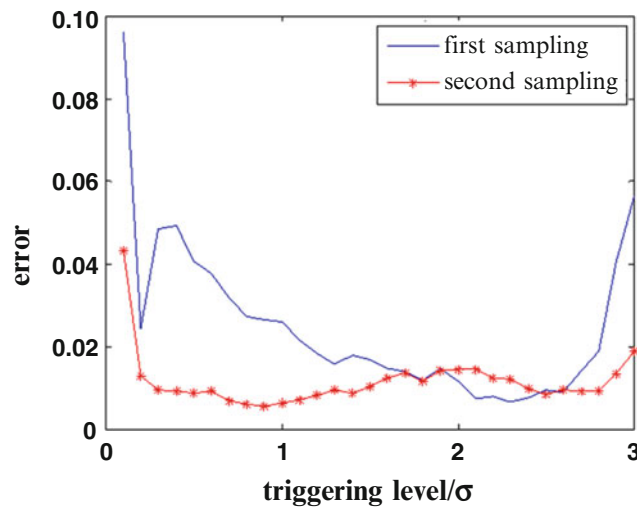


Fig. 17.4 RDS quality changes with triggering level for single sampling

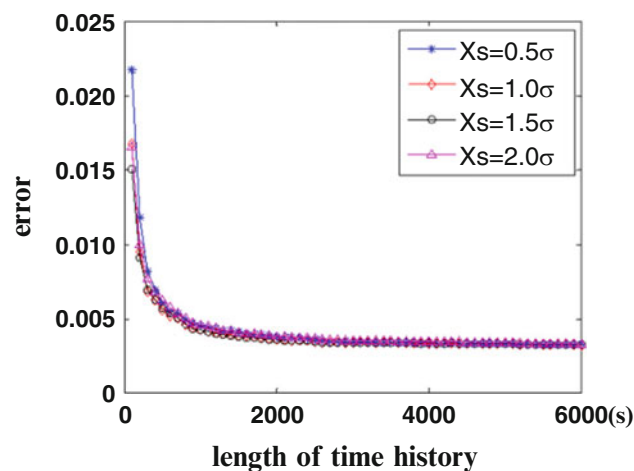


Fig. 17.5 RDS quality changes with length of time history

where  $\delta$  is the linear combination of RDSs under various triggering levels. For a linear system, it is easy to prove that  $\delta$  is also a kind of RDS of the response.

Through the averaging process of ARDS, the differences of RDS's quality caused by different triggering level values in practical engineering can be avoided. Meanwhile, the noise can be reduced to some extent.

#### (2) Change of RDS's quality with length of time history

The length of time history ranges from 100 s to 6000 s, with the increment step of 100 s. As shown in Fig. 17.5, RDS's quality is improved obviously with the increase of length of time history when it is less than 1000 s. but when time length is longer than 1000 s, the quality of RDSs tends to be stable. The three assessment indexes show the same law.

From the above analysis, it can be seen that the three indexes are all can be used to assess the quality of RDS.

In order to study the influence of length of time history on the modal parameters identified based on the RDSs, ITD method is used to extract the frequency and damping ratio. The results show that for this structure, when length of time history is greater than 2000 times of basic period, that is 1570 s, modal parameter identification effect tends to be stable relatively, as shown in Fig. 17.6. Therefore, length of time history is recommended to be longer than 2000 times of basic period in practical engineering application.

According to Figs. 17.4 and 17.6, the variation trend of modal parameter identification is consistent with the change of RDS's quality, especially the identification of frequency. Hence RDS's quality can be used to predict the appropriate length of time history.



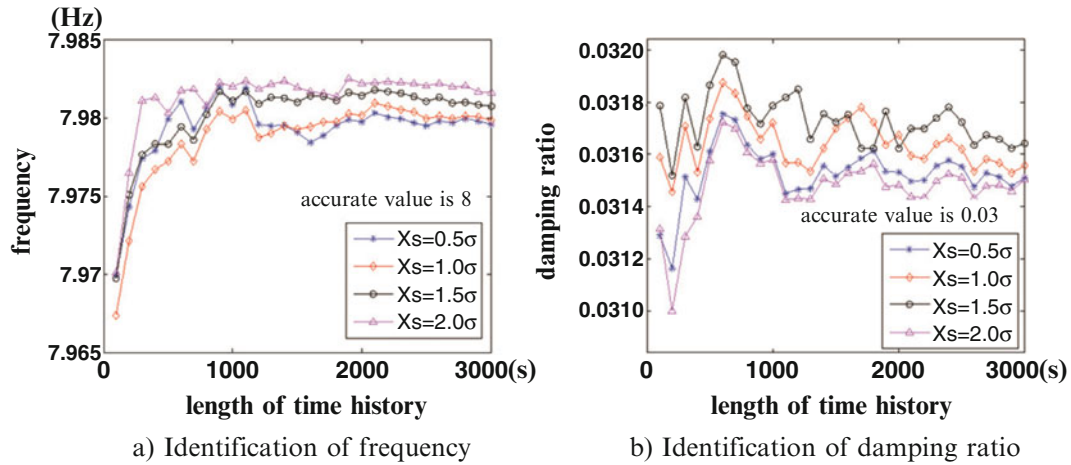


Fig. 17.6 Frequency and damping ratio changes with length of time history

## 17.4 Numerical Simulation of a 6-DOF System

Consider a linear vibration system with 6 degrees of freedom, the values of mass matrix  $M$ , stiffness matrix  $K$ , and damping matrix  $C$  are given as follows:

$$M = \begin{bmatrix} 2 & 0 & 0 & 0 & 0 & 0 \\ 0 & 2 & 0 & 0 & 0 & 0 \\ 0 & 0 & 2 & 0 & 0 & 0 \\ 0 & 0 & 0 & 2 & 0 & 0 \\ 0 & 0 & 0 & 0 & 3 & 0 \\ 0 & 0 & 0 & 0 & 0 & 4 \end{bmatrix} N \cdot s^2/m \quad K = 600 \cdot \begin{bmatrix} 1 & -1 & 0 & 0 & 0 & 0 \\ -1 & 2 & -1 & 0 & 0 & 0 \\ 0 & -1 & 2 & -1 & 0 & 0 \\ 0 & 0 & -1 & 2 & -1 & 0 \\ 0 & 0 & 0 & -1 & 3 & -2 \\ 0 & 0 & 0 & 0 & -2 & 5 \end{bmatrix} N/m$$

$$C = 0.05M + 0.001K + 0.2 \begin{bmatrix} 1 & \dots & 1 \\ \vdots & \ddots & \vdots \\ 1 & \dots & 1 \end{bmatrix}_{6 \times 6} N \cdot s/m$$

In numerical simulation, the excitation is zero-mean stationary white noise, and displacement response signals at various degrees of freedom are obtained. The sampling frequency is 100 Hz, and 20% of measurement noise is considered.

According to the multi-triggering method,  $x_{s1}$  is  $0.5 \sigma_x$  and  $x_{s2}$  is  $2.0 \sigma_x$ . The result of RDS's quality is presented in Fig. 17.7. It can be seen that the RDS's quality by the multi-triggering method is much better than any other single triggering. This model's basic period is 1.25 s, so the value of 2500 s will be adopted as length of time history. ERA is used to identify modal parameter, and the identification results are shown in Table 17.1. The identification results are pretty good, which means that multi-triggering method and length of time history recommended in this paper are effective.

## 17.5 Engineering Application

The space truss canopy of a stadium is about 120 m long and 40 m wide as shown in Fig. 17.8. The accelerometers are placed on the nodes of lower chords as shown in Fig. 17.9. The sampling rate is 128 Hz. RDS is obtained by multi-triggering method, and the length of time history is 1000 s, for the calculated basic period is 0.5 s.

ERA method based on the RDS is used to identify frequency and damping ratio. Meanwhile, FDD method is adopted for modal identification. The results are shown in Table 17.2. According to the results, the identification effects are comparatively consistent. Hence, the value selection methods for triggering level and length of time history proposed in this paper are effective.

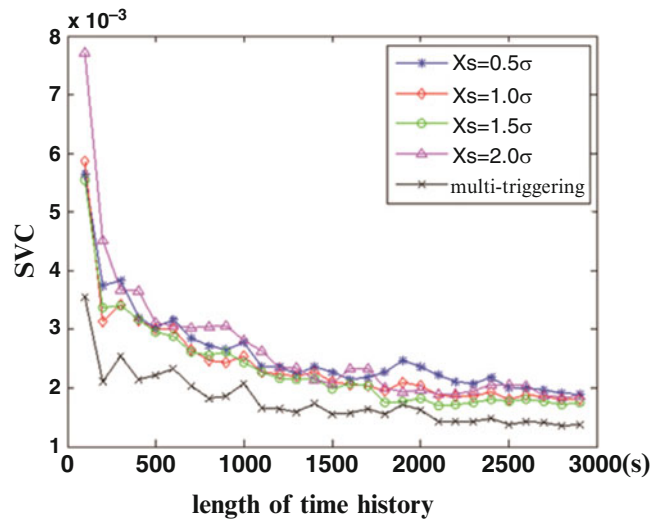


Fig. 17.7 RDS quality changes with length of time history

Table 17.1 Results of modal identification of the 6-DOF model

Modal order	Frequency (Hz)					Damping ratio (%)				
	Accurate value	$1.0\sigma_x$	$1.5\sigma_x$	$2.0\sigma_x$	Multi-triggering	Accurate value	$1.0\sigma_x$	$1.5\sigma_x$	$2.0\sigma_x$	Multi-triggering
1	0.801	0.806	0.805	0.803	0.801	5.240	4.704	4.953	5.511	5.291
2	2.140	2.139	2.139	2.142	2.141	1.070	1.094	1.196	1.144	1.141
3	3.151	3.148	3.147	3.151	3.149	1.130	1.195	1.184	1.216	1.173
4	4.247	4.256	4.251	4.254	4.251	1.430	1.403	1.484	1.486	1.462
5	5.039	5.023	5.043	5.036	5.037	1.660	1.783	2.207	2.209	1.677
6	5.368	5.346	5.356	5.362	5.364	1.740	2.424	2.238	1.847	1.674

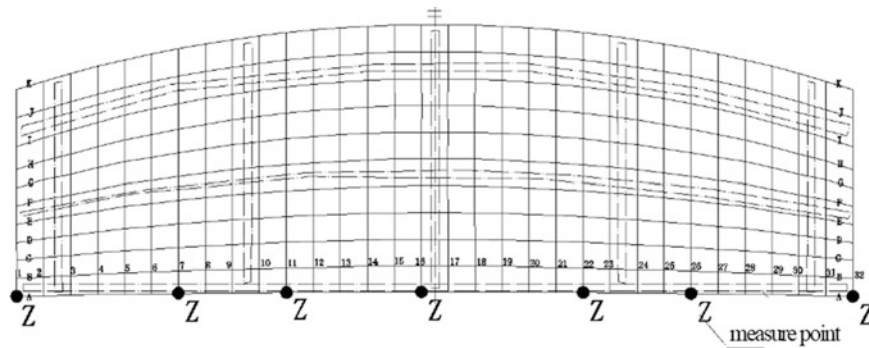


Fig. 17.8 The space truss of the stadium

### 17.6 Conclusions

Through data statistics in a large scale practical structure, a new criterion for triggering level and a suggested length of time history for enhancing the quality of the RDS are proposed.

(1) Relatively good quality of RDS focuses on the triggering level value interval of  $(0.5-2.0) \sigma_x$ . In practical application, more reliable RDS can be obtained by multi-triggering method.



**Fig. 17.9** Sensor placement

**Table 17.2** Structure model identification of a space truss

Modal order	FDD		RDT-ERA	
	Frequency (Hz)	Damping ratio (%)	Frequency (Hz)	Damping ratio (%)
1	1.950	4.246	1.981	4.080
2	2.250	1.865	2.246	1.120
3	3.033	2.925	3.004	2.490
4	3.450	2.535	3.449	3.070
5	3.999	4.818	3.838	4.600
6	4.323	1.240	4.313	1.490

(2) The quality of the RDS increases as the length of time history increases. The result is relatively stable when the length of time history reaches 2000 times of basic period.

(3) The feasibility and validity of the proposed multi-triggering method and the length of time history are verified through numerical simulation and practical engineering application. This provides a good base for the application of RDT.

## References

1. Cole, H.: A. On-the-line analysis of random vibrations. *AIAA J.*, (1968).
2. Cole, H. A.: On-line failure detection and damping measurements of aerospace structures by random decrement signature. *Monogr. Oceanogr. Methodol.* (1973)
3. Ibrahim, S.R.: Random decrement technique for modal identification of structures. *J. Spacecr. Rockets.* **14**(11), 696–700 (1977)
4. Vandiver, J.K., Dunwoody, A.B., Campbell, R.B., et al.: A mathematical basis for the random decrement vibration signature analysis technique. *J. Mech. Des.* **104**(2), 307–313 (1982)
5. Bedewi, N. E.: The mathematical foundation of the auto and cross random decrement technique and development of a system identification technique for detection of structural deterioration. PhD Dissertation, University of Maryland, USA (1986)
6. Brincker, R., Krenk, S., Jensen, J. L.: Estimation of correlation functions by the random decrement technique. *Proceedings of the 9th International Modal Analysis Conference (IMAC)* (1991)
7. Yang, J.N., Lei, Y., Lin, S., et al.: Identification of natural frequencies and Dampings of in situ tall buildings using ambient wind vibration data. *J. Eng. Mech.* **130**, 570–577 (2004)
8. Shiryayev, O.V.: Improved structural health monitoring using random decrement techniques. PhD Dissertation, Wright State University, USA (2008)
9. Chen, B., Yang, Q., Wang, K., et al.: Full-scale measurements of wind effects and modal parameter identification of Yingxian wooden tower. *Wind Struct.* **17**(6), 609–627 (2013)
10. Asmussen, J. C.: Modal analysis based on the random decrement technique-application to civil engineering structures. PhD Dissertation, Department of Building Technology and Structural Engineering, University of Aalborg, Denmark (1997)
11. Brincker, R., Jensen, J. L., Krenk, S.: Spectral estimation by the random dec technique. *Proceedings of the 9th International Conference on Experimental Mechanics* (1990)
12. Ibrahim, S.R., Mikulcick, E.C.: A method for the direct identification of vibration parameters from the free response. *Shock Vib. Bull.* **47**(4), 183–198 (1977)
13. Juang, J.N., Pappa, R.S.: An eigensystem realization-algorithm for modal parameter-identification and model-reduction. *J. Guid. Control. Dyn.* **8**(5), 620–627 (1985)
14. Huang, C.S., Yeh, C.H.: Some properties of randondec signatures. *Mech. Syst. Sig. Process.* **13**(3), 491–507 (1999)
15. Rice, S.O.: Mathematical analysis of random noise. *Bell Syst. Tech. J.* **23**, 282–332 (1944)

# Chapter 18

## Experimental Study on the Rotor Dynamics Influence Upon the Modal Characteristics of an Induction Machine

F. Chauvicourt, M. Ballweg, W. Desmet, H. Van der Auweraer, and C.T. Faria

**Abstract** The rotor of an electric machine is the direct transfer of torque and speed to the drivetrain through the shaft. As such, its vibrations might deteriorate the efficiency but also, irreversibly, the machine itself. It is particularly important to identify critical frequencies at which resonance may occur. In this paper, a newly identified structural mode is extracted experimentally on an induction machine and justifies the need for more investigations. This mode involves bending of the end-plates of the stator, together with bending of the rotor component which can potentially be a dangerous mode shape. The results are gathered by carrying various experiments in which experimental modal analyses are carried out for characterization of the test specimens. The influence of the rotor dynamics on the behavior of the complete machine is collected by testing two different rotors, alone, and then assembled with the exact same stator.

**Keywords** Electric machine • Rotor • Stator • Uncoupling • Experimental modal analysis

### 18.1 Introduction

Electric machines are widely used nowadays either in industries, transportation systems or even in small scale household appliances. In any of these cases, particular specifications are required and design efforts are shared upon the type of needs. The noise and vibrations of such machines is already extensively studied and research literature demonstrates the need for using different study approaches depending on the application. For instance, small and big machines dynamics get affected by the windings added mass differently [1], such that scalability principles are not considerable. Moreover, the choice on the type of machine is crucial since the most important acoustic noise sources differ from one type to another [2]. In the case of factory application, one often requires safety and thus damping of critical resonances, particularly at the location of the output shaft vibrations.

Apart from the stator structural dynamics, the rotor also plays a significant role in the overall behavior. Attached to the stator through the bearings, the contact between the two parts adds an extra structural path for vibrations to be transferred through. A first assumption to make is to consider the rotor being an added mass to the structure at the bearing mounting points. However, this might not be sufficient in some cases. Studies present new types of modelling such as composite beam elements where Timoshenko's beam theory is used [3], or Thin Layer Elements [4, 5]. This type of standalone rotor model can be implemented in a complete model in which the stator dynamics are present. The connections between the rotor and the stator are modelled using joint connections [4, 5] or a set of springs [6]. The present study investigates the distinction between stator dynamics with and without a rotor experimentally.

---

F. Chauvicourt (✉)  
Siemens Industry Software N.V, ResearchPark 1237, Interleuvenlaan 68, 3001 Leuven, Belgium

Katholieke Universiteit Leuven, Leuven, Belgium

Université Libre de Bruxelles, Bruxelles, Belgium  
e-mail: [fabien.chauvicourt@siemens.com](mailto:fabien.chauvicourt@siemens.com)

M. Ballweg  
Siemens Large Drives, Bad Neustadt, Germany

W. Desmet  
Katholieke Universiteit Leuven, Leuven, Belgium

H. Van der Auweraer • C. T. Faria  
Siemens Industry Software N.V, ResearchPark 1237, Interleuvenlaan 68, 3001 Leuven, Belgium

The modal characteristics of an induction machine (rated power 22 kW) with two different rotors and without any rotor are experimentally determined in order to identify the rotor dynamics influence on the overall machine behavior. Section 18.2 details the experimental setup used for each of the test specimens together with the validity checks of the measurements. In Sect. 18.3 the results are displayed for each sample, i.e. the two rotors, the stator alone and the stator with the two rotors independently. The last section discusses and presents conclusions on the effects of the rotor dynamics upon the complete machine behavior.

## 18.2 Experimental Setup

As previously mentioned, the influence of the rotor dynamics is assessed in this paper through structural modal experiments. In this framework two rotors of different topologies are studied. It is important to note that both rotors are designed for the machine to operate normally, even though their geometry differs. Five independent experiments are carried out: the two rotors alone (R1, R2), the stator alone (S) and then the stator assembled with each of the two rotors (SR1, SR2).

The modal characteristics for every experiment are gathered through Experimental Modal Analysis (EMA). Depending on the structure to test, a different setup especially with adequate excitation technique had to be chosen. An impact hammer (PCB Piezotronics SN20541) and a miniature shaker (LMS Qsource SN045) allowed to achieve consistent, repeatable and coherent measurements respectively up to 2,800 Hz and 5,500 Hz. Moreover, not only the excitation technique but also specific boundary conditions had to be defined properly. Free-free structural responses are of interest since they are the intrinsic dynamics of the structure. Therefore, flexible ropes were carefully chosen depending on the mass of each specimen, given that they shall eliminate the interference between flexible and rigid modes by allocating the latter at very low frequency; e.g. less than 1 Hz.

Depending on the structure under test, a number of measurement points were set and corresponding meshes are shown in Fig. 18.1. It is important to note that only points in green were measured given the symmetries of the rotor and the strong interest in bending modes only—purely radial modes being non-existent in our frequency range and torsion modes as well. Triaxial accelerometers (PCB Piezotronics SN 356A22) were used to collect acceleration data. Table 18.1 summarizes the characteristics for different specimens, the excitation used for each of them and their mesh resolution for the later modal analyses.

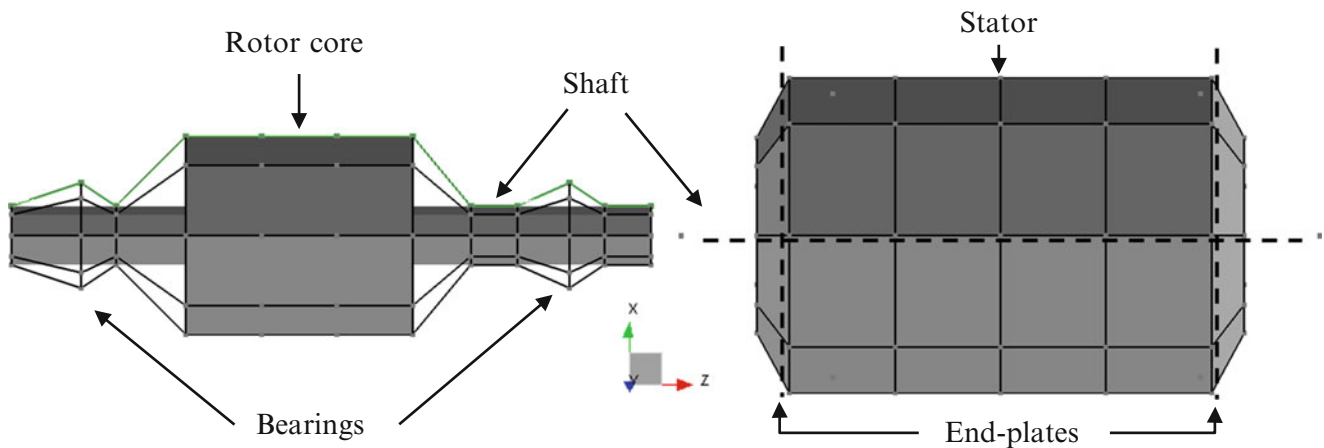


**Fig. 18.1** Experimental mesh resolution for the rotors (*left*) and the assembly (*right*)

**Table 18.1** Test specimens and hardware setup

Specimen name	Mass (kg)	Number of measurement points	Excitation device
R1	37	12 × 3D	Hammer
R2	43	12 × 3D	Hammer
S	85	58 × 3D	Shaker
SR1	122	58 × 3D	Shaker
SR2	128	58 × 3D	Shaker

An important note: EMAs rely on the linearity/reciprocity principle. Indeed when the measured FRFs are acquired one needs to extract the modal characteristics i.e. the natural frequencies and damping ratios. This extraction process assumes a linear mathematical parametric equation for each of the measured FRFs  $H_{ij}(\omega)$ . The present measurement campaign included a validation step for linearity of the structure by means of test check steps such as reciprocity and linearity [7]. Equation (18.1) shows the Multiple-Degree-of-Freedom (MDOF) modal model where the unknowns are the residuals ( $A_k$ ), damping ratios ( $\xi_k$ ) and eigenfrequencies ( $\omega_k$ ) for each mode ( $k$ ).

$$H(\omega) = \sum_{k=1}^n \frac{A_k}{j\omega - \lambda_k} + \frac{A_k^*}{j\omega - \lambda_k^*} \quad (18.1)$$

$$\text{Where } \lambda_k, \lambda_k^* = -\xi_k \omega_k \pm j\sqrt{1 - \xi_k^2} \omega_k.$$

Curve-fitting is a common solution to determine the unknown values although it is not trivial to implement. Algorithms such as Least Squares Complex Exponential (LSCE) [8], Single Degree of Freedom (SDOF) and PolyMAX [9] are used for that purpose. In this study, PolyMAX implemented into LMS Test lab software is used since it allows easy, fast and high quality parameter estimation for highly damped structures.

### 18.3 Results and Discussions

EMAs were performed on the two rotors R1 and R2 alone and their intrinsic dynamics was assessed independently from the stator. Figure 18.2 shows the summation of all the FRFs measured on both rotors. Additionally, the two first flexible modes A and B are displayed in Fig. 18.3 and are naturally similar to the first bending modes of a free-free beam (red dotted line).

Knowing that R1 is lighter than R2, one could expect the R1 natural frequencies higher than for R2. However the frequencies discrepancies are not entirely justified by the mass variation such that one can conclude that R1 is stiffer than R2.

The influence of those intrinsic rotor dynamics on the overall machine behavior was checked by performing experiments on the assembly of the stator with each rotor. Figure 18.4 shows the summation of all the FRFs measured for these different structural combinations S, SR1 and SR2.

From this set of results, three conclusions can be drawn:

- An overall damping effect is noticeable particularly for the three peaks C,
- An extra mode D appears when attaching a rotor to the stator assembly,
- The mode D depends on the rotor dynamics.

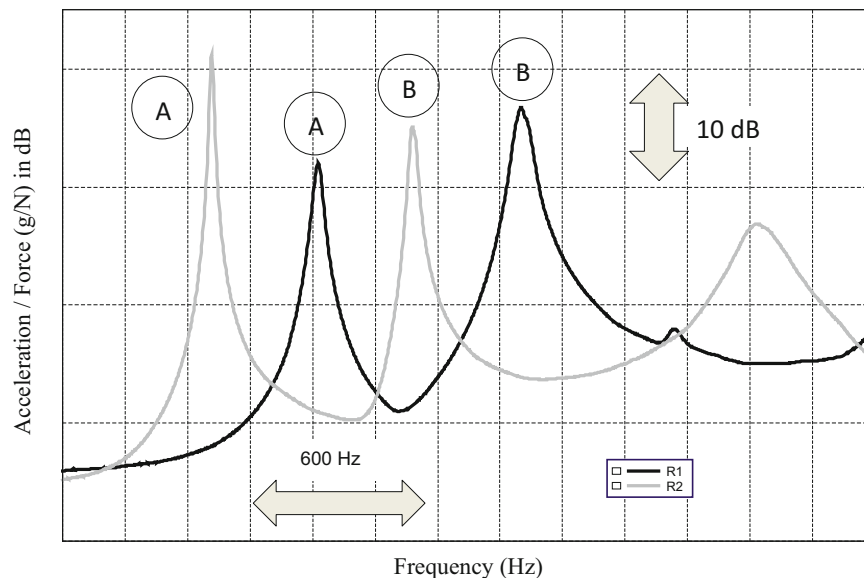


Fig. 18.2 Summation FRFs for R1 and R2

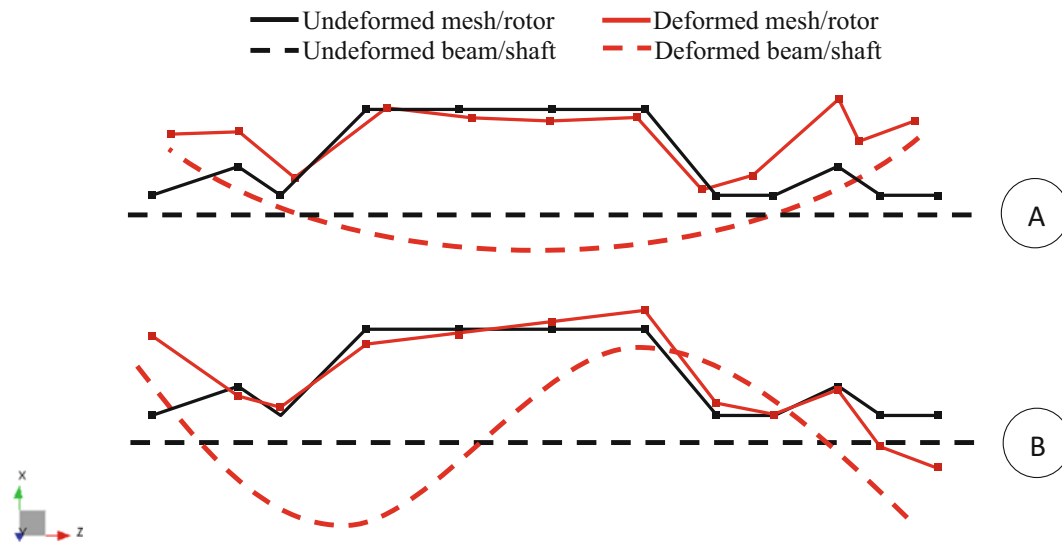


Fig. 18.3 Two first bending modes A and B for R1 (also valid for R2) from EMA

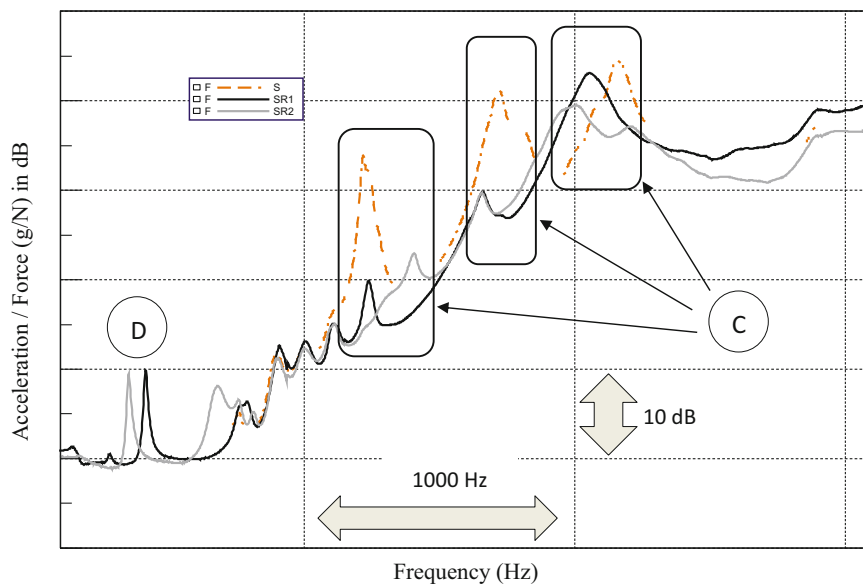


Fig. 18.4 Summation FRFs for S, SR1 and SR2

The decrease in amplitude of the FRFs at lower frequencies justifies the stiffening effect of the rotor upon the overall machine behavior. Damping is also increased especially at the three peaks that correspond to modes showing a bending deformation of the end-plates only. This makes physical sense since attaching the rotors to the stator at the bearings is similar to the simply supported configuration case, which brings more energy dissipation.

The extra mode D shows an axial bending of the stator assembly together with a rotor bending following mode A shape. Figure 18.5 displays this mode for better understanding. In fact the rotational degree of freedom around Y-axis at the bearing connection points is identical for each of the components, this means that the rotor and the stator are uncoupled for this mode, which will then be called uncoupled bending mode.

Finally, one can notice a frequency shift of this newly identified mode depending on the rotor attached to the stator. The direction of shift is dictated by the one from the rotor dynamics; i.e. S1 is stiffer and lighter than S2, while SR1 is also stiffer and lighter than SR2 for the uncoupled bending mode. It is also important to note that some other modes for SR1 and SR2 are not necessarily frequency shifted depending on the rotor attached. It indicates that the added dynamics from the rotors do not perform stiffen nor flex the structure for every mode. The natural frequencies indeed shifted accordingly to what effect the rotor has on each of the corresponding modes.



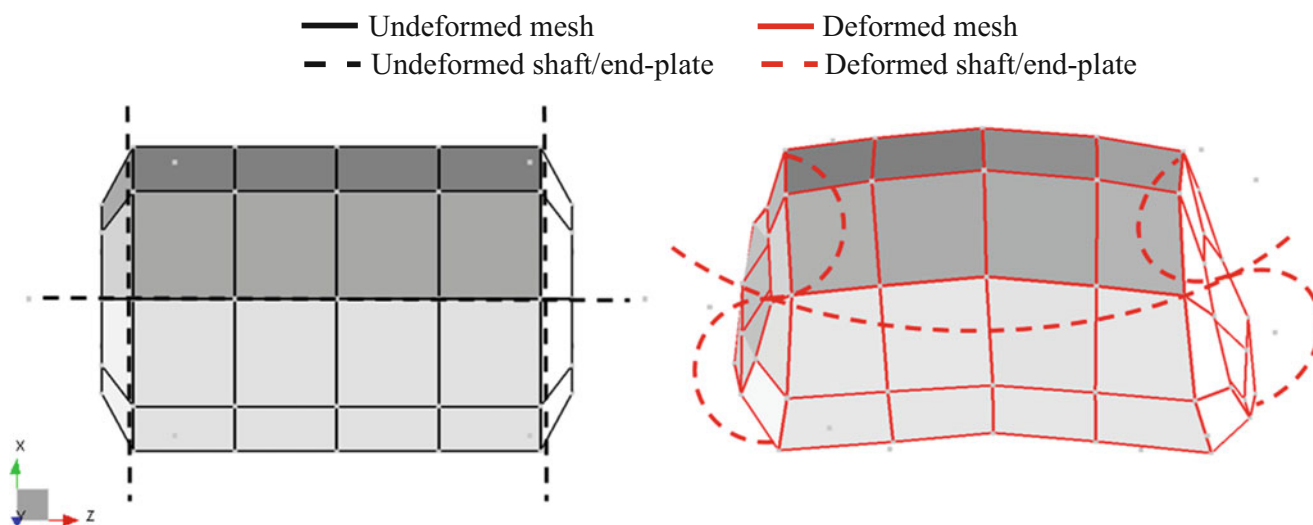


**Fig. 18.5** Extra mode shape D for SR1 (also valid for SR2) from EMA

## 18.4 Conclusions

In this paper, the rotor dynamics influence upon the modal characteristics of an induction machine was studied experimentally by performing EMAs on a set of specimens. Two rotors R1 and R2 of different topologies, but still compatible with the same stator, showed different structural dynamics behaviors; R1 being lighter and stiffer than R2. These rotors were then attached to the stator S through the bearings and EMAs were performed again on the complete structures (SR1 and SR2). Therefore, one could compare the dynamics of SR1 with SR2 but also with the stator alone S. As shown in Fig. 18.4, an overall damping effect is noticeable, particularly at high frequencies where the peaks correspond to end-plates modes, stiffened by the added rotor. Most importantly, an extra mode appears when the rotor is attached to the stator, and depends entirely on the rotor dynamics. It involves axial bending of the stator together with a rotor bending, in such a way that the two components are uncoupled at this frequency. This effect might be dangerous in operational conditions and justifies the need for more investigations.

**Acknowledgements** The authors would like to acknowledge the financial support of the European Commission via the EU funded Marie Curie ITN project called ADvanced Electric Powertrain Technology (ADEPT), grant number 607361 [10].

## References

1. Verma, S.P., Williams, K., Singal, R.K.: Vibrations of long and short laminated stators of electrical machines, part I: theory, experimental models, procedure and set-up. *J. Sound Vib.* **129**, 1–13 (1989)
2. Hendershot J.R.: Causes and sources of audible noise in electric motors. In: Kuo B.C. (ed.) *Proceedings of 22nd Incremental Motion Control Systems and Devices Symposium*, Champaign, IL, pp 259–270 (1993)
3. Mair M., Haas S., and Ellermann K.: Modeling of a rotor of an electrical machine using composite beam elements. In: *International Conference on Electrical Machines (ICEM)*, pp. 1642–1647 (2014)
4. Gaul L. and Schmidt A.: Experimental identification and simulation of rotor damping. In: *Dynamics of Coupled Structures*, Vol. 1, pp. 209–218, Springer (2014)
5. Clappier M. and Gaul L.: Frequency domain dynamic simulation of an electrical machine rotor. In: *Proceedings of ICSV 23, the International Congress on Sound & Vibration* (2016)
6. Claesson, E.: Modelling of roller bearings in ABAQUS. MSc Thesis, Chalmers University (2014)
7. Heylen W., Lammens S. and Sas P.: *Modal analysis theory and testing*. Book, Katholieke Universteit Leuven, Departement Werktuigkunde (2006)
8. Guillaume P. et al.: Frequency-domain maximum likelihood identification of modal parameters with confidence intervals. In: *Proceedings of ISMA 23, the International Conference on Noise and Vibration Engineering*, Leuven, Belgium, 16–18 Sept (1998)
9. Peeters, B., et al.: The PolyMAX frequency-domain method: a new standard for modal parameter estimation? *Shock. Vib.* **11**(3–4), 395–409 (2004)
10. Stefanskyi A., Dziechciarz A., Chauvicourt F., Sfakianakis G.E., Ramakrishnan K., Niyomsatian K., Curti M., Djukic N., Romanazzi P., Ayat S., Wiedemann S., Peng W., Stipetic S.: Researchers within the EU funded Marie Curie ITN project ADEPT, grant number 607361, (2013–2017).

# Chapter 19

## Optimal Modal Parameter Estimation for Highly Challenging Industrial Cases

Mahmoud El-Kafafy, Bart Peeters, and Patrick Guillaume

**Abstract** In this paper, the recently-developed MLMM method (Maximum Likelihood estimation of a Modal Model) will be introduced and applied to challenging industrial cases. Specific about the method is that the well-established statistical concept of maximum likelihood estimation is applied to estimate directly a modal model based on measured Frequency Response Functions (FRFs). Due to the nature of this model, the optimal modal parameters are estimated using an iterative Gauss-Newton minimization scheme. The method is able to tackle some of the remaining challenges in modal analysis. For instance, in highly-damped cases (e.g. acoustic cavity modal analysis, trimmed body modal analysis) where it is needed to use a large amount of excitation locations to sufficiently excite the modes and to obtain a reliable modal model, the more classical modal parameter estimation methods sometimes fail to achieve a high-quality curve-fit of the measured FRF data. Due to the iterative minimization of the cost function, MLMM is able to estimate a model that very closely represents the measurements. Another benefit of the method is that additional constraints can be imposed to the model. For instance, it is possible to impose that real modes and participation factors are estimated and/or to impose that the estimated modal model is reciprocal (as prescribed by the modal theory). More classical modal parameter estimation methods have rarely the possibly to fully integrate these constraints and the obtained modal parameters are typically altered in a subsequent step to satisfy the desired realness and reciprocity constraints. It is obvious that this may lead to sub-optimal results, as for instance evidenced by a degradation of the quality of the fit between the identified modal model and the measurements. The applicability of MLMM to estimate a constrained modal model will be demonstrated using challenging industrial applications.

**Keywords** Experimental modal analysis • Maximum likelihood estimation • Modal model • Reciprocity • Real modes

### 19.1 Introduction

The modal parameters are basically defined as the eigenvalues and eigenvectors of the linear dynamic model for a vibratory structure. For a certain vibratory structure, a linear model can be written in terms of the frequency response functions (FRFs) as:

$$\{X(\omega_k)\} = [H(\omega_k)] \{F(\omega_k)\} \quad (19.1)$$

where  $\{X(\omega_k)\} \in \mathbb{C}^{N_o \times 1}$  the discrete Fourier transformed (DFT) displacement response with  $N_o$  the number of measured outputs,  $\{F(\omega_k)\} \in \mathbb{C}^{N_i \times 1}$  the Fourier transformed force inputs with  $N_i$  the number of measured inputs,  $[H(\omega_k)] \in \mathbb{C}^{N_o \times N_i}$  the FRFs matrix, and  $\omega_k$  is the frequency variable at frequency line  $k$ . Different frequency-domain parametric models can be used to represent the frequency response functions (FRFs) matrix of a linear time-invariant system describing the relation between the DFT spectra of the input and output signals [1]. The model that is used mostly is the rational form model: a rational of two polynomials either in  $s$ -domain or in  $z$ -domain. Another model that is also well known is the state-space

---

M. El-Kafafy  
Vrije Universiteit Brussel (VUB), Pleinlaan 2, B-1050 Brussel, Belgium

Helwan University, Cairo, Egypt

B. Peeters (✉)  
Siemens Industry Software, Interleuvenlaan 68, B-3001 Leuven, Belgium  
e-mail: [bart.peeters@siemens.com](mailto:bart.peeters@siemens.com)

P. Guillaume  
Vrije Universiteit Brussel (VUB), Pleinlaan 2, B-1050 Brussel, Belgium

representation. In this paper, the so-called “modal model” is used, where the FRFs matrix is directly written in terms of the modal parameters:

$$\hat{H}(\theta, \omega_k) = \left( \sum_{r=1}^{N_m} \frac{\Psi_r L_r}{j\omega_k - \lambda_r} + \frac{\Psi_r^* L_r^*}{j\omega_k - \lambda_r^*} \right) + \frac{[LR]}{(j\omega_k)^2} + [UR] \quad (19.2)$$

with  $\hat{H}(\theta, \omega_k) \in \mathbb{C}^{N_o \times N_i}$  the frequency response functions (FRFs) matrix with  $N_o$  outputs and  $N_i$  inputs,  $N_m$  the number of the identified modes,  $\omega_k = 2\pi f_k$  the circular frequency at frequency  $f_k$  [Hz],  $\Psi_r \in \mathbb{C}^{N_o \times 1}$  the  $r^{\text{th}}$  mode shape where  $r = 1, 2, \dots, N_m$ ,  $\lambda_r = -\sigma_r + j\omega_{d,r}$  the  $r^{\text{th}}$  pole with  $\sigma_r$  the damping factor of mode  $r$  and  $\omega_{d,r}$  the damped natural frequency [rad/s],  $(\cdot)^*$  stands for the complex conjugate of a complex number,  $L_r \in \mathbb{C}^{1 \times N_i}$  is the  $r^{\text{th}}$  participation factors vector,  $[LR] \in \mathbb{R}^{N_o \times N_i}$  and  $[UR] \in \mathbb{R}^{N_o \times N_i}$  are the lower and upper residual terms used to compensate for the out-of-band modes (assuming a displacement over force FRF in this case), and  $\theta$  is the parameter vector (i.e.  $\theta = [\Psi_r, L_r, \lambda_r, LR, UR]$ ). The multiplication  $\Psi_r L_r$  is called the residue matrix  $R_r$  of the  $r^{\text{th}}$  mode.

Curve fitting aims to match the analytical expression (19.2) (or an equivalent model) to experimental FRF data over a chosen frequency range. During the process, some or all of the modal parameters in the model are determined. Most of the existing modal parameter estimation methods are achieving the full estimation process in two steps. In the first step, the poles ( $\lambda_r$ ) and the participation factors ( $L_r$ ) are estimated using rational-polynomial-based models. Then, the mode shapes  $\Psi_r$  and the residuals terms ( $[LR]$ ,  $[UR]$ ) are estimated in a second step by solving a linear least-squares problem using (19.2). In [2], the modal parameters are estimated using a frequency-domain output-error optimization technique that uses the pole-residue model as a parameterization form.

The experimentally-driven modal model (19.2) can be used for several modal analysis applications (e.g. structural modifications, noise prediction, FEM updating, sensitivity analysis, etc. [3–5]). For these applications and according to the modal theory, the estimated modal models have to fulfill some important properties. For instance, in the FEM calibration process, the experimentally driven modal models have to incorporate real mode shapes rather than complex ones. This is because the mode shapes obtained from the finite element models are typically real in nature, whereas the mode shapes obtained from experimental measurements are complex. Also in acoustic modal analysis, it can be desired to obtain real mode shapes instead of complex ones to avoid phase lag between different mode shape components so that easier to interpret mode shapes are obtained. In structural modifications prediction and structure coupling/decoupling applications, obtaining a high quality reciprocal modal model is an important requirement. The existing modal parameter estimation methods rarely consider those two important constraints (i.e. real modes and FRFs reciprocity), and the obtained modal models are typically altered in a subsequent step to satisfy the desired constraints. This may lead to sub-optimal results, as for instance evidenced by a degradation of the quality of the fit between the final identified modal model and the measurements. A comprehensive review on the constrained modal parameter estimation is given in [7]. Apart from those two physically motivated constraints, it was also observed that the existing modal parameters estimation techniques are facing some difficulties when fitting an FRFs matrix with so many columns, i.e. in case where many input excitation locations have to be used in the modal test. For instance, obtaining clean and symmetric mode shapes when performing structural modal analysis of a full car requires many excitation locations to get sufficient excitation of the modes. Another important example where the use of many excitation sources is required is the acoustic modal analysis of a car cavity. The high level of damping in the car cavity requires many excitation locations to get sufficient excitation of the acoustic modes [6, 8–10].

These are true remaining challenge and of great interest to the automotive OEMs. In this paper, a recently developed modal parameter estimation method called MLMM (Maximum Likelihood estimation of a Modal Model) will be introduced and applied to some challenging industrial cases.

## 19.2 Maximum Likelihood Estimation of a Modal Model: MLMM

### 19.2.1 MLMM Theory

The iterative MLMM modal parameter estimation method is a multivariable (i.e. MIMO) frequency-domain modal estimation method that uses the modal model to represent the measured frequency response functions (FRFs) over a chosen frequency band. The MLMM method is originally introduced in [11] and further improved in terms of the computational time in [12]. In [7], the MLMM method is adapted to take into account some desired and physically motivated constraints in the optimization process. The MLMM method belongs to the category of the maximum likelihood estimators that is known to be

asymptotically consistent and efficient [1, 13, 14]. The ‘‘MLMM’’ abbreviation stands for Maximum Likelihood (estimation of a) Modal Model. The MLMM method optimizes the modal model (19.2) directly instead of optimizing a rational fraction polynomial model. The optimization process tunes the parameters of the modal model to minimize the following quadratic-like cost function so that a best match between the modal model and the measurements is obtained:

$$\ell_{MLMM}(\theta) = \sum_{i=1}^{N_i} \sum_{o=1}^{N_o} \sum_{k=1}^{N_f} |E_{io}(\theta, \omega_k)|^2 \quad (19.3)$$

with  $E_{io}(\theta, \omega_k) \in \mathbb{C}$  the weighted residual (i.e. the error between the measured FRF  $H_{io}(\omega_k)$  and  $\widehat{H}_{io}(\theta, \omega_k)$  represented by the modal model (19.2)). This residual is a nonlinear function of the modal model parameters  $\theta$ , and it is defined as:

$$E_{io}(\theta, \omega_k) = \frac{H_{io}(\omega_k) - \widehat{H}_{io}(\theta, \omega_k)}{\sigma_{H_{io}}^2(\omega_k)} \quad (19.4)$$

where  $\sigma_{H_{io}}^2(\omega_k)$  is the variance of the measured FRF and  $\theta$  is a column vector contains all the parameters of the modal model (19.2) (i.e. poles, participation factors, mode shapes and residual terms). In the cost function (19.3), the measurements with small uncertainty (i.e.  $\sigma_{H_{io}}^2(\omega_k)$  is small) are more important than those with a large uncertainty (i.e.  $\sigma_{H_{io}}^2(\omega_k)$  is large). The true ML estimator uses the complete covariance matrix as weighting functions in the equation error, however obtaining this matrix correctly (i.e. full rank matrix) is not feasible from the practical point of view, which is particularly true for the modal testing cases where so many outputs and inputs are measured. Therefore, only the diagonal elements of this matrix are used as it is shown in equation (19.4). The variance can be easily calculated using the coherence functions and the FRFs themselves. The consequences of using only the diagonal elements of the covariance matrix is that the estimator will be less efficient (i.e. the uncertainty bounds on the estimates will be higher), but the consistency property will be kept [1, 13]. If the equation error is taken as unweighted one, which could be the case if the FRFs variance is not available, the MLMM will become a non-linear least-squares (NLS) estimator, which is asymptotically consistent but not efficient (i.e. the delivered uncertainty bounds are meaningless). The minimization of the cost function (19.3) is achieved by implementing the Levenberg-Marquardt algorithm (a combination of Gradient and Newton-Gauss methods). The  $p^{\text{th}}$  iteration step of the algorithm is given by:

$$\Re(J_{p-1}^H J_{p-1} + \alpha_{LM} \text{diag}(J_{p-1}^H J_{p-1})) \delta\theta_{p-1} = -\Re(J_{p-1}^H E_{p-1}) \quad (19.5)$$

with  $J = \partial E / \partial \theta$  the complex-valued Jacobian of the vector  $E(\theta, \omega_k)$ ,  $\delta\theta_p = \theta_p - \theta_{p-1}$ , and  $\alpha_{LM}$  the Levenberg-Marquardt parameter. Increasing the parameter  $\alpha_{LM}$  will enlarge the convergence region of the cost function. Once the cost function reaches a convergence, the optimum parameters of the modal model over a chosen frequency range are obtained. The convergence of the cost function is defined either by a relative error between two consecutive calculated cost functions or by reaching a given maximum number of iterations. If the variance of the FRFs is used as a weighting function in the error equation, the confidence bounds on the estimated modal parameters can be obtained by inverting the so-called Fisher information matrix [1] as follows:

$$\text{cov}(\theta) = [2 \Re(J^H J)]^{-1} \quad (19.6)$$

where  $J$  is the Jacobian of the last iteration in the optimization process. The diagonal elements of  $\text{cov}(\theta)$  are the variances of the estimated modal parameters. References [7, 11, 12] give a detailed description of the implementation equations of the MLMM method. Since MLMM is an iterative method that performs a nonlinear optimization process, initial values for the all the modal parameters of expression (19.2) are needed to start the optimization process. The polyreference least-squares complex frequency-domain (pLSCF) estimator [15, 16], known as Polymax, will be used to generate initial values for the poles and the participation factors. Then, the initial values for the mode shapes, lower and upper residuals can be determined easily by solving linear least-squares problem using (19.2).

## 19.2.2 Constrained MLMM: Reciprocal Modal Model & Real Mode Shapes

### 19.2.2.1 Reciprocity Constraint

A reciprocal frequency response functions (FRFs) matrix requires symmetric residues ( $R_r = \Psi_r L_r$ ) and symmetric residual matrices ( $[LR], [UR]$ ). If MIMO measurements are available, this condition can be checked on the FRFs matrix:  $H_{oi}(\omega_k) = H_{io}(\omega_k)$  for the  $o^{\text{th}}$  row and the  $i^{\text{th}}$  column. On the level of the modal model, evaluating (19.2) for DOF  $o$  and  $i$  shows that the reciprocity principle for a specific mode  $r$  and the upper and lower residual terms yields:

$$\Psi_{i_r} L_{o_r} = \Psi_{o_r} L_{i_r} \ \& \ LR_{oi} = LR_{io} \ \& \ UR_{oi} = UR_{io} \quad (19.7)$$

Hence, to identify a reciprocal modal model with the MLMM method the residual matrices have to be symmetric and the participation factors have to be identical (up to scaling factor) to the mode shape coefficients at the input stations. Therefore, to identify a reciprocal modal model using the iterative MLMM method the same optimization procedure described in Sect. 19.2.1 will be achieved taking into account the reciprocity constraint in the optimized modal model (19.2). Imposing reciprocity in the identified modal model means that (19.2) will be reformulated as follows:

$$\hat{H}(\theta, \omega_k) = \left( \sum_{r=1}^{N_m} \frac{Q_r \phi_r L_r}{j\omega_k - \lambda_r} + \frac{Q_r^* \phi_r^* L_r^*}{j\omega_k - \lambda_r^*} \right) + \frac{[LR]_{rec}}{(j\omega_k)^2} + [UR]_{rec} \quad (19.8)$$

with  $Q_r \in \mathbb{C}$  the scaling factor (the ratio between the mode shape element at the driving point DOF and the corresponding participation factor),  $\phi_r \in \mathbb{C}^{N_o \times 1}$  the mode shape vector in which the mode shape element that corresponds to a driving point DOF are imposed to be identical to the participation factors element that corresponds to that driving point DOF,  $L_r \in \mathbb{C}^{1 \times N_i}$  the participation factors row vector,  $[UR]_{rec} \in \mathbb{R}^{N_o \times N_i}$  and  $[LR]_{rec} \in \mathbb{R}^{N_o \times N_i}$  the upper and lower residual matrices in which the symmetry property is imposed. The iterative MLMM method will optimize the reciprocal modal model (19.8) in such a way that the best match between the measurements and the modal model is obtained.

### 19.2.2.2 Real Mode Shapes

Estimation of real (normal) mode shapes requires that the structure under test has a proportional damping which is a quite hypothetical form of damping. The main reason for the introduction of the proportionally damped systems assumption is that the numerical complexity of the calculations with this assumption is lower than for the general viscous damping. Systems with proportional damping form a compromise between the undamped system models from finite element model analysis and the generally viscously damped system models from experimental modal analysis. The hypothesis of proportional damping of a given mode corresponds to a purely imaginary residue matrix [2, 3]. This corresponds to  $\Re(\Psi_r L_r) = 0$  in equation (19.2). To identify a modal model that incorporates real mode shapes, the constraint  $\Re(\Psi_r L_r) = 0$  will be imposed in the optimization process of the MLMM method described in Sect. 19.2.1 giving at the end a modal model with purely imaginary residues.

In case reciprocity and the real mode shapes constraints are applied simultaneously, which is often needed for advanced engineering based on the experimental modal model, the MLMM method, using the optimization procedure described in Sect. 19.2.1, will identify the modal model (19.8) with imposing that  $\Re(Q_r \phi_r L_r) = 0$  where  $Q_r$ ,  $\phi_r$ , and  $L_r$  are the same as they are defined in Sect. 19.2.2.1. In the optimization process of the MLMM method it is also taken into account for each mode that the pole remains stable during the iterations (i.e. its real part is negative). Moreover, when applying the reciprocity and real mode shapes constraint simultaneously the frequency mass sensitivity is negative, and the residue at the input point is negative imaginary [7].

## 19.3 Applications

In this section, the applicability of the iterative constrained MLMM in the frame of structural modal testing and the vibro-acoustic modal analysis will be presented by means of three different data sets. The first part of this section will deal with the application of the constrained MLMM method in the field of structural modal testing using two different data sets measured

from two different fully equipped cars. The second part of this section will show the applicability of the constrained MLMM method in the field of the acoustic modal analysis using acoustic data set measured for a fully trimmed car cavity. These cases are challenging because of the high level of damping, high modal density, and the (very) large amount of columns of the FRFs matrix to be fitted. Since the main objective of the users applying the reciprocity and real mode shapes constraints is to obtain models that accurately represent the structure under test, the main criterion that is going to be used as a validation tool is the quality of the fit between the obtained modal model and the measured data. The quality of the obtained modal model from the iterative MLMM method will be compared to the one obtained from the well-known Polymax estimator [15, 16]. Polymax relies on a (non-iterative) linear least-squares optimization to estimate the modal parameters. The poles and the participation factors are calculated first by fitting a right matrix fraction description polynomial model to the measured FRFs. Then, the mode shapes together with the residual terms are calculated in a second LSFD step by fitting the modal model to the measured FRFs. Although the real mode shapes and reciprocity constraints can be applied in the existing LSFD estimator the obtained constrained modal model from the LSFD solution is not always of high quality since the LSFD belongs to the linear least-squares estimators, which are known to be biased estimators. Another disadvantage of the existing LSFD estimator is that the reciprocity condition is not applied to the lower and upper residual terms. The iterative MLMM method is specifically developed to overcome both drawbacks.

### 19.3.1 Structural Modal Analysis Applications

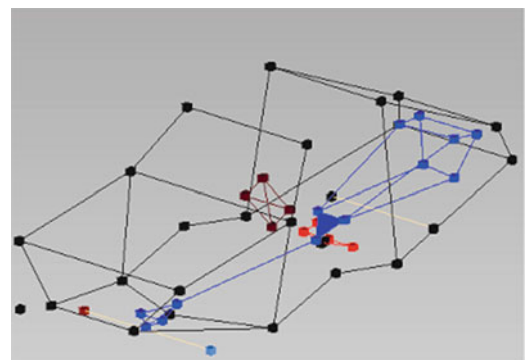
In this subsection, the applicability of the iterative constrained MLMM method in the frame of structural modal testing, more specifically in automotive modal analysis, will be presented by means of two different data sets measured on two different fully equipped cars. The main difference between the two data sets is the number of references (i.e. excitation sources) used to measure the FRFs matrix. The second data set has 26 inputs, while the first one has four inputs. Having more references (inputs) leads to have a higher modal density since many close modes will be excited and estimated. Therefore, this difference in the number of inputs between the two data sets will increase the data size in terms of the total number of the FRFs to be fitted and the number of modes to be optimized.

#### 19.3.1.1 First Fully Equipped Car Example: With a Reasonable Amount of Input Locations

In this example, the accelerations of the fully equipped car were measured at 154 locations, while 4 shakers were simultaneously exciting the structure. This gives a total of 616 FRFs. At the shaker locations, accelerometers were also installed to measure the accelerations. Therefore, the data set has four driving points; hence, a  $4 \times 4$  block of the full FRFs matrix is expected to be symmetric due to the fact that the FRFs of the collocated DOFs should be reciprocal. More details about this test setup can be found in [17]. Figures 19.1 and 19.2 show the car geometry and some measured FRFs respectively. The iterative MLMM will be applied to the 616 measured FRFs with the aim to obtain an accurate experimentally-driven modal model that verifies the reciprocity and real mode shapes conditions. To start the iterative MLMM method, initial values for the modal model parameters (19.2) will be generated by applying Polymax to the measured FRFs.

Figure 19.3 shows the Polymax stabilization chart from which about 18 physical modes become visible in the analysis band. Starting from these initial values for the modal model parameters, the iterative MLMM estimator was then used to optimize the modal model (19.8) with imposing that the mode shapes are real (Purely imaginary residues:  $\Re(Q_r \phi_r L_r) = 0$ ).

**Fig. 19.1** First fully equipped car geometry





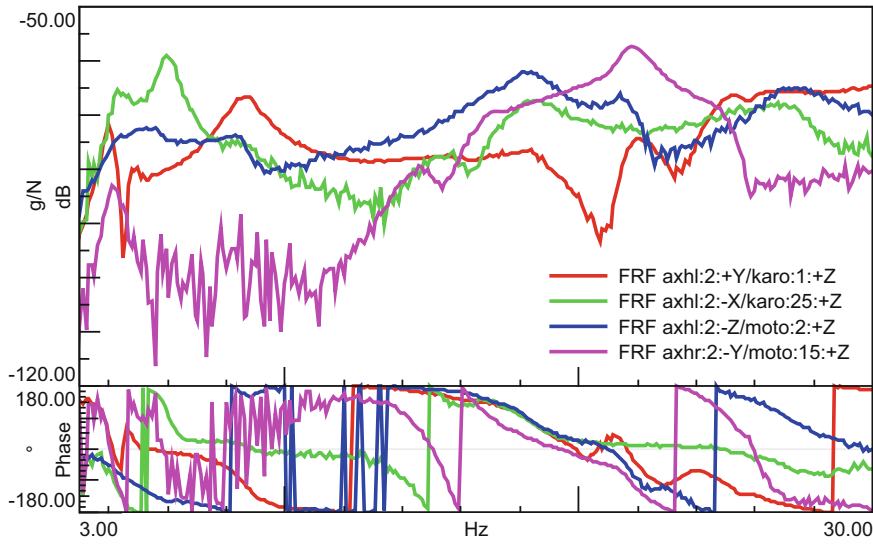


Fig. 19.2 Typical FRFs for the first car example

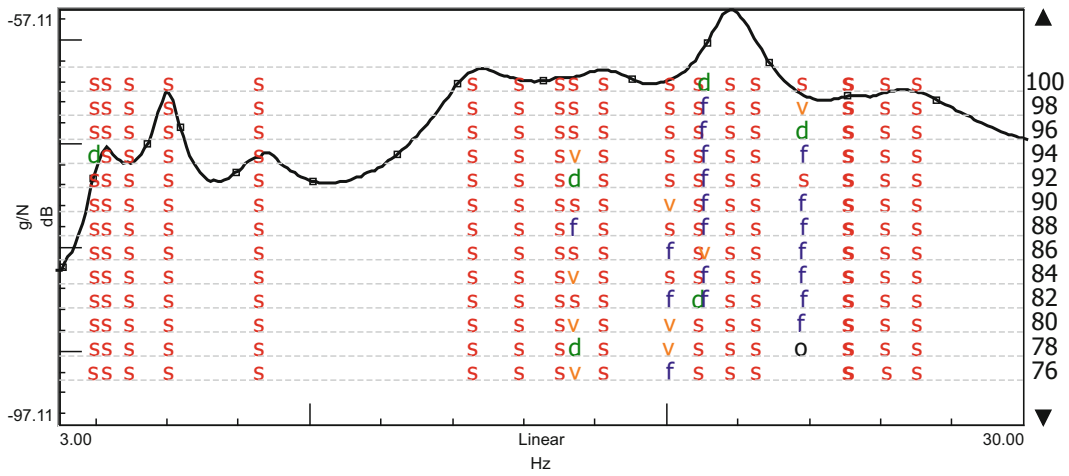


Fig. 19.3 The 1st fully equipped car example: Polymax stabilization chart

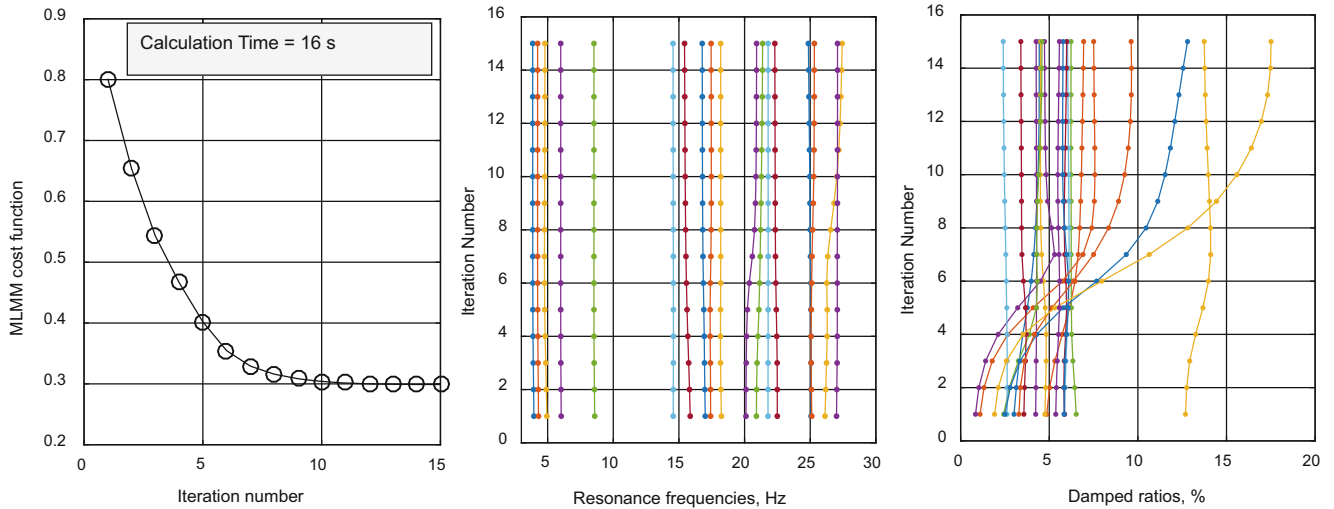
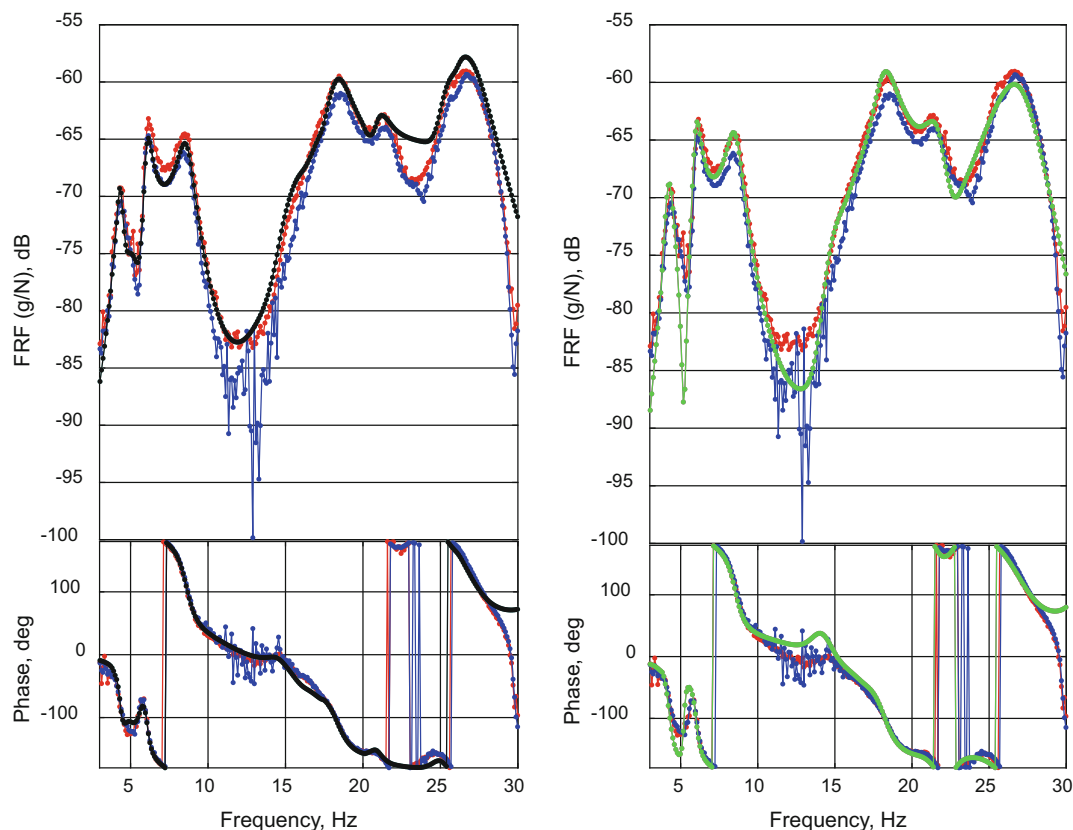


Fig. 19.4 The decrease of the MLMM cost function and the evolution of the frequencies and damping ratios at each iteration





**Fig. 19.5** Improved FRF curve fit for reciprocal FRFs (FRF Karo1+Z/Karo 25+Z & FRF Karo25+Z/Karo 1+Z) when using MLMM as compared to the Polymax estimator: (Left) Polymax estimator; (Right) iterative MLMM estimator. Red & blue: measured reciprocal FRFs; Black: synthesized FRF by Polymax; Green: Synthesized FRF by iterative MLMM

In Fig. 19.4, the decrease of the MLMM cost function (19.3) and the evolution of the frequencies and damping ratios at each iteration are shown. In the same figure, the calculation time taken by the MLMM method is given. It is clear that while iterating, MLMM is successfully decreasing the error between the model and the measured FRFs. The frequency values seem to be very consistent during the iteration, while for some modes the damping ratio estimates are increasing considerably. This is consistent with the fact that natural frequencies are typically estimated with much smaller uncertainty than damping ratios [18, 19].

In Figs. 19.5 and 19.6, the synthesized FRFs are compared with the measured ones for some selected reciprocal and non-reciprocal FRFs respectively. From Fig. 19.5, one can see that the FRFs are well measured where the reciprocity principle is verified between the FRFs that are expected to be reciprocal (the red and blue measurement curves do not differ too much). Therefore, the traditional approach of imposing the reciprocity constraint after the Polymax modal parameter estimation, is expected to also yield acceptable results. Nevertheless, the optimal MLMM solution is still significantly better. This can be seen by comparing both approaches in the frequency range between 20 and 30 Hz in Fig. 19.5. In Fig. 19.6, in which the fit quality is shown for some non-reciprocal FRFs, one can see that the MLMM synthesis results in general are superior to the results from the traditional approach. These results show that with the iterative MLMM an accurate modal model that verifies some physical motivated constraint like FRFs reciprocity and real mode shapes can be obtained.

In Fig. 19.7, the modal assurance criterion (MAC) between real and complex mode shapes estimated by MLMM starting from the same initial mode set is represented. It can be seen from that figure that the real and complex mode shapes are in general in a good agreement except for modes 9, 11, 12, 15, 16 and 18. By checking the level of the complexity of those modes, one can see from Fig. 19.7 that those modes have the lowest Modal Phase Collinearity (MPC) and highest Mean Phase Deviation (MPD) respectively in comparison with the other modes (see [22] for definition of MPC and MPD). Moreover, it can be seen from the stabilization chart that most of those modes (except mode 18) are either very close modes or not well stabilized in the stabilization chart. Therefore, those modes are seemingly coupled with high level of uncertainties.

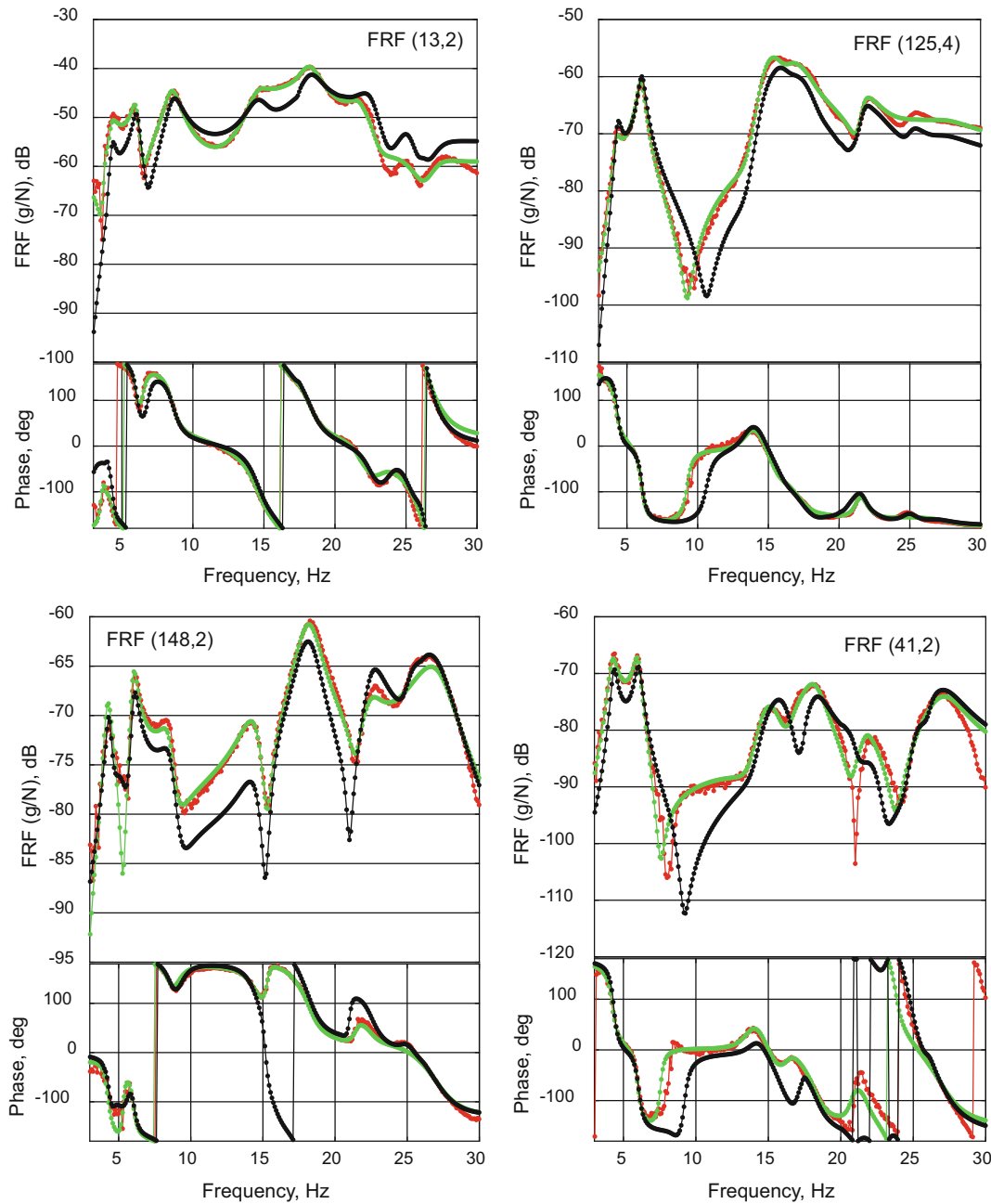


**Fig. 19.6** Improved FRF curve fit for non-reciprocal FRFs (measurement in red) when using MLMM (green) as compared to Polymax (black)

**19.3.1.2 Second Fully Equipped Car Example: With a Very Large Number of Input Locations**

The second example that will be used is a data set measured on a midsize car. The car was excited at 26 locations, while the acceleration responses were measured at 149 locations. Therefore, the FRFs matrix contains 3874 FRFs. The challenges with this data set are the huge amount of references used to obtain the FRFs matrix and the high modal density, which make the fitting process with the existing methods to be troublesome.

In Fig. 19.8, some measured FRFs are shown. The aim of this modal test was to obtain an experimental modal model that will be used for stiffness identification and structural modification purposes. Obtaining an accurate reciprocal modal model that incorporates real mode shapes was an important requirement. For confidentiality reasons, no absolute frequency values will be shown. An initial modal model is created by applying Polymax to the measured FRFs as explained in Sect. 19.3.1.1. Figure 19.9 shows the Polymax stabilization chart. Although the FRFs matrix has so many references and the model size used

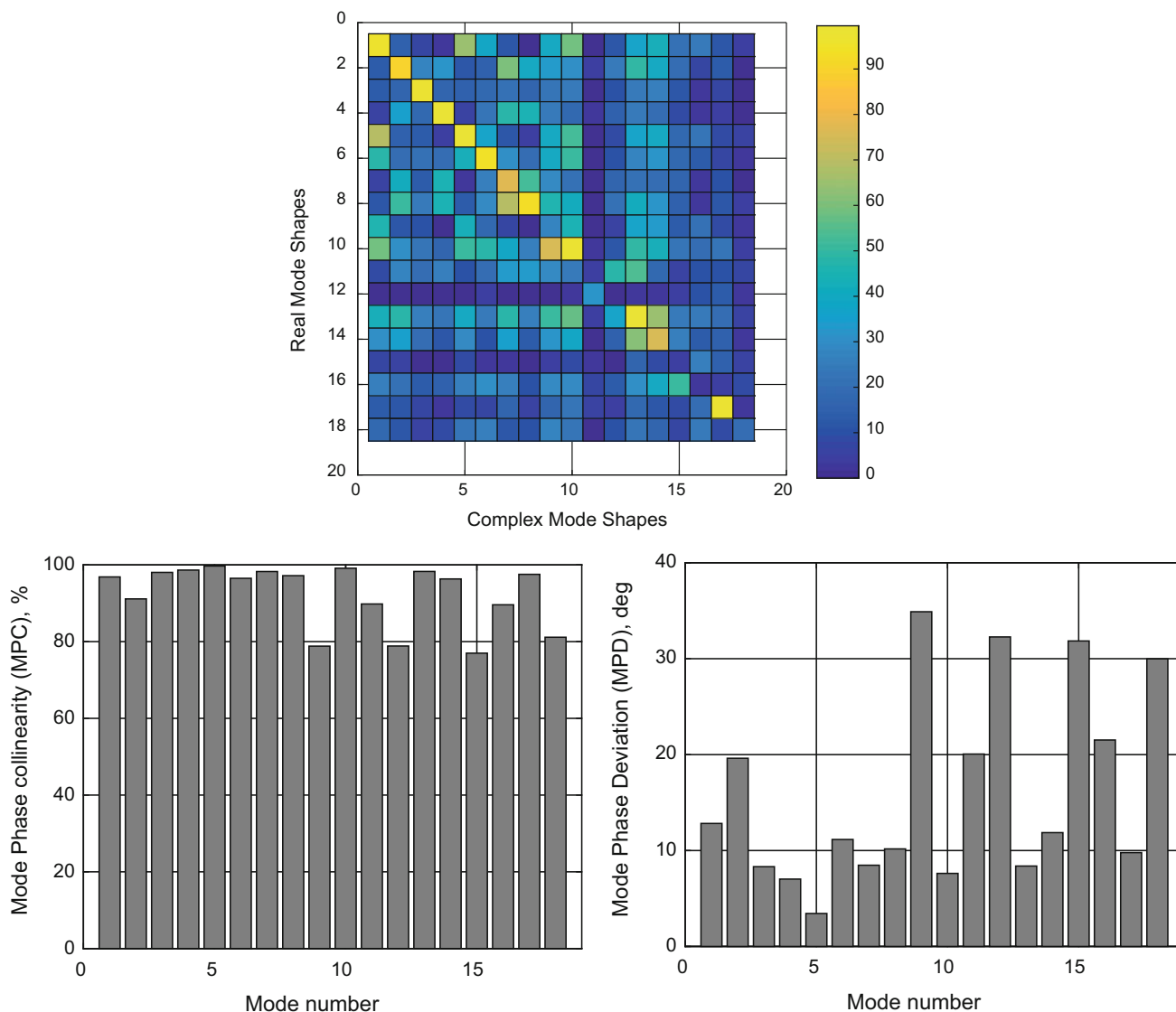


**Fig. 19.7** (Top) Cross MAC between complex and real mode shapes estimated by MLMM; (Bottom-Left) Complex mode shapes Modal Phase Collinearity (MPC); (Bottom-Right) Complex mode shapes Mean Phase Deviation (MPD)

is relatively high, Polymax is still able to give a relatively clear stabilization chart in a numerically stable way. This was the main motivation behind selecting Polymax as starting values generator for the MLMM method. The MLMM method is then applied with the aim to further improve the initial Polymax modal model. In the MLMM optimization process the reciprocity and real mode shapes constraints are imposed. In Fig. 19.10, the performance of the MLMM method during the different iterations is represented in terms of the decreasing of the cost function and the evolution of the resonance frequencies and damping ratio. The accuracy of both the final MLMM model and the initial model is evaluated in Fig. 19.11 where the synthesized FRFs from both models are compared to the measured ones.

It can be seen from Fig. 19.10 that the error between the measurements and the optimized modal model is successfully decreased through the different iterations of the MLMM method, which at the end gives a modal model that outperforms the initial one. This is also very clear from the results shown in Fig. 19.11 where it can be seen that the MLMM modal model is far better than the initial modal model. In comparison with the previous example (Sect. 19.3.1.1, FRF matrix with only 4 inputs), this example (with 26 inputs) shows clearly that the traditional methods are having difficulties in fitting an FRF matrix with a very large amount of columns. As a global measure of the accuracy of the estimated modal models, Table 19.1 presents the global mean fitting error and correlation between the measured and the synthesized FRFs. One can see from this table that the global fit error is significantly decreased and likewise the correlation between the measured and the synthesized FRFs increases. The complexity of the mode shapes with and without imposing real mode shapes during the

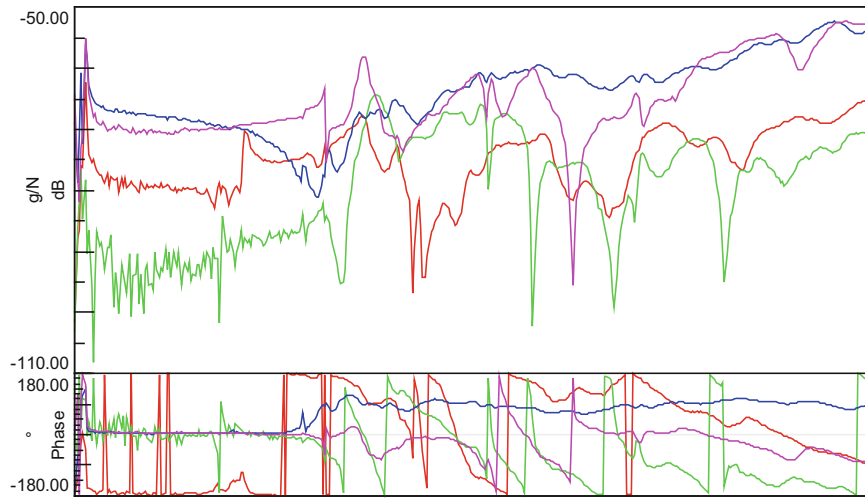


Fig. 19.8 Typical FRFs for the second car example (the frequency axis is made invisible for confidentiality reasons)

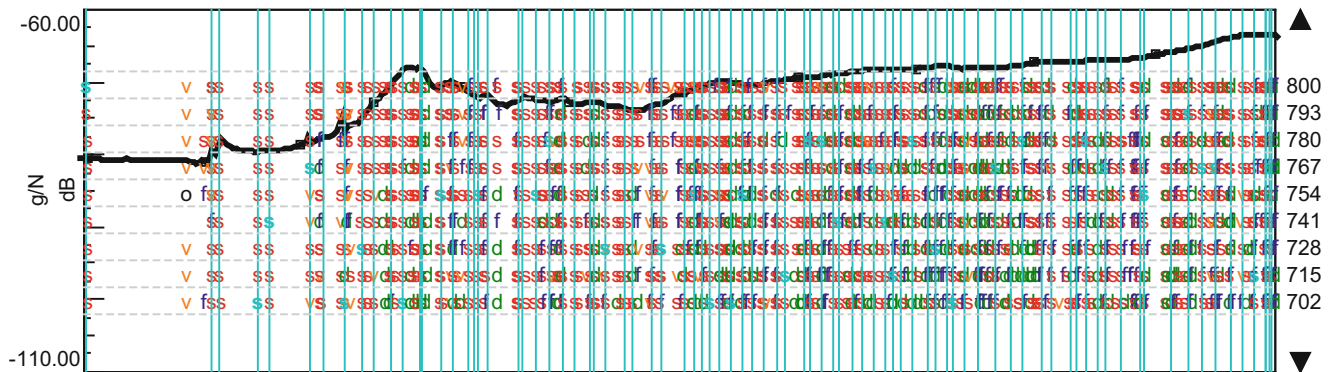


Fig. 19.9 The 2nd fully equipped car example: Polymax stabilization chart

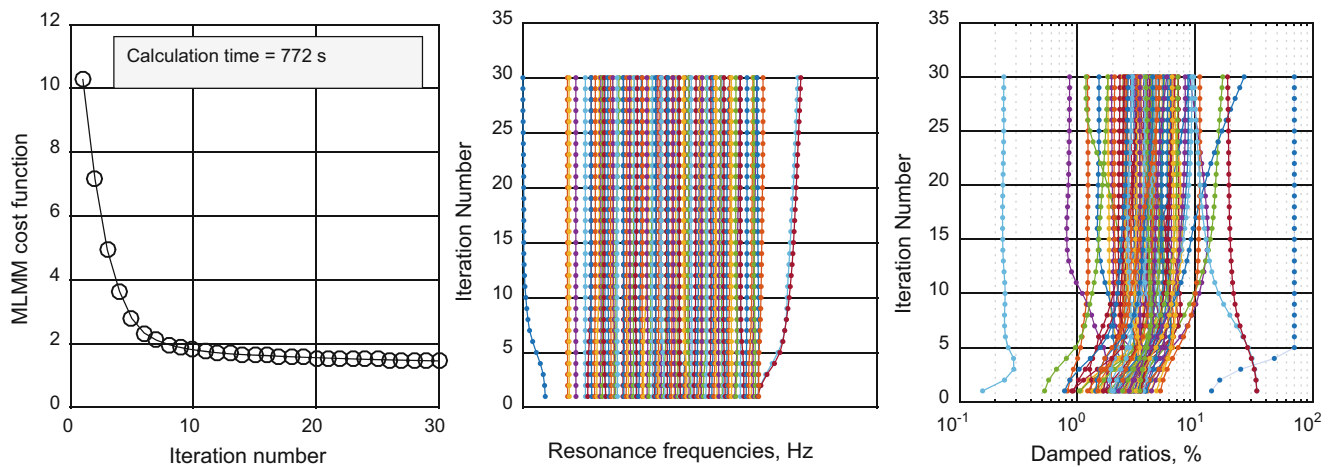
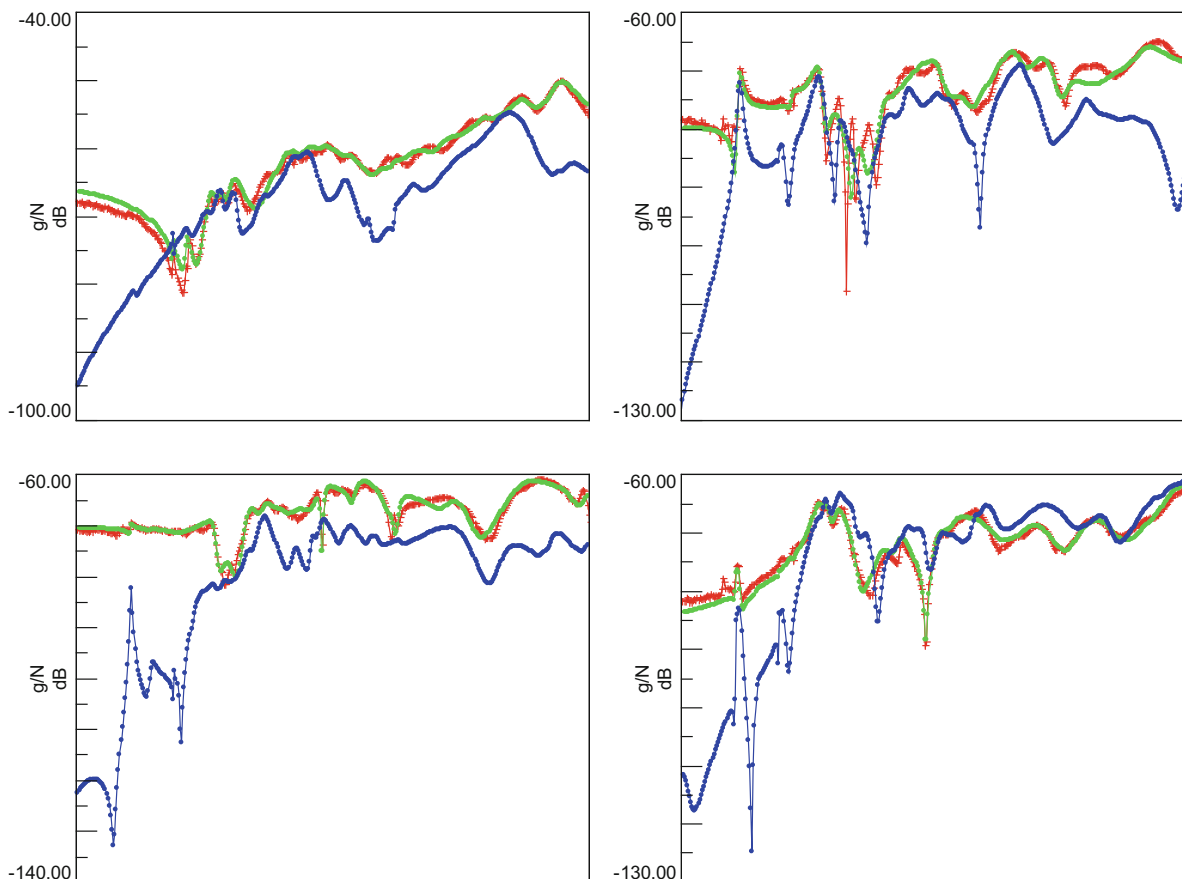


Fig. 19.10 The decrease of the MLMM cost function and the evolution of the frequencies and damping ratios at each iteration

MLMM iterations can be assessed in Fig. 19.12 for some modes. The mode shapes in both cases were also compared using the modal assurance criterion (MAC). From the complexity plots, it can be concluded that the MLMM with the real mode shape constraint activated normalizes the mode shapes and the obtained normal mode shapes agree well with the complex counterparts in terms of MAC value and the resonance frequency values for the selected set of modes. It should be mentioned that for those complex mode shapes that have low MPC value, they do not agree well with the estimated real modes in terms of MAC value.



**Fig. 19.11** The quality of the identified modal model in terms of the goodness of the fit for some selected FRFs: measured FRFs (Red), synthesized FRFs using linear least squares solution (Blue), and synthesized FRFs using MLMM method (Green) (the frequency axis is made invisible for confidentiality reason)

**Table 19.1** 2nd fully equipped car example: mean fitting error & correlation between the measured and synthesized FRFs

	Polymax (linear least-squares)	Iterative MLMM (nonlinear least-squares-based optimization)
Mean fitting error [%]	47.7	9.1
Mean fitting correlation [%]	74.9	92.7

### 19.3.2 Acoustic Modal Analysis Application

This experimental case concerns the cabin characterization of fully trimmed sedan car using acoustic modal analysis. The acoustic modal analysis of a car cavity (cabin), in general, implies the use of many excitation sources (up to 12 sources in some cases) and the presence of highly-damped modes [9, 20]. Due to the high level of the modal damping in such application, the many excitation locations are required to get sufficient excitation of the modes across the entire cavity and to avoid mode shape distortions that typically occur when a low number of acoustic sources are used. It has been observed that the classical modal parameter estimation methods have some difficulties in fitting an FRF matrix that consists of many (i.e. 4 or more) columns, i.e. in cases where many input excitation locations have been used in the experiment [9, 20].

Multiple inputs multiple output (MIMO) test were carried out inside the cavity of the Sedan car where 34 microphones located both on a roving array with spacing equal to around 20 cm and near to boundary surfaces captured the responses simultaneously. A total of 18 runs were performed to measure the pressure distribution over the entire cavity (both cabin and trunk) resulting in 612 response locations (in this paper a subset of  $N_o = 527$  have been used). For each run, up to 12 loudspeakers switched on sequentially were used for acoustic excitation. The excitation sources locations used in this paper ( $N_i = 10$  out of the available 12) are shown in Fig. 19.13 (Right). Continuous random white noise was chosen as excitation signal and the FRFs were measured up to 800 Hz using  $H_1$  estimator with 150 averages. Some typical measured FRFs are shown in Fig. 19.14. More details about the measurements procedure can be found in [21].

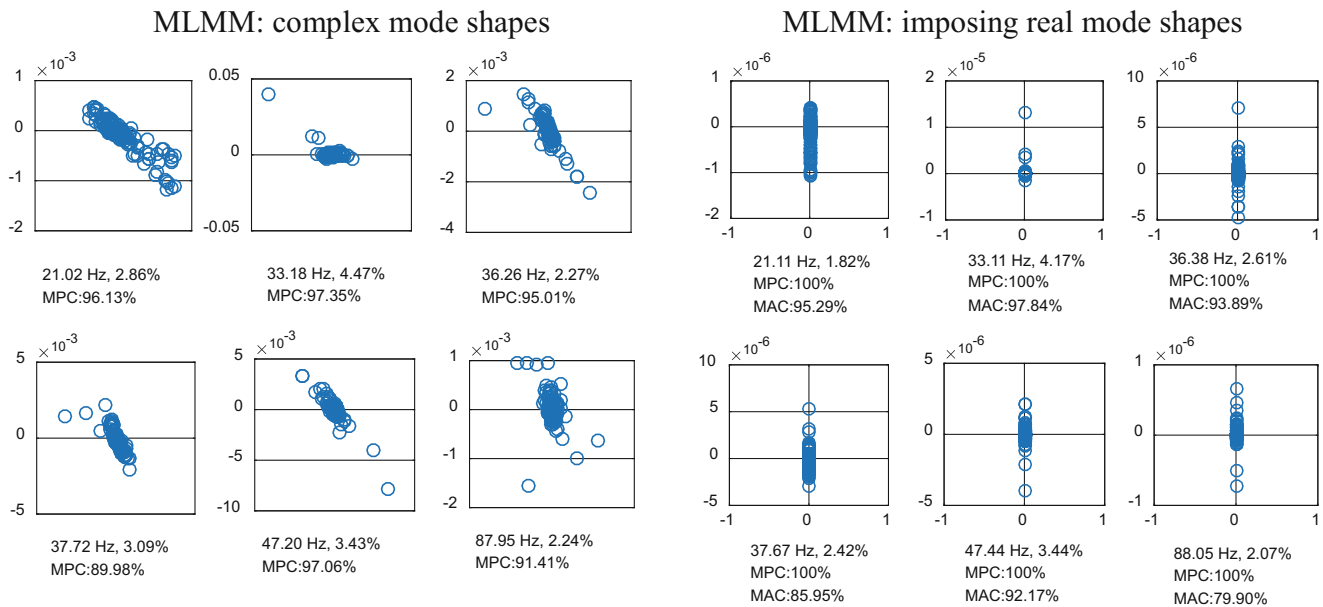


**Fig. 19.12** Mode shape complexity plots for some selected modes (for the plot at the right side, the MAC is calculated with respect to the complex mode shapes)

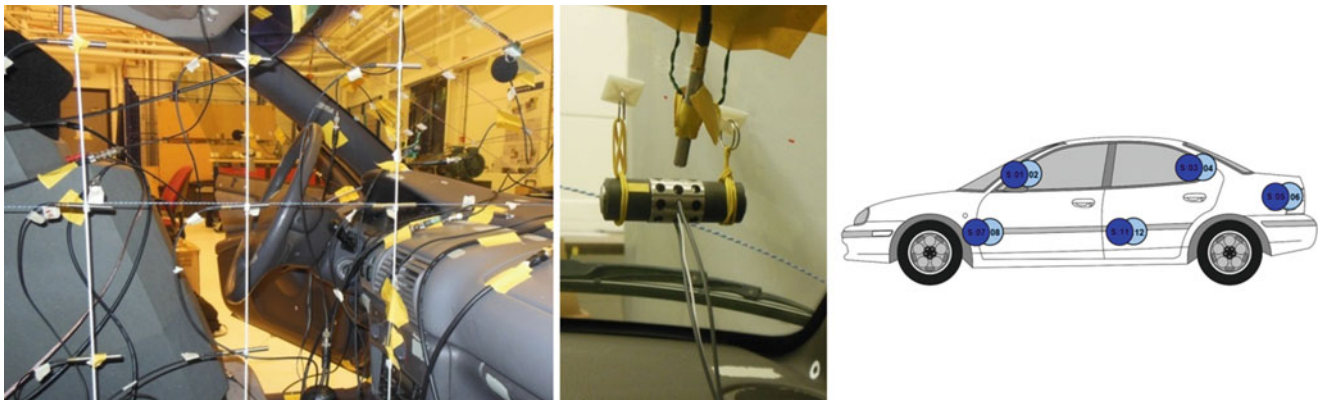


**Fig. 19.13** Sedan car under test: (Left) Microphones roving array inside the cavity; (Middle) one of the acoustical sources; (Right) source locations

A frequency band from 44 till 220 Hz was selected for modal parameter estimation. Polymax was applied to the large database (527 microphones, 10 acoustic sources, 450 spectral lines). In order to have a sufficient number of lines in the stabilization diagram, a model order of 150 was used. Based on the stabilization diagram, 13 modes were retained. The acoustic cavity and the flexible walls of the cavity constitute a coupled vibro-acoustic system and hence the modes of the system generally will consist of an acoustic part (pressure waves in cavity air) and a structural part (flexural waves in cavity walls). Therefore and despite the fact that both excitation and response measurement quantities are from the acoustic domain, also more structurally related modes may be retrieved from the analysis. Nevertheless, it appears that the selected modes are to a large extent “acoustically dominant” modes. Using the same Polymax poles, both real and complex mode shapes have been estimated. The curve-fitting quality is represented in Table 19.2 (Polymax columns). Afterwards, 10 MLMM iterations are applied to the Polymax initial estimates, both using the general complex mode formulation of the modal model and the constrained real modal model. Also the MLMM results are represented in Table 19.2. Whereas Table 19.2 provides averaged results over all FRFs, Fig. 19.15 shows the curve-fitting results of a typical FRF. From Table 19.2 it can be concluded that, obviously, the fitting quality degrades when using real instead of complex mode shapes in Polymax. When comparing MLMM with Polymax, it is clear that substantial improvements are obtained in terms of curve-fitting quality, both for general complex modes and real modes. Interesting to observe is that the real MLMM results are superior to the complex Polymax results, indicating that although the real modal model has less parameters that can be tuned, still superior results are obtained, thanks to the optimization process in MLMM.



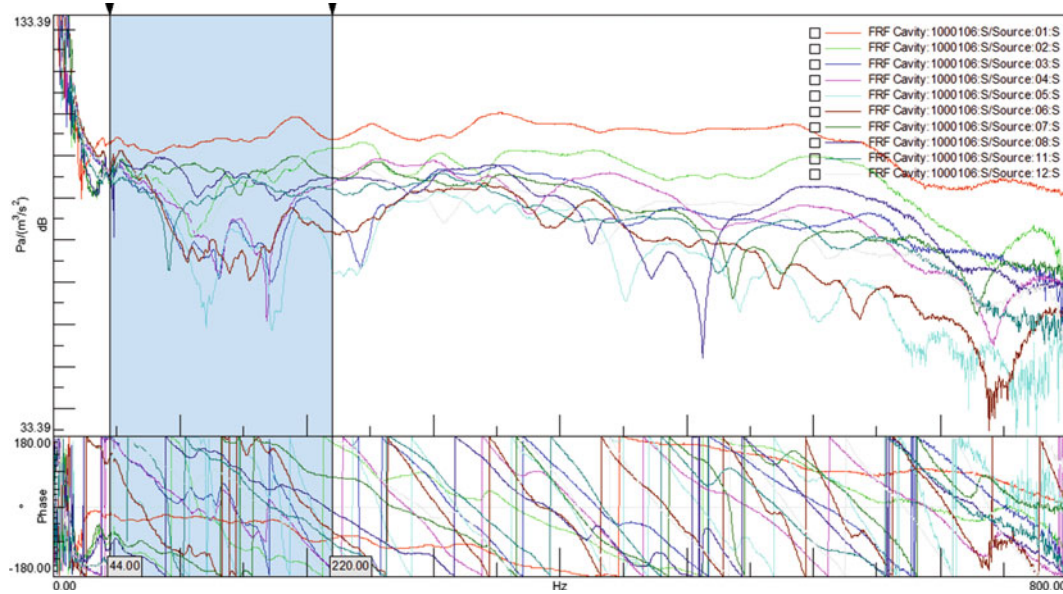


**Fig. 19.14** Typical FRF of one microphone measured in the cavity due to 10 excitation sources: full measured frequency band is shown with the selected band for modal analysis highlighted

**Table 19.2** Mean fitting error & correlation between the measured and synthesized FRFs: 1-step Polymax versus 10 iterations in MLMM (In both cases a real and a complex model is fitted)

	Polymax (linear least-squares)		Iterative MLMM (nonlinear least-squares-based optimization)	
	Real	Complex	Real	Complex
Mean fitting error [%]	27.7	20.9	9.6	5.6
Mean fitting correlation [%]	79.3	84.6	92.1	95.2

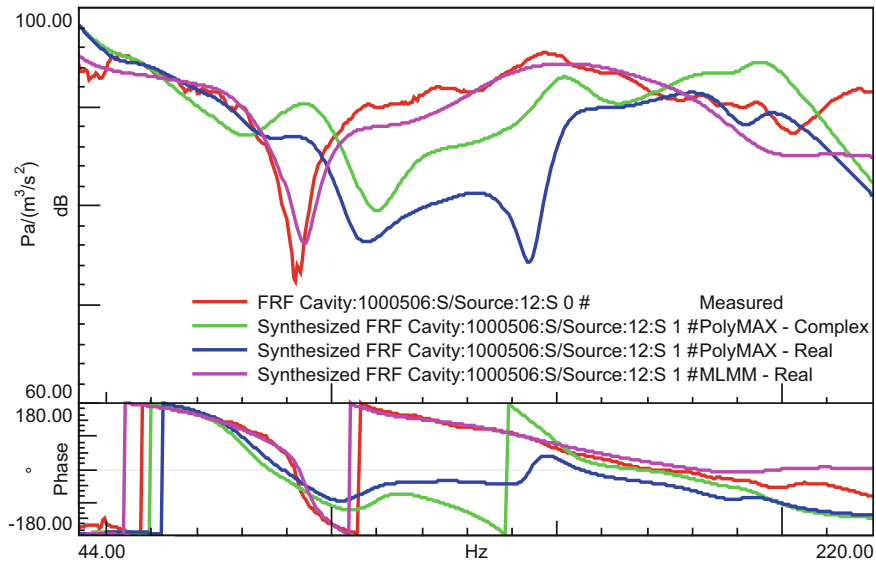


**Fig. 19.15** Typical acoustic FRF curve-fitting results. MLMM with real modes performs better than the traditional (real and complex) approach Polymax cases

A comparison between real and complex mode shapes is made in Fig. 19.16. Several mode shape pairs have lower MAC values. These are precisely the modes that show quite some complex behaviour when using the general (complex) modal model (wave propagation when animating the mode shape, higher complexity indicators such as MPC and MPD [22]). An example of such mode shape pair is provided in Fig. 19.17. The (complex) mode shape (Right) had quite high complexity



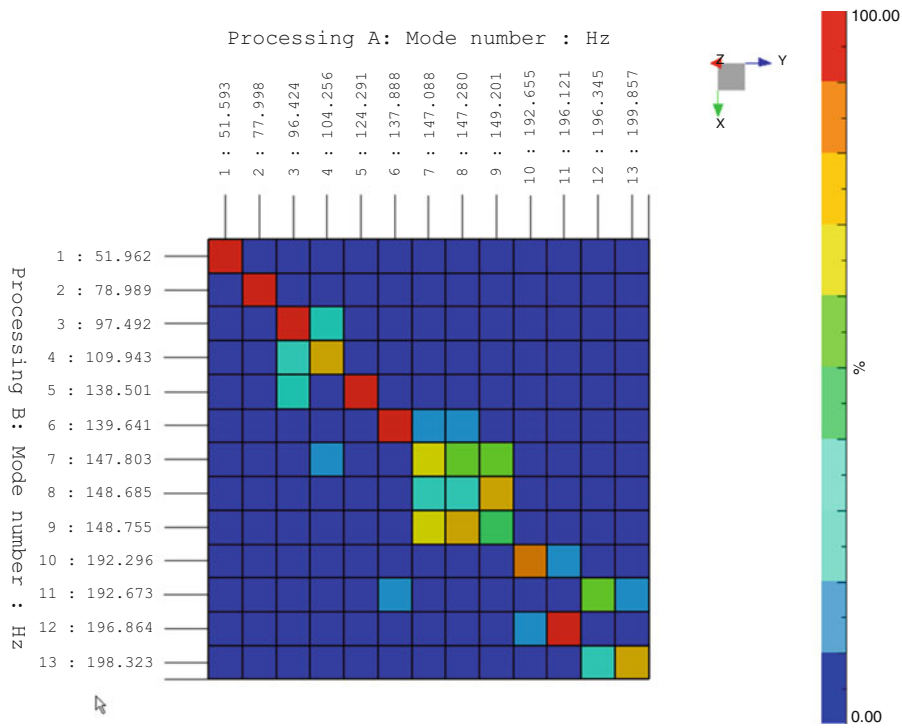


Fig. 19.16 MAC values between complex and real mode shapes (MLMM with 10 iterations)

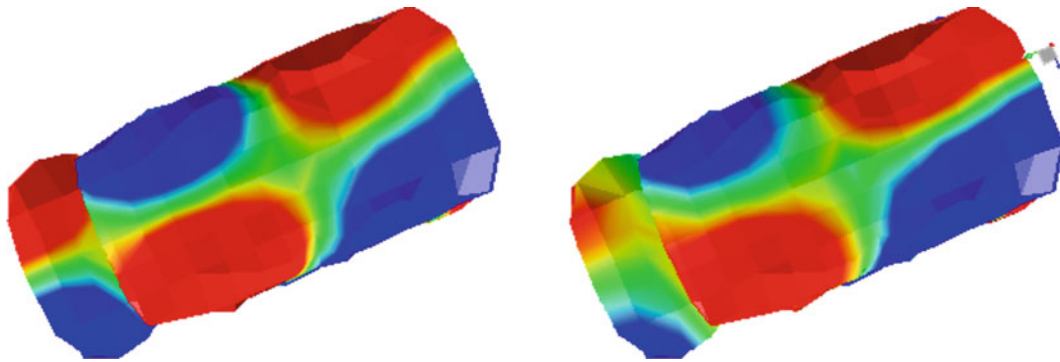


Fig. 19.17 (Left) Easily interpretable Real mode shape; (Right) complex mode shape with phase differences

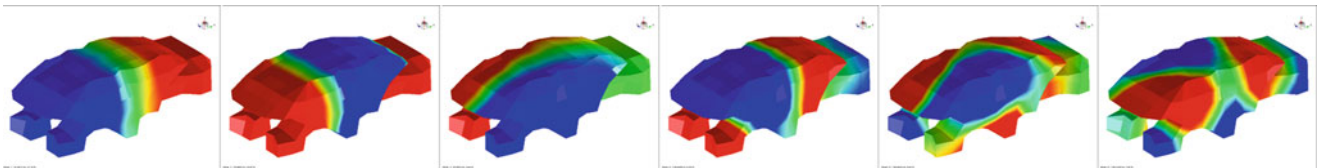


Fig. 19.18 Real mode shapes obtained by applying MLMM

indicators: MPC = 84%, MPD = 26°). The MAC between the real and complex mode shape is 81%. Real mode shapes are typically easier to interpret and may be more suited for correlation with FE models [23]. Some other real MLMM mode shapes are represented in Fig. 19.18.

## 19.4 Conclusions

An advanced iterative frequency-domain modal parameter estimation technique called MLMM is presented and successfully validated using some real challenging industrial applications. The MLMM method estimates directly the modal model by minimizing iteratively the errors between the measured FRFs and the modal model using a non-linear optimization technique. The main design requirement of the MLMM method was to deliver high quality modal models that could accurately fit an entire FRF matrix with a (very) large amount of columns; while at the same time to incorporate some physically motivated constraints like FRF reciprocity and real (normal) mode shapes. The application of the MLMM method to the structural and acoustic modal testing domains showed that the MLMM method compared to the traditional modal estimators is capable to achieve its target of delivering more accurate modal models; even when the constraints are taken into account.

## References

1. Pintelon, R., Schoukens, J.: *System Identification: A Frequency Domain Approach*. Wiley IEEE Press (2012)
2. Balmes, E.: Frequency domain identification of structural dynamics using the pole/residue parametrization. In: *Proceedings of the 14th International Modal Analysis Conference*, Dearborn, MI, USA, 1996
3. Heylen, W., Lammens, S., Sas, P.: *Modal Analysis Theory and Testing*. Katholieke Universiteit Leuven, Department Werktuigkunde, Heverlee (2016)
4. Snoeys, R., Sas, P., Heylen, W., Van der Auweraer, H.: Trends in experimental modal analysis. *Mech. Syst. Signal Process.* **1**(1), 5–27 (1987)
5. Van der Auweraer, H.: Structural dynamics modeling using modal analysis: applications, trends and challenges. In: *Proceedings of IEEE Instrumentation and Measurement Technology Conference*, Budapest, Hungary, 2001
6. Tsuji, H., Maruyama, S., Yoshimura, T., Takahashi, E.: Experimental method extracting dominant acoustic mode shapes for automotive interior acoustic field coupled with the body structure. *SAE Int. J. Passenger Cars Mech. Syst.* **6**(2), 1139–1146 (2013)
7. El-Kafafy, M., Peeters, B., Guillaume, P., De Troyer, T.: Constrained maximum likelihood modal parameter identification applied to structural dynamics. *Mech. Syst. Signal Process.* **72–73**, 567–589 (2016)
8. Accardo, G., El-kafafy, M., Peeters, B., Bianciardi, F., Brandolisio, D., Janssens, K., Martarelli, M.: Experimental acoustic modal analysis of an automotive cabin. In: De Clerck, J. (ed.) *Experimental Techniques, Rotating Machinery, and Acoustics*, vol. 8, pp. 33–58. Springer International Publishing (2015)
9. Peeters, B., El-Kafafy, M., Accardo, G., Knechten, T., Janssens, K., Lau, J., Gielen, L.: Automotive cabin characterization by acoustic modal analysis. In: *Proceedings of the JSAE Annual Congress*, Japan, 2014
10. Yoshimura, T., Saito, M., Maruyama, S., Iba, S.: Modal analysis of automotive cabin by multiple acoustic excitation. In: *Proceedings of ISMA2012-USD2012*, Leuven, Belgium, 2012
11. El-Kafafy, M., De Troyer, T., Peeters, B., Guillaume, P.: Fast maximum-likelihood identification of modal parameters with uncertainty intervals: a modal model-based formulation. *Mech. Syst. Signal Process.* **37**, 422–439 (2013)
12. El-kafafy, M., Accardo, G., Peeters, B., Janssens, K., De Troyer, T., Guillaume, P.: A fast maximum likelihood-based estimation of a modal model. In: Mains, M. (ed.) *Topics in Modal Analysis*, vol. 10, pp. 133–156. Springer International Publishing (2015)
13. Guillaume, P., Verboven, P., Vanlanduit, S.: Frequency-domain maximum likelihood identification of modal parameters with confidence intervals. In: *Proceedings of the 23rd International Seminar on Modal Analysis*, Leuven, Belgium, 1998
14. Hermans, L., Van der Auweraer, H., Guillaume, P.: A frequency-domain maximum likelihood approach for the extraction of modal parameters from output-only data. In: *Proceedings of ISMA23, the International Conference on Noise and Vibration Engineering*, Leuven, Belgium, 1998
15. Guillaume, P., Verboven, P., Vanlanduit, S., Van der Auweraer, H., Peeters, B.: A poly-reference implementation of the least-squares complex frequency domain-estimator. In: *Proceedings of the 21st International Modal Analysis Conference (IMAC)*, Kissimmee (Florida), 2003
16. Peeters, B., Van der Auweraer, H., Guillaume, P., Leuridan, J.: The PolyMAX frequency-domain method: a new standard for modal parameter estimation? *Shock Vib.* **11**(3–4), 395–409 (2004)
17. Van der Auweraer, H., Liefoghe, C., Wyckaert, K., Debille, J.: Comparative study of excitation and parameter estimation techniques on a fully equipped car. In: *Proceedings of the International Modal Analysis Conference (IMAC)*, Kissimmee, FL, USA, 1993
18. El-kafafy, M., Guillaume, P., Peeters, B.: Modal parameter estimation by combining stochastic and deterministic frequency-domain approaches. *Mech. Syst. Signal Process.* **35**(1–2), 52–68 (2013)
19. Peeters, B., El-Kafafy, M., Guillaume, P.: The new PolyMAX Plus method: confident modal parameter estimation even in very noisy cases. In: *Proceedings of the International Conference on Noise and Vibration Engineering (ISMA)*, Leuven, Belgium, 2012
20. Tsuji, H., Maruyama, S., Yoshimura, T., Takahashi, E.: Experimental method extracting dominant acoustic mode shapes for automotive interior acoustic field coupled with the body structure. *J. Passenger Cars Mech. Syst.* **6**(2), 1139–1146 (2013)
21. Accardo, G., El-kafafy, M., Peeters, B., Bianciardi, F., Brandolisio, D., Janssens, K., Martarelli, M.: Experimental acoustic modal analysis of an automotive cabin. In: *Proceedings of International Modal Analysis Conference (IMAC XXXIII)*, Springer, Orlando, FL, 2015
22. Siemens Industry Software: *LMS Test.Lab Modal Analysis 16A - User Manual*. Leuven, Belgium (2016)
23. Hwang, K.H., Choi, S.C., Van Genechten, B., Jeon, J.H., Brechlin, E.: Acoustic finite element model validation of vehicle interior cabin from acoustic mode and transfer function. In: *Proceedings of NAFEMS World Congress*, San Diego, CA, USA, 2015